Author:
Cross, Ted

Title:
Seismic risk assessment through non-linear time-history analysis of template buildings in Nepal
RC with infills and stone masonry

Seismic Risk Assessment Through Non-Linear Time-History Analysis of Template Buildings in Nepal: RC with Infills and Stone Masonry

Theodore Cross

Department of Civil Engineering

University of Bristol

A dissertation submitted to the University of Bristol in accordance with the requirements for award of the degree of Doctor of Philosophy in the Faculty of Engineering

Date of submission: 06/05/2022

Word count: 73,720

Abstract

The implicit risk of unreinforced template masonry (URM) and reinforced concrete (RC) with masonry infill structures is assessed. Template design is an approach used by non-governmental organisations (NGOs) in developing countries where a single design is replicated at many sites as a method of reducing design and approval costs. Pahar Trust has provided the design of a template RC with infill school and a URM health centre for this research. These structures are used as benchmark cases for assessing the implicit risk to template across Nepal, allowing the assessment of the suitability of the template approach. Implicit risk is the unavoidable seismic risk to a structure built according to local design codes.

A detailed finite element (FE) model of the template RC with infill school is developed, and non-linear time history analysis is used to find the fragility curves for various limit states. These fragility curves are integrated with up-to-date seismic hazard maps to assess the varying risk across Nepal. This showed that the risk values for the code-compliant structure were below threshold values from Europe at all locations across Nepal.

The spectral-based FAST method is adapted and verified for the Nepalese context. The FAST method was initially conceived for Southern European RC buildings with hollow clay brick infills. It is updated for Nepal by reviewing the local code prescriptions, construction practices and material properties for RC masonry infills. The input parameters are updated, and the method is validated using numerical models and a building dataset with damage information from Gorka 2015. The method captures the dominance of the low damage states in the specific Kathmandu neighbourhood considered but still overestimates the overall damage.

Continuous micro-modelling of an unreinforced irregular masonry pier is verified. An FE model of an experimental campaign carried out by (Senaldi et al., 2018) is developed, and the shear capacity of the numerical model is compared to the experimental values. The code-based approach from CNR-DT 212/2013. (2014) is used as a further point of comparison. The comparisons show that continuous micro-modelling can accurately capture the shear capacity and failure mechanism.

Finally, a continuous micro-model of the Pahar Trust template health centre is developed, and NLTHA is used with a cloud analysis to derive fragility curves. An established equivalent SDOF approach is also used for deriving fragility curves as a point of comparison. The risk assessment is then carried out, which shows that the URM health centre exceeds European benchmark risk thresholds in some areas of Nepal.

Dedication and Acknowledgements

I would like to acknowledge the support of the Engineering and Physical Sciences Research Council grant code EP/R513179/1, UK.

This PhD would not have been possible without the support, guidance and supervision of Dr Flavia De Luca. Flavia and I both joined the University of Bristol in 2014, where she was allocated as my first-year tutor. Since then, she has been my tutor/supervisor every year and has taught me so much about engineering and beyond. Flavia's dedication to her work as an academic is unrivalled. I would also like to give special mention to Dr Raffaele De Risi, who has been an incredible second supervisor throughout this PhD and whose contributions have been greatly appreciated.

Most people insert a comment in their dedications such as "one page is not long enough to mention all the people who have supported me in this work". I will not be taking this approach.

I want to thank the University of Bristol Cycling Club. Particular thanks are aimed at Hugh Brashaw, James Pittard, Ollie Beresford, Charlie Lacaille, Andrew Kirby, Charlotte Davies, Jamie Atkins, and Carl Jolly. I would also like to thank Kate Mactear for assisting me during my small foray into running. Sport has been an important part of my University experience, and I would like to thank you all for the good times.

I would also like to thank people I have lived with over the last three and a half years, including Joe Beardsley, Archie Cross, Elliot Notman, Lizzy Jewitt and James Pittard (again). I would like to thank our impeccable communal cooking system, which seems to be incomprehensible to the rest of society.

I would like to thank those who supported my work in Pescara including Professor Guido Camata and Dr Massimo Petracca. I would also like to thank those friends in Pescara who made my time there thoroughly enjoyable, including Hannah Cartwright and Francesca Marafini.

Special thanks goes to fellow researchers at the University of Bristol including Luke Bowen, Maya Gumussoy, and Teoman Efeoglu.

Big Thanks to Cain Harniess for proof reading Chapter 3.

I would like to thank Pahar Trust for kindly providing the designs of two Template structures.

I want to thank my family including Mum, Dad, Archie, Eugene and Stella. I would also like to give special mention to my grandad who has inspired much of the family to follow in his footsteps and study civil engineering.

Finally I would to thank Lottie for all the good times over the last 2.5 years and for many more to come.

Author's Declaration

I declare that the work in this dissertation was carried out in accordance with the requirements of the University's *Regulations and Code of Practice for Research Degree Programmes* and that it has not been submitted for any other academic award. Except where indicated by specific reference in the text, the work is the candidate's own work. Work done in collaboration with, or with the assistance of, others, is indicated as such. Any views expressed in the dissertation are those of the author.

SIGNED: ..... DATE:.....

List of Publications

Parts of this thesis are based on the following publications:

1. **Cross, T**., De Luca, F., De Risi, R., Ranamagar, T. R., Mitchell, T., & Sweetman, A. (2020). Mapping the seismic safety of RC" template schools" in Nepal. *International Journal of Disaster Risk Reduction, 51*, 101844.[1]
2. **Cross, T**., De Luca, F., De Risi, R., Rana, T. R., Mitchell, T., & Sweetman, A. (2019). Pounding in Nepalese school buildings. In *Society for Earthquake and Civil Engineering Dynamics Conference*. SECED.[1]
3. **Cross T**, De Luca F, Woods GED, Giordano N, Pokhrel RM and De Risi R, (2021) FAST NEPAL: Regionally Calibrated Spectral Method for Reinforced Concrete With Masonry Infills. *Front. Built Environ*. 7:689921. doi: 10.3389/fbuil.2021.689921
4. **Cross T**, De Luca F, De Risi R, Camata G, and Petraca M, (2022) Micro-modelling of stone masonry template buildings as a strategy for seismic risk assessment in developing countries. Engineering Structures. Accepted for Publication[1]

The following publications were carried out during this PhD and contributed to the development of research skills and understanding, however they are not presented in this thesis:

1. **Cross, T**., Lombardi, L., De Luca, F., De Risi, R., Beardsley, J., de Podesta, M., ... & Sextos, A. (2019, June). Performance comparison of lead rubber bearing and friction pendulum isolation systems on a school in Kathmandu. In 2nd International Conference on Natural Hazards & Infrastructure| 23–26 June 2019| Chania, GREECE (pp. ID-244). National Technical University of Athens.[1]
2. **Cross, T**., De Luca, F., & De Risi, R. (2020, September). An experimental comparison of micro-modelling and meso-modelling for an unreinforced masonry wall. In *17th World Conference on Earthquake Engineering*.[1]
3. Syrett, L., **Cross, T**., De Risi, R., De Luca, F.,Schildkamp, M., (2022). Comparison of pushover curves of a two-storey stone cement masonry building with and without additional concrete bands. In *3rd European Conference on Earthquake Engineering and Seismology* (Submitted for peer review)[2]

[1] The first authors contribution included: methodology, data curation, analysis , data visualisation and writing. Co-authors reviewed and supervised the work

[2] Work supervised and numerical model Developed by Cross, T. Paper written by first author

Contents

Table of Figures

Table of Tables

Chapter 1: Introduction

1.1 Background and Motivation

Nepal is a seismically vulnerable country situated on the Indian and Eurasian Plate boundary between India and Tibet. As a developing country, the infrastructure in Nepal often lacks sufficient seismic design due to economic restraints. A combination of this seismic hazard and financial conditions results in a country that frequently endures heavy socioeconomic and humanitarian setbacks. This was highlighted in 2015 when a magnitude 7.8 **M**w earthquake occurred 40 miles east of Kathmandu, causing over 8,800 deaths and over 22,000 injuries (Government of Nepal, 2019).

After the 2015 Gorkha earthquake, Non-Governmental organisations (NGOs) played a significant role in helping Nepal rebuild vital pieces of infrastructure such as education and health care, with 770 out of the 7553 reconstructed schools being carried out by NGOs (Ministry of Education, Science & Technology, 2021). NGOs supported the immediate relief phase of the recovery as well as the long-term recovery of Nepal.

NGOs often use template designs to construct schools and health centres in developing countries. A template design is the design of a structure that can be used repeatedly across a country to reduce the design and approval costs, in contrast to a bespoke seismic design typically site-specific (i.e. typical practice in developed seismically vulnerable countries). These designs have slight modifications at different sites based on the site conditions and the availability of construction materials. In collaboration with the Asian Development Bank and the Japanese International Cooperation Agency (JICA), the Nepalese Department of Education has set out strict guidelines on school designs (Nepal Department of Education, 2016). This was set up in response to many schools in Nepal not being designed in adherence to seismic codes even when they are in place (D'Ayala et al., 2020). Once a design has been developed and satisfies these criteria, it must be approved by the Nepalese Department of Education. On top of ensuring that the schools meet the required guidelines, the Nepalese department of education is also responsible for ensuring that all school buildings are designed under the Nepalese Building Codes (Jones et al., 2016). This is one of the reasons why NGOs in Nepal use template designs as standard practice.

Seismic resistant construction techniques in Nepal have developed over the last 30 years with the introduction of the first Nepalese seismic construction code in 1994 (NBC 105, 1994),

which was brought into law in all cities by 2003 (Pant, 2015). Despite these advancements, Nepal still has a problem with code compliance caused by over 80% of buildings being built by their owner (Dixit, 2004). As a developing country, the construction practices in Nepal are often based on the availability of materials and the skills of the local tradespeople. Current construction practices are centred around the use of mud-bonded masonry. Over recent years reinforcing steel has become more common in Nepalese cities, causing reinforced concrete to become one of the most common building materials in Kathmandu (Chaulagain, 2012).

The implicit risk of a structure is defined as the unavoidable seismic risk to a structure designed and constructed according to local design codes, which refer to specific reliability levels and accepted level of safety (EN 1990-1, 2000). For instance, implicit risk has been assessed across Italy (Iervolino & Dolce, 2018), which found that buildings with a greater seismic hazard had a greater seismic risk despite the codes mandating a higher seismic design level and different requirements in terms of structural detailing.

Quantifying implicit risk relating to a specific template design within a particular country can be very important for NGOs to assess the level of safety at which they operate. A common misconception is that a structure built according to the latest structural codes will survive all possible earthquakes. By evaluating the implicit risk to the template design across a country with varying seismic hazard, NGOs can make an informed decision about the suitability of a given design in different locations.

This thesis looks at the seismic vulnerability of Nepal and applies some of the latest modelling techniques to quantify the risk of specific template design referred to different structural typologies, i.e., reinforced concrete (RC) with masonry infills and unreinforced masonry (URM) with specific reference to stone masonry. Using seismic risk data, infrastructure decisions can be made based on the current infrastructure seismic reliability. Furthermore, this risk information can be used to attempt to drive the local construction industry away from practices that result in high risk and towards a future of seismically robust construction. This thesis will assist these decisions by providing an accurate overview of seismic risk to RC and URM template buildings.

RC with infills is relatively well-developed in the Nepalese urban environment and less prone to template practice (e.g., varying number of storeys). There is still a strong Nepalese nuance in how these structures are realised relative to European RC structures with masonry infills. A general approach, suitable for regional vulnerability analyses, is developed to assess the risk to

Nepalese RC with infill structures. Unreinforced masonry (URM) is commonly used in Nepal, with 42% of structures being formed of mud bonded brick/stone (Government of Nepal, 2012). URM is more common in rural locations and is typically applied to building that are one or two storeys high. Bamboo, timber and cement bonded brick/stone are also commonly used building typologies in Nepal (Government of Nepal, 2012) however they will not be the subject of research in this thesis.

1.2 Objectives

This thesis aims to use the latest structural modelling, fragility, and risk assessment methods to add to Nepal's understanding of seismic risk. Specifically, much of this thesis focuses on the use of template masonry and reinforced concrete by NGOs and their suitability in an area of variable seismic risk. The key objectives of this thesis are:

- To use a template design of a reinforced concrete (RC) structure with masonry infills to carry out a seismic risk assessment and hence infer the suitability of this technique in Nepal. RC with infill is an increasingly common structural typology in Nepal (Chaulagain, 2012). A further point of comparison will be to assess the efficiency of an intensity measure of a modified version of SA_{avg} relative to peak ground acceleration (PGA).
- To assess the importance of modelling the structural contribution of masonry infills in RC structures with masonry infills. RC structures with masonry infills are a common structural typology worldwide, often adding to the structure's stiffness. However, many structural codes do not account for this additional stiffness. This thesis aims to carry out a full seismic risk assessment on a structure with and without the structural contribution of the masonry infills.
- To update an established method of large-scale seismic vulnerability assessment (FAST method) for the Nepalese context. The FAST method is a rapid method for assessing the seismic vulnerability of RC-infilled structures (De Luca et al., 2014; De Luca et al., 2015), which is updated for the Nepalese context using local codes and material tests.
- To validate the latest masonry micro-modelling techniques for use on irregular stone masonry. Irregular stone masonry is one of Nepal's most common building typologies and can be split into rubble, semi-dressed, and dressed. This thesis aims to validate continuum micro-modelling on semi-dressed irregular masonry, using experimental pseudo-static pushover results from Senaldi et al. (2018).

- To investigate the effect of irregular bond pattern on the capacity of a masonry wall. A set of criteria are obtained for an equivalent regular wall to assess the necessity of measuring each stone of an irregular masonry wall.
- To use continuum micro-modelling on a template design of an unreinforced masonry structure to carry out a seismic risk assessment. Pahar Trust has also generously provided the design of an unreinforced masonry health centre. This is the basis of a case study for the suitability of template structures formed of unreinforced masonry. The health centre design is a single-story building with a sloped timber roof, and a nominal amount of reinforcement is provided in reinforced concrete bands at the sill, lintel and roof level.
- To investigate the necessity of a full multiple degree of freedom (MDOF) FE model by also carrying out the seismic risk assessment for an equivalent single degree of freedom (SDOF) system. The reduced requirement in computational power allows the use of incremental dynamic analysis (IDA) to derive the fragility curve. These fragility curves can then be compared to those derived from the MDOF model.

1.3 Outline

This thesis is split into seven chapters. Chapter 1 presents the introduction (as detailed above); Chapter 2 reviews the relevant literature; Chapter 3 covers the seismic risk of template RC structures; Chapter 4 examines the Nepal FAST method; Chapters 5 and 6 discuss the seismic risk to unreinforced masonry structures, and Chapter 7 draws and presents conclusions. The main themes of this thesis are indicated in Figure 1.1.

Figure 1. 1 Main themes of this thesis

Chapter 2 presents and reviews much of the relevant literature, specifically looking at the seismic vulnerability of Nepal in conjunction with structural modelling methods and risk assessment methods. This literature review looks at current construction practices and their seismic implications. It also looks at hazard assessments for Nepal and the implication for future earthquakes. The fundamentals of the finite element approach are explained and how it is applied for reinforced concrete and masonry. Various material models for steel and concrete are summarised. Different methods of modelling masonry structures are summarised, including the equivalent frame method, equivalent strut modelling, continuum modelling, the discrete element method (DEM), and continuous micro-modelling. The background on seismic risk assessment is then be presented to examine different methods of assessing the seismic hazard of an area. Several methods of deriving the fragility of a structure are presented: the cloud method, incremental dynamic analysis, the modified cloud method, and empirical fragilities. Finally, an overview of how fragility and hazard can be combined to find seismic risk is presented.

Chapter 3 covers the seismic risk assessment of the RC infilled template school structure provided by Pahar trust. The details of a non-linear finite element model of the structure are presented, followed by a description of how an equivalent strut model is applied. A model is created with and without considering the masonry infills. This is used as a point of comparison. A ground motion selection is carried out based on the criteria set out by Jalayer et al. (2017). NLTHA is then be carried out and the results used in a cloud analysis to derive the fragility curves. Fragility curves are derived explicitly for the exceedance of limit states based on threshold interstorey drift levels and for the occurrence of pounding. Using a seismic hazard map from Stevens et al. (2018), a complete seismic risk assessment is carried out in all locations across Nepal. These risk values are then compared to benchmark values from literature as to draw conclusions on the seismic safety of this template school.

Chapter 4 develops the FAST method (De Luca et al., 2015) for the Nepalese context. The FAST method is updated using local data for the drift at each damage state and the material properties. The Nepal FAST method is then applied to a catalogue of 6869 RC buildings with masonry infills. The results are then be compared to the observed damage from the Gorkha 2015 earthquake. The Nepal FAST method is also be applied to the RC school with masonry

infills from chapter 3. The fragility values from the two approaches can subsequently be used as a point of comparison.

Chapter 5 presents the application of the latest continuous micro-modelling methods for unreinforced masonry and verifies them based on the literature. The horizontal load capacity of a masonry pier is evaluated using both a code-based analytical approach and a numerical approach. The results are compared to experimental results from Senaldi et al. (2018). The effect of regularisation on a masonry pier is evaluated by comparing the shear capacity of an irregular pier and an equivalent regular pier. Finally, the sensitivity of specific mortar material properties is assessed for the shear capacity of masonry piers.

Chapter 6 applies the previous masonry modelling approach to a single story template structure provided by Pahar Trust. A detailed micro-model is created with an RC fibre section for the RC bands and linear elastic beam-column elements for the roof. A static pushover analysis is carried out on this multiple degree of freedom (MDOF) model. The pushover curve is used to develop a single degree of freedom model. An incremental dynamic analysis is used to derive fragility curves from the SDOF system, which has been developed, with a cloud analysis being performed on the MDOF model. This is followed by comparing the fragility curves of the two modelling approaches. Lastly, the full seismic risk assessment is carried out for both modelling approaches, and the risk values are compared to benchmark values.

Chapter 7 raises conclusions derived from the previous chapters. The implications of the risk values from chapters 3 and 6 are discussed, showing how various levels of ground motion may affect structures designed/built by the Pahar Trust. The results of the Nepal FAST method are explained, and conclusions are drawn on how the Nepalese building stock could perform in various earthquakes. The limitations of this research is summarised, and areas of further development are suggested.

Chapter 2: Review of Literature on the Seismic Risk to Nepal and Structural Modelling of Masonry and RC Buildings

Objectives of this chapter

This chapter will seek to lay out the relevant literature for this thesis. It will cover RC finite element modelling, masonry modelling techniques and seismic risk assessment. It will also cover background on the seismic risk to Nepal, covering previous earthquakes and current seismic design codes and building conventions. Limitations and issues presented in modern seismic risk assessment will also be covered in this chapter. The objectives of this chapter are as follows:

- Explain the importance of seismic design in Nepal by considering historical events and their respective consequence.
- Summarise typical construction practices in Nepal and how they may affect seismic performance. This will include structural codes and how they have changed in recent years.
- Review up to date approaches for developing finite element (FE) models of reinforced concrete structures and summarise the different approaches for modelling the contribution of masonry infills.
- Evaluate the different approaches for modelling masonry buildings, including equivalent frame approach, discrete element method and micro modelling.
- Summarise the key points on probability-based seismic risk assessment and its importance in developing countries.

2.1 Introduction

Seismic risk assessment is a holistic approach to determining the probability of a structure displaying damage or collapse due to an earthquake. Seismic risk assessment requires a high amount of information about the structure and the seismic hazard. Although the benefits of a seismic risk assessment are typically outweighed by the cost and complexity, particularly in a developing country. However, this may not be the case with a template structure where a single seismic risk assessment can be carried out for the structure, which is repeated multiple times across the country.

This literature review will look at the crucial relevant literature for the following chapters. One of the most important factors when carrying out a seismic risk assessment for different building typologies in Nepal is reviewing the background information on Nepal's construction practices and recent seismic events in Nepal. A background understanding of the local construction practices supports reasonable assumptions made when carrying out aspects of the risk assessment, such as finite element modelling and hazard selection. By reviewing previous earthquakes, we can understand the effect earthquakes have on local infrastructure and therefore the local community. This helps to highlight the importance of developing the understanding of the seismic risk to Nepal.

Current approaches for developing finite element (FE) models will be reviewed. Initially, the underlying concepts of finite element will be examined, such as non-linear geometric effects and approaches for damping. Following this, the current practices for applying finite element method to reinforced concrete (RC) structures will be reviewed. Finally, the varying approaches to modelling unreinforced masonry will be reviewed. This review will highlight which aspects of finite element modelling are applicable for the case of Nepalese buildings and will also expose areas of the literature which are not yet consolidated.

Different methods of deriving fragility curves are then reviewed. The characteristics of the finite element model will typically determine the suitability of different approaches for deriving fragility curves (i.e. a model that requires a high computational demand typically requires a fragility analysis method that requires fewer analyses). Different hazard assessment methods will then be reviewed. Although hazard assessment is not a focus of this thesis, a background understanding of how seismic hazard is measured is an important factor as this data plays a crucial role in seismic risk assessment.

This chapter should provide a background understanding of the core concepts relating to the seismic risk assessment of Nepal's unreinforced masonry and RC structures. It should also highlight the importance of further developing the understanding of seismic risk in Nepal to allow better decision making and ultimately drive down the impact of subsequent earthquakes.

2.2 Seismic Risk in Nepal

Nepal experiences a high level of seismic activity as it is situated on the most active segment of the Main Himalayan Thrust (MHT) (Ram and Wang, 2013). The Himalayas are formed of four East-West spanning faults, including the South Tibetan Detachment System (STDS), the Main Central Thrust (MCT), the Main Boundary Thrust (MBT), and the Main Frontal Thrust

(MFT). The MCT, MBT and MFT combine to form the Main Himalayan Thrust. These faults are shown in Figure 2.1. These faults have led Nepal to experience frequent earthquakes, including 1255, 1408, 1505, 1833, 1934 and 2015, each with a magnitude over 7.5. Gorkha 2015 is considered the deadliest earthquake in Nepal's history for several reasons, including high levels of population growth, rapid urbanisation, and low-quality infrastructure construction (Ram and Wang, 2013). The 1934 earthquake, magnitude $\mathbf{M}_w$ 8.1, is the largest in Nepal's recorded history, with an estimated 200,000 damaged buildings and 81,000 collapsed buildings. Although it did not have the highest death toll, this is likely due to a smaller Nepalese population in 1934 (Chaulagain, 2018). The Modified Mercalli intensity scale (MMI) is an intensity measure developed in 1902 which measures the intensity of an earthquake in terms of its effect on the surrounding infrastructure. The MMI scale ranges from I (not felt) to XII (extreme). The 1934 earthquake exhibited an MMI of X, IX and VII across Kathmandu Valley with high levels of liquefaction.

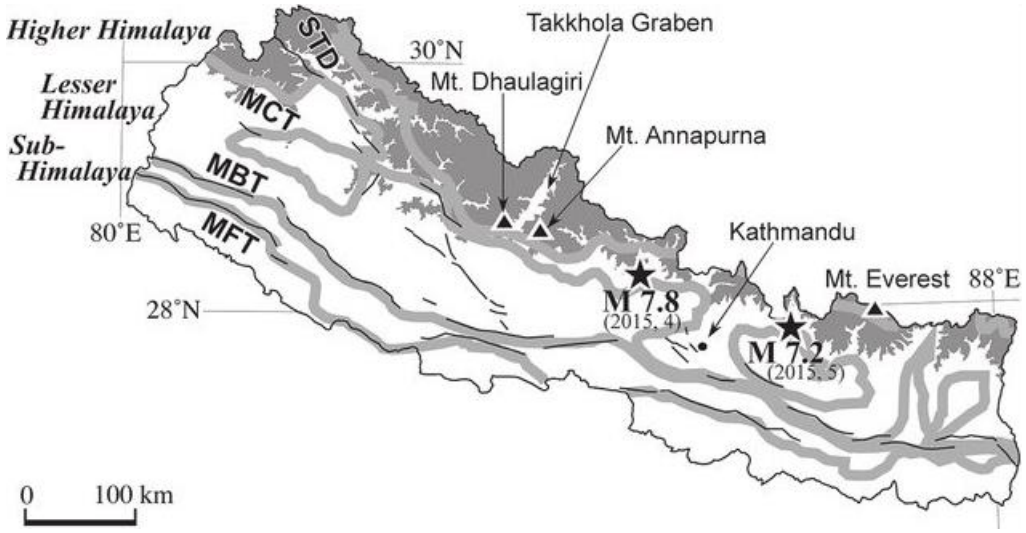

Figure 2. 1: Map of Main Central Thrust (MCT), the Main Boundary Thrust (MBT), and the Main Frontal Thrust (MFT) (Sakai et al. 2017)

The Nepalese National Society for Earthquake Technology (NSET, 2001) has made predictions for an earthquake with shaking equal to the 1934 earthquake. These predictions are based on the state of infrastructure at publication (2001). They concluded that 60% of buildings would likely be heavily damaged, half of the bridges in Kathmandu valley will be impassable, and 10% of roads would sustain moderate damage. 95% of water pipes would be significantly damaged. This emphasises the importance of improving the seismic resilience of Nepalese infrastructure. This thesis will focus on buildings, specifically in the education and health sector.

On April 25th, 2015, an earthquake of magnitude $\mathbf{M}_w$ 7.8 struck roughly 80 km northwest of Kathmandu near Gorkha. This was the largest earthquake in Nepal since 1934. Two aftershocks of $\mathbf{M}_w$ 6.6 and 6.7 occurred in the hour immediately after the mainshock, and a further aftershock of $\mathbf{M}_w$ 7.3 occurred 17 days later, causing more fatalities (Elliot et al., 2016). The earthquake led to the destruction of over 250,000 buildings Homes (Liang & Zhou 2016). The earthquake caused damage to buildings, roads, hydroelectric infrastructure and water services. An assessment carried out after the event by the National Planning Commission (NPC) of Nepal concluded that a total of $7 billion worth of damage occurred (Nepal National Planning Commission, 2015). The NPC also concluded that the earthquake pushed at least 700,000 people into poverty.

The Gorkha 2015 Earthquake severely affected the education system in Nepal. It was reported that 870,000 students could not return to school immediately after the event. (United Nations, 2015). This was due to the destruction of 28,570 classrooms and damage to 12,440 classrooms. Before the 2015 earthquake, efforts were made to increase Nepalese school buildings' seismic safety. In 2012, the Nepalese Department of Education (DoE) prepared the school safety action plan, which involved retrofitting 260 school buildings. At the time of the 2015 earthquake, 160 of these retrofits had been completed, and none experienced any damage (Nepal National Planning Commission, 2015). The projected time to reconstruct schools was 2-3 years, with 15,000 temporary learning centres being used during the reconstruction phase.

Non-governmental organisations play an important role in reconstructing Nepalese schools, with 770 out of 7553 reconstructed schools being carried out by NGOs (Ministry of Education, Science & Technology, 2021) after the 2015 earthquake. NGOs typically specialise in the type of school that they construct. This can mean using one building technology, serving one area or using one design. Although that can improve the efficiency of the project (i.e. deliver more schools in a given time or budget), it can lead to the delivery of schools not most suited by the local community (Westoby et al., 2021). An example of this is highlighted in Westoby et al. (2021), where an example is given where a community received construction materials for a masonry building. However, due to damage to the roads supplying this community, the bricks would often arrive broken, and sand would often spill out. This could have been avoided by more flexibility in construction methods and using locally sourced materials. The NGOs involved in reconstructing schools after the Gorkha earthquake included Save the children (Save the Children, 2016) and the Disaster Emergency Committee (Disaster Emergency

Committee, 2016). One of the methods used by NGOs is to have a template design where the same design is replicated at multiple locations with slight adjustments made based on local materials or site conditions.

This overview of the seismic risk to Nepal demonstrates the importance of researchers investigating the suitability of the current construction practices in Nepal and assessing the likely consequences of another seismic disaster. Assessing the seismic risk to infrastructure in Nepal allows the government to make informed decisions regarding building regulation and public investment. An accurate picture of the seismic vulnerability of local infrastructure can enable emergency responders to make a more informed decision in the event of an earthquake. A seismic risk assessment of Nepal also allows NGOs to make informed decisions on where and how to improve the infrastructure in the local communities.

2.3 Construction Practices and Codes in Nepal

Although Nepal is still a developing nation, it has made significant advances in construction technology over the last 20 years. Typical building materials in Nepal are unreinforced masonry with mud mortar, unreinforced masonry with cement mortar, reinforced concrete with masonry infills and bamboo. Reinforced concrete structures have risen to prominence in recent decades(Dizhur et al., 2016), however they are still concentrated in the cities and did not form a significant proportion of the residential buildings in the 2011 Nepalese Census, shown in Figure 2.2. The distribution of these building typologies for houses can be seen in Figure 2.2a (Government of Nepal, 2012). The foundations of Nepalese residential buildings are typically made with mud-bonded bricks/stone or cement-bonded bricks/stone. The distribution of foundation materials can be seen in Figure 2.2b. The roofing type for Nepal is relatively evenly split between thatch/straw, galvanised iron, tile/slate and reinforced concrete, as shown in Figure 2.2c (Government of Nepal, 2012).

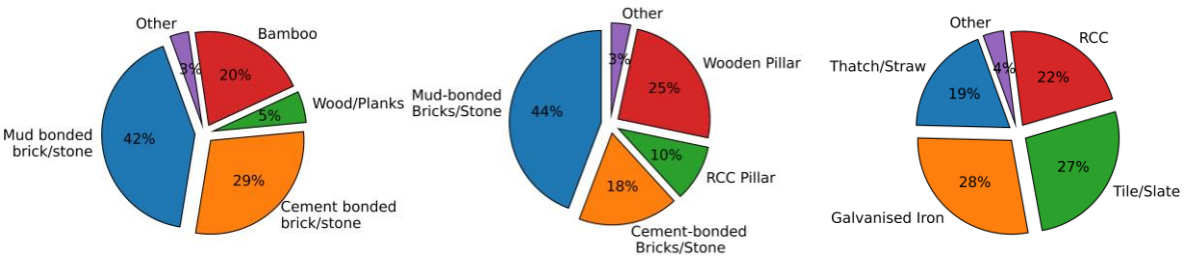

(a) (b) (c)

Figure 2. 2: Distribution of building materials for the (a) outer wall, (b) foundation, (c) roof (figure made based on data from 2011 census (Government of Nepal, 2012))

(a)

(b)

(c)

Figure 2. 3 Examples of (a) rubble stone masonry in cement mortar (Schildkamp et al., 2019) (b) RC with masonry infills (Varum et al., 2017) (c) Concrete blocks with cement mortar (Shrestha et al.,2021)

RC infilled buildings are among the most common structural typologies in urban and semi-rural areas in Nepal, such as the Kathmandu Valley. RC with infills are used for residential, office, and institutional use and has rapidly become prominent over the last few decades (Dizhur et al., 2016). The masonry infill is usually formed of solid clay bricks with cement mortar or even mud mortar. These infills are not typically designed to resist lateral loads; however, they can increase the stiffness and, therefore, the structure's natural frequency. In recent years medium-rise buildings (10 – 20 storeys) have become more common in Kathmandu. These are often formed of RC with masonry infill. These were shown to provide adequate structural performance in the 2015 earthquake with little recorded structural damage, however, there was significant non-structural damage recorded (Barbosa et al., 2017).

Unreinforced masonry (URM) is primarily considered the most vulnerable building typology in Nepal (Brando et al., 2017). In Kathmandu, URM buildings are typically square or rectangular in plan; however, due to the demand for residential buildings in Kathmandu, it is not uncommon for additional stories to be added to existing structures. In Kathmandu, fired clay bricks are typically used with mud mortar. However, in more rural locations, stone is more

commonly used. In many cases, URM structures are owner built and are widely not designed with any design codes. Most municipalities in Kathmandu have a system for granting building permits, however these permits usually do not require a strength requirement. The acquisition of a building permit depends on ground coverage, height, toilet provision, and liquid waste disposal. Kathmandu and Lalitpur now require structural drawings for buildings greater than three stories or over 1000 sq. ft in plan (Mishra, 2019). Recent mandatory rule of thumb codes (NBC-202:1994., 1994) have been released but are rarely followed (Pokharel et al., 2017). Stone masonry can come into three broad categories, rubble, semi-dressed and dressed. More recent unreinforced masonry structures have a nominal amount of reinforcement in the form of shallow RC bands. These bands are intended to add horizontal stiffness to the structure and ensure a box effect. The Nepalese code (NBC-203:2015., 2015) recommends these bands are formed of RC; however, where this is not possible, provisions are provided for bamboo and timber horizontal bands. These horizontal bands are recommended to be placed at plinth, sill, and lintel levels. A full review of how different countries' seismic codes are applied to the case of unreinforced masonry construction can be found in Schildkamp et al. (2020).

Nepal has various codes for the design of masonry buildings, referred to as Nepalese Building Codes (NBC). These building codes were first written and released in 1994 but were not brought into law until 2003. They are now legally binding in all 130 municipalities; however, this does not cover towns and villages (Pant, 2015). These initial codes included NBC 105 (1994), titled “Seismic design of buildings in Nepal”. NBC 105 (1994) states it should be used with the Indian standard Code of Practice for Earthquake Resistant Design and Construction of Buildings (IS 4326.,1976). NBC 105 (1994) is intended for use with structures greater than 20 m^2 in plan, a height greater than 5 m, a building with water tanks up to 200 m^2, and all buildings with public access. NBC 105 (1994) uses the seismic coefficient method (more recently referred to as the equivalent static method) for buildings less than 40 m tall, regular in plan, and with no abrupt changes in lateral stiffness. Buildings that do not fit these criteria should use the modal spectrum method. Further details on the design spectrum can be found in Section 4.2.1. In 2020 NBC 105 (1994) was updated with NBC 105 (2020). This gave a more detailed approach for carrying out the equivalent static method. In NBC 105 (2020), the criteria for applying the equivalent static method are that the building is less than 15 m tall, has a period of less than 0.5s and the building is considered regular. NBC 105 (2020) uses an updated design spectrum shape which is significantly more conservative than NBC 105 (1994) but not as

conservative as (EN 1998-1, 2004). This is further explained in Section 4.2.1. NBC 105 (1994) and NBC 105 (2020) both provide PGA maps for Nepal based on probabilistic seismic hazard analysis (PSHA). Further details on these maps are given in Section 2.6.1.

Nepal Building Code 203 (NBC 203, 2015) provides guidelines for designing earthquake-resistant buildings from low strength masonry. Low strength masonry is defined as masonry that has non-erodible blocks (e.g., bricks and stone) with mud mortar as a binder. NBC 203 (2015) recommends that mud mortar be free of organic material and pebbles, and the sand content should be below 30%. It is suggested that dressed stones should be used to achieve accurate bedding and jointing. Provisions are also given for boulders and quarry stones. Bricks must conform to the Nepal Standard NS: 1/2035 and have a compressive strength no lower than 3.5 N/mm^2.

NBC 203 (2015) suggests that horizontal reinforced concrete bands are installed at plinth, sill, and lintel levels. The bands should be continuous and should be adequately tied to vertical reinforcement. The horizontal bands should be at least 75 mm deep at the sill and lintel level and at least 150 mm deep at the plinth level. The 75 mm deep bands should have at least two longitudinal reinforcement bars, and the 150 mm deep bands should have at least four longitudinal reinforcement bars.

Although building codes in 2015 suggested a design PGA of 0.36 g for Kathmandu and the Gorkha earthquake caused a PGA of 0.15 g, many buildings were damaged. This implies that the issue was not at the design requirements level but the lack of enforcement of the codes (Karmacharya et al., 2018). The lack of code implementation is caused by over 80% of buildings being built by their owner (Dixit, 2004). The National Society for Earthquake Technology (NSET) is a Nepalese non-governmental organisation advocating for reducing earthquake risk and increasing earthquake preparedness across Nepal. One of the main ways they try to achieve this is by increasing code compliance. This is achieved by educating local builders and craftsmen in construction techniques that could reduce the seismic risk (Dixit, 2004).

Construction practices in Nepal are usually based on the availability of building materials and the skillset of the local workforce. Nepalese census data has shown that mud bonded brick is the most common building material, and due to the brittle nature of mud, it can cause sudden failure when under seismic loads. Nepalese building codes have progressively tried to modify building habits to reduce the seismic risk whilst not being too cumbersome for the construction

workers and still using available materials. Examples of this are nominal vertical and horizontal reinforcement in mud bonded masonry structures. The introduction of increasingly more stringent building codes has encouraged the Nepalese construction industry to change their practices; however, code compliance still results in many buildings being built below the specified level.

2.4 Finite Element Modelling

Finite element modelling (FEM) is a widely used numerical method for characterising the response of solid structures. In FEM, the structural system is discretised into a finite number of elements. These finite elements interact with each other at node points. The element is modelled with a set of analytical functions that represent the displacement, stress and strain fields within the element.

These elements fit into three main categories: beam/column (1D), shell (2D) and solid elements (3D). Other element types include membrane elements, cable elements and zero-length elements, these are not covered in this thesis, but further information can be found in Mackerle (2002).

A beam-column element can be implemented into a finite element using four approaches: plastic hinge, non-linear spring hinge, finite length hinge and fibre sections. Both the plastic hinge and the non-linear spring hinge use a zero-length element at each end of the element. By concentrating the plasticity, these elements are relatively numerically efficient. The finite length hinge uses distributed plasticity along a predefined element length at each end. The finite length hinge more accurately captures the yielding of the member over the end of the member; however, it is less numerically efficient than the concentrated hinge methods.

The final method uses an integration of a series of cross-sections along the length of the beam. This is often referred to as a fibre section and is the most commonly used method due to its compromise between accuracy and computational cost. The assumption is that these plane sections remain in-plane, which is the case at low levels of displacement. The cross-section is integrated numerically along predefined sections of the beam using a force or displacement-based approach (Deierlein et al., 2010).

A shell element is a 2D element typically in 3D space. It is typically used on objects where one dimension is more than 20 times smaller than the other dimension. Shell elements require a 3D volume to be converted into a series of surfaces. Shell elements typically have a significantly

shorter meshing time than a solid element approach. Shell elements are not prone to shear locking, and the computational time is substantially shorter than for solid elements.

2.4.1 Non-linear Geometric Effects

Two types of geometric non-linearities affect a deformed frame structure. These are *P-δ* effects and *P-Δ* effects. *P-δ* effects relate to the local deformation relative to the chord between the two end nodes. This is shown in Figure 2.4a. *P-δ* typically slightly reduces the buckling capacity of axial members, however, the effect is relatively small at low levels of deformation and is therefore often not accounted for (Deierlein et al., 2010). *P-Δ* are commonly caused by drifts in a building and are caused by the offset vertical load, as shown in Figure 2.4b. The forces are typically significantly higher and ultimately cause a loss of lateral stiffness.

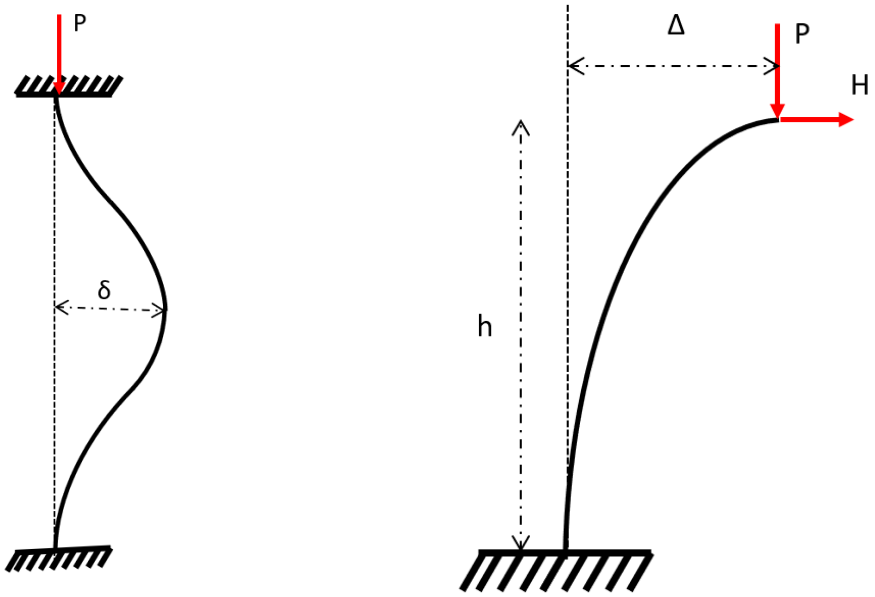

(a) (b)

Figure 2. 4: (a) schematic of P-δ effects in a fixed-fixed column, (b) schematic of P-Δ effects in a laterally loaded column

2.4.2 Damping

Damping is caused by the loss of energy through friction and other resistive forces and results in the reduction of the amplitude of an oscillation. The internal damping of a material is not necessarily related to the frequency. Damping methods that are independent of the frequency are referred to as hysteretic damping (also known as material damping). Hysteretic damping is not applicable for a non-linear model, and therefore, a frequency-dependent model is required (Nakamura, 2016). For non-linear transient analysis, Rayleigh damping is commonly used. Rayleigh damping is formed of the sum of a mass proportional component and a stiffness

proportional component. The equation of motion (i.e. the sum of forces is zero) is given in Equation 2.1, where $[M]$ is the mass matrix, $\{U\}$ is the displacement vector and $[K]$ is the stiffness matrix. The equation for the damping vector, {D(t)}, can be given by Equation 2.2, where α and β are the mass and stiffness coefficients, respectively. The mass and stiffness coefficient equations are shown in Equations 2.3a and 2.3b. Rayleigh damping assumes an equal damping ratio at the two corner frequencies, referred to as ω_1 and ω_2, as shown in Figure 2.5. The values used for these corner frequencies are subject to debate and depend on material and structural system; however, first and third modes are commonly used (Chopra, 2007). Figure 2.5 shows the Rayleigh damping with a target damping ratio of 5% and corner frequencies of 1 rads^{-1} and 2 rads^{-1}. It can be seen in Figure 2.5 that at lower frequencies, the damping is mass-dominated, and at higher frequencies, the damping is stiffness dominated.

$$[M]\{\ddot{U}\} + \{D(t)\} + [K]\{U\} = 0 \tag{2.1}$$

$$\{D(t)\} = (\alpha[\mathrm{M}]+\beta[\mathrm{K}])\,\{\dot{U}\} \tag{2.2}$$

$$\alpha = \frac{2h\omega_1\omega_2}{\omega_1 + \omega_2} \tag{2.3a}$$

$$\beta = \frac{2h}{\omega_1 + \omega_2} \tag{2.3b}$$

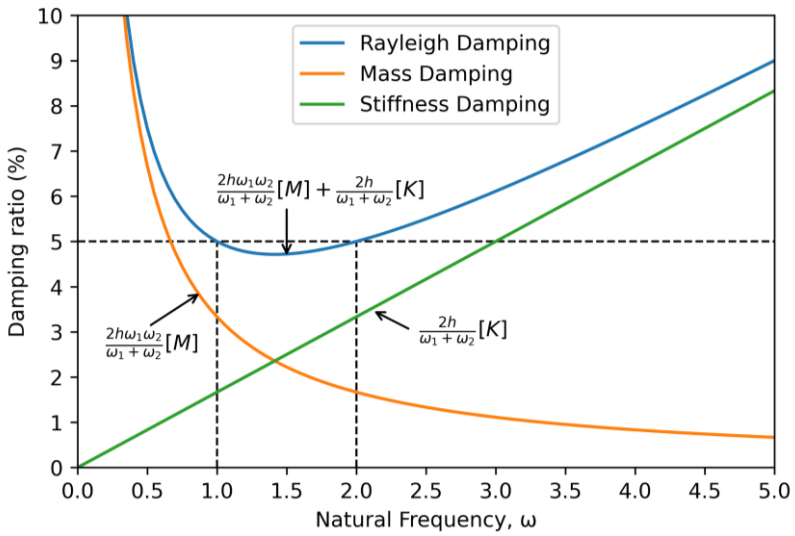

Figure 2. 5: An example of Rayleigh damping with a target damping ratio of 5% and corner frequencies of 1 rads^{-1} and 2 rads^{-2} (recreated from (Chopra, 2007))

The target damping ratio varies based on the level of damping typically offered by a given material. Literature has shown that 2% is a suitable target damping ratio for a reinforced concrete building. The structure's first and third fundamental period is used as the corner frequency (Dolšek and Fajfar, 2001). Newmark and Hall (1982) investigated the recommended damping ratios for different material properties using experimental data. Two sets of values are given, one set for the "working stress levels" where the stress is less than half of the yield strength and one set where the stress level is near the yield point. These results are shown in Table 2.1.

Table 2. 1: Suggested damping ratio for a variety of materials at working stress and near yield stress states, as suggested by Newmark and Hall (1982)

Stress Level	Material	Damping ratio (%)
Working stress (up to 50% of yield stress)	Welded steel, pre-stressed concrete, well-reinforced concrete	2-3
	Reinforced concrete with considerable cracking	3-5
	Riveted or bolted steel, Timber structures with nailed or bolted connections.	5-7
Near yield stress	Welded steel, pre-stressed concrete (without loss of prestressing)	5-7
	Prestressed concrete with no stress remaining	7-10
	Reinforced concrete	7-10
	Riveted or bolted steel, Timber structures with bolted connections.	10-15
	Timber structures with nailed connections	15-20

The upper and lower frequencies used to calculate mass proportional damping factor (α) and stiffness proportional damping factor (β) have been the subject of much research. A commonly used system is using the first and third fundamental period of a structure (Chopra, 2007); however, for the context of masonry corner frequencies ω_1 and ω_2 can be calculated from Equations 2.4a and 2.4b, where T^* is the initial period of the bilinear idealisation of an equivalent SDOF, μ is the available ductility of the bilinear system, and f_N is the frequency corresponding to the nth mode of vibration, where n is the mode which exceeds 85% participation mass in the direction of the analysis (Mouyiannou et al., 2014)

$$f_1 = \frac{1}{T^*\sqrt{\mu}} \qquad (2.4a) \qquad\qquad f_2 = f_N \qquad (2.4b)$$

2.5 Reinforced Concrete Structural Modelling

Reinforced concrete frame structures are typically implemented into a FE model using beam-column elements and a series of fibre sections to model the varying reinforcement over the

length of the element. Fibre sections are based on the assumption that deformations are small and plane sections remain in plane. The fibre section uses flexibility-based fibre elements. These elements are formed of a section subdivided into longitudinal fibres running parallel to the direction of the member. The constitutive response of the fibre is derived through the integration of the uniaxial response of the constitutive fibres (Taucer et al., 1991). Assuming equilibrium of the stress field across the fibre section, the displacement of fibres and, therefore, the curvature of the section can be calculated. The uniaxial response of the fibres are based on material models set out in Section 2.5.1 and Section 2.5.2. The two main formulations for beam-column elements are force-based and displacement-based. Force-based elements assume equilibrium between the element and the section forces. Section forces are found using interpolation from the system. The interpolation is based on the assumption that the axial force is constant and the moment distribution is linear along the element. The accuracy of a force-based approach can be improved by increasing the number of integration points or the number of elements. A displacement-based approach is more typically used in finite element approaches and is based on the principle of virtual displacements (PVD). Section displacements are interpolated from an approximate displacement field (Terzic, 2011). Implementing an FE model of an RC building requires the design of the reinforcement and a detailed model of the non-linear response of the concrete and steel.

2.5.1 Concrete Constitutive Models

When modelling RC frame structures using a fibre section, it is important to consider the 1D hysteretic stress-strain relationship of the concrete. When concrete acts in a reinforced concrete column, the concrete core within the transverse reinforcement acts as confined. This therefore requires a distinct concrete constitutive model for both the unconfined and confined concrete (Wu et al., 2018). This literature review will consider uniaxial concrete constitutive models as this is what is used in the fibre sections throughout this thesis. Many studies have been carried out on the stress-strain relationship of confined concrete starting in the 1950s when Chan (1955) investigated the axial strain-stress relationship of confined concrete. His proposed model is shown in Figure 2.6a. Chan found a strength increase of more than 50% relative to unconfined concrete and an increase in the ultimate strain of over 500%. A series of empirical factors relate the initial elastic stiffness to the stiffness from A to B and B to C. In confined concrete, the factor relating to the initial stiffness to the stiffness from B to C is a negative value to model the softening of the concrete.

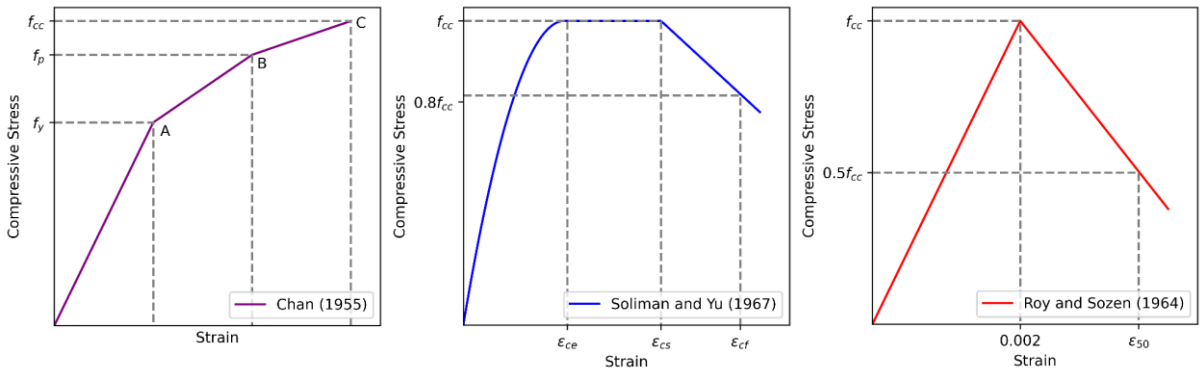

(a) (b) (c)

Figure 2. 6: Historical models of the stress-strain relationship of concrete. (a) Chan's Curve (1955), (b) Soliman and Yu's Curve (1967), (c)Roy and Sozen's curve (1964) (figure recreated using data from Sheikh, (1982)).

Soliman and Yu (1967) developed a stress-strain relationship for confined concrete as a function of the concrete cylinder strength (f'_c) and the ratio of the area of confined concrete to the area of concrete, as shown in Figure 2.6b. The first section of the curve is a parabola, up to the peak confined strength of concrete (f_{cc}), followed by a constant strength followed by a linear softening. The strain values at which each section finishes are established using an empirical equation that is a function of the cylinder strength and the ratio of the area of confined concrete to concrete.

Roy and Sozen (1964) developed a bi-linear idealisation for the stress-strain relationship of concrete, as shown in Figure 2.6c. They concluded that the confinement did not affect the concrete's peak strength, and only the post-peak stiffness was affected by the presence of the confining steel. They proposed an empirical formula for the strain value at which the concrete has softened to half its original strength (ε_{50c}), which is a function of the height of the section (h), the ratio of the volume of transverse steel to the volume of concrete (ρ_s) and the spacing of hoops (s).

The Kent and Park (1971) model was developed and later updated by Park et al. (1982). These two models and the model for unconfined concrete are shown in Figure 2.7. The unconfined and the initial Kent and Park (1971) model have a common initial branch (from A to B), given by Equation 2.5, where $f'c$ is the peak strength of concrete, ε_0 is the strain at maximum stress, and ε_c is the strain. The initial branch of Park et al. (1982) is given by Equation 2.6, which scales Kent and Park (1971) by k. The equation for k is given by Equation 2.7, where ρ_s is the ratio of the volume of steel hoops to the concrete core, and f_{yh} is the yield strength of the transverse reinforcement.

$$fc = f'c\left[\frac{2\varepsilon_c}{0.002k} - \left(\frac{\varepsilon_c}{0.002k}\right)^2\right] \tag{2.5}$$

$$f''c = kf'c \tag{2.6}$$

$$k = 1 + \frac{\rho_s f_{yh}}{f'c} \tag{2.7}$$

The softening section of the hysteretic response is given by Equation 2.8, where Z is the slope of decreasing strain indicated in Figure 2.7. The formulation of Z is given in Equation 2.9, where b'' is the width of the concrete core and s_h is the spacing of the hoops. The final section of the compressive response indicates that the concrete has a residual strength equal to 20% of the peak strength. This can be seen in Figure 2.7.

$$f_c = f_c''[1 - Z(\varepsilon_c - \varepsilon_o)] \tag{2.8}$$

$$Z = \frac{0.5}{\frac{3 + 0.29f_c'}{145f_c' - 1000} + \frac{3}{4}\rho_s\sqrt{\frac{b''}{s_h}} - 0.002K} \tag{2.9}$$

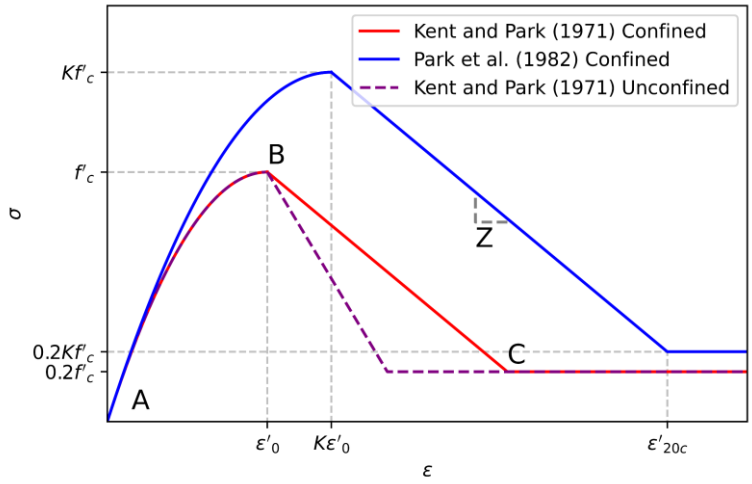

Figure 2. 7: Model for confined and unconfined concrete from Kent and Park (1972) and the modified confined model presented by Park et al. (1982) (figure recreated using data from Sheikh, (1982))

The most common concrete constitutive model is the Mander model (Mander et al., 1988). The Mander model uses the stress-strain relationship for confined concrete initially proposed by Popovics (1973) and shown in Figure 2.8. The uniaxial stress-strain relationship is given in Equation 2.10, where f_c and ε_c are the axial stress-strain of the concrete, f'_{cc} and ε'_{cc} are the

peak stress and corresponding strain, and r is a factor to account for the brittleness of the material, calculated using Equation 2.11. In Equation 2.11, E_c is the elastic modulus of the concrete. The peak stress is found using the failure criteria proposed by Mander and Priestley (1988) and given in Equation 2.12.

$$\frac{f_c}{f'_{cc}} = \frac{(\varepsilon_c/\varepsilon'_{cc}) \cdot r}{r - 1 + (\varepsilon_c/\varepsilon'_{cc})^r} \tag{2.10}$$

$$r = \frac{E_c}{E_c - f'_{cc}/\varepsilon'_{cc}} \tag{2.11}$$

$$f'_{cc} = f_{co}\left(2.254\sqrt{1 + 7.94\frac{f_l}{f_{co}}} - 2\frac{f_l}{f_{co}} - 1.254\right) \tag{2.12}$$

In Equation 2.12 f_l is the effective confining pressure given by Equation 2.13, where k_e is the confinement effectiveness coefficient. K_e is calculated using Equations 2.14a and 2.14b for circular and square sections, respectively. In Equation 2.14, s' is the hoop spacing, d_c is the confined core diameter, and p_{cc} is the ratio of the area of longitudinal reinforcement to the area of core concrete. In Equation 2.13 f'_l is the effective confining pressure provided by the steel. This can be found by assuming equilibrium at the yield point of the steel. This is shown in Equation 2.15, where f_{sy} is the yield strength of the hoops and A_{sp} is the area of the transverse steel cross-section.

$$f_l = f'_l \cdot k_e \tag{2.13}$$

$$k_e = \frac{1 - \frac{s'}{2d_c}}{1 - \rho_{cc}} \tag{2.14a}$$

$$k_e = \frac{\left(1 - \frac{s'}{2d_c}\right)^2}{1 - \rho_{cc}} \tag{2.14b}$$

$$f'_l \cdot s \cdot d_c = 2f_{sy} \cdot A_{sp} \tag{2.15}$$

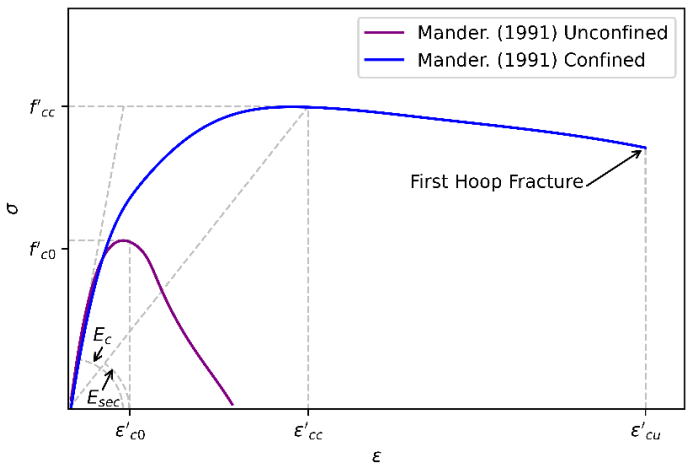

Figure 2. 8: Model for confined and unconfined concrete from (Mander et al., 1988) using the confined concrete initially proposed by Popovics (1973)

2.5.2 Steel Constitutive Model

Many hysteretic models have been used to find the response of steel rebar. One of the most prominent hysteretic response models was developed by Menegotto and Pinto (1973) and later updated for isotropic hardening rules by Filippou et al. (1983). The non-linear backbone is given by Equation 2.16, where ε^* is the effective strain and σ^* is the effective stress given by Equations 2.17a and 2.17b. R is the parameter that affects the shape of the transition curve from E_0 to E_∞ where E_0 is the initial stiffness and E_∞ is the eventual stiffness and is equal to zero.

$$\sigma^* = b\varepsilon^* + \frac{(1-b)\varepsilon^*}{(1+\varepsilon^*)^{1/R}} \tag{2.16}$$

$$\varepsilon^* = \frac{\varepsilon - \varepsilon_r}{\varepsilon_0 - \varepsilon_r} \tag{2.17a}$$

$$\sigma^* = \frac{\sigma - \sigma_r}{\sigma_0 - \sigma_r} \tag{2.17b}$$

2.6 Masonry Modelling

Masonry is one of the oldest building materials due to it being easily accessible and can be implemented without advanced tools. Masonry can be formed of bricks or stone laid on top of each other (dry masonry), or masonry can be formed of brick or stone connected with layers or mortars. The block in masonry can be formed of stone, brick or concrete block, and the mortar can be formed of cement, lime or mud. This thesis will focus on unreinforced stone masonry with mud mortar. Unreinforced masonry is a material that is notoriously difficult to numerically model due to its heterogeneous composition and anisotropic physical properties.

2.6.1 Masonry Material Characterisation

The material properties required to model masonry largely depend on the modelling approach (see Sections 2.5.2 and 2.5.3). These broadly come under two categories masonry constituent properties and masonry assemblage properties. Macro-models do not discretize the mortar and the block and therefore require the material properties of the masonry assemblage. Micro-models require material properties for the mortar and block independently. Certain material properties such as fracture energy require accurate lab equipment and therefore are not prescribed by codes. Details on the procedure for finding fracture energy can be found in da Porto et al. (2010).

Masonry assemblage properties are required for macro-modelling approaches. These are typically obtained from experimental tests of wallettes, stacks and triplets. A compression test of a masonry wallette (CEN. 2002), as shown in Figure 2.6a, can be used to obtain f_u (ultimate

compression strength), E_c (secant modulus), and ν (poisons ratio). A masonry wallette is formed and fixed at the base. It is then progressively loaded until failure. The specimen must be at least three bricks high and two bricks wide. Equations 2.18a and 2.18b are then used to find the compressive strength and elastic modulus. In Equation 2.18a, f_i is the compressive strength, $F_{i,max}$ is the max vertical load, and A_i is the area of the wallette. In Equation 2.18b, E_i is the elastic modulus, and ε_i is the strain at one-third of the peak load.

$$f_i = \frac{F_{i,max}}{A_i} \qquad (2.18a) \qquad E_i = \frac{F_{i,max}}{3 \times \varepsilon_i \times A_i} \qquad (2.18b)$$

A diagonal compression test can be used to find the tensile strength (f_t), the maximum shear stress (τ), and the shear modulus (G). A masonry wallette is positioned at a 45-degree angle, and a compressive force is applied across opposing corners, as shown in Figure 2.9b. The peak shear strength is found using Equation 2.19a, where p is the peak diagonal compressive load, A_n is the net effective area given by Equation 2.19b, where w is the width of the sample, h is the height of the sample, t is the thickness of the sample, and n is the fraction of the net section that is solid (usually assumed to be 1). The tensile strength can be found using Equation 2.20, where α is a coefficient that varies based on the masonry typology. α is assumed to equal 0.707 in ASTM (2002), although this is considered unconservative by Brignola et al. (2008), who suggest a value of 0.35 for the case of irregular masonry. RILEM (1994) suggest a value of 0.5 should be used for the case of irregular masonry.

$$\tau = \frac{0.707 \times P}{A_n} \qquad (2.19a) \qquad A_n = \left(\frac{w+h}{2}\right) \times t \times n \qquad (2.19b)$$

$$f_t = \frac{\alpha \times P}{A_n} \qquad (2.20)$$

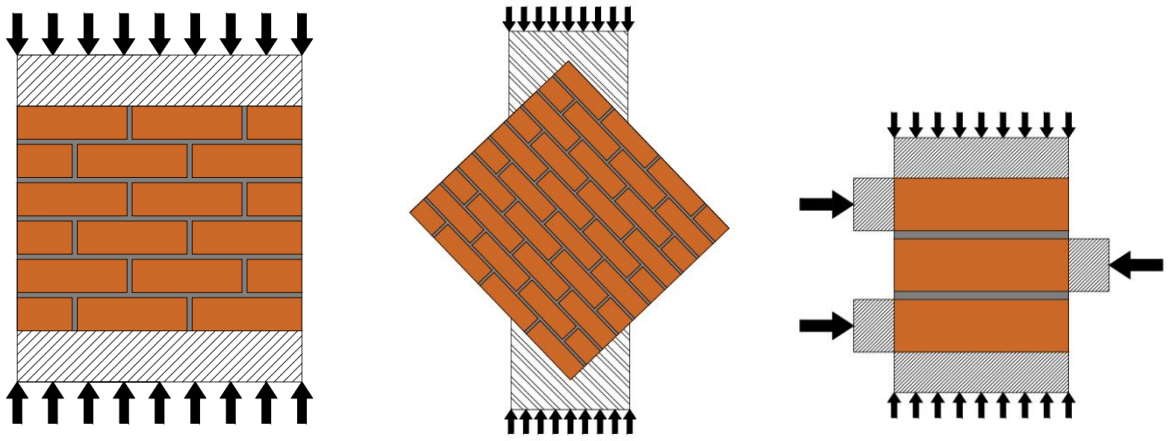

Figure 2. 9: Schematic of (a) Wallette compression test (CEN. 2002), (b) diagonal compression test, (c) triplet shear test(CEN. 2007)

A shear triplet test CEN. (2007) can be used to obtain the *c* (cohesion) and μ (friction angle) of the mortar joint. A shear triplet test involves a stack of three bricks with a layer of mortar between each, as shown in Figure 2.9c. The test specimen is positioned with the bricks spanning vertically, and the sample is supported such that the central brick can be pushed through. A compressive force is applied to the masonry specimen up to a predetermined level. The shear force is applied to the central brick until the mortar joints fail. This process is repeated several times at various levels of confining pressure. Linear regression of the results can then be used to calculate the cohesion and friction angle.

The two main tests to obtain mortar properties are the flexural and compressive strength tests. The mortar specimen is 40 mm x 40 mm x 160 mm and is left to set for 28 days. The sample is then simply supported at a span of 100 mm, and a central load is applied. The vertical load is applied at a rate of 10 N/s to 50 N/s. The peak load *F* is then recorded. Equation 2.21 is used to find the flexural strength (*f*), where *F* is the peak load, *l* is the distance between the support rollers, *b* is the width of the specimen, and *d* is the depth of the specimen (EN 1015-11. 2019).

$$f = 1.5\frac{F \times I}{b \times d^2} \tag{2.21}$$

A mortar compression test is usually carried out using the two stubs from the flexural test (EN 1015-11. 2019). They are flattened off, and a vertical compressive load is then applied at a rate of 10 N/s to 50 N/s. The peak load is recorded and then divided by the area to find the peak compressive strength.

Masonry constituent properties cover the properties of the block. The block would typically be brick or stone, although a concrete block is sometimes used. The Indian standards prescribe four types of tests for bricks (IS 1077, 2005). These are compressive strength, water absorption, efflorescence and tolerance tests. The compressive test requires five bricks to be submerged in room temperature water for 24 hours. The frogs are then filled with mortar. The bricks are then left to dry and then resubmerged for 7 days. A compression test is then carried out on each brick with the frogs facing up. The mean of the five tests is used. The water absorption test involves putting the bricks in an oven for 48 hours. It is then removed, weighed, and submerged for 24 hours before reweighing. Absorption is the percentage of weight gain due to submersion.

2.6.2 Macro-modelling

Masonry is a composite material formed of mortar and brick, each with its own mechanical characteristics. Macro-modelling attempts to homogenise masonry and create a homogeneous material that has an equivalent response to the mason assemblage. Macro-modelling does not distinguish between the units and the joints and assumes the stresses will be continuous throughout the material. The two main methods of doing this are the equivalent frame method and continuum modelling. Equivalent strut models are also used for unreinforced masonry infills.

2.6.2.1 Equivalent Frame Method (EFM)

The equivalent frame method takes each masonry wall, divides it into piers and spandrels, and then models the structure as a frame where the deformation is concentrated in these portions. Although this can be considered a rough approximation of an unreinforced masonry structure, this method can accurately capture the strength of a structure subject to a lateral load and the displacement of a structure at the ultimate limit state (Magenes et al., 1998). Many software packages (Lagomarsino et al., 2013) still use this method today because it requires relatively little computing power compared to more detailed approaches. The equivalent frame method does not require individual experimental tests on bricks and mortar for the masonry properties.

The first step is to divide the wall up into piers and spandrels. Four different methodologies can be used to divide a façade into piers and spandrels. The first method is AVG (average effective height), where the line defining the boundary of the pier travels from the corner of the opening to the corner of the façade or corner of the next opening. This results in the height of the pier being the average of the height of the neighbouring piers. This can be seen in Figure 2.10a. The second criterion is called the MIN (minimum effective height) criterion, whereby the minimum height of the masonry wall between two openings is used. This can be seen in Figure 2.10b. The third method is referred to as the LIM (limited effective height) criterion and is broadly the same as the AVG criterion; however, the inclination of the borderline of the pier is limited to 30°. This can be seen in Figure 2.10c. The final criterion is the LIN (rigid lintel) criterion which assumes a rigid lintel, and therefore, the boundary to the edge of the wall follows the same criterion as MIN. However, between the openings, the same criterion as LIM is used (Morandini et al., 2019). This is shown in Figure 2.10d.

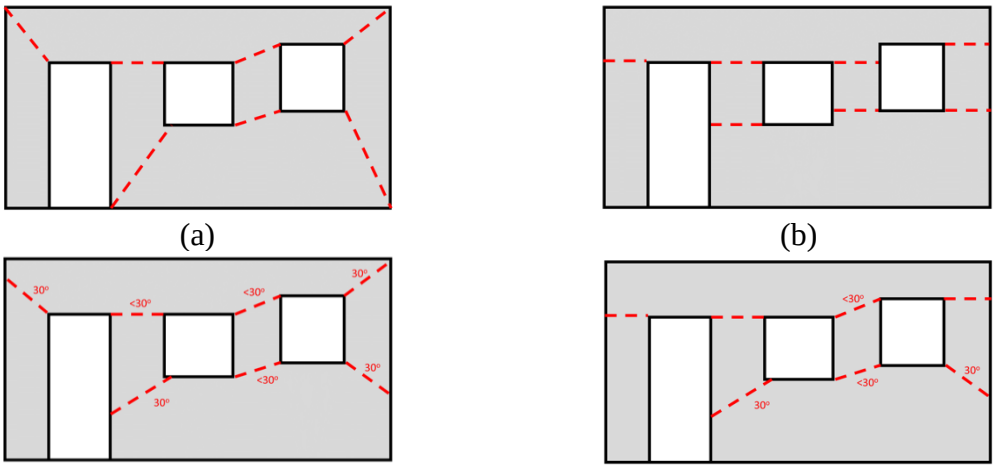

Figure 2. 10: Different pier-spandrel discretisation methodologies. (a) AVG, (b) MIN, (c) LIM, (d) LIN (recreated based on a figure from Morandini et al., 2019)

Piers can be modelled as a beam-column element with a shear and flexural (or rocking) response. The shear and flexural responses are assumed to have an elastic-plastic bi-linear behaviour. Where the failure criteria are not met, the beam-column element can be assumed to be linear elastic. The flexural capacity can be calculated assuming an equivalent rectangular stress block. Equation 2.22 shows the formulation of the ultimate moment (M_u), where D is the height of the pier, t is the thickness of the wall, and p is the mean vertical stress on the wall. K is a coefficient to consider the stress distribution at the toe (0.85 is commonly used), and f_u is the compressive strength of masonry (Magenes et al., 1998). Once M_u is obtained, a plastic hinge forms and rotation can occur at a constant moment.

$$M_u = \frac{D^2 tp}{2}\left(1 - \frac{p}{Kf_u}\right) \tag{2.22}$$

The shear strength (V_{max}) is obtained using Equation 2.23, where τ_u is the ultimate shear stress. Three different failure modes can govern the ultimate shear stress. These are failure along bed joints (τ_{cs}), diagonal cracking across the panel from mortar failure (τ_{ws}), and diagonal cracking across the panel from brick failure (τ_b). The ultimate shear stress is the minimum of the three stresses, as shown by Equation 2.24.

$$V_{max} = Dt\tau_u \tag{2.23}$$

$$\tau_u = min(\tau_{cs}, \tau_{ws}, \tau_b) \tag{2.24}$$

$$\tau_{cs} = \frac{1.5c + p\mu}{1 + 3\frac{c\alpha_v}{p}} \quad (2.25)$$

$$\tau_{ws} = \frac{c + p\mu}{1 + \alpha_v} \quad (2.26)$$

$$\tau_b = \frac{f_{bt}}{2.3(1 + \alpha_v)}\sqrt{1 + \frac{p}{f_{bt}}} \quad (2.27)$$

The shear stress causing shear failure along bed-joints (τ_{cs}) is given by Equation 2.25, where c and μ are the cohesion and shear strength of the mortar joints, respectively, and α_v is the shear ratio of the section. The shear stress leading to diagonal shear cracks from mortar failure (τ_{ws}) is given by Equation 2.26, and the shear stress leading to diagonal shear cracks from brick (τ_b) is provided by Equation 2.27 where f_{bt} is the tensile strength of bricks. Once the shear load exceeds $0.9V_{max,}$ plastic shear deformation occurs at constant shear force. The chord rotation (θ) can then be calculated as the sum of the flexural rotation and shear deformation. The rotation due to the shear is limited to 0.5%, and the flexural rotation is limited to 1.0% (Magenes et al., 1998). These rotation values have been found from experimental tests on piers (Magenes et al., 1997). A squat wall is more likely to exhibit a shear-dominated response, whereas a slender will is more likely to have a flexural (rocking) dominated response. The capacity of the spandrels is calculated mainly in the same way as the piers. There is commonly a rigid link between the piers and the spandrels, and the beam-column elements are assumed to have a lumped plasticity.

2.6.2.2 Continuum Modelling

Continuum modelling of masonry typically uses shell elements to carry out finite element analysis. The masonry is represented by a continuous discretised shell element formed of a homogeneous anisotropic continuum with a single set of material properties. To obtain these material properties, material testing must be carried out on samples of the masonry assemblage instead of the constituent parts. Continuum models have been created with various yield surfaces for the continua material. These include a Rankine/Hill yield surface (Lourenco et al., 1997), the Drucker Prager (Petracca et al., 2017) and the Willam and Warnke failure criterion (Bayraktar et al., 2010). The Material is then implemented on a discretised shell element.

2.6.2.3 Equivalent Strut Model

Equivalent strut modelling is commonly used to model masonry infills. An equivalent strut model was first used to mimic the response of infills in 1961 (Holmes, 1961). A pin joined strut was implemented with a width equal to one-third of the infills diagonal length and material properties equal to the infill. This was implemented on concrete infilled frames. Chrysostomou et al. (1992) developed previous models to propose a "compression-only three struts model". Although this model significantly improved previous models, it did not accurately capture the force transfer and slip along the infill frame interface. A further single strut model has been developed by (Al-Chaar, 2002), whereby a single strut is placed at a distance of l_{column} along the length of the column, as shown in Figure 2.11b. l_{column} is calculated in Equation 2.28, where θ is the angle between the infill diagonal and the horizontal. This eccentricity of the single strut is suggested as most of the infill forces are resisted by the column elements. The three strut model is shown in Figure 2.11a, where the offset distance z_b and z_c, are given in Equations 2.30a and 2.30b, respectively, where C_{od} and C_d are the stiffness distribution factors for the off-diagonal and diagonal struts, respectively. The equivalent strut width (b_w) can be found using Equation 2.31.

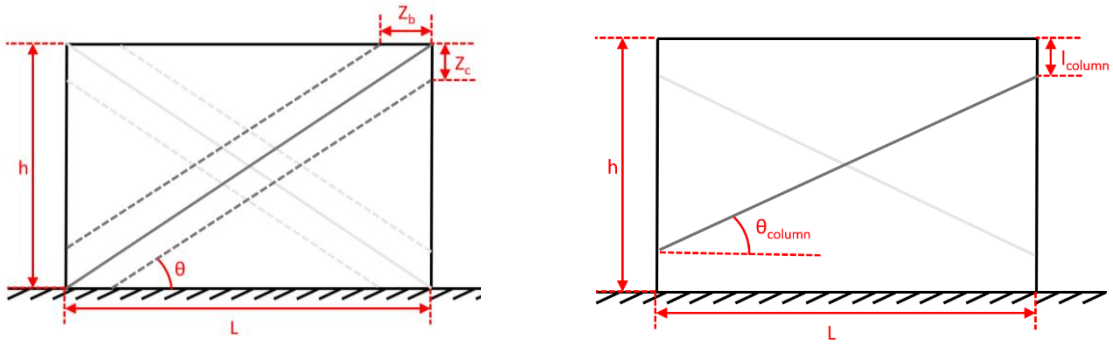

(a) (b)

Figure 2. 11: (a) Compression-only three struts model, (b) Equivalent eccentric single strut

$$l_{column} = \frac{b_w}{cos(\theta)} \tag{2.28}$$

$$\theta_{column} = \tan\left(\frac{h - \frac{b_w}{cos(\theta)}}{l}\right) \tag{2.29}$$

$$Z_b = \frac{C_d b_w + C_{od} b_w}{2\sin(\theta)} \tag{2.30a}$$

$$Z_c = \frac{C_d b_w + C_{od} b_w}{2cos(\theta)} \tag{2.30b}$$

$$b_w = d_w 0.175 \lambda {h_w}^{-0.4} \quad (2.31)$$

Previous studies have given many formulations for the strut width, as given in Table 2.2.

Table 2. 2: Previous formulations for the strut width in the equivalent strut models.

Reference	Equation	Comments
(Smith and Carter, 1969)	$w_{ds} = 0.58 \left(\frac{l}{h}\right)^{-0.445} (\lambda H)^{0.335d} \frac{l}{h}^{0.064}$	I is the length of the infill, h is the height of the infill, λ is the Relative panel-to-frame stiffness, and H is the height of the frame.
(Holmes, 1961)	$w_{ds} = \frac{d_w}{3}$	d_w is the diagonal length of the infill
(Paulay & Priestley, 1992)	$w_{ds} = \frac{d_w}{4}$	
(Mainstone, 1971)	$w_{ds} = d_w 0.175 (\lambda H)^{-0.4}$	
(Liauw & Kwan, 1984)	$w_{ds} = \frac{0.95 h_m \cos\theta}{\sqrt{\lambda h_m}}$	θ is the incline of the strut from horizontal as shown in Figure 2.11b

Caliò et al. (2012) proposed a discrete element macro-model approach for simulating the in-plane response of unreinforced masonry walls. This approach has been shown to replicate the response of numerical and experimental masonry piers for nonlinear incremental static analysis. This simplified approach is only applicable for the in-plane response of a wall, therefore, it must be applied for an assemblage of masonry walls. This is a common limitation of many of the simplified macro approaches (e.g. equivalent strut model), but this limitation is reduced by using a series of walls parallel to each other (Caliò et al., 2012).

Various methods have been used to compensate for masonry infills' reduced strength and stiffness due to openings. An approach to compensate for the openings is to apply an opening factor ($\lambda_{opening}$) to the width of the strut, subsequently reducing its stiffness and strength. Equation 2.32 calculates the opening factor where α_w is the infill wall opening percentage (Al-Chaar et al. 2002).

$$\lambda_{opening} = 1 - 1.6\alpha_w + 0.6{\alpha_w}^2 \quad (2.32)$$

2.6.3 Micro-modelling

Micro-modelling is a finite element technique for masonry which individually models the brick/block and mortar (and sometimes the brick-mortar interface). Micro-modelling typically allows better capturing of the failure mechanisms. However, it requires more detailed material testing as it requires a discrete set of material properties for the brick and mortar. Micro-modelling comes in two main forms discrete element method (DEM) and finite element method

(FEM). FEM can further be split up into 2D-C where both the mortar and the block are modelled as non-linear continuum material (Figure 2.12a), 2D-D, where the blocks are modelled with a continuum elastic model, the mortar is modelled with a non-linear interface element, and an interface model is used within the block as to model cracking within the brick as proposed in Macorini et al. (2011) and shown in Figure 2.12b. Finally, 2D-CD, where the blocks are modelled with a non-linear continuum and the mortar is modelled with an interface element (Figure 2.12c).

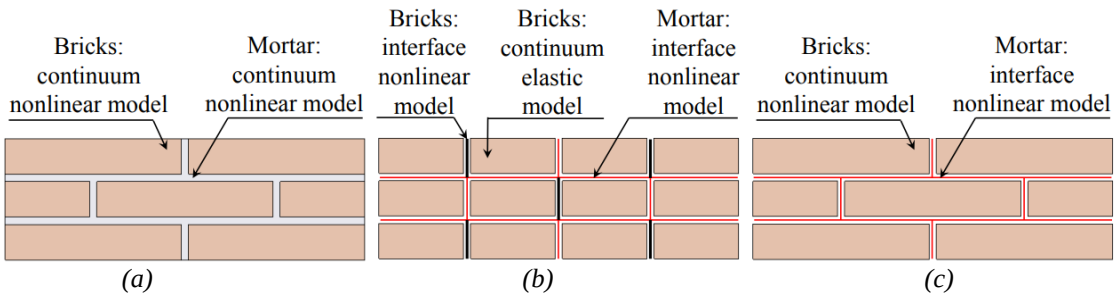

Figure 2. 12: Visual demonstration of different types of micro-modelling (a) 2D-C (b) 2D-D (c) 2D-CD (Petracca et al., 2022)

2.6.3.1 Discrete Element Method (DEM)

The discrete element method (DEM) assumes that a series of elements, which are often rigid or linear elastic, are connected through a series of elastoplastic interface elements. The main advantage of this method is that it can more accurately capture the failure mechanism of the masonry relative to continuous macro-modelling and equivalent frame method. Cundall (1971) first proposed the discrete element method for modelling soil, and there were no interface elements between particles to resist tension and traction. This model was later updated by Meguro et al. (1990) to include elastic spring and dashpots. Since the discrete element method has progressed, it has many similarities to a typical finite element model, such as the discretisation of the block unit. There are four characteristics of DEM (Lemos, 2007):

1. Although certain DEM models have deformable blocks, the majority of the deformations are concentrated in the interaction.
2. Interactions between blocks are achieved through point contacts or edge to edge contact elements. No attempt is made to achieve a continuous stress distribution.
3. They are designed to allow complete separation between blocks, allowing analysis to continue at large displacements.
4. Tend to use time-stepping algorithms

The interaction between blocks is based on several point contact elements which exert a force on the block, which is a function of the distance between the two blocks at the relevant point. The block itself is typically modelled as a rigid block. This assumption works well when the strength and stiffness of the block are significantly larger than the mortar (i.e. stone with mud mortar). More recently, discrete element models have used deformable blocks, where each block is discretised into a FE mesh. These deformable blocks are often assumed to be linear elastic to avoid a large computational demand. The majority of DEM models follow three key features:

1. Blocks are assumed to be either rigid or deformable. Where deformable blocks are used, an FE mesh is used.
2. A deformable contact approach is used whereby the contact stresses are derived from the relative displacement of neighbouring blocks.
3. An explicit solution is used for static and dynamic analysis

One commonly used DEM code is UDEC (universal distinct element code), which was later developed into a 3D version called 3DEC (Israelsson, 1996). 3DEC allowed fully dynamic analysis and allowed rigid or deformable blocks. The deformable blocks could be elastic or exhibit Mohr-Coulomb plasticity. The material properties for the discontinuities were coulomb-slip or continuous-yielding.

The discrete element method has been modified to account for potential failure in the bricks/blocks. Lourenço and Rots (1997) proposed a model where the bricks are modelled with a linear continuum with a vertical interface element. This was intended to overcome the inability of the previous model to capture a direct tensile failure to the brick.

2.6.3.2 Continuous micro-modelling

In a continuous micro-model, both the mortar and the block (brick or stone) are formed of a plane-stress continuum element with a non-linear hysteretic response. This approach has progressed in recent years (Petracca et al., 2017, Abdulla et al., 2017, Lourenço, 1997). It is typically more computationally demanding than alternatives and requires detailed material properties for the block and mortar. This approach is similar to classical FEA approaches, where both the mortar and the brick are discretised. This allows a constitutive material law that allows for the explicit evaluation of a solution.

To accurately capture the damage and plasticity of masonry, a tension-compression plastic damage model is proposed by Petracca et al. (2022). This model is an extension of the tension-

compression damage model proposed by Petracca et al. (2017). The initial damage model is based on the work of Cervera et al. (1995) and Wu et al. (2006). In the Petracca et al. (2017) model, permanent deformations were not accounted for therefore leading to it not being suitable for cyclic analysis however, this was updated to include plasticity in Petracca et al. (2022).

The nominal stress tensor ($\boldsymbol{\sigma}$) is given by Equation 2.33 where $\bar{\boldsymbol{\sigma}}^{+}$ and $\bar{\boldsymbol{\sigma}}^{-}$ are the positive and negative components of the effective stress tensor, and d_c^{+} and d_c^{-} are the positive and negative cracking damage variables. The cracking damage variable reduces the strength and stiffness of the effective stress tensor. The positive and negative components of the effective elastic stress tensor are a function of ${d_{pl}}^{+}$ and ${d_{pl}}^{-}$, the positive and negative plastic damage variables. $\tilde{\boldsymbol{\sigma}}$ is defined as the trial effective stress tensor and is given by Equation 2.35, $\bar{\boldsymbol{\sigma}}_{\boldsymbol{n}}$ is the effective stress at time step n and $\boldsymbol{C_0}\colon(\boldsymbol{\varepsilon}-\boldsymbol{\varepsilon_n})$ is the elastic trial stress increment. Further details on the iterative process used to find the components of the trial effective stress tensor can be found in Petracca et al. (2022).

$$\boldsymbol{\sigma} = (1-d_c^{+})\bar{\boldsymbol{\sigma}}^{+} + (1-d_c^{-})\bar{\boldsymbol{\sigma}}^{-} \tag{2.33}$$

$$\bar{\boldsymbol{\sigma}}^{\mp} = \left(1-d_{pl}^{\mp}\right)\tilde{\boldsymbol{\sigma}}^{\mp} \tag{2.34}$$

$$\tilde{\sigma} = \bar{\sigma}_n + C_0\colon(\varepsilon-\varepsilon_n) \tag{2.35}$$

The failure criteria are based on Lubliner et al. (1989). The damage surface is given by Equation 2.36 and Equation 2.37 for the tensile and compressive strength. In these equations $H(-\tilde{\sigma}_{min})$ and $H(\tilde{\sigma}_{max})$ are the Heaviside functions of the minimum and maximum eigenvalues. These are applied to ensure that the tensile surface is active only if at least one eigenvalue is positive and that the compressive surface is only active if at least one of the eigen vectors is negative. This ensures that compressive damage cannot occur under tensile states and tensile damage cannot occur under compressive states. α is given by Equation 2.38, where k_b is the ratio of the compressive bi-axial strength to the uniaxial compressive strength. In Equations 2.36 and 2.37 $\tilde{I}_1$ is the first invariant of the trial effective stress tensor and $\tilde{J}_2$ is the second invariant of the trial effective deviatoric stress tensor. β is given by Equation 2.39, where f_{cp} is the compressive peak strength and f_t is the tensile strength.

$$\tilde{\tau}^{-} = H(-\tilde{\sigma}_{min})\left[\frac{1}{1-\alpha}\left(\alpha\tilde{I}_1 + \sqrt{3\tilde{J}_2} + k_1\beta\langle\tilde{\sigma}_{max}\rangle\right)\right] \tag{2.36}$$

$$\tilde{\tau}^{+} = H(\tilde{\sigma}_{max})\left[\frac{1}{1-\alpha}\left(\alpha\tilde{I}_1 + \sqrt{3\tilde{J}_2} + \beta\langle\tilde{\sigma}_{max}\rangle\right)\frac{f_t}{f_{cp}}\right] \tag{2.37}$$

$$\alpha = \frac{k_b - 1}{2k_b - 1} \tag{2.38}$$

$$\beta = \frac{f_{cp}}{f_t}(1-\alpha) - (1+\alpha) \tag{2.39}$$

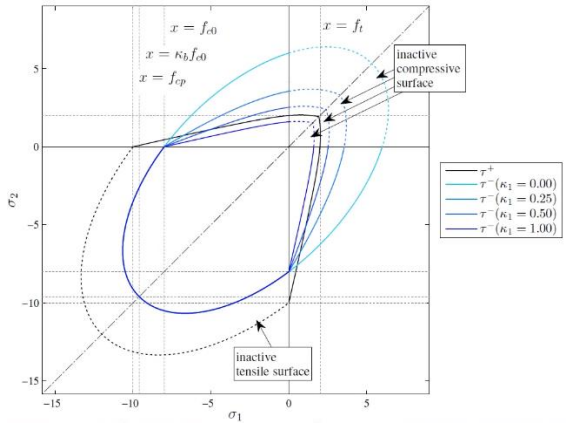

Figure 2. 13: Lubliner et al. (1989) failure surface in 2d stress (taken from Petracca et al. 2017)

To apply damage to the material model, the damage parameters r^+ and $r^-$are used. The values represent the largest equivalent stresses as shown in Equations 2.40 and 2.41, where f_t and f_{c0} are the elastic limit in tension and elastic limit in compression. These damage parameters can be used to find the total strain counterparts, as shown in Equation 2.42, which can be used with the hardening functions f^+ and f^- to find the degradation in stiffness.

$$r^{+}(t) = max\left(\underset{s\in[0,t]}{max}\,\tau^{+}(s); f_t\right) \tag{2.40}$$

$$r^{-}(t) = max\left(\underset{s\in[0,t]}{max}\,\tau^{-}(s); f_{c0}\right) \tag{2.41}$$

$$\varepsilon_{tot}{}^{\mp} = \frac{r^{\mp}}{E} \tag{2.42}$$

$$q^{\mp} = f^{\mp}\left(\varepsilon_{tot}^{\mp}\right) \tag{2.43}$$

The hardening functions are proposed in Petracca et al. (2017). The tensile damage d^+ is given by the exponential softening law given in Equation 2.44, where H_{dis} is the discreet softening parameter, r^+ is the tensile damage threshold, and r^+_0 is the initial tensile damage threshold (i.e. the elastic limit when under uniaxial compression). To ensure that the response is

independent of the discretisation size, the softening part of the response must be modified such that Equation 2.45 is satisfied. In Equation 2.45 g_f is the fracture energy per unit volume, G_f is the fracture energy per unit length, and l_{dis} is the length of the damage zone. The softening law is given in Equation 2.46, where f_t is the tensile strength and E is the elastic modulus. The discrete softening parameter is given by Equation 2.47, where l_{mat} is given in Equation 2.48 and l_{dis}, the length of the damage zone, is assumed to be the characteristic length of one finite element (l_{ch}). The smallest dimension is used in a discretisation where the elements are not of regular sizes. The uniaxial tensile response of the tension/compress continuum material is shown in Figure 2.14a. The fracture energy per unit volume (g_t) affects the softening rate in the material's tension region. This can be shown in Figure 2.14a.

$$d^r(r^+) = 1 - \frac{r_0^+}{r^+} exp\left\{2H_{dis}\left(\frac{r_0^+ - r^+}{r_0^+}\right)\right\} \tag{2.44}$$

$$g_f l_{dis} = G_f \tag{2.45}$$

$$g_f = \left(1 + \frac{1}{H_{dis}}\right)\frac{f_t^2}{2E} \tag{2.46}$$

$$H_{dis} = \frac{l_{dis}}{l_{mat} - l_{dis}} \tag{2.47}$$

$$l_{mat} = \frac{2EG_f}{f_t^2} \tag{2.48}$$

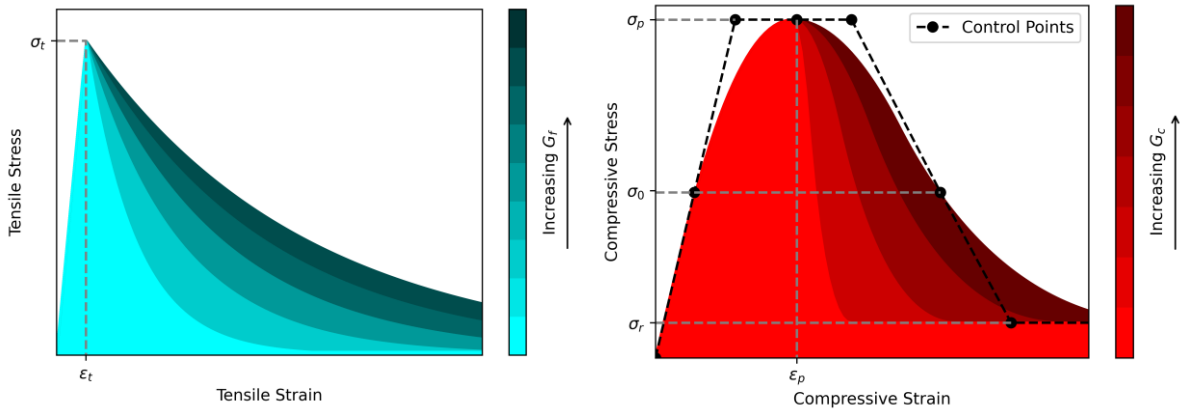

(a) (b)

Figure 2. 14: (a) Uniaxial tension (b) Uniaxial compression of "tension/compression damage model" used for mortar and stone in masonry micro-model Petracca et al. (2017).

The compressive damage index is formed of five parts. The first part is a linear elastic part. This is followed by a hardening part and two separate softening parts, which are finally followed by a residual plateau. These five sections can be seen in Figure 2.14b. The hardening and softening parts follow a quadratic Bézier curves, using the endpoints and the tangent at the endpoint as the three required initial conditions. This is 2.49. As shown in Figure 2.14, the area beneath the stress-strain curve is equal to the fracture energy G_c. Therefore the position of the control points in Equation 2.49 are a function of the fracture energy as to ensure that the area under the curve is equal to the fracture energy. Finally the damage index can be calculated using Equation 2.50.

$$\Sigma(\xi) = \begin{cases} \mathcal{B}(\xi, \varepsilon_0, \varepsilon_i, \varepsilon_p, \sigma_0, \sigma_i, \sigma_p) & \varepsilon_0 < \xi \leq \varepsilon_p \\ \mathcal{B}(\xi, \varepsilon_p, \varepsilon_j, \varepsilon_k, \sigma_p, \sigma_j, \sigma_k) & \varepsilon_p < \xi \leq \varepsilon_k \\ \mathcal{B}(\xi, \varepsilon_k, \varepsilon_r, \varepsilon_u, \sigma_k, \sigma_r, \sigma_u) & \varepsilon_k < \xi \leq \varepsilon_u \\ \sigma_u & \xi > \varepsilon_u \end{cases} \tag{2.49}$$

$$d^-(r^-) = 1 - \frac{\sum(\xi)}{r^-} \tag{2.50}$$

The plasticity is implemented using the method outlined in Petracca et al. (2022). The plastic damage variables used in Equation 2.34 are calculated using Equation 2.51 where $q_{pl}^{\mp}$ are the effective plastic hardening variables and $\tilde{r}^{\mp}$ are the positive and negative damage thresholds. The effective plastic hardening variables are found using Equation 2.52 where $\omega^{\mp}$are the plastic damage factors used to quantify the amount of plasticity in the material. They range from 1 (purely plastic) to 0 (no plasticity). The damage thresholds are given by Equation 2.53 where ${\varepsilon_{tot}}^{\mp}$ is the total strain and ${\lambda_n}^{\mp}$ is the equivalent plastic strain.

$$d_{pl}^{\mp} = 1 - \frac{q_{pl}^{\mp}}{\tilde{r}^{\mp}} \tag{2.51}$$

$$q_{pl}^{\mp} = q^{\mp} + (1 - \omega^{\mp})(r^{\mp} - q^{\mp}) \tag{2.52}$$

$$\tilde{r}^{\mp} = E({\varepsilon_{tot}}^{\mp} - {\lambda_n}^{\mp}) \tag{2.53}$$

2.7 Seismic Risk Assessment

Seismic risk assessment can be broadly separated into empirical and analytical. Empirical risk assessment methods are typically a probabilistic assessment of a certain building typology in a specific area based on its performance in previous earthquakes. Analytical methods usually use

the design of the building or properties of the building to create a numerical or analytical model of the structure to assess the expected impact of an earthquake.

2.7.1 Hazard Analysis

There are two main approaches for estimating the seismic hazard of an area: probabilistic seismic hazard analysis (PSHA) and deterministic seismic hazard analysis (DSHA). PSHA is based on historical records of earthquakes and applies statistical methods to find the probability of an earthquake in the future. DSHA is based on the study of geology in which the likelihood of an earthquake can be calculated.

2.6.1.1 Probabilistic Seismic Hazard Analysis

PSHA aims to quantify the rate of exceedance of specific ground motion properties. The numerical application of PSHA was first proposed by Cornell (1968). The ground motion property used has typically been peak ground acceleration (PGA), although more recent studies use spectral acceleration at a specific period. The main fundamental assumption of PSHA is that an earthquake of magnitude (M) and distance (R) is a continuous random variable. There are four main steps to carrying out a PSHA: 1) earthquake source identification, 2) source characterisation, 3) attenuation function selection and 4) earthquake hazard calculation (Purwana et al., 2019).

The earthquake source identification involved identifying any earthquake source that could cause a damaging earthquake. This information can be obtained through historical earthquake data or geological data. The source can either be identified as a fault line, or an areal region is used if the individual fault lines cannot be identified. Source characterisation involved predicting the expected magnitude of the earthquake. The Gutenberg & Richter (1944) relationship is used to find the relationship between the magnitude and the annual exceedance rate. This relationship is obtained using historical data and statistical methods and is typically denoted $f_M(m)$. The characterisation of the source also involves identifying the earthquake distance from a specific site. This calculation assumes an equal probability of the earthquake occurring at any point along the fault or in an area. Geometric and statistical approaches are used to derive a probability function of the distance at a specific site, denoted $f_R(r)$. A ground motion prediction equation (GMPE) is used to estimate ground motion intensity at a given site. These GMPEs use variables such as the magnitude, distance, faulting mechanism and site effects. Finally, the previous information is combined using Equation 2.54 to find the

relationship between intensity measure (IM) and the annual exceedance rate. This is denoted *P(IM > x)* in Equation 2.54 (Baker, 2013).

$$P(IM > x) = \int_{m_{min}}^{m_{max}} \int_{0}^{r_{max}} P(IM > x \mid m,r) f_M(m) f_R(r) dr dm \quad (2.54)$$

PSHA has become the foundation of many structural codes over the last 50 years. The Nepalese Building Code first introduced a Hazard map in 1994 in the National Building Code for seismic design of buildings in Nepal (NBC-105:1994., 1994). The hazard map for a return period of 500 years from NBC-105:1994 (1994) is shown in Figure 2.15a, where it can be seen that Kathmandu has a PGA of 0.36 g. After the release of NBC-105:1994 (1994), several PSHA studies have been carried out, as shown in Table 2.3. Several of these studies used the data from Gorkha 2015. It can be seen from Table 2.3 that all of the studies are significantly higher than NBC-105:1994 (1994). In 2020 an updated version of the National Building Code for seismic design of buildings in Nepal (NBC-105:2020., 2020) was released. Although there was a new hazard map, the 475 year return period earthquake intensity for Kathmandu is 0.35 g. The hazard map can be seen in Figure 2.15b.

Table 2. 3: PGA values for a 475 year return period earthquake in Kathmandu from a variety of PSHA studies assuming soft soil and a V_{s30}=1000m/s (taken from Pokhrel et al., 2019)

Reference	PGA (g)
Parajuli et al., (2010)	0.51
Thapa and Guoxin (2013)	0.525
Chaulagain et al. (2015)	0.38
Ghimire and Parajuli (2016)	0.61
Subedi and Parajuli (2016)	0.51
Rahman and Bai., (2018)	0.55
Stevens et al. (2018)	0.75
Pokhrel et al. (2019)	0.72

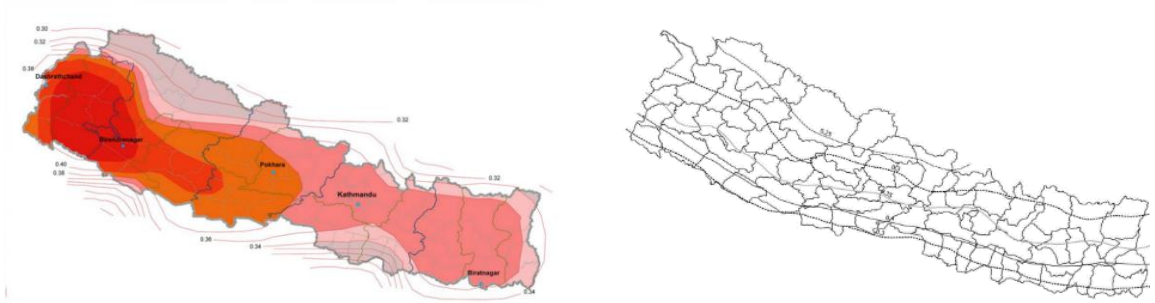

(a) (b)

Figure 2. 15: Seismic hazard maps from (a) NBC-105:1994 (1994) colourised and redrawn by NSET (BCDP, 1994). (b) NBC-105:2020 (2020)

2.7.2 Fragility Analysis

A fragility curve describes the likelihood of a structure incurring damage from an earthquake. A fragility curve relates some intensity measure (IM) of an earthquake to the probability of that structure exceeding a given limit state. A fragility curve is frequently considered to follow a lognormal cumulative distribution function (CDF) (Porter et al., 2007), as shown in Equation 2.55, where η is the median intensity value, and β is the standard deviation in log space.

$$P(DCR > 1 \mid IM) = \Phi\left(\frac{\ln \eta_{DCR|IM}}{\beta_{DCR|IM}}\right) \tag{2.55}$$

A vulnerability curve relates an IM to the repair cost. Fragilities can typically be developed empirically from historical data (Giordano et al., 2021), typically collected in the aftermath of an earthquake, or fragility curves can be developed from an analytical or numerical model of the building or building typology (Choi et al., 2004).

Several different intensity measures (IM) can be used for fragility analysis. These broadly come into three categories: frequency response based, peak based, and cumulative/duration based. These can be seen in Table 2.4.

Table 2. 4: Selection of different intensity measures Kiani et al., (2017).

Category	Symbol	Description
Frequency response based	$Sa(T_i)$	Spectral acceleration at T_i
	$Sa_{avg}(T_i, T_j)$	The geometric mean of the spectral acceleration between T_i and T_j
	DSI	Displacement spectrum intensity
Peak based	*PGA*	Peak ground acceleration
	PGV	Peak ground velocity
	PGD	Peak ground displacement

Cumulative/duration based	*AI*	Arias intensity
	CAV	Cumulative absolute energy
	$Ds_{5\text{-}75}$	Significant duration. The interval between 5% and 75% of the Arias intensity

2.7.2.1 Empirical Fragilities

Empirical fragilities are derived from historical data on buildings' response to an earthquake. This has two significant issues. Often the only data available is from the post-earthquake reconnaissance survey. All this damage data will be from the same earthquake, resulting in a low dispersion of intensity measure. The second issue with historical data is that it is rarely sufficient for all building typologies to be able to derive a series of statistically significant fragility curves. The steps for deriving empirical fragilities are as follows:

1. Identify the severity of the shaking (i.e. the IM) at each building. This requires a shake map for the relevant area for the relevant earthquake. These shake maps can be derived from instrumental measurements of the earthquake and information of the local geology and the characteristics of the earthquake. Once a shake map is obtained and the geographical data of the damage data, then an IM for each damage point can be found.
2. The damage data must be converted into the required damage state (DS). Damage survey data can often be in the form of photographs of buildings in the aftermath of an earthquake. These Photographs can be converted to DS using the EMS-98 scale outlined in Table 2.5.

Table 2. 5: Damage levels from the European Macroseismic scale (Grünthal, 1998)

Grade	Name	Description
1	Negligible damage	Cracking of non-structural elements, such as dry walls or external cladding
2	Moderate Damage	Major damage to the non-structural elements, minor damage to load-bearing elements
3	Substantial to heavy damage	Significant damage to load-bearing elements but no structural collapse
4	Very heavy damage	Partial structural collapse (i.e. individual floor or portion of the building)
5	Destruction	Full collapse

3. Several statistical methods can be used to derive fragility curves from historical data, the most common of which is the maximum likelihood method. This method obtains the probability distribution function parameters that maximise the historical data's likelihood function. It is assumed that the fit is a lognormal distribution, and therefore, the optimisation function for the parameters for the fragility curve is as shown in Equation 2.56. The data

must first be distributed into a series of IM bins of an equal number of data points, these are typically PGA bins. In Equation 2.56, n_i is the number of buildings in the bin that exceed the damage level, ϕ is the standard normal cumulative distribution function, PGA_i is the average PGA in the ith bin, N_i is the total number of data points in bin i and m is the number of bins. $\hat{u}_{log,}$ and β are the logarithmic mean and standard deviation for the fragility function.

$$\hat{\mu}_{log}, \hat{\beta} = arg \max_{\mu_{log},\beta} \sum_{i=1}^{m} \left[n_i ln \left(\phi \left(\frac{\ln(PGA_i) - \mu_{log}}{\beta} \right) \right) + (N_i - n_i) ln \left(1 - \phi \left(\frac{\ln(PGA_i) - \mu_{log}}{\beta} \right) \right) \right] \quad (2.56)$$

2.7.2.2 Analytical/Numerical Fragilities

Fragility curves can be obtained using a numerical or analytical model of a building. A failure criterion must then be established for each limit state, and a set of ground motions must be used to assess the ground motion variability in the response. The main advantage of analytical fragilities is that they do not require damage data of existing structures, therefore can be applied to buildings before a large earthquake or even before the building is constructed. A numerical fragility is typically for a specific structure, however the FAST method (De Luca et al. 2015) can be used to derive fragility curves for building typologies.

A numerical model can be created of a structure, ranging from a single-degree-of-freedom (SFOF) model to a detailed multiple-degree-of-freedom (MDOF) finite element model. A finite element model of a structure often does not consider the inherent uncertainties in material properties and structural loading. Certain studies have investigated the effect of material properties in fragility assessment. Kim & Han (2013) investigated the impact of the ultimate strength of concrete, yield strength of reinforcing steel and the damping ratio on the vulnerability of a structure. This, therefore, leads to all the uncertainty being derived from the record-to-record variability.

Once a model of the structure has been created, there are many methods to find the fragility curves. The main techniques are cloud analysis, incremental dynamic analysis (IDA) and multi-stripe analysis. All of these methods require transient analysis using a ground motion set. There are various methods for carrying out a ground motion selection. Most of them are fundamentally developed around ground motions similar to what may occur at the structure's site. Alternatively, ground motion selections are based on finding the point the building exceeds

a limit state and are therefore based on the structure's response. A code-based ground motion selection is typically based on the response spectrum of the ground motions being similar to that of the code based elastic response spectrum for that site (EN 1998-1. 2004). In Eurocode 8 (EN 1998-1. 2004), the provision is set that between $0.2T_1$ and $2.0T_1$ (where T_1 is the fundamental period of the structure in the direction in which the motion is going to be applied), at no point should the mean 5% damping response spectra be lower than 90% of the 5% damping elastic response spectra. An example of a Eurocode 8 (EN 1998-1. 2004) compatible ground motion set is shown in Figure 2.16. EN 1998-1. (2004) further states that there should be more than 3 ground motions and that the mean PGA should not be lower than the PGA of the site.

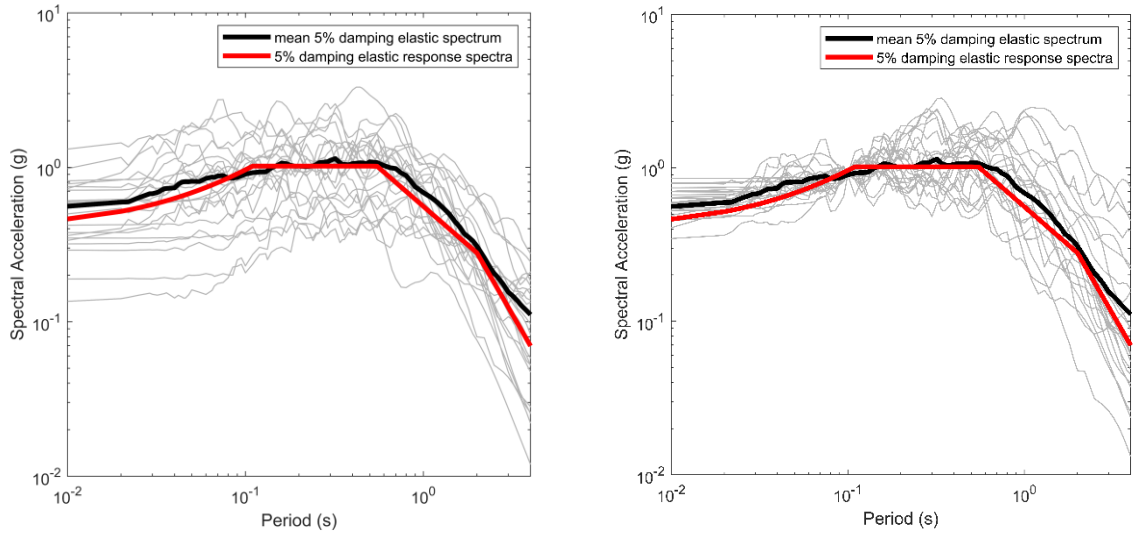

(a) (b)_

Figure 2. 16: (a) Example of a code (EN 1998-1. 2004) compatible ground motion selection set and the corresponding elastic response spectra. (b) example of a scaled ground motion set for an IDA (figure formed using data from the PEER NGA West 2 (2014) database)

For cloud analysis, various criteria must be satisfied to ensure that the fragilities are independent of the ground motion selections. Jalayer et al. (2017) set out three criteria:

1. The record selection should have a large dispersion of S_a (or the relative intensity measure used for the fragility curve) to reduce the standard error level in the regression slope.
2. At least 30% of the nonlinear time history analyses should cause the demand capacity ratio (DCR) to exceed 1 for each limit state.
3. No more the 10% of the ground motion selection should be from the same event.

Due to the scaling applied when carrying out an IDA, only the restriction on the number of motions from a single event is applicable. IDA has been criticised for requiring linear scaling of ground motions. The scaling can lead to an artificially high spectral acceleration at the non-target spectral acceleration. This can be seen in Figure 2.16b, where the ground motions have all been scaled such that their spectral acceleration at a period of 0.1s is 0.9 g. It can be that as a result, the peak spectral acceleration at 1-2 s has been increased. Certain codes (FEMA P695, 2009) provide a ground motion set depending on if the site is near-field or far-field, where near-field is defined as less than 10 km from the rupture and far-field is further than 10 km from the rupture. FEMA P695 (2009) recommends using the far-field for collapse assessment due to the irregularities caused by ground motions from close to the rupture.

Multi-stripe analysis (MSA) addresses the shortcomings of the IDA by carrying out multiple ground motion selections to form a series of different ground motion suites for different intensity levels (Jalayer et al., 2009). As MSA allows multiple ground motion suites, excessive scaling can be avoided. Therefore, the analysis implicity accounts for the different ground motion properties of high-intensity vs low-intensity ground motions (Adam et al., 2013).

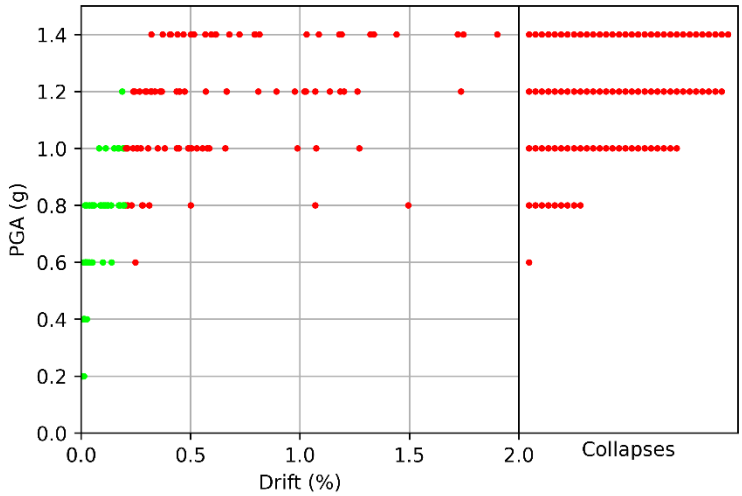

Figure 2. 17 Illustration of the multi-stripe analysis for the collapse case

The main advantage of cloud analysis is that it can be carried out without ground motion scaling, and it requires fewer non-linear time-history analyses (NLTHA). Cloud analysis uses the NLTHA results in a linear regression probability model. Linear regression is carried out for the demand capacity ratio for a given limit state against a given intensity measure (IM). An example of this can be seen in Figure 2.18a, and the equation for this is given in Equation 2.57. This linear regression can be used to find $\eta_{Y|Sa}$ (the median Y at a given Sa), where Y is the

demand capacity ratio, and Sa is a given IM. The logarithmic standard deviation of the DCR given a certain IM ($\sigma_{logY|Sa}$) is provided by Equation 2.58, where Y_i and $\eta_{Y|Sa}$ are the DCR and IM from each analysis in the NLTHA. The fragility curve is assumed to follow a lognormal cumulative distribution function, as shown in Figure 2.18b.

$$E[\log Y \mid S_a] = \log \eta_{Y|S_a} = \log a + b \log S_a \tag{2.57}$$

$$\sigma_{\log Y|S_a} = \sqrt{\frac{\sum_{i=1}^{n} \left(\log Y_i - \log \eta_{Y|S_{a,}}\right)^2}{n-2}} \tag{2.58}$$

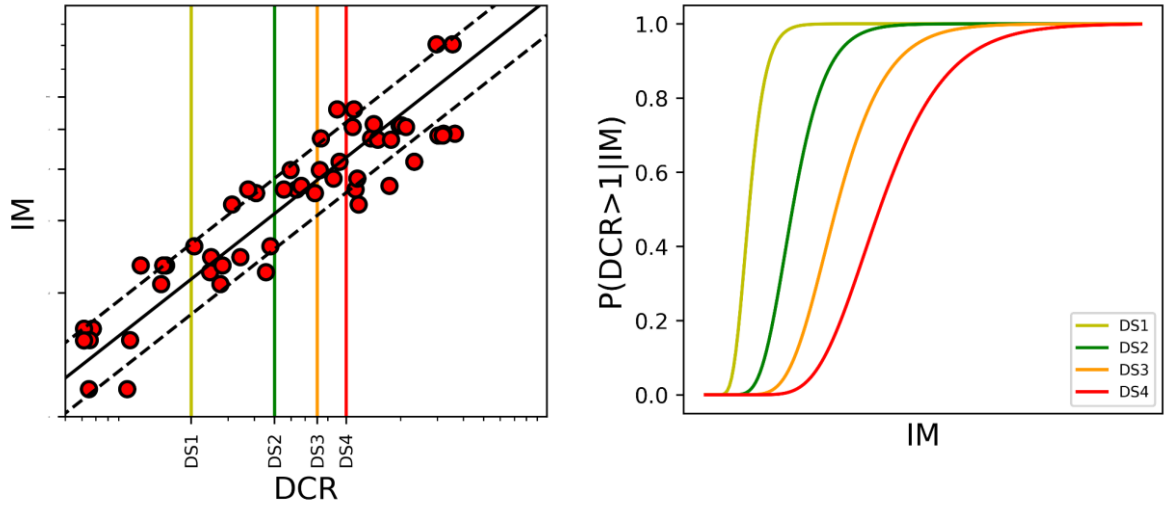

(a) (b)

Figure 2. 18: Cloud analysis (a) Linear regression of NLTHA results. (b) Fragility curves corresponding to the damage states.

The cloud analysis has been further adapted (Jalayer et al., 2017) for the condition where some of the analyses do not converge/collapse. The collapse case is also referred to as dynamic instability. In this scenario, the results can be split up into those that cause dynamic instability (referred to as *C*) and those that do not cause dynamic instability (referred to as *NoC*). Typical cloud analysis is carried out on the data that does not undergo dynamic instability, this is indicated by Equation 2.60. The fragility curve is shown in Equation 2.59. The term $P(DCR_{LS}>1|S_a,C)$ is the probability of a limit state being exceeded given that dynamic instability has been achieved. This can be assumed to be equal to one. The term $P(C|S_a)$ is the probability of collapse at a given intensity measure. This is given using logistic regression of the NLTHA results that collapse and those that don't, as shown in Equation 2.61.

$$\begin{aligned} P(DCR_{LS} > 1 \mid S_a) &= P(DCR_{LS} > 1 \mid S_a, NoC) \cdot \left(1 - P(C \mid S_a)\right) \\ &+ P(DCR_{LS} > 1 \mid S_a, C) \cdot P(C \mid S_a) \end{aligned} \tag{2.59}$$

$$P(DCR_{LS} > 1 \mid S_a, NoC) = \Phi\left(\frac{\ln \eta_{DCR_{LS}|S_a,NoC}}{\beta_{DCR_{LS}|S_a,NoC}}\right) = \Phi\left(\frac{\ln\ a \cdot S_a^b}{\beta_{DCR_{LS}|S_a,NoC}}\right) \quad (2.60)$$

$$P(C \mid S_a) = \frac{1}{1 + e^{-(\alpha_0 + \alpha_1 \cdot \ln\ S_a)}} \quad (2.61)$$

Incremental dynamic analysis (IDA) was first formalised by Vamvatsikos and Cornell (2002) to respond to increased available computing power. In the IDA, all ground motions are scaled such that they have a consistent level of some intensity measure. This intensity measure is typically peak ground acceleration or spectra acceleration at the structure's first fundamental period. Other intensity measures have been used, such as SA_{ave} (Bayat et al. 2015, Kohrangi et al. 2017b). The given analysis is then carried out for the scaled ground motions before the target intensity measure is increased, and the process is repeated. An IDA plot is shown in Figure 2.19a, where the peak roof displacement of a structure is shown against the PGA. To derive the fragility curves, the log-normal distribution is taken at the point where the demand is equal to the capacity for a given limit state, this can be seen in Figure 2.19b.

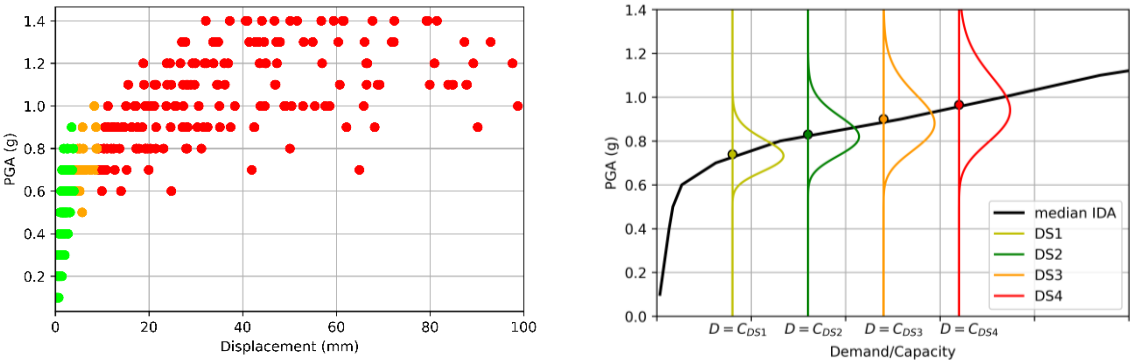

(a) (b)

Figure 2. 19: IDA plot showing (a) scatter plot of PGA against roof displacement (b) Graphical representation of the lognormal distribution of PGA for each damage state.

IDA curves can exhibit hardening, whereby an increased intensity does not lead this an increased response. This is caused due to the earlier part of the ground motion being amplified, causing part of the structure to yield earlier. When the peak section of the ground motion arrives, the structure responds differently due to the earlier yielding. Once the IDA curves have been obtained, there are three main ways to get the fragility curves: empirical cumulative distribution, moment method and maximum likelihood estimation method (Flenga et al., 2021).

Empirical cumulative probability is applied by taking a discrete number of stripes at the point where the engineering demand parameter (EDP) is equal to the capacity at some limit state. The limit state point is used to define the number of ground motions that have exceeded the

capacity at a given IM. This is shown in Figure 2.20a, where a stripe has been taken at a PGA of 0.8 g. It can be seen that of 14 ground motions, 6 exceed the capacity limit. Therefore, on the fragility curve, the probability at 0.8 g is 6/14, as shown in Figure 2.20b. This is shown by Equation 2.62, where n is the number of analyses exceeding limit capacity and m is the total analysis. The process is repeated for a range of IMs.

The moment method for calculating fragility curves from IDA results involves finding the IM values at which the limit capacity is exceeded and then fitting a log-normal distribution to the IM values using Equation 2.63 for the median (μ) and Equation 2.64 for the dispersion (β). μ and β can then be used in the log-normal cumulative distribution function (CDF) given by Equation 2.55 where ϕ in the standard normal CDF, as is done with the empirical fragilities. In Equation 2.66, n is the number of analyses, and IM_i is the level of intensity measure at which the analysis exceeds the capacity. Figure 2.21 shows the moment method.

$$P[EDP > C] = \frac{n}{m} \tag{2.62}$$

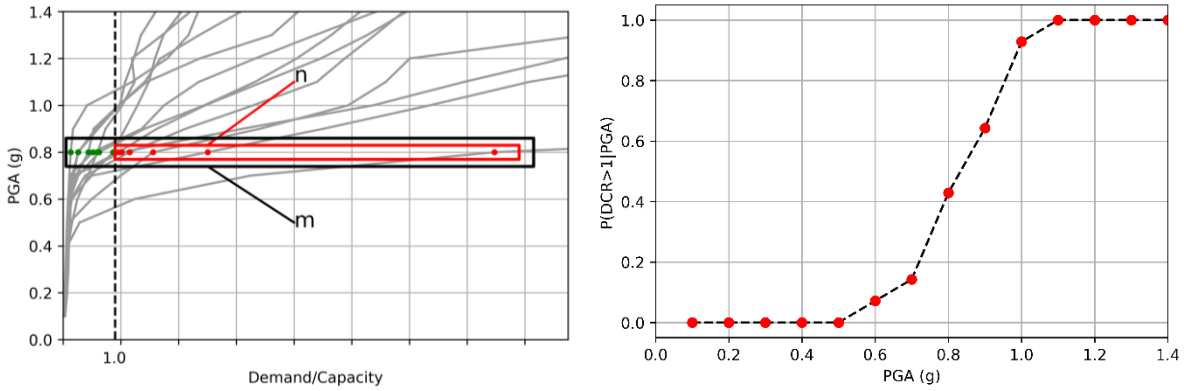

(a) (b)

Figure 2. 20: Application of empirical fragility (a) derivation of probability value at 0.8 g (b) example of empirical fragility (recreated based on data from Flenga, 2021)

$$\mu = \frac{1}{n}\sum_{i=1}^{n} \ln\, IM_i \tag{2.63}$$

$$\beta = \sqrt{\frac{1}{n-1}\sum_{i=1}^{n} (\ln\,(\mathrm{IM}_i) - \mu)^2} \tag{2.64}$$

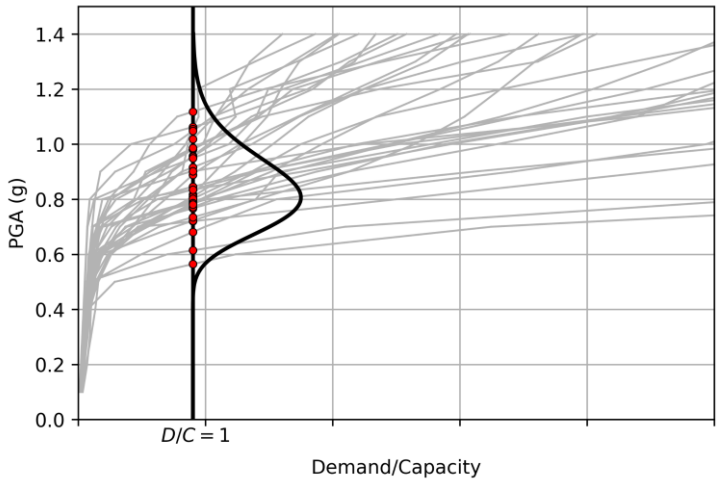

Figure 2. 21: Graphical representation of using the moment method to calculate the fragility from IDA results.

The third method of finding fragility curves from IDA results is the maximum likelihood estimation (MLE) method. The maximum likelihood method derives median (μ) and dispersion (β) values to be more compatible with the empirical fragility. This is achieved by maximising the likelihood function in Equation 2.65, where m is the number of different intensity levels, z_j is the number of ground motions exceeding a given capacity, and n_j is the total number of seismic excitations. IM_j is the specific intensity measure for that part of the summation.

$$\{\mu,\beta\} = \max_{\mu,\sigma} \sum_{j=1}^{m} \left\{ \ln \binom{n_j}{z_j} + z_j \ln \Phi\left(\frac{\ln(IM_j) - \mu}{\beta}\right) + (n_j - z_j)\ln\left(1 - \Phi\left(\frac{\ln(IM_j) - \mu}{\beta}\right)\right)\right\} \tag{2.65}$$

2.7.3 Risk Assessment

A seismic risk assessment involves combining the seismic hazard (refer to Section 2.6.1) and a structure's fragility (refer to Section 2.6.2) to determine failure probability. A failure probability is typically given as an annual probability of a structure exceeding a given limit state. The failure probability can then be combined with an exposure function to find the seismic risk. The exposure function is the expected losses given a certain failure.

The failure probability is found from the hazard and fragility curve, as shown in Figure 2.22 and detailed in Equation 2.66, where $H(a)$ is the hazard curve, and $p_F(a)$ is the fragility curve. It should be noted that the differential fragility function is a log-normal probability function.

$$p_F| = -\int_0^\infty \frac{dH(a)}{da} p_F(a) da = \int_0^\infty H(a) \frac{dp_F(a)}{da} da \quad (2.66)$$

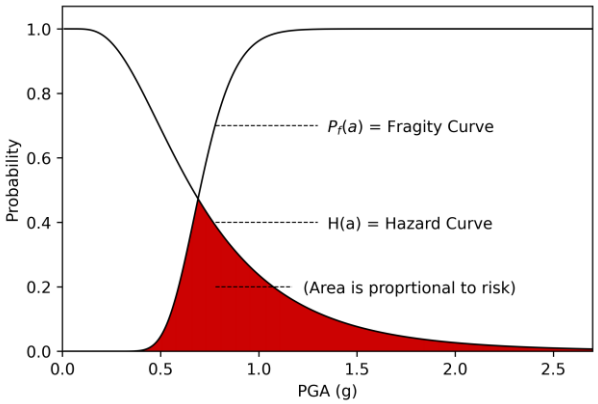

Figure 2. 22: Hazard curve and fragility curve shown on the same axis.

2.6.3.1 Target Risk Assessment Values

In several structural codes, seismic risk has been used to assess the suitability of a structure. ASCE (2005) uses threshold risk values for different seismic design categories (SDC). These SDCs are based on the importance and consequence of the structure. The risk value can be seen in Table 2.6. Studies in literature have also suggested target risk values. Pinto et al. (2014) recommended risk values shown in Table 2.7. These risk values are based on the importance class from Eurocode. The Chinese code GB50010-2010 (2010) sets out the requirements of: 1) no damage under a regular earthquake, 2) no unrepairable damage under a moderate earthquake 3) no collapse. These criteria are interpreted by Lu et al. (2014) to mean a probability of less than 63.2% of exceeding LS_1 in 50 years and less than 2% probability of exceeding LS_4 in 50 years.

Table 2. 6: Target risk values suggested by ASCE (2005)

SDC	Annual Probability	Probability in 50 years	Return period
1	1×10^{-3}	5%	1000 years
2	4×10^{-4}	2%	2500 years
3	1×10^{-4}	0.5%	10,000 years
4	4×10^{-5}	0.2%	25,000 years
5	1×10^{-5}	0.05%	100,000 years

Table 2. 7: Target risk values suggested by Pinto et al. (2014).

Limit State	Importance Class I	Importance Class II	Importance Class III	Importance Class VI
SLD	0.064	0.045	0.030	0.022
SLS	0.0068	0.0047	0.0032	0.0024
SLC	0.0033	0.0023	0.0015	0.0012

2.8 Conclusions

The chapter has reviewed much of the recent literature surrounding seismic risk in Nepal. It highlighted Nepal's issues, such as their high level of seismic hazard and unengineered, owner-built structures. This literature review also highlighted remedial efforts, past and present, to increase the seismic resilience of Nepalese infrastructure. These efforts included a phased introduction of design codes that were gradually brought into law in all cities in Nepal. These design codes included "mandatory rules of thumb" designed to ensure the local construction industry could follow them. These codes show how developments in seismic safety in Nepal are being implemented and subsequently decrease the risk to the local population. This highlights the importance of further developing the understanding of seismic safety in Nepal. However, it also highlights that they will likely not be implemented if the recommended actions are not sympathetic to the local construction techniques.

This chapter also reviewed some of the literature on the structural modelling of reinforced concrete and masonry. Although some more sophisticated modelling techniques may not be accessible to developing countries, many of these methods may become more widely available with increasing computational power. For reinforced concrete, this literature review covered how the models for the material properties had developed over time and presented the material models that are subsequently used in this thesis. Various methods of modelling masonry were presented, including equivalent frame, continuum macro-modelling, equivalent strut, discrete element method and continuous micro-modelling. This literature review showed that the more detailed models were typically more accurate at capturing local failure mechanisms, however they required a more detailed geometry and a more detailed set of material properties.

The process of carrying out a seismic risk assessment was then summarised. This reviewed probabilistic and deterministic seismic hazard assessment and discussed the advantages and disadvantages. These two approaches have been shown to have limitations, with PSHA now being the defacto for design codes. Certain Nepalese PSHA studies were summarised, including the PSHA maps from NBC-105:1994 (1994) and NBC-105:2020 (2020). This literature review showed a wide range of values from various PSHA studies and explained how their values could severely affect the final risk assessment. Several methods of finding a fragility curve were summarised, including empirical methods, incremental dynamic analysis, and cloud analysis. Empirical fragility curves do not typically account for record-to-record variability as all the data is generally collected from a single earthquake. This, therefore,

highlighted the importance of using analytical and numerical methods to obtain fragility curves. Cloud analysis and incremental dynamic analysis also had issues, with incremental dynamic analysis having problems inherent in a scaled ground motion set and cloud analysis requiring a ground motion selection set which causes limit state exceedance in over 30% of cases. The numerical method of combining the hazard and fragility curve to find the seismic risk was presented. Finally, code-based target risk levels were summarised. This underscores the importance of carrying out a reliable seismic risk assessment. It is becoming a more popular assessment method and is already used in the US nuclear industry (ASCE, 2005).

This literature review has highlighted many complex issues surrounding a seismic risk assessment. Using a template design for a structure allows a single seismic fragility assessment to be carried out. The seismic risk assessment can then be carried out at all locations across the country, allowing an evaluation of the structure's suitability in a country of varying seismic hazard. However, this chapter highlighted that due to the sophisticated analysis methods a high computational demand, it is not suitable to carry out a full seismic risk assessment for all buildings in developing countries. Using a single template design, a seismic risk assessment can become a more viable option for NGOs who want to ensure their structures meet the most stringent risk threshold. A seismic risk assessment for a building typology can also inform government decisions on the impact of potential investment in seismic resilience and more stringent codes and code implementation.

Chapter 3: Risk Assessment of Template Schools Using RC Modelling

Part of this chapter is based on the following references.

Cross, T., De Luca, F., De Risi, R., Ranamagar, T. R., Mitchell, T., & Sweetman, A. (2020). Mapping the seismic safety of RC" template schools" in Nepal. *International Journal of Disaster Risk Reduction*, *51*, 101844.[1]

Cross, T., De Luca, F., De Risi, R., Rana, T. R., Mitchell, T., & Sweetman, A. (2019). Pounding in Nepalese school buildings. In *Society for Earthquake and Civil Engineering Dynamics Conference*. SECED.[1]

Objectives of this chapter

This chapter will seek to use an up-to-date finite element (FE) model of a template structure to assess the seismic risk across Nepal. Non-linear time history analysis (NLTHA) will be used on the FE model of a two-storey reinforced concrete (RC) building with masonry infills. The results of these analyses will be used to perform a cloud analysis and derive the fragility curves of the structure for pounding, damage limit state and life safety limit state. The results of this fragility analysis are then compared with results from the literature. These fragility curves can then be combined with hazard studies from literature to assess the seismic risk to the structure across Nepal. The fragility analysis and subsequent risk assessment will be carried out on the FE model of the structure with and without modelling the contribution of the masonry infills. These results can be compared to assess the importance of modelling the infills. The objectives of this chapter are as follows:

- Develop a non-linear FE model of a template structure using up-to-date modelling techniques accounting for the non-linearities in the RC and the masonry infills. Where possible local data for material properties are used.
- Carry out NLTHA using a compatible ground motion set.

[1] The first authors contribution included: methodology, data curation, analysis , data visualisation and writing. Co-authors reviewed and supervised the work

- Explicitly assess the pounding fragility of the structure to evaluate the implications of the pounding in the general risk assessment.
- Assess the limit state fragility of the structure using a cloud analysis on the results from the NLTHA.
- Use one of Nepal's most up-to-date hazard maps to assess the risk to the structure across Nepal for the damage limitation and life safety limit state.
- Assess the impact of modelling the masonry infills on the final seismic risk to the structure.

3.1 Introduction

Both non-governmental organisations (NGOs) and intergovernmental organisations play a crucial role in the reconstruction of schools after a large earthquake; this was seen in Haiti in 2010 (World Bank, 2013) and Nepal in 2015 (Unicef, 2018). Structural characteristics of schools, such as large rooms with large openings (doors and windows) and a high concentration of people, make them especially vulnerable (Gentile et al., 2019a). It is common practice to use a "template design", where one design is used at many sites to reduce design time and cost.

The Nepalese Department of Education set out strict guidelines on the design of schools (Nepal Department of Education, 2016). Each school design must be approved by the Nepalese Department of Education before construction. The Department of Education is also responsible for ensuring all the school buildings follow the Nepalese building code (Jones et al., 2016). This process can be costly and time-consuming. Therefore, many NGOs use a template school design to avoid repeating this process multiple times. These designs may have minor alterations at different sites based on the availability of materials (Pahar Trust, 2019). Applying a single design across a country with a non-homogeneous seismic hazard leads to a varying seismic risk of the structures. Furthermore, updated probabilistic seismic hazard analysis (PSHA) studies have peak ground acceleration (PGA) values reflecting the updated knowledge on the seismic sources. These more recent studies have given PGA values significantly higher than pre-Gorkha values. This study uses the results of recent PSHA studies in combination with the results of NLTHA to assess the seismic risk of a template school across Nepal and, therefore, to evaluate the variability of the "implicit risk" in the template school practice all around the country. The implicit risk is the unavoidable seismic risk that a building will exceed a given limit state (Building Seismic Safety Council, 1988). In this context, implicit risk directly quantifies the risk of a structure designed according to code standards assessed explicitly

through direct integration of hazard and fragility for different limit states (e.g., Iervolino et al., 2018).

Regional-scale seismic safety assessments are carried out on critical infrastructure such as schools. It allows local governments to address seismic safety issues using methods specific to their infrastructure and seismic hazard (Grimaz et al., 2016). Regional-scale seismic risk assessment has previously been applied to RC schools with masonry infills in Italy as part of a seismic loss assessment for the Italian school building stock (O'Reilly et al., 2019, Perrone et al., 2020a).

PSHA is the methodological approach underpinning the seismic hazard in most modern design codes, such as Eurocode 8 (EN 1998-1, 2004) and the Unified Building Code (UBC-97, 1997). PSHA studies can be limited by the availability of data for the tectonic faults in an area, fault modelling techniques, and ground motion prediction equations (GMPEs) available. Many PSHA studies have been carried out on Nepal with widely varying results. PGA values for Kathmandu with a 475-year return period varied from 0.35g-0.55g for PSHA studies carried out before the Gorkha 2015 earthquake (Chaulagain et al. 2015a, Ram and Wang, 2013). More recent studies, benefitting from the additional evidence provided by the 2015 earthquake, have put the PGA for Kathmandu over 0.65g when considering a 475-year return period (Stevens et al., 2018, Pokhrel et al., 2019). For more details, refer to Section 2.6.1.1. These high levels of variation in PSHA results will significantly impact the risk of template schools.

Pahar Trust is a charity based in the UK and founded in 1991 by Tom Langridge MBE and Chandra Bahadur Gurung. Their work is split into construction work and educational improvements. The construction work involves constructing four to six reinforced concrete (RC) schools per year, and the educational improvements involve teacher training and resource improvements (Pahar Trust, 2020). Pahar Trust has provided the design of a template school for this study. It is a six-classroom school, set across two storeys and made of RC with masonry infills. The structure has a seismic gap to reduce the torsional effects caused by the off-centre staircase.

A seismic fragility assessment will be used to assess this template school which will then be combined with the hazard curves across Nepal to determine the variation of seismic risk across the country. A fragility curve relates a measure of ground shaking (i.e. Intensity Measure, IM) to the probability of exceeding some level of response or damage state. The exceedance of limit

states is defined in terms of interstorey drift (ISD) however, this does not consider pounding. A fragility curve can be derived explicitly for the occurrence of pounding where information of the neighbouring buildings is available (Tubaldi et al., 2012). Fragility curves can be obtained empirically, using historical data, or numerically by performing structural analysis on the building (Choi et al., 2004). Further details on methods of fragility assessment can be found in Section 2.6.2. Cloud analysis is a method to obtain a fragility curve by using linear regression in log-space with the results of non-linear time history analysis (NLTHA) with a range of ground motions (e.g., Jalayer et al., 2014). A critical demand parameter or capacity limit is set based on the limit state, and a cumulative probability function is obtained. Integration is then used with the hazard curves provided by Stevens et al. (2018) to evaluate the mean annual frequency (MAF) of exceeding various limit states.

This chapter addresses the suitability of template schools across a region of varying seismic hazard and assesses the influence on risk assessment associated with the explicit consideration of masonry infill contribution in the structural model. The fragility of the structure due to pounding is compared to the fragility of the structure due to the exceedance of a threshold ISD level. A comparison of the efficiency of different intensity measures is carried out for the considered structures considering as IM the peak ground acceleration (PGA) and the average spectral acceleration (AvgSA) (Kohrangi et al., 2017a, De Luca et al., 2019).

Finite element models are developed to obtain a fragility curve for the template school experiencing pounding or exceeding damage limitation or life safety limit state. These fragility curves can be used to assess how the structure will most likely respond to a given ground motion. A hazard curve is used to identify what level of intensity of an earthquake is expected in a given time period. The information from the hazard curve and fragility curves can then be combined to calculate what the risk is for the structure. This risk is measured in terms of the probability of the structure exceeding a specific limit state in a given time. These risk levels can finally be compared to reference levels from design codes to assess whether these template schools have an acceptable level of seismic risk.

3.2 Seismic Hazard and Ground Motion Selection

Seismic hazard selection is essential for seismic risk assessment, as described in Section 2.6.1. The seismic hazard can also play an important role in ground motion selection for the NLTHA as design codes typically recommend selecting a ground motion suite similar to design ground motions at the site (EN 1998-3, 2005). As discussed in Section 2.6.2.2, fragility analysis

methods such as cloud analysis also have requirements for ground motion selection (i.e., a certain proportion of the analyses exceed a DCR of 1). These requirements often conflict.

3.2.1 PSHA

To calculate risk in this study, a seismic hazard map is required for Nepal. Several PSHA studies have been carried out for Nepal with varying results (Chaulagain et al., 2015a, Ram and Wang, 2013, Stevens et al., 2018, Pokhrel et al., 2019). Further details can be found in Section 2.6.1.1. For this study, the PSHA study carried out by Stevens et al. (2018) is used for risk assessment, as it was carried out using an up-to-date characterisation of the Main Himalayan Thrust (MHT) as a single thrust based on the evidence from the 2015 earthquake (Elliott et al., 2016, Stevens et al., 2018). Stevens et al. (2018) carry out the PSHA using a series of fault and area sources, and the Gutenberg-Richter relationship is used to find the maximum moment. Openquake is then used to carry out the PSHA and find the PGA at 2% and 10% probability of exceedance in 50 years, these results are shown in Figure 3.1.

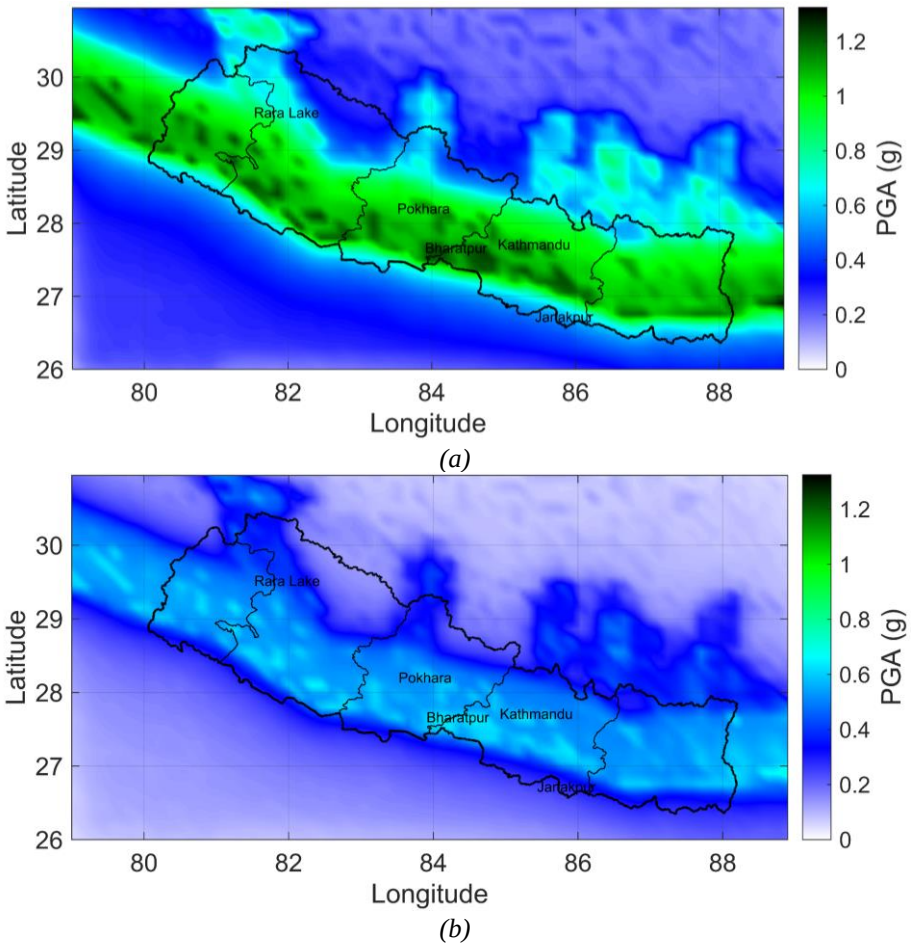

(a)

(b)

Figure 3. 1: Maps generated using data from Stevens et al. (2018) (a) PSHA study for 2% probability of exceedance in 50 years (2475-year return period). (b) PSHA study for 10% probability of exceedance (475-year return period) in 50 years.

Stevens et al. provide hazard maps for the 2% and 10% probability of exceedance in 50 years. These maps are shown in Figure 3.1. Stevens et al. (2018) also provided the complete hazard curves for five locations shown in Figure 3.2: Bharatpur, Janakptur, Kathmandu, Pokhara and Rara Lake, as indicated in the maps in Figure 3.1.

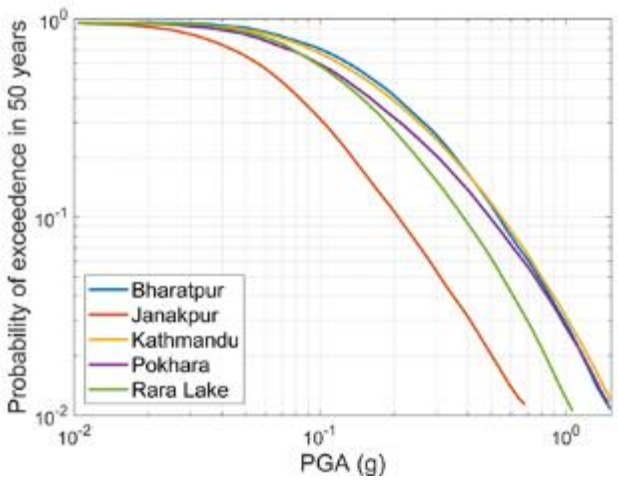

Figure 3. 2: Hazard curves for five locations across Nepal as provided in Stevens et al. (2018)

For full integration of risk at all locations, the full hazard curve is needed at each geographic point, for further details on risk integration, refer to Section 2.7.3. Data from Figure 3.1 provides only two points for the curve at each geographic point; thus, a curve must be fitted based on those two known points. For brevity, Stevens et al. (2018) provide the full hazard curve for five locations across Nepal, as shown in Figure 3.2. These curves and the two PGA values given at each location can be used to interpolate a full hazard curve for each location. Interpolation is often used in areas where data is scarce. At first, linear regression in log-space was used with the two known points (see Figure 3.3a). The error was calculated by evaluating the difference in the area beneath the hazard curves provided by Stevens et al. (2018) and the fitted line. The error between the linear approximations and the five known curves (Figure 3.2) was evaluated, leading to a mean error of 31.2%. This is not considered an acceptable level of error, and a second-order approximation was used, as proposed by Vamvatsikos (2014). Three initial conditions are required to allow a unique solution of a 2nd order polynomial. For each geographic location provided by Stevens et al. (2018), two points on the hazard curve are

provided, and for the third point, an earthquake with a PGA of 0.01 g or over has a 100% probability of occurrence in 50 years is assumed. This assumption can be seen in Figure 3.3a and holds true for all hazard curves provided, as shown in Figure 3.2. The second-order approximation in log-space can be seen in Equation 3.1.

$$H(s) = k_0 exp\left(-k_2 ln^2(s) - k_1 ln(s)\right) \tag{3.1}$$

k0, *k1* and *k2* are coefficients that can be found to have unique values for a second-order polynomial that passes through three known points. When this method is used to approximate the hazard curve, it results in a probability greater than 1 for low PGA events (Figure 3.3a). Given the first quadratic fit, the third point, which was previously assumed to be a 100% probability of a 0.01 g event in 50 years, is moved to a greater PGA value whereby the quadratic has a maximum at 1. The result can be seen in Figure 3.3b. Figure 3.3b shows that this results in a drop at smaller PGA values. This is avoided by setting the probability to a constant level of 1 before the peak. This final method of approximation can be seen in Figure 3.3c. This is shown to be an accurate approximation with a mean error of 4.1%. This method of approximating the hazard curve can then be applied to all geographic points using the two input values. Applying this fitting method to the data provided by Stevens et al. (2018) allows a unique hazard curve to be found at each geographical location across Nepal. This will therefore allow the risk integration in Section 3.6 to be carried out across Nepal.

(a)

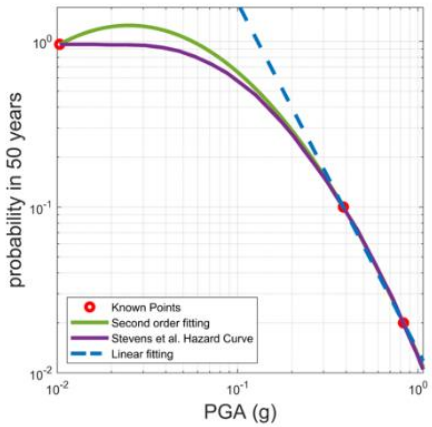

(b)

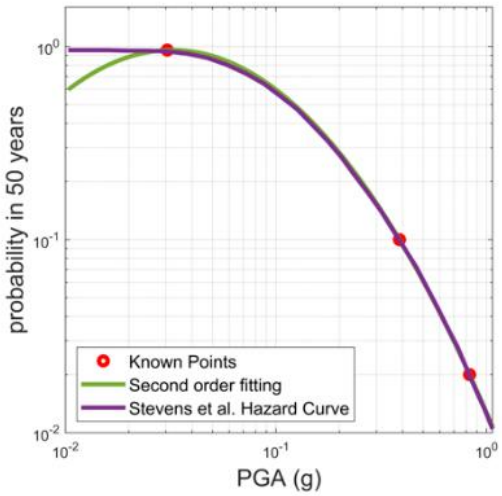

(c)

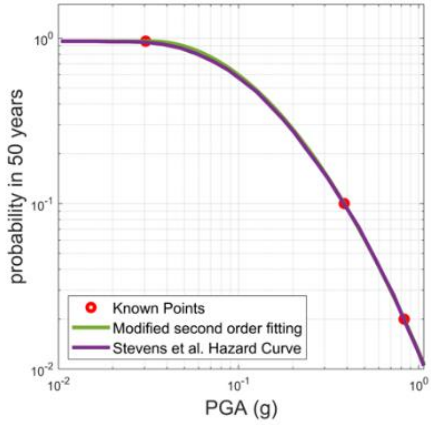

Figure 3. 3: Approximation of hazard curve. (a) Linear approximation and second-order approximation using the third known point as 100% probability of a 0.01 g event in 50 years (b) Second-order approximation with the third point set so the maximum is equal to 1. (c) All PGA values lower than the third known point are set equal to 1.

3.2.2 Ground motion selection

This study will assess the fragility of pounding and exceeding limit states independently. As it is preferable to exceed a demand capacity ratio of one when carrying out cloud analysis (Jalayer et al. 2017), the ground motion selection is a function of the demand capacity ratio, hence it is necessary to carry out two independent ground motion selections.

3.2.2.1 Limit State Ground Motion Selection

A ground motion record selection is required to perform a nonlinear dynamic analysis of the template school structure for the fragility assessment of exceeding limit states. This analysis is carried out with two ground motion sets. The first ground motion set is the far-field ground motion set suggested by FEMA P695 (2009). This ground motion set contains 22 pairs of horizontal motions and is available from the PEER NGA West 2 (2014) ground motion

database. Ground motion set 1 (GM 1) is referred to as the "far-field" ground motion set by FEMA P695 and is used for collapse assessment. All these ground motions have a fault rupture distance greater than 10 km and have magnitudes that range from 6.5 **M**w to 7.6 **M**w. The ground motion catalogue can be found in Table 3.1, and the 5% elastic response spectrum is shown in Figure 3.4a.

Table 3. 1: Main characteristics of FEMA P695 far-field earthquakes

Earthquake	Year	Epicentre Distance (km)	PGA (g)	Magnitude	Duration (s)
Northridge	1994	13.3	0.52	6.7	29.99
Northridge	1994	26.5	0.48	6.7	19.99
Duzce, Turkey	1999	41.3	0.82	7.1	55.90
Hector Mine	1999	26.5	0.34	7.1	45.31
Imperial Valley	1979	33.7	0.35	6.5	99.92
Imperial Valley	1979	29.4	0.38	6.5	39.035
Kobe, Japan	1995	8.7	0.51	6.9	40.96
Kobe, Japan	1995	46	0.24	6.9	40.96
Kocaeli, Turkey	1999	98.2	0.36	7.5	27.085
Kocaeli, Turkey	1999	53.7	0.22	7.5	30.00
Landers	1992	86	0.24	7.3	44.00
Landers	1992	82.1	0.42	7.3	27.965
Loma Prieta	1989	9.8	0.53	6.9	39.955
Loma Prieta	1989	31.4	0.56	6.9	39.945
Manjil, Iran	1990	40.4	0.51	7.4	53.52
Superstition Hills	1987	35.8	0.36	6.5	40.00
Superstition Hills	1987	11.2	0.45	6.5	22.30
Cape Mendocino	1992	22.7	0.55	7.0	36.00
Chi-Chi, Taiwan	1999	32	0.44	7.6	90.00
Chi-Chi, Taiwan	1999	77.5	0.51	7.6	90.00
San Fernando	1971	39.5	0.21	6.6	28.00
Friuli, Italy	1976	20.2	0.35	6.5	36.345

Indian standards (IS 1893 Part 1, 2002) do not specify a ground motion selection method but state that NLTHA "*shall be based on an appropriate ground motion and shall be performed using accepted principles of dynamics*". Many other seismic codes use a ground motion selection method for NLTHA based on seismic hazard at the site of the structure (ASCE 7 10, 2010, FEMA P-58-1, 2018). As the template school is implemented across an area of varying seismic hazard, it is not possible to apply these methods for this analysis. FEMA P695 presents

22 far-field ground motion sets and 28 near-field ground motion sets. These ground motions are independent of the site and are considered efficient for assessing record-to-record variability. The far-field ground motion set was used as these are the ground motions recommended by FEMA P695 (2009) for collapse assessment. FEMA P695 (2009) states that near-fault motions should not be used for collapse assessment due to "*unresolved issues concerning the characterization of near-fault hazard and ground motion effects*". These ground motion effects include forward directivity, fling-step, basin, surface wave, and soft soil effects (Chen et al., 2019).

The second ground motion set was formed of five pairs of horizontal recordings from the Gorkha 2015 earthquake. Four of these recordings were made available by the Faculty of Engineering, Hokkaido University, Japan (Rupakhety et al. 2017), with the final one being made available by USGS (2016). The Gorkha 2015 earthquake, which had a moment magnitude of 7.8 **M**w, had an epicentre 80 km west-northwest of the Centre of Kathmandu and destroyed 6000-8200 schools (Giordano et al., 2020). Figure 3.4b shows that all the ground motions except for KTP have amplification in the high period range. This is due to the sediments and the topography of the Kathmandu Valley (Asimaki et al., 2017; Gilder et al., 2020). The KTP station does not experience this amplification as it is positioned on a rock outcrop near the basin's western edge. This amplification resulted in relatively low damage in low-rise structures and high levels of non-structural damage to tall buildings (Brando et al., 2017). The ground motion catalogue for GM 2 can be found in Table 3.2.

Table 3. 2: Main Characteristics of the five ground motion recordings from Kathmandu Valley of the Gorkha 2015 earthquake.

	Orientation	**Latitude**	**Longitude**	**Location**
KATNP	000, 090	27.71307	85.3161	Kanti Path
KTP	230, 320	27.68182	85.27261	Kirtipur Municipality Office
THM	090, 180	27.68072	85.3772	University Grant Commission Office, Bhaktapur
TVU	000, 090	27.68145	85.28821	Central Department of Geology
PTN	090, 360	27.68082	85.31897	Engineering College, Pulchowk

Two ground motion sets are used as ground motion set 1 offers exposure to a wide range of far-field ground motions with a moment magnitude ranging from 6.5 to 7.6 and a PGA ranging from 0.21 g to 0.82 g. The Gorkha ground motion set allows us to highlight how the Gorkha earthquake may have affected these school buildings in 2015, and this can further be used as a point of comparison with other local schools.

It can be seen from Figure 3.4 that the response spectra have different shapes and different intensities (i.e. GM 1 is significantly higher with respect to GM 2). In particular, the variation in PGA is greater for GM 1 (COV = 0.42) compared to GM 2 (COV = 0.25). These differences between the two ground motion sets are expected as GM1 accounts for the inter-event variability that is not accounted for in GM2 (i.e., all ground motion records from the same event).

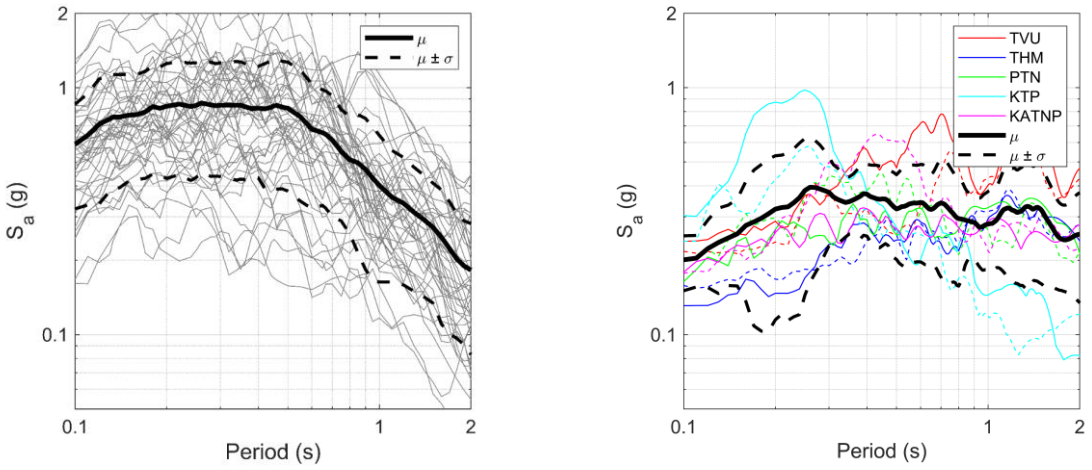

(a) *(b)*

Figure 3. 4: 5% damped elastic response spectrum for (a) "far-field" ground motion set by FEMA P695 (b) Gorkha 2015 ground motions

Parts of Kathmandu could potentially experience earthquakes up to $\mathbf{M}_w$ 9.2 (Stevens and Avouac, 2016), which is higher than either of the ground motion sets. Jalayer et al. (2017) set out several criteria for ground motion selection to meet for the fragility curves to be considered reliable. It is shown in Section 3.5.2 that these criteria are met, and hence the fragility curve can be reliable at extreme IM measures.

3.2.2.2 Pounding Ground Motion Selection

The pounding fragility assessment was carried out with a different ground motion selection which contained three ground motion sets. The first group of ground motions (pounding ground motion set 1) is the same as GM2 in the limit state ground motion selection and is detailed in Table 3.2. This contains five available recordings of the 2015 Gorkha earthquake (Rupakhety et al., 2017). The elastic response spectrum of these motions is shown in Figure 3.4b, where it can be seen there is significant amplification in the spectral acceleration in the large period range (1s-6s). This is due to basin effects caused by the loose fluvio-lacustrine deposits and

source effects of the Gorkha earthquake (Rajaure et al., 2016). KTP is not affected by basin effects as it is situated on a rock outcrop near the western basin edge.

The second ground motion set (pounding ground motion set 2) is selected from the NGA-west 2 database. It is compatible with Eurocode 8 type 1 spectral shape for soil class C (predominant in the Kathmandu valley) anchored at 0.38g (see Figure 3.5a). Importance class iii is used. The PGA value of 0.38g is used as it is the 10% in 50 years exceedance value for PSHA studies carried out before the Gorkha earthquake (e.g., Chaulagain et al., 2015), in the following referred to as "pre-Gorkha" PSHA. 11 couples of ground motions are used, no scaling is used, and none of the motions are pulse-like motions. The spectrum matching was done following Eurocode 8 (EN 1998-3, 2005), whereby between 0.2T1 and 2.0T1, the arithmetic mean of the 5% damped elastic response spectrum is at no point lower than 90% of the design spectrum. The main characteristics of this ground motion set can be seen in Table 3.3.

The third ground motion set (pounding ground motion set 3, in the following referred to as "post-Gorkha") uses the same ground motions as the previous set but multiplied by an additional scaling factor to increase the PGA in line with post-Gorkha PSHA studies. A scaling factor of 1.579 is used, resulting in a PGA of 0.60g. which is the value obtained from a post-Gorkha PSHA (Stevens et al., 2018), see Figure 3.5b. The scale factor for the ground motions should not exceed specific maximum values to avoid bias in the results; this limit varies from 2 to 4 (Bommer and Acevedo, 2004).

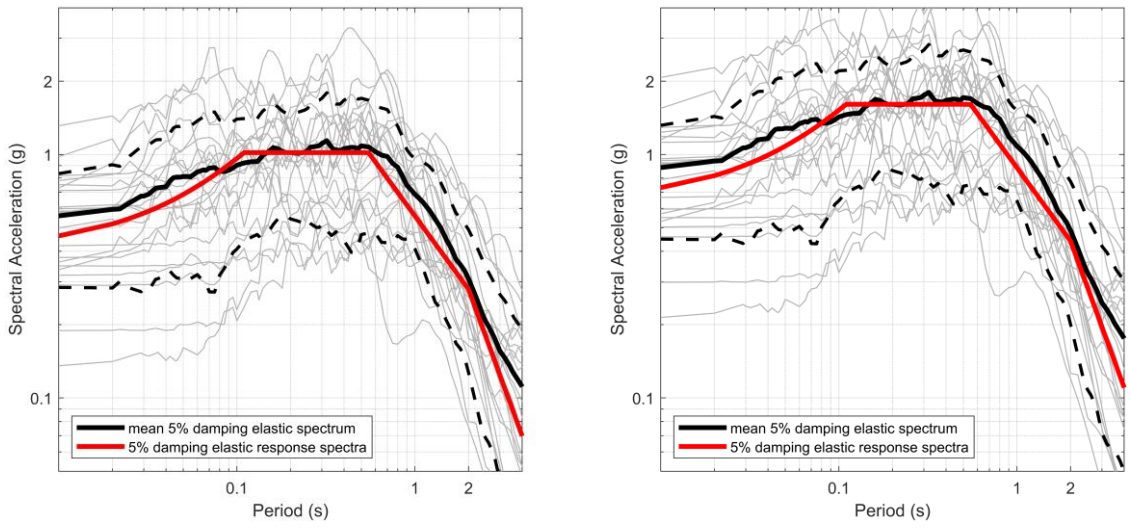

(a) (b)

Figure 3. 5: 5% damped elastic response spectrum for (a) EC 8 compliant (pre Gorkha PSHA) motions (b) EC 8 compliant (post-Gorkha PSHA) motions.

Table 3. 3: Main Characteristics of the spectra compatible ground motion set (pounding ground motion set 2)

Earthquake	Station	Orientation	Year	Vs30 (m/s)	Rjb (km)	M_W
Chi-Chi, Taiwan	TCU084	000, 090	1999	665.2	0	7.6
Christchurch, New Zealand	Hulverstone Drive Pumping Station	266, 356	2011	206	4.32	6.2
Chuetsu-oki, Japan	Nagaoka	000, 090	2007	514.3	3.97	6.8
Gazli, USSR	Karakyr	000, 090	1976	259.59	3.92	6.8
Loma, Prieta	LGPC	000, 090	1989	594.83	0	6.9
Mammoth Lakes 01	Long Valley Dam	000, 090	1980	537.16	12.56	6.1
Manjil, Iran	Abbar	000, 090	1990	723.95	12.55	7.4
Parkfield-02, CA	Parkfield - Fault Zone 14	000, 360	2004	246.07	8.45	6.0
St Elias, Alaska	Icy Bay	090, 180	1979	306.37	26.46	7.5
Tottori, Japan	TTRH02	000, 090	2000	310.21	0.83	6.6
Westmorland	Westmorland Fire Station	090, 180	1981	193.67	6.18	5.9

3.3 Structural modelling

Pahar Trust provided the design of a template school, a two-storey building with six classrooms. The total height of the building is 5.8 m, and the dimensions in plan are 4.9 m and 20.3 m, see Figure 3.6. The template school is a reinforced concrete frame with masonry infill, one of the structural typologies commonly used for schools in Nepal (De Luca et al., 2019). The design included the beam-column layout, shown in Figure 3.6c, and the layout of the steel reinforcements, shown in Figure 3.7. The steel class for the rebar was specified as FE500, and the concrete was defined as being M20. M20 concrete is defined by the Indian standard (IS456-2000, 2000) as concrete with a 15 cm x 15 cm x 15 cm cube strength with a characteristic value of (f_{ck}) of 20 MPa. FE500 steel has a yield stress of 500 MPa and a Young's modulus of 210 GPa, as set out by the India standards (IS 1786, 2008). M20 concrete has a characteristic strength of 20 MPa and a Young's modulus of 22.3 GPa, as set out by Indian standards (IS456-2000, 2000). The masonry infill was specified as "*fired brick masonry*" with a mortar of a cement-sand ratio of 1:6. Due to the nature of construction practices in Nepal, the materials

and the modelling techniques used have inherent uncertainties that could significantly affect the final risk assessment. These can be reduced with a high level of onsite quality control. These uncertainties are not accounted for in this study, focusing instead on the variability of risk caused by the hazard. It can be noted that the quality of construction practices in projects carried out by NGOs is typically higher with respect to the general population. This is often due to the presence of a qualified engineer onsite. The structure has a 102 mm (4 inch) seismic gap, as shown in Figure 3.6c between gridlines 3a and 3b, to avoid torsion caused by the off-centre staircase. The beam and column section properties can be seen in Figure 3.7. As there is no structural interaction across the seismic gap, as shown by the probabilistic assessment of pounding in Cross et al. (2019), the building was split into two separate finite element (FE) models.

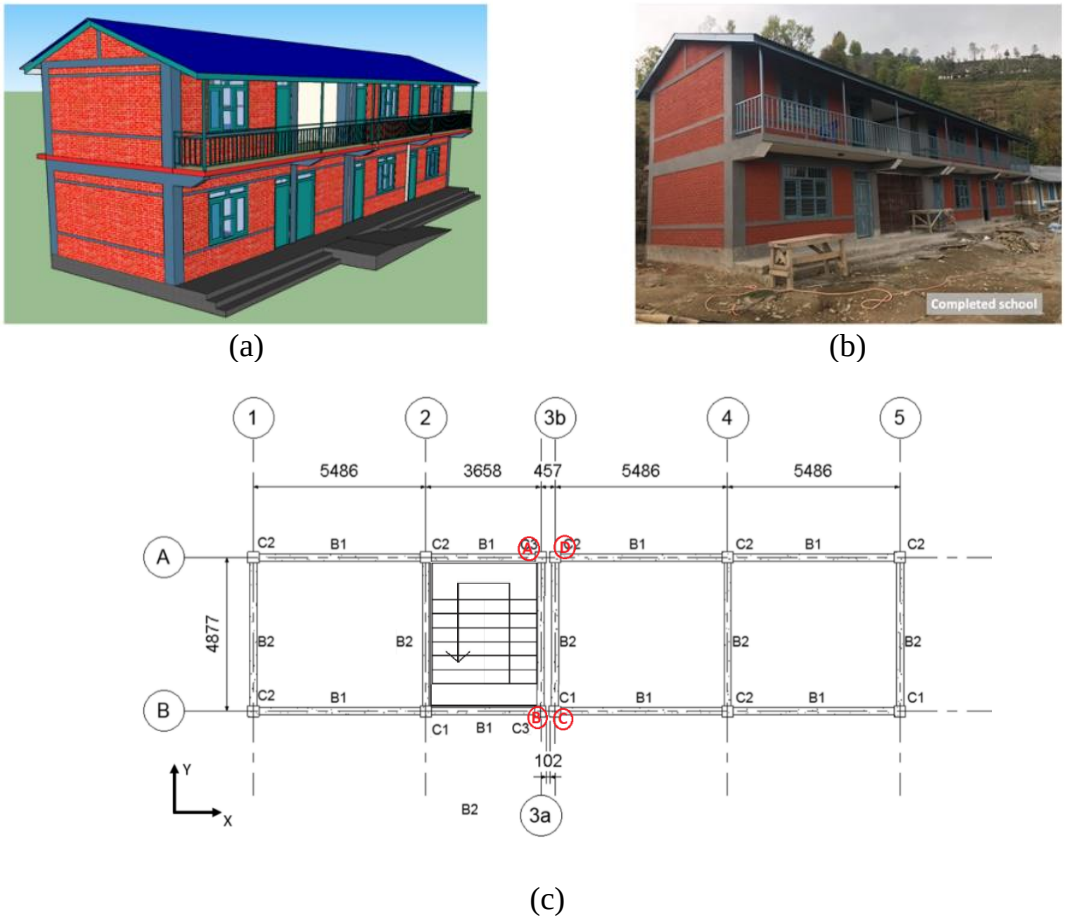

(a) (b) (c)

Figure 3. 6 Pahar Trust template RC with infill school: (a) 3D architectural rendering; (b) example of a realised project; (c) beam and column layout of the template school (units in mm) (Pahar Trust, 2020).

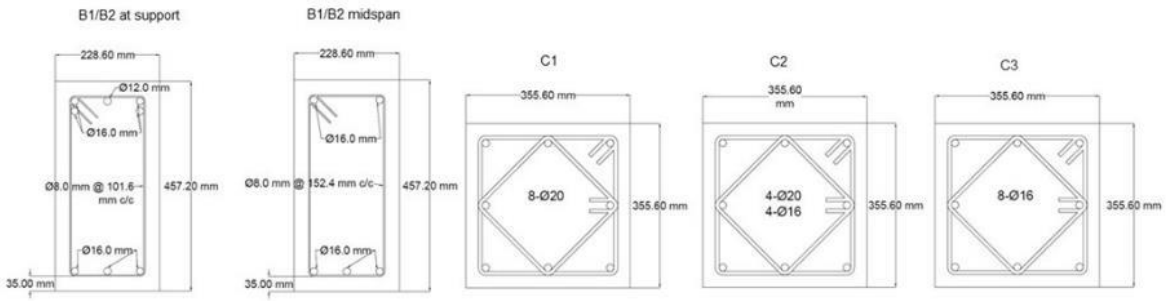

Figure 3. 7 Beam and column section properties of Pahar Trust template school (Pahar Trust, 2019)

A non-linear finite element model in OpenSees was developed based on the structural drawings provided. In particular, two models were developed. The first model only accounted for the RC beams and columns and did not consider the structural contribution of the masonry infills. This approach is consistent with the design practice adopted by the Nepalese National building code (NBC 201, 1994). Infills should be considered according to Eurocode 8; however they are sometimes not considered in design practice. This model will hereafter be referred to as the "bare model". The second model will explicitly consider the masonry infills' structural contribution using a triple strut model, as described in Section 2.5.2.3. This model will hereafter be referred to as the "infilled model".

3.3.1 Element Classification

A preliminary ductility classification is carried out to ensure that maximum shear resulting from flexural behaviour (V_{flex}) does not exceed the element's shear capacity (V_{shear}). Such assessment is carried out by classifying the elements by employing the shear capacity model proposed by the Eurocode 8 part 3 (EN 1998-3, 2005). As implemented by De Luca and Verderame (2013), the approximate classification assumed here classifies elements as ductile elements, limited ductility elements, or brittle elements. The maximum shear resulting from flexural behaviour can be calculated using Equation 3.2. Such classification is a preliminary assessment of the seismic performance of the RC elements in the structure. The equation for V_{flex} relies on the following 3 assumptions. In the instance where assumptions a and b are not met (typically a beam), the check must be carried out for positive and negative bending.

a) the total longitudinal reinforcement is made of tension and compression reinforcement
b) there is the same steel area in tension and compression
c) both the tension and compression reinforcing steel have yielded

$$V_{flex} = \frac{1}{L_v}\left[\frac{Nh}{2}(1-v) + f_y A_s (d-d')\right] \tag{3.2}$$

In Equation 3.2, N denotes the axial load applied to the element based on seismic gravity loads, L_v is the shear length, h represents the height of the section, v symbolises the normalised axial force, and f_y is the yield strength of steel. A_s is the cross-sectional area of longitudinal steel reinforcement, d is the effective depth, and d' is the depth to the compression reinforcement. The normalised axial force, v (also known as the axial load ratio) is the ratio of the applied axial load to the axial load capacity defined as the product of the design concrete strength and the cross-sectional area. The shear capacity is calculated using Equation 3.3 from Eurocode 8 part 3, where μ^{Δ}_{pl} denotes the ratio of the plastic part of the cord rotation, γ_{el} is a safety factor set to 1.15 for primary seismic elements, and x is the compression zone depth. A_c is column cross-sectional area, f_c is concrete compression strength, ρ_{tot} is total longitudinal reinforcement ratio, and V_w is the contribution of transverse reinforcement to shear resistance, given by Equation 3.4. For $V_{shear,min}$, μ^{Δ}_{pl} is assumed to take a value of 0, meaning there is no plastic rotation, and for $V_{shear,max}$, it is assumed to take the max value of 5 as imposed by Eurocode 8.

$$V_{shear} = \frac{1}{\gamma_{el}}\left[\frac{h-x}{2L_v} min(N, 55A_c f_c) + \left(1 - 0.05 min\left(5, \mu^{\Delta}_{pl}\right)\right) \times \left[0.16 \max(0.5, 100\rho_{tot})\left(1 - 0.16 min\left(5, \frac{L_v}{h}\right)\right)\sqrt{f_c}A_c + V_w\right]\right] \quad (3.3)$$

$$V_w = \left(1 - 0.05 min\left(5; \mu_{\Delta pl}\right)\right) \cdot \left(\rho_w f_{yw} b \cdot z\right) \quad (3.4)$$

For each element V_{flex}, $V_{shear,min}$ and $V_{shear,max}$ are calculated, and the criteria set out in Table 3.4 were used to classify the ductility of the element. Each element must also be classified for the negative flexure demand if the reinforcement in the section is asymmetric (i.e., typical case for beams).

Table 3. 4: Classification of RC element behaviour

Criteria	Classification
$V_{shear,max} > V_{flex} < V_{shear,min}$	Ductile
$V_{shear,max} > V_{flex} \geq V_{shear,min}$	Limited Ductility
$V_{shear,max} \leq V_{flex} > V_{shear,min}$	Brittle

The element classification performed on the school building led to an expected ductile behaviour for all elements, which then influenced the modelling approach implemented for beams and columns.

In addition, the shear capacity of the columns is also checked under the Nepalese Standard (NBC 110, 1994), which uses the shear capacity model from the Indian Standard (IS 456,

1978). The shear capacity of the column is calculated using Equation 3.5, where τ'_c is the shear strength given by the Indian Standard (IS 456, 1978) developed by Taylor (1972) as a function of the concrete grade and the percentage longitudinal reinforcement. The f_y denotes the yield strength of the steel, A_{sv} denotes the total cross-sectional area of shear steel, d represents the effective depth, and s_v is the spacing of the shear reinforcement. Using the Indian Standard, the peak shear demand over capacity ratio is 0.74 in the analysis in this chapter, showing that the column will not experience shear failure.

$$V_u = \tau'_c bd + \frac{0.87 f_y A_{sv} d}{s_v} \tag{3.5}$$

3.3.2 Bare Model

A fibre model was created of the RC frame of the structure. This was implemented in OpenSees using the "Hinge Radau" function (Scott et al. 2006), which uses two-point Gauss-Radau integration over the hinge length. The fibre section is implemented over the hinge length as detailed in Section 2.5 to reduce computational time. The length of the plastic hinge (L_{pl}) is calculated following Eurocode 8 part 3 (EN 1998-3, 2005), where L_v is the shear length assumed as the half-length of the element (see Lombardi, 2019).

Pahar Trust specifies the grade of steel rebar as "FE500". This is implemented into the fibre model using the constitutive nonlinear hysteretic steel model developed by Menegotto and Pinto (1973) and extended by Filippou et al. (1983). For FE500 steel, a yield strength of 500 MPa is used, and Young's modulus of 210 GPa is used in accordance with Indian standards (IS 1786, 2008).

The strength class of concrete is specified by Pahar trust as being M20. This is the lowest permissible strength class of concrete for reinforced concrete by the Indian standard (IS456-2000, 2000). This concrete has a characteristic 28-day crushing strength of 20 MPa and a target (mean) strength of 30 MPa. M20 concrete has a cement:sand:aggregate ratio of 1:1.5:3 and has an elastic modulus of 22.3 GPa (IS456-2000, 2000). Other studies within Nepal have assumed the same concrete properties (Chaulagain et al., 2015b).

The Kent-Scott-Park (Scott et al., 1982) model is used for the hysteretic response of the concrete in the FE model. See more details in Section 2.4.3.1. The additional strength of the concrete due to the confinement was found using the Kent and Park model (1971) that was modified (Park et al., 1982). This alters the unconfined compressive strength by a factor K, as

shown in Equation 3.6, where *f'c* is the peak strength in the unconfined concrete and *f''c* is the strength of the confined concrete.

$$f''_c = Kf'_c \tag{3.6}$$

The factor K is calculated using Equation 3.7, where ρ_s is the ratio of the volume of the confining steel to the volume of the concrete core and f_{yh} is the yield stress of the confining steel.

$$K = 1 + \frac{\rho_s f_{yh}}{f'_c} \tag{3.7}$$

This results in a unique confined concrete compressive strength for each section as the ratio of confining steel varies in each section.

3.3.3 Infilled Model

The masonry infills are implemented using a triple strut model in the finite element (FE) model. Using struts to replicate the effect of the masonry infill was first proposed in the 1960s (Polyakov, 1960). In this study, the three-strut model is used as it has been implemented in many studies of RC with masonry infill (Perrone et al., 2020b) and has been verified with experimental data (Blasi et al., 2018). Since this method was initially proposed, there have been several improvements; however, some failure mechanisms exhibited by masonry infills are still not accounted for (Stavridis et al., 2010). The triple strut model cannot account for out of plane failure mechanisms and does not accurately capture the infill's interaction along the RC frame's length (Asteris et al., 2011). More details on various strut models can be found in Section 2.5.2.3.

The individual hysteretic properties for each strut are modelled using a piecewise linear load-displacement behaviour. The shape of this hysteretic response is calculated according to Panagiotakos and Fardis (1996) using the overstrength factor for solid bricks (i.e., 1.55) calibrated by Blasi et al. (2018). This method is commonly used in literature and verified using experimental data (e.g., Noh et al., 2017, Blasi et al., 2018)

To implement this model three material properties are required for the masonry wall, these are the Young modulus of the masonry infill (E_{inf}), cracking shear strength of masonry infill (τ_{cr}) and the shear modulus of the masonry infill (G_w). Both E_{inf} and τ_{cr} are taken from the experimental work carried out by Shahzada et al. (2012). This experimental work carried out a diagonal compression test on a masonry specimen typical of Pakistan, where the construction techniques are similar to those in Nepal (Varum et al., 2016). This masonry specimen was

formed of burnt clay bricks and mortar with a cement-to-sand ratio of 1:6. This is the same type of brick and sand-to-cement ratio as specified by Pahar Trust. The E_{inf} value is taken to be 1,227 MPa, and the τ_{cr} value is assumed to be 0.05 MPa. The shear modulus of the masonry (G_w) can be taken as 40% of the elastic modulus according to Eurocode 6 (EN 1996-1-1 2005). The final material property required is the Youngs modulus of the concrete (E_c); this is taken to be 22.3 GPa, as outlined in Section 3.3.2. These material properties are summarised in Table 3.5.

Table 3. 5 Material properties for the model of masonry infill

Property	Symbol	Value	Reference
Young modulus of masonry infill	E_{inf}	1,227 MPa	(Shahzada et al, 2012)
Cracking strength of masonry	τ_{cr}	0.05 MPa	(Shahzada et al., 2012)
Shear modulus of masonry	G_w	491 MPa	(EN 1996-1-1 2005)
Young modulus of concrete	E_c	22.3 GPa	(IS456-2000, 2000)

The hysteretic response of the struts is also a function of the geometry of the wall, which varies across the structure. The three dimensions of the infill are t_w, L_w and h_w, which are the thickness, length and height of the infill wall, respectively. Using these dimensions, the diagonal length of the wall (d_w) can be calculated. The angle of the diagonal dimension of the panel (θ), shown in Figure 3.8, is also required. The final geometric parameter is the moment of inertia of the RC column (I_c).

Table 3. 6: Equations used to model the hysteretic response of the triple strut model in accordance with Panagiotakos and Fardis (1996) and Blasi et al. (2018)

Parameter	Symbol	Equation
Cracking force	f_{cr}	$f_{cr} = \tau_{cr} L_w t_w$
Peak shear strength	f_{max}	$f_{max} = 1.55 f_{cr}$
Residual shear strength	f_{res}	$f_{res} = 0.1 f_{max}$
Relative panel-to-frame stiffness	λ	$\lambda = \sqrt[4]{\frac{E_{inf} t_w \sin(2\theta)}{4 E_c I_c h_w}}$
Width of the equivalent truss section	b_w	$b_w = d_w 0.175 \lambda h_w{}^{-0.4}$
Initial stiffness of strut	K_1	$K_1 = \frac{G_w t_w L_w}{h_w}$
Post cracking stiffness	K_2	$K_2 = \frac{E_{inf} t_w b_w}{d_w}$
Softening stiffness	K_3	$K_3 = -0.01 K_1$

The peak shear strength (f_{max}) is taken as $1.55 f_{cr}$, as shown in Table 3.6, as is specified for solid clay bricks in Blasi et al. (2018). The residual shear strength (f_{res}) of the struts is taken as $0.1 f_{max}$

based on the experimental results of Panagiotakos and Fardis (1996). The softening stiffness is taken as -0.02K_1 based on the results of experimental work (Crisafulli, 1997).

The total strength and stiffness are distributed between the three struts. The central strut has 50% of the total strength and stiffness, and the offset struts have 25% of the total strength and stiffness, as suggested by Chrysostomou (1991), shown in Figure 3.8b. More recent modelling techniques use a single strut while using superposition of vertical and horizontal forces on the RC frame to represent the internal shear forces caused by the masonry infill (Gentile et al., 2019b). The offset distance of the non-central struts (Z_c and Z_b) is calculated using the equation provided by Al-Chaar (2002) and shown in Figure 3.8a, where θ is the inclination angle of the strut and C_{od} and C_d are the stiffness distribution coefficients for the off-centre and central strut respectively.

The struts are implemented into OpenSees with the truss elements and the uniaxial *pinching4* material. The material is set to have a near-zero tensile stiffness resulting in a compression-only material. It is shown by Blasi et al. (2018) that the pinching4 material has a very similar response to the hysteretic model laid out by Panagiotakos and Fardis (1996). The hysteretic behaviour of *pinching4* is defined by three parameters α, β, and γ. These values were taken from the calibration in Blasi et al. (2018) as α =0.15, β =0.1, and γ =0.8, which were the most representative values based on comparing experimental results of RC infilled frames.

An opening factor ($\lambda_{opening}$) is applied to the width of the strut to reduce the stiffness accounting for the openings in the infill panel. Using the structural drawings provided by Pahar trust (2019), the infill wall opening percentage (α_w) is 25%. The empirical equation given in Equation 3.8 was first proposed by Al-Chaar et al. (2002) and further verified as the most accurate equation available in literature using experimental data. Equation 3.8 is only applicable where the infill wall opening percentage is less than 60%. The opening factor is calculated for the Pahar trust template school as 0.638, so it applies to this case.

$$\lambda_{opening} = 1 - 1.6\alpha_w + 0.6{\alpha_w}^2 \tag{3.8}$$

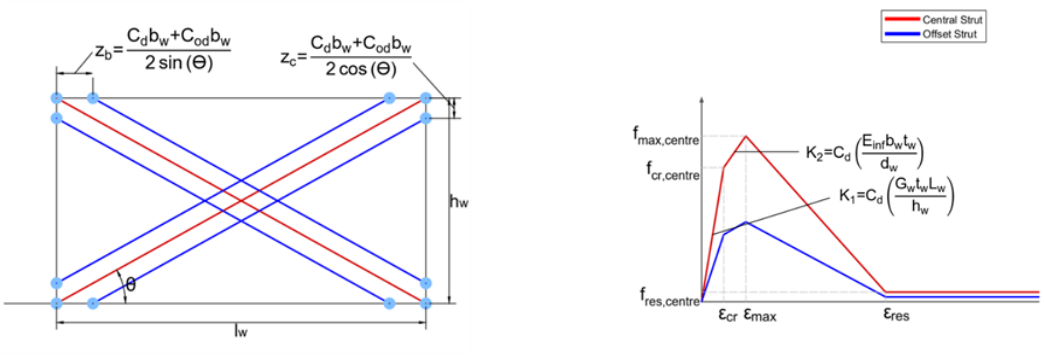

(a) *(b)*

Figure 3. 8: (a) Visual representation of triple strut model. (b) Backbone curve of individual struts.

The triple strut model is implemented in each bay, as shown in Figure 3.9. Due to each bay having a different geometry and the RC sections, the final model has a different strut response in each bay.

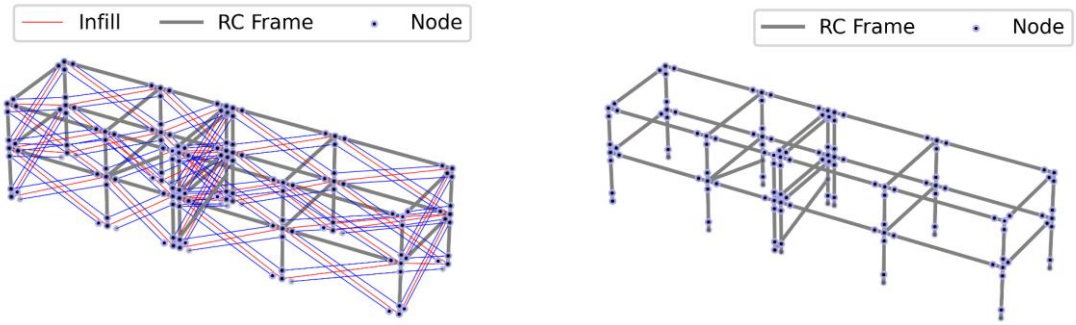

(a) (b)

Figure 3. 9: Visual representation of the finite element model for the (a) infilled model (b) bare model

3.3.4 Modal Properties

A modal analysis was performed on the four structural models. For the modal analysis, the school can be considered as two structures as the sections of the structure at either side of the seismic gap have no structural interaction. They will subsequently be referred to as structure 1 and structure 2, where structure 1 has the staircase. The modal analysis assumes the stiffness of each material is equal to the initial stiffness (i.e., uncracked). However, as both our material models for concrete and steel exhibit degradation, the modal properties of the structure will change throughout the nonlinear time history analysis. Table 3.7 shows the first six periods for each structure for both the infilled and bare models. The stairs are modelled as a single inclined beam following the modelling approach suggested by Lombardi et al. (2019). The modal participation masses can be found in Table 3.8 to Table 3.11 for the first six modes of each of the four structures, and the mode shapes for the first two modes can be seen in Figure 3.10. It

can be seen from Figure 3.10 that for both the infilled model without the staircase and the bare model without the staircase, the first two mode shapes are translational in the x and y directions, with the modal participation factors above 90% in the respective direction. The third mode shape is rotational about the z-axis with a modal participation above 90% for both the infilled and bare models. The mode shapes are not as distinct in the structures with the off-centre staircase as the offset centre of stiffness causes a higher torsional component in the first modes. This can be seen in the participation masses in Table 3.9 and 3.11 and Figure 3.10. As is expected, due to the additional stiffness caused by the masonry infills, the infilled structure has a significantly lower period for the first vibrational modes.

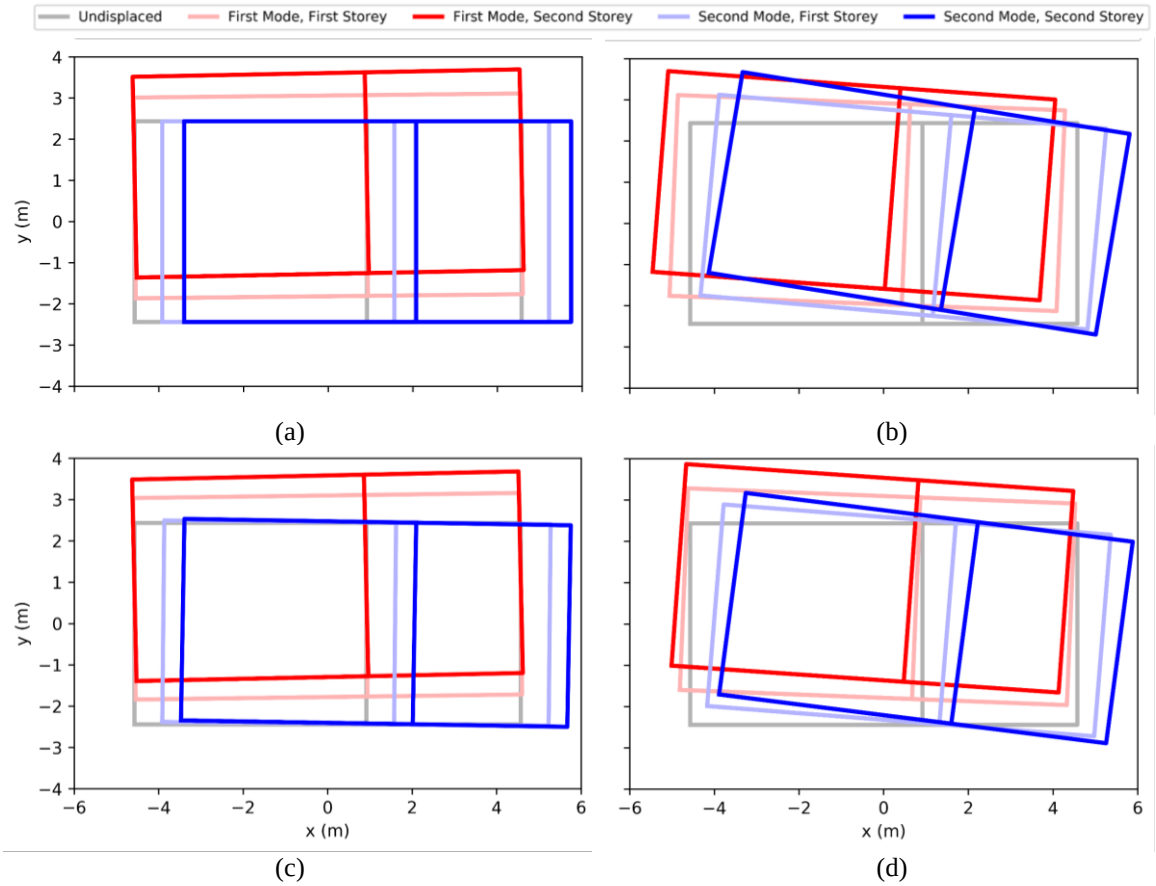

Figure 3. 10: Mode shapes of (a) without stairs, bare model (b) with stairs, bare model (c) without stairs, infilled model (d) with stairs, infilled model

Table 3. 7: Modal properties of the bare and infilled structures at either side of the seismic gap; structure 1 is the model with the staircase (w-s), and structure 2 is the model without the staircase.

	Bare		**Infilled**	
	Structure 1 (w-s)	**Structure 2**	**Structure 1 (w-s)**	**Structure 2**
Mode 1 (s)	0.329	0.352	0.082	0.092
Mode 2 (s)	0.321	0.329	0.066	0.066
Mode 3 (s)	0.189	0.307	0.058	0.064
Mode 4 (s)	0.099	0.103	0.029	0.033
Mode 5 (s)	0.097	0.100	0.024	0.024

Mode 6 (s)	0.042	0.093	0.022	0.023

Table 3. 8: Modal participation masses of the bare structure with no staircase

Mode	MX [%]	MY [%]
1	0.000	90.951
2	92.402	0.000
3	0.000	0.463
4	0.000	8.499
5	7.598	0.000
6	0.000	0.087

Table 3. 9: Modal participation masses of the bare structure with an off-centre staircase

Mode	MX [%]	MY [%]
1	60.622	16.067
2	31.484	30.076
3	0.007	38.892
4	7.853	0.002
5	0.033	0.352
6	0.001	14.611

Table 3. 10: Modal participation masses of the infilled structure with no staircase

Mode	MX [%]	MY [%]
1	0.000	92.624
2	93.631	0.005
3	0.373	0.569
4	0.000	6.740
5	5.413	0.007
6	0.582	0.055

Table 3. 11: Modal participation masses of the infilled structure with an off-centre staircase

Mode	MX [%]	MY [%]
1	0.501	81.080
2	92.223	0.068
3	1.346	14.049
4	0.015	4.603
5	5.172	0.006
6	0.742	0.196

3.3.5 Pushover Analysis

A static pushover (SPO) analysis is carried out for both the structures in the x-direction and the y-direction. The SPO is carried out in accordance with the Eurocode 8 (EN 1998-1, 2004) lateral load pattern, where the load at each floor is proportional to the product of the mass and height of that storey. The pushover curves in the x-direction of the building with and without infills are shown in Figure 3.11. It can be seen that the degradation of the masonry infills causes a rapid loss of lateral strength at 0.04% drift before the infills reach a residual capacity at 0.13% drift.

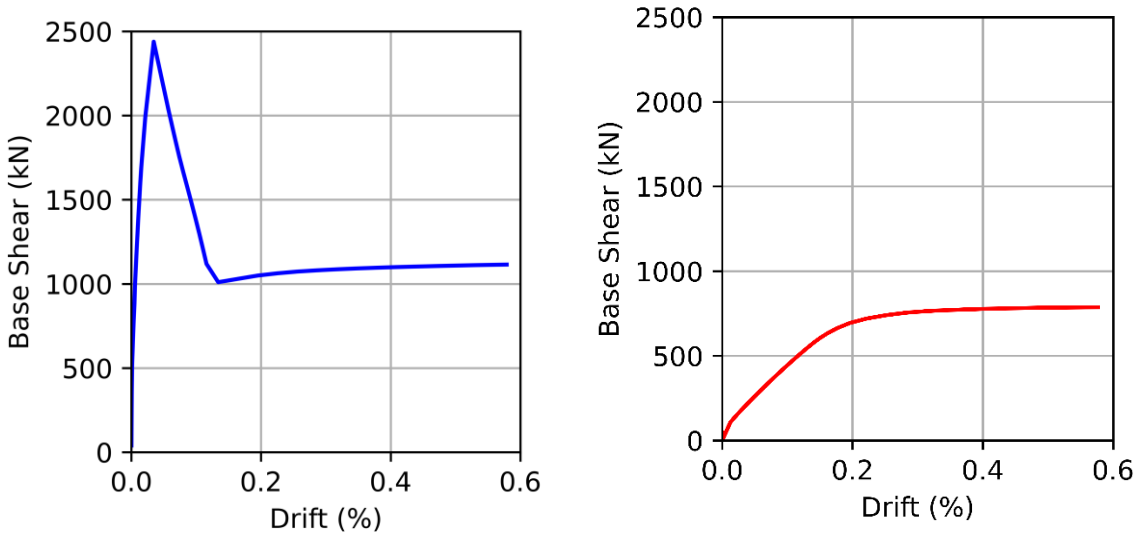

(a) (b)

Figure 3. 11: Static Pushover Analysis results (a) Infilled Structure (b) Bare Structure

3.4 Fragility Assessment for Pounding

An evaluation of the bare model's vulnerability to pounding is carried out to assess the influence on the structure's overall fragility. Pounding is defined as collisions between adjacent buildings during an earthquake and has been identified as one of the leading causes of structural damage (Karayannis and Favvata, 2004). Despite modern codes requiring adequate separating distance between adjacent buildings, structural pounding occurs for four main reasons: (i) sometimes the suggested separation does not account for modern construction techniques that allow large displacements due to an inelastic response; (ii) high cost of land in densely populated cities; (iii) errors in selection and interpretation of seismic hazard and (iv) structures designed following outdated codes where minimum separation gap had not been provided (Favvata, 2017).

Structural pounding occurs in two main types: slab-to-slab and slab-to-column. Slab-to-column is considered significantly more severe as the shear load to the column can cause localized failure, leading to progressive global collapse (Skrekas et al. 2014). The Pahar Trust template school should only be susceptible to slab-to-slab pounding as the floor slabs are at the same level. Four main factors affecting the pounding of two structures are; (i) the separation distance; (ii) the height of the structures; (iii) the period of the structure (higher period pounding more likely), and (iv) different periods for adjacent buildings (this causes out of phase vibrations) (Lin and Weng, 2001).

The pounding assessment will be carried out using NLTHA with the pounding ground motion sets outlined in Section 3.2.2.2. These ground motions are different from those used for the seismic risk assessment for limit states in Section 3.5. This is due to the selected ground motion sets such that failure occurs in some of the analyses.

3.4.1 Non-Linear Time History Analysis for the Assessment of Pounding

Non-linear time history is carried out with each of the 27 pairs of ground motions. Each set was run twice, swapping the two components along the two principal directions of the buildings. This approach is implemented in the European (EN 1998-1., 2004) and US (FEMA P-1050., 2015) design codes. For further details on code-based ground motion selection, refer to De Luca et al. (2019). The two recorded ground motions were applied along the principle directions of the structure (i.e. the x and y direction). This gives a total of 54 analyses. Figure 3.12 shows the displacement of the top of building 1 for the ground motion giving the largest displacement in each set. For the Gorkha ground motion set, this was the KTP recording, and for the spectrum compatible sets, the Tottori recording is shown. It can be seen that the post-Gorkha ground motion results in a significantly larger displacement due to the non-linear response of the structure, and it shows a significant residual displacement with respect to the maximum response obtained with the pre-Gorkha set. The Gorkha record does not show any residual displacement.

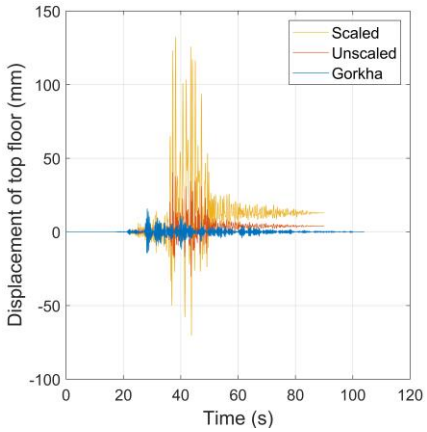

Figure 3. 12 The displacement of the top of the structure in response to pre-Gorkha, post-Gorkha and Gorkha earthquakes.

Pounding occurs when the displacement between point A and point D or point B and point C, as depicted in Figure 3.6c, is less than zero. Although this is a slight conservative approximation, extreme torsion values could allow the x-coordinate of the adjacent nodes to overlap while pounding may not occur. Due to the Pahar Trust school's regular arrangement,

extreme torsion is not applicable to this study. It should also be noted that pounding could occur at the midpoint of the beam, this type of interaction is not considered. For each ground motion, the closest distance relevant for pounding is recorded and plotted in Figure 3.14. This is calculated as shown in Figure 3.13 using Equation 3.9. Displacement in the x-direction (see Figure 3.6c) is always positive. P is the distance between the two structures (i.e., 102 mm in the case of the Pahar Trust school).

$$\max(d_1 - d_2) > P \tag{3.9}$$

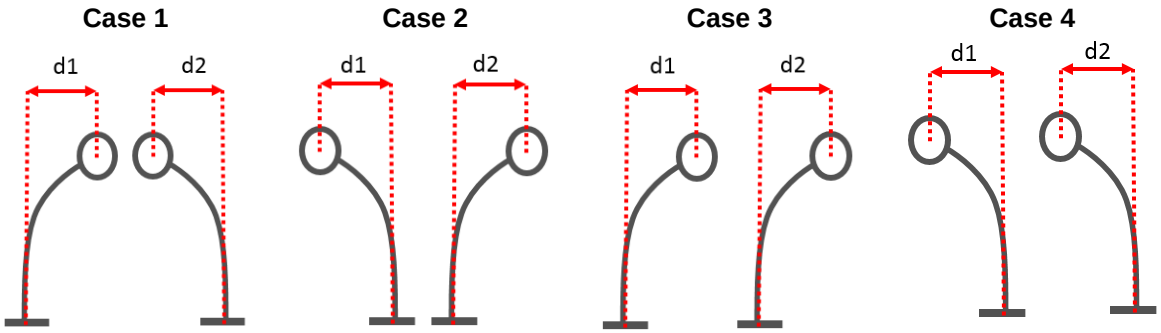

Figure 3. 13: Four possible displacement scenarios for pounding.

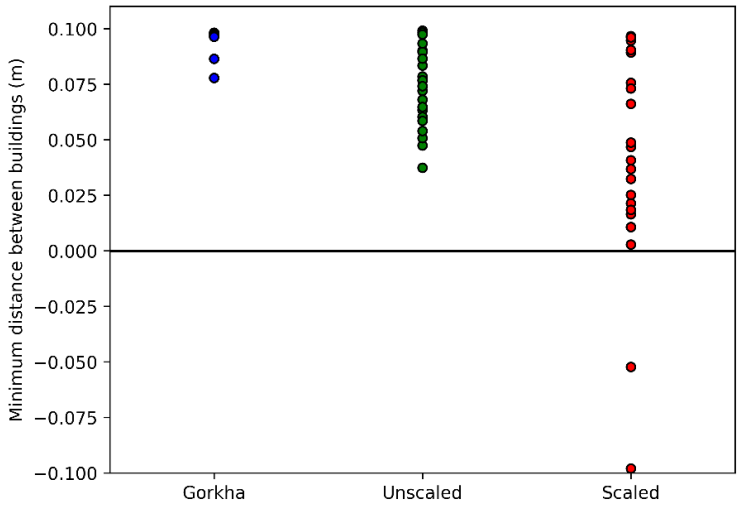

Figure 3. 14: Minimum distance between adjacent structures

From Figure 3.14, it can be seen that with the Gorkha ground motion set that no pounding occurred, and the closest point to pounding was 81 mm, which occurred during the KTP ground motion recording. It can be seen in Figure 3.4b that KTP has the largest spectral acceleration at the first period of the structure as it is situated on a rock. We can conclude that the site effects in the Kathmandu basin caused Pahar schools to be less likely to exhibit pounding in the 2015 earthquake.

The pre-Gorkha PSHA ground motion set is significantly closer to pounding, with the Tottori ground motion being 12 mm from pounding, however no pounding occurs. The closest point to pounding is during the Tottori ground motion. This ground motion has a PGA that is significantly higher than the mean, however it is not the highest in the ground motion set. This is due to the building being more out of phase in the Tottori analysis.

The post-Gorkha PSHA ground motion set experiences pounding in 3/22 of the ground motions. It can be seen that the pounding goes up by more than a factor of 1.58 as the ground motion is scaled by. This is due to the non-linear response of the structure. Pounding occurs within one standard deviation of the mean, indicating that a typical ground motions selection compatible with Eurocode 8 spectra and using a post-Gorkha PSHA will exhibit pounding. Reconnaissance reports from Gorkha 2015 (Shakya et al., 2016) showed a limited amount of pounding between large RC buildings.

3.4.2 Pounding Fragility Analysis

For pounding, a specific fragility curve can be obtained using the linear regression approach for cloud analysis (Jalayer et al., 2015). For more details on the cloud analysis, refer to Section 2.6.2.2. The robust fragility method uses the Bayesian probability framework to take into account both the uncertainties in the modelling and the record-to-record variability. The robust fragility method results in an efficient approach to consider the inherent uncertainties with respect to the probability distribution parameters. Further details can be found in Jalayer et al. (2015) and Jalayer et al. (2017).

An intensity measure of PGA is used to allow the fragility curves to be compared to those from the limit state risk assessment. The linear regression is shown in Figure 3.15a, and the resulting fragility curve is shown in Figure 3.15b. The fragility curve in Figure 3.15b gives the cumulative probability function for the occurrence of damage to the buildings because of pounding recorded at the top storey of the school. It can be observed that the designed seismic gap of 102 mm provides a safe solution against pounding with a 50% probability of occurrence for a PGA value of 2.77 g. Further analyses are needed to validate this result as the use of the scaling of the same records for pre-Gorkha, and post-Gorkha suites can introduce bias in the fragility estimation through cloud analysis (Jalayer et al., 2015). The bias is usually caused by the scaling of the ground motion set leading to a different shape of the elastic response spectra. This discrepancy in the shape of the elastic response spectra leads to a different structural response. Baker (2007) found that scaling is acceptable when ε is kept consistent between the

scaled ground motion and the target spectra. ε is defined as the number of standard deviations between the observed spectral value and the median prediction from an attenuation function.

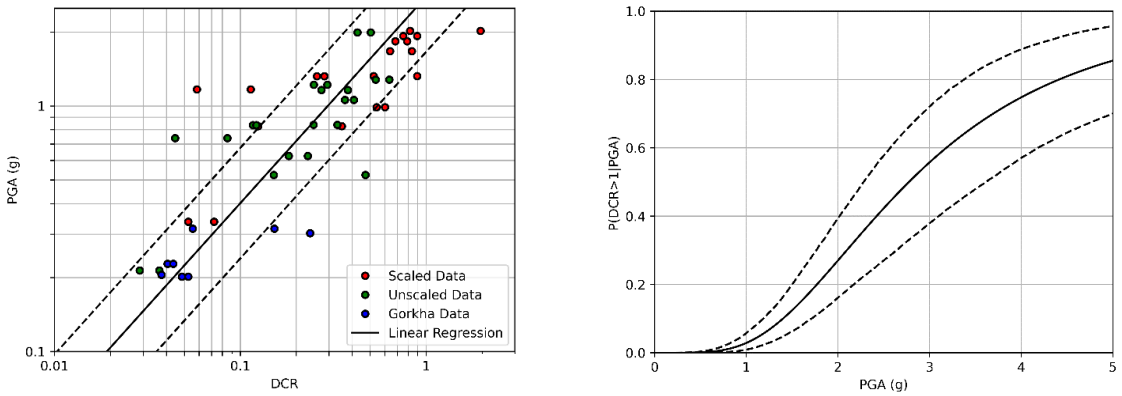

(a) (b)

Figure 3. 15: (a) Linear regression of pounding against the spectral acceleration. (b) Fragility curve for pounding.

3.5 Limit State Fragility Assessment

3.5.1 Non-linear time history analysis

Non-linear time history analysis is carried out using the model outlined in Section 3.3 and the ground motion selection outlined in Section 3.2.2.1. Rayleigh damping is implemented using a critical damping ratio of 2% (Dolšek et al., 2001) and the first and third fundamental periods to evaluate the mass proportional damping coefficient and stiffness proportional damping coefficient (Chopra, 2007). Further details on this can be found in Section 2.4.2. P-Delta Coordinate Transformation is used to account for second-order effects caused by the lateral loads. Additional information on this can be found in Section 2.4.1.

Figure 3.16 shows the shear demand for the 1994 Northridge earthquake and a column's shear capacity with section C1 (shown in Figure 3.7) according to the Indian standard and Eurocode using Equations 3.3 and 3.5, respectively, from Section 3.3.1. As the Eurocode 8 Part 3 (EN 1998-3, 2005) calculation is a function of the length of the member, the shear check is carried out for the squat and slender column as defined by the infill structural modelling. The squat column is the column from the floor to the off-centre strut, and the slender column is the column from the lower to the upper off-centre strut, as shown in Figure 3.8. Northridge 1994 earthquake (RSN 953) is used as it has the highest peak shear demand of all the ground motions, and section C1 is used as it has the lowest amount of shear reinforcement. This further shows that the shear capacity is not exceeded.

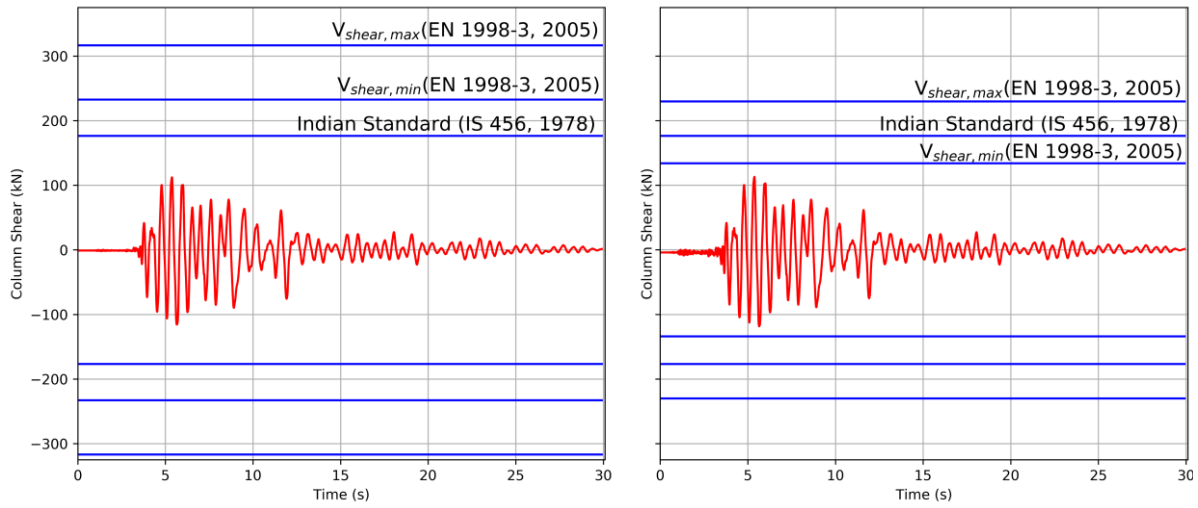

Figure 3. 16: Shear demand for Northridge 1994 earthquake (RSN 953) from GM 1 with a shear capacity of section C1 according to the Indian Standard (IS 456, 1978) and Eurocode 8 Part 3 (EN 1998-3, 2005) (a) Slender column (b) Squat column. Shear demand (in red) shown for structure 1 infilled model.

3.5.2 Fragility analysis

A fragility curve is defined as the relationship between the conditional probability of a structure exceeding a specific limit state and a seismic load intensity. This study considers two limit states: damage limitation (DL) and life safety (LS). Damage limitation is defined as a level of damage that does not limit the use of the building, and the subsequent repair cost would not be disproportionately high. Life safety limit state is defined as a level of damage such that there is no immediate risk to the lives of the occupants.

The intensity measure (IM) is used to quantify the ground shaking related to seismic events. In literature, commonly used IMs are PGA and spectral acceleration at the first mode ($S_a(T_1)$) (Tothong and Luco, 2007). An efficient IM is one that, when unchanged, gives low levels of variability in the given demand capacity ratio (DCR) (i.e., a low standard deviation in log space). The demand capacity ratio (DCR) is defined as a ratio of an engineering demand parameter (EDP), such as interstorey drift or chord rotation, to the critical demand parameter, such as a code specified interstorey drift limit. The dispersion can be calculated using Equation 3.10, where *a* and *b* are two constants found in the linear regression for that specific fragility function (Bayat et al. 2015), *Y* is the DCR, and *N* is the number of samples.

$$\beta_{Y|IM} \cong \sqrt{\frac{\sum(ln(Y_i) - ln(b\ ln(IM) + ln(a)))^2}{N-2}} \tag{3.10}$$

A sufficient intensity measure results in the fragility function being unaffected by other ground motion properties such as magnitude. The more sufficient an IM is, the more results in the DCR are mainly independent of the ground motion selection (e.g., Ebrahimian et al., 2014).

Shome et al. (1998) demonstrated that the 5% damped $S_a(T_1)$ is a more efficient IM than the PGA of the ground motion. More recently, it has been shown that *AvgSA* is a more efficient IM than $S_a(T_1)$ (Bayat et al., 2015, Kohrangi et al., 2017b). *AvgSA* is the geometric mean of the spectral acceleration values between periods c_1T_1 and c_nT_1, where c_1 and c_n are lower and upper bound factors. Previous work has shown that 0.2T1 and 3.0T1 are appropriate choices for the upper and lower bound with a logarithmic spacing between, as this has demonstrated strong sufficiency and efficiency (Eads et al., 2015).

$$Sa_{avg}(c_1T_1, \dots, c_nT_1) = \left(\prod_{i=1}^{N} Sa(c_iT_1)\right)^{\frac{1}{N}} \quad (3.11)$$

This study uses a modified version of *AvgSA* where the upper limit equals $3.0T_{1,bare}$ where $T_{1,bare}$ is the first period of the bare structure. The Lower limit will be set to $0.2T_{1,infilled}$, where $T_{1,infilled}$, is the infilled structure's first period. This intensity measure which accounts for the dynamic response of all structures (bare and infilled, with and without stairs), is referred to as $AvgSA_{mod}$. This allows the suitable comparison of the fragility curves of both structures as they will have a common IM. The upper limit is 1.056s, and the lower limit is 0.0164s.

The two sets of records discussed in Section 3.2.2.1 are used to perform a cloud analysis. Their suitability as seismic input for cloud analysis is checked according to the general criteria set out in Jalayer et al. (2017) and provided in the following:

1. The record selection should have a large dispersion of S_a (or the relative intensity measure) to reduce the standard error level in the regression slope.
2. At least 30% of the nonlinear time history analyses should cause the demand capacity ratio (DCR) to exceed 1.
3. No more than 10% of the ground motion selection should be from the same event.

The ground motion selection presented in Section 3.2.2.1 is compliant with the first of the criteria set out by Jalayer et al. (2017). The first of the Jalayer criteria is satisfied as $AvgSA_{mod}$ ranges from 0.14 g to 0.94 g with a standard deviation of 0.216 g. The second of the Jalayer criteria is also satisfied with the bare model having 78% of records yielding a DCR greater than 1. The infilled model has 40% of records giving a DCR greater than 1. The third Jalayer criterion is satisfied for GM1; however, it is not met for GM2 as all recordings are from the

Gorkha 2015 earthquake. If the two sets are considered together, still the condition is not met as 18% of the records are from the Gorkha earthquake. The linear regression is also completed without the Gorkha ground motions, as shown in Figure 3.17, to assess whether using a single event for five of the recordings dramatically influences the results. It can be seen that the linear regression results are very closely aligned.

Cloud analysis uses a linear regression-based probabilistic model with the results of nonlinear dynamic analysis to find a cumulative probability function for the occurrence of exceeding a critical demand parameter (CDP). A suitable critical demand parameter is first established for each limit state. In the analysis of RC structures without masonry infill, a CDP of 0.5% interstorey drift ratio (IDR) for DL is used as set out in Eurocode 8 for buildings that have brittle non-structural elements (EN 1998-1, 2004). The DL criteria for the infilled model is defined as the IDR when all infills have exceeded peak load. This typically occurs between 0.1% and 0.2% (Ricci et al., 2016). The peak load of each infill varies as it is a function of the material properties and geometry of that specific masonry infill. During the static pushover (SPO) analysis, the peak base shear occurred with a peak IDR of 0.19%, this is used as the damage limitation criteria for the infilled model. The life safety limit state is 2% for both the infilled and bare models (ASCE/SEI 41-17, 2017). The demand capacity ratio (DCR) is defined as the ratio of the peak demand to the structures at either side of the seismic gap, in the dynamic analysis results, to the CDP.

This study assesses the fragility using the cloud method. This involves using linear regression in the logarithmic space of the IM against the DCR. This gives the statistical constants *a* and *b* shown in Equation 3.12, where *Y* is the DCR. This can then be combined with the standard deviation given in Equation 3.13 to find the fragility curve using Equation 3.14 (Jalayer et al., 2014).

$$E[\log(Y)\,|IM] = \log \eta_{Y|IM} = \log a + b \log IM \tag{3.12}$$

$$\sigma_{\log(Y)|IM} = \beta_{Y|IM} = \sqrt{\frac{\sum_{i=1}^{N}\left(\log Y_i - \log \eta_{Y|IM_i}\right)^2}{N-2}} \tag{3.13}$$

$$P(Y > 1|IM) = P(\log Y > 0|IM) = 1 - \Phi\left(\frac{-\log \eta_{Y|IM}}{\sigma_{\log(Y)|IM}}\right) = \Phi\left(\frac{\log \eta_{Y|IM}}{\sigma_{\log(Y)|IM}}\right) \tag{3.14}$$

The cloud analysis was carried out using both ground motion sets (presented in Section 3.2.2.1) with the bare and infilled models. The $AvgSA_{mod}$ was used as an IM to compare the two structural models. Figure 3.17 shows the linear regression (LR) in logarithmic space for the two models while also showing the level of dispersion by showing the plus and minus one logarithmic standard deviation (calculated according to Equation 3.13). Figure 3.17 also shows the linear regression for the FEMA P695 (FEMA) ground motion set independent of the linear regression on all ground motions (Total). This is done to assess the effect of using five ground motions from one earthquake. It shows that the results are not significantly affected by the Gorkha ground motion set, where five recordings are from one earthquake. The linear regression is carried out independently for each limit state, with Figures 3.17a and 3.17c showing the linear regression for the damage limit state and Figures 3.17b and 3.17d showing the linear regression for the life safety limit state.

Figure 3.18 shows the robust fragility curves and the plus and minus one standard deviation curves, according to Jalayer et al. (2014), for both the bare and the infilled model. The infilled structure has a lower probability of exceeding LS or DL at any level of $AvgSA_{mod}$. The median (η) and logarithmic standard deviation (β) parameters of the four fragilities presented in Figure 3.18 are summarised in Table 3.12.

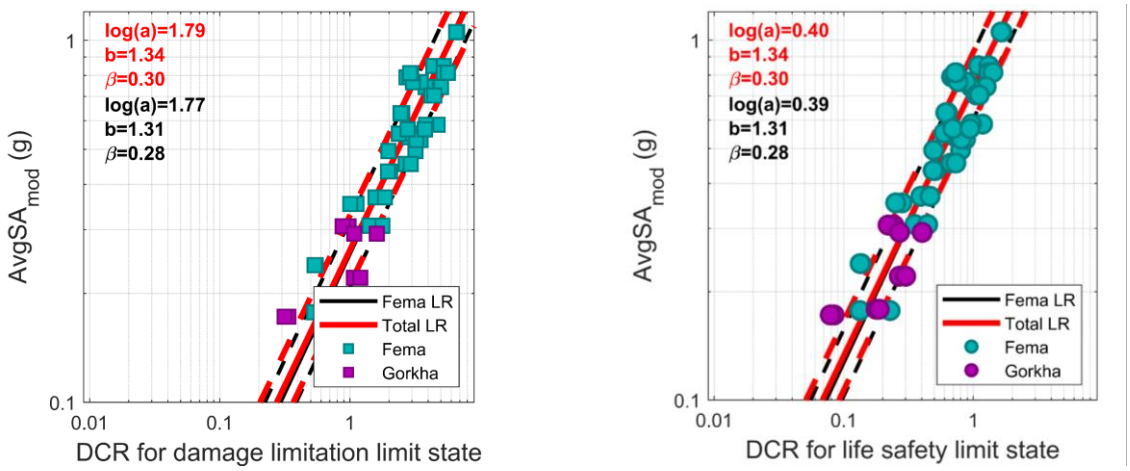

(a) (b)

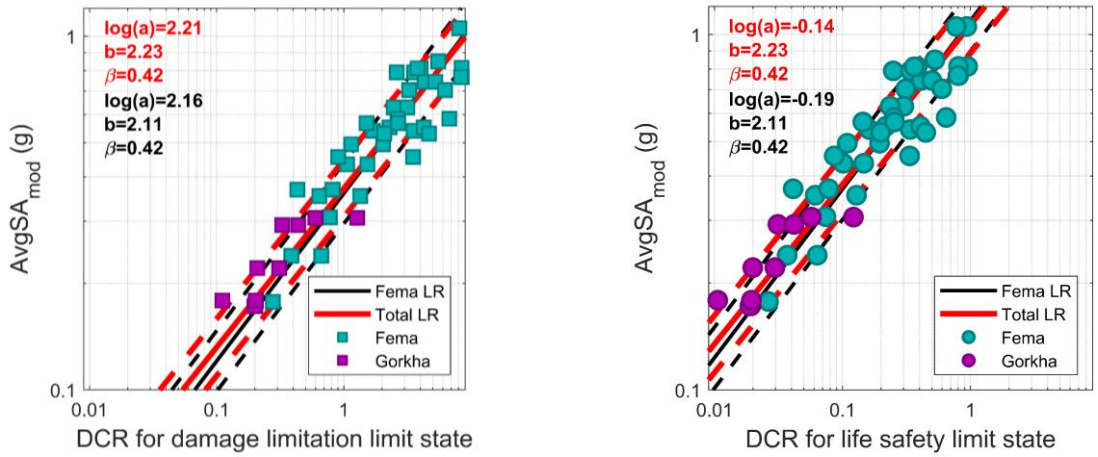

Figure 3. 17: Linear regression in logarithmic space for DCR at DL and LS vs AvgSAmod a) bare model, DL state b) bare model, LS c) infilled model, DL d) infilled model, LS

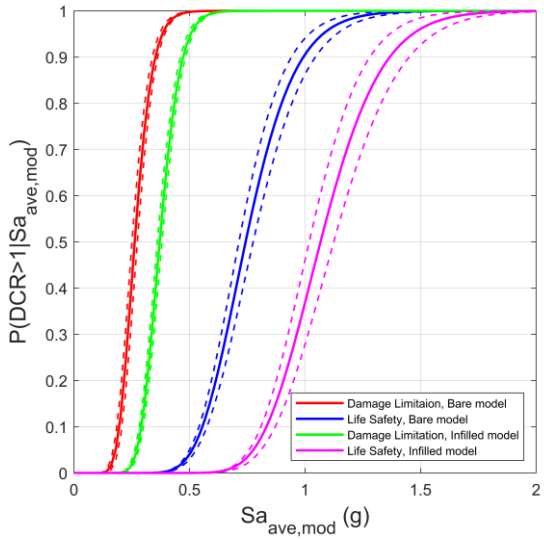

Figure 3. 18: Fragility curves for the DL and LS for both the infilled and the bare model using an intensity measure of $AvgSA_{mod}$

Due to the PSHA study described in Section 3.2.1, providing the expected PGA values across Nepal, a fragility analysis must be carried out using PGA data. Although using PGA as an intensity measure has been shown to have lower sufficiency and efficiency than *AvgSA* (Eads et al. 2015), it allows the integration of the PSHA study and the fragility assessment. The DCR remains unchanged. Figure 3.19 shows the linear regression, with Figure 3.20 showing the fragility curves. Figure 3.17 and Figure 3.19 show that $AvgSA_{,mod}$ is more efficient with the β value being 17% lower for the cloud analysis where $AvgSA_{,mod}$ is used relative to PGA. The η and β parameters of the four fragilities presented in Figure 3.20 are also summarised in Table 3.12. Table 3.12 shows that the infilled building has significantly higher η values, as

expected, due to the additional strength. For PGA, at the DL limit state, the infills increase the η value by 41.9%, and for the LS limit state, the η value increases by 43.6%.

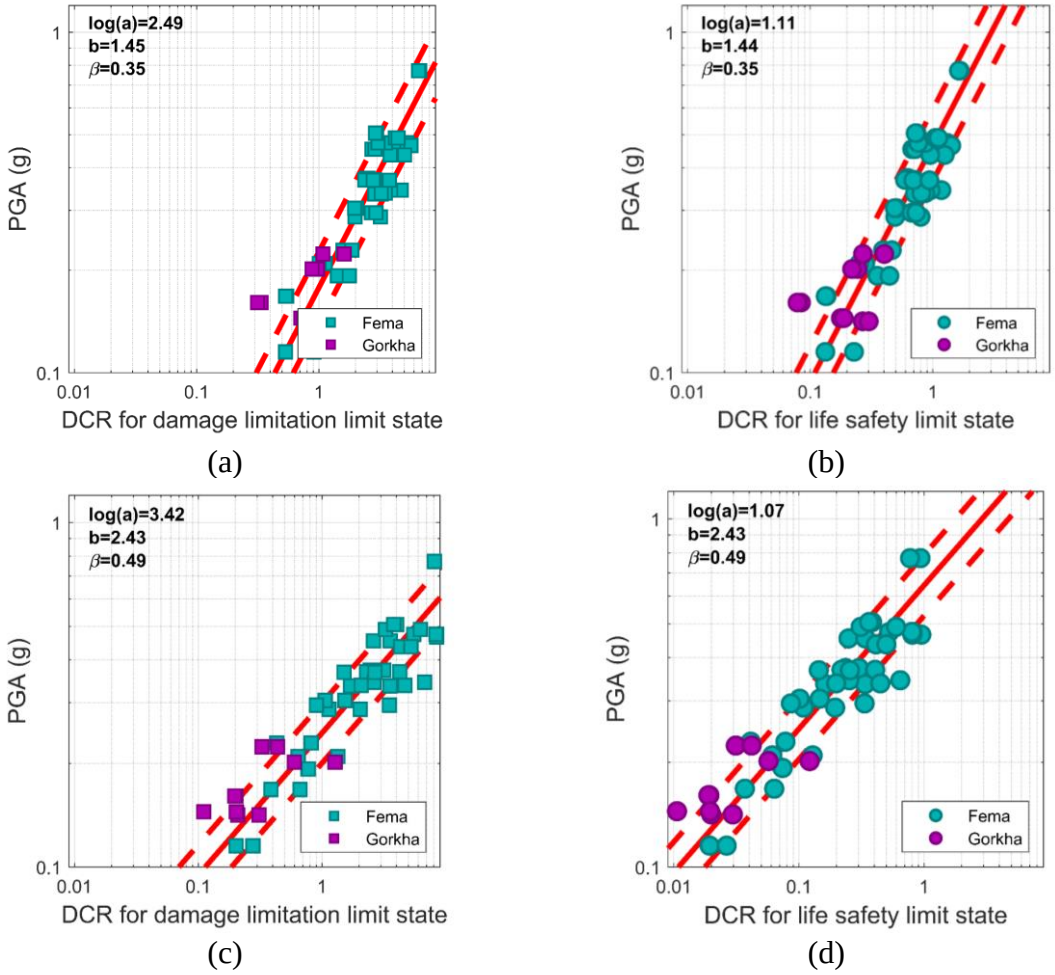

Figure 3. 19: Linear regression in logarithmic space for the DL and LS vs the peak ground acceleration a) bare model, DL b) bare model, LS c) infilled model, DL d) infilled model, LS

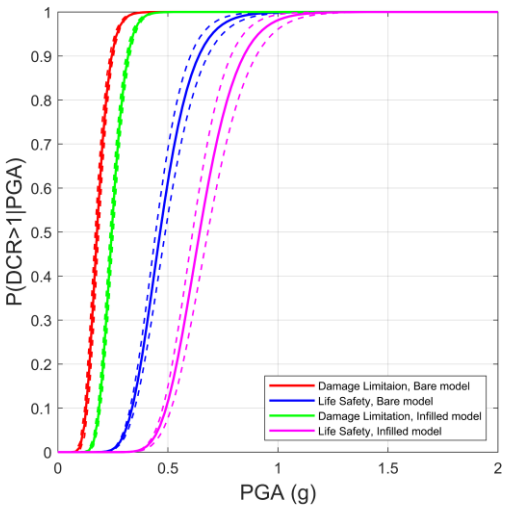

Figure 3. 20: Fragility curves for the DL and LS for both the infilled and the bare model using an intensity measure of PGA

Table 3. 12: Parameters of the fragility curves presented in Figure 3.18 and Figure 3.20

IM	Model	Limit State	η [g]	β
AvgSA,mod	Bare	DL	0.263	0.228
		LS	0.743	0.226
	Infilled	DL	0.371	0.188
		LS	1.067	0.193
PGA	Bare	DL	0.178	0.249
		LS	0.465	0.250
	Infilled	DL	0.245	0.205
		LS	0.644	0.211

3.5.3 Damage Distribution

Using the fragility curves derived previously, and the PGA values at each location provided by Stevens et al. (2018), the damage distribution of the template school at each location across Nepal can be found. The damage distribution is defined as the relative probability of the structure exceeding a given limit state given a specific level of ground shaking, in this case, PGA. Figure 3.21a shows that the bare model exceeds LS for the 2% in 50 years earthquake, with over 99% probability, in Rara Lake, Pokhara, Bharatpur and Kathmandu, with Janakpur having a 40% probability of exceeding DL and 60% probability of exceeding LS. This demonstrates how the varying seismic hazard results in the template school having a variable level of seismic risk. Figure 3.21b shows that for the 10% earthquake in 50 years, the bare model at Rara Lake, Pokhara, Bharatpur and Kathmandu exceeds LS or DL, with Janakpur having a 30% probability of experiencing no damage.

The damage distribution for the infilled model of the template school can be seen in Figure 3.22. Specifically, Figure 3.22a shows that for the 2% in 50 years earthquake (2475 year return period), Rara Lake, Pokhara, Bharatpur and Kathmandu are expected to exceed LS, and Janakpur is expected to either exceed DL with an 11% chance of exceeding LS. Figure 3.22b shows that for the 10% earthquake in 50 years (475 year return period), Rara Lake, Pokhara, Bharatpur and Kathmandu most likely exceed DL and Janakpur has an 82% probability of experiencing no damage.

Seismic fragility curves can be used with consequence functions to derive the damage ratio under different seismic actions. Consequence functions express the repair to replacement ratio of each limit state. This vulnerability assessment method is carried out for the case of Nepalese in Giordano et al. (2021), where the HAZUS-FEMA (2015) consequence functions are used. The vulnerability assessment lies outside the scope of this study.

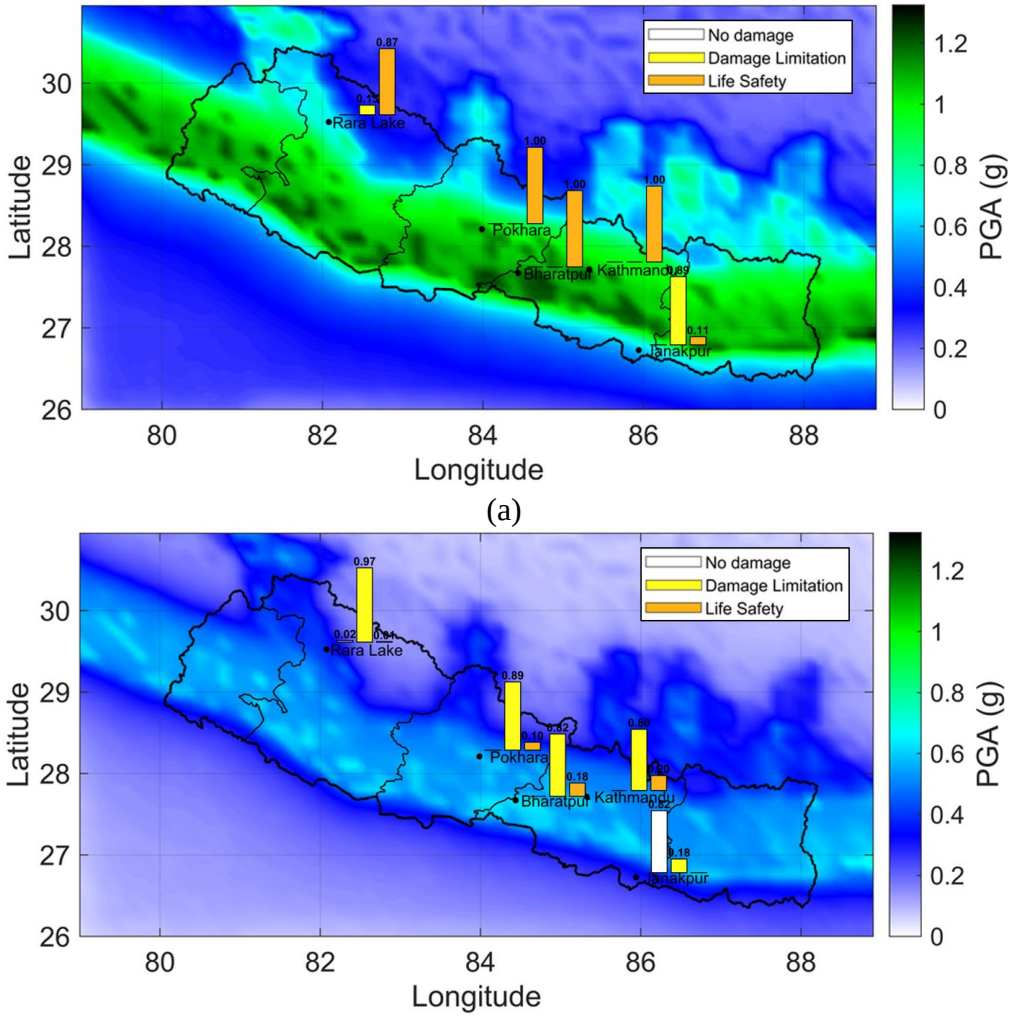

Figure 3. 21: Damage distribution of bare model of the template schools at five locations across Nepal (a) for the 2% probability in 50 years (2475 year return) earthquake (b) for the 10% probability in 50 years (475-year return) earthquake

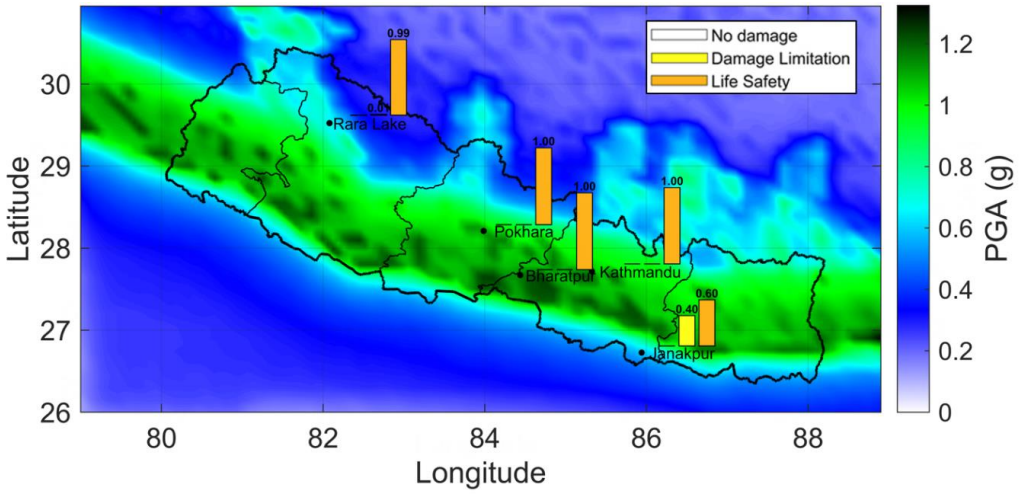

(a)

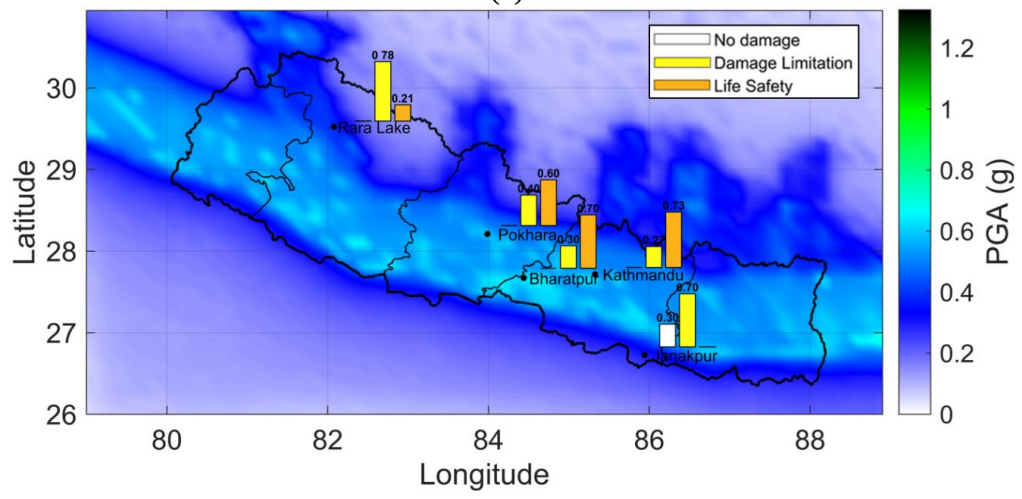

(b)

Figure 3. 22: Damage distribution of infilled model of the template schools at five locations across Nepal (a) for the 2% probability in 50 years (2475 year return) earthquake (b) for the 10% probability in 50-year (475-year return) earthquake

3.6 Risk Assessment

3.6.1 Combining Limit State and Pounding Fragility Curves

Using the fragility curves for pounding and the fragility curve for the exceedance of limit states, we can combine the curves to find the probability of exceeding life safety or pounding at a given level of PGA. Equation 3.15 shows how the probability of exceeding LS or pounding ($P(LS \cup Pounding|\ PGA)$) is calculated using the pounding fragility ($P(Pounding|\ PGA)$) and LS fragility ($P(LS|\ PGA)$). The probability of exceeding LS or pounding is calculated numerically at each PGA step, using Equation 3.15. In the probability of exceeding LS or pounding, the DCR exceeds one when either pounding occurs or the structure exceeds the life safety limit state. Figure 3.23 quantitively shows that the risk due to pounding is insignificant relative to the risk of the structure exceeding life safety limit state. It can be seen in Figure 3.23

that the pounding fragility curve is never limiting the structural behaviour with respect to the fragility curve for exceeding LS limit state. Therefore, it is not necessary to consider pounding while carrying out the seismic risk assessment for this structure.

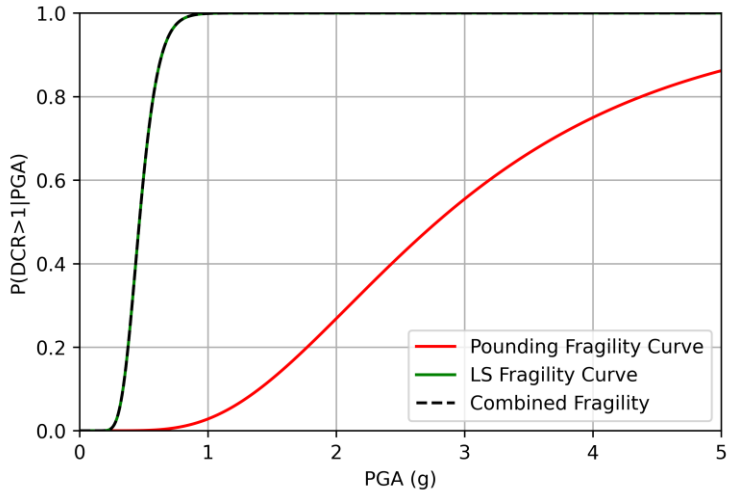

Figure 3. 23: Comparison of the fragility curves for exceeding Life Safety, pounding and the combined fragility curve.

$$P(LS \cup Pounding \mid PGA) = P(LS \mid PGA) + P(Pounding \mid PGA) - P(LS \cap Pounding \mid PGA) \quad (3.15)$$

3.6.2 Risk assessment

Using the hazard curve at each point across Nepal and the fragility curves for each limit state, the annual probability of exceeding each limit state can be found using Equation 3.16. P_{LS} is the annual probability of exceeding a given limit state, $H(s)$ is the hazard curve, and $P_{ls/s}$ is the fragility curve. Numerical integration can be carried out by discretising the hazard curve into equal parts assumed to be piecewise linear. This is shown in Equation 3.17, where $P_{F/Scgi}$ is the probability of exceeding the given limit state at the mid-point of s_i and s_{i+1}. The integration results are presented in the maps shown in Figure 3.24 to Figure 3.27. Further details on seismic risk assessment can be found in Section 2.6.3.

$$P_{LS} = \int_0^{\infty} P_{ls/s} \left(\frac{dH(s)}{ds} \right) ds \quad (3.16)$$

$$P_{LS} = \sum_{i=1}^{n} [H(s_i) - H(s_{i+1})] \, P_{ls/Scgi} \quad (3.17)$$

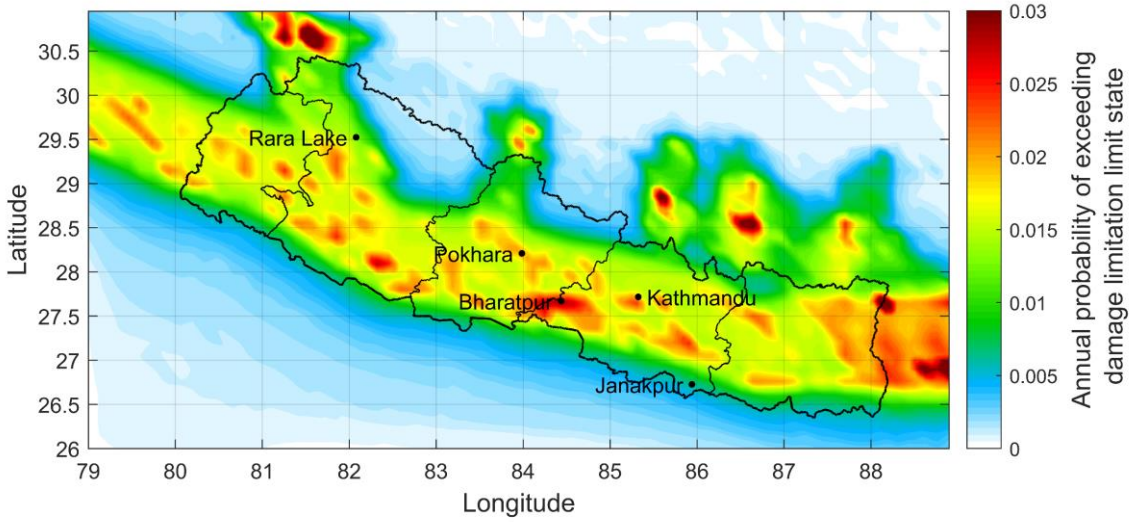

Figure 3. 24: Annual probability of exceeding DL for the bare model

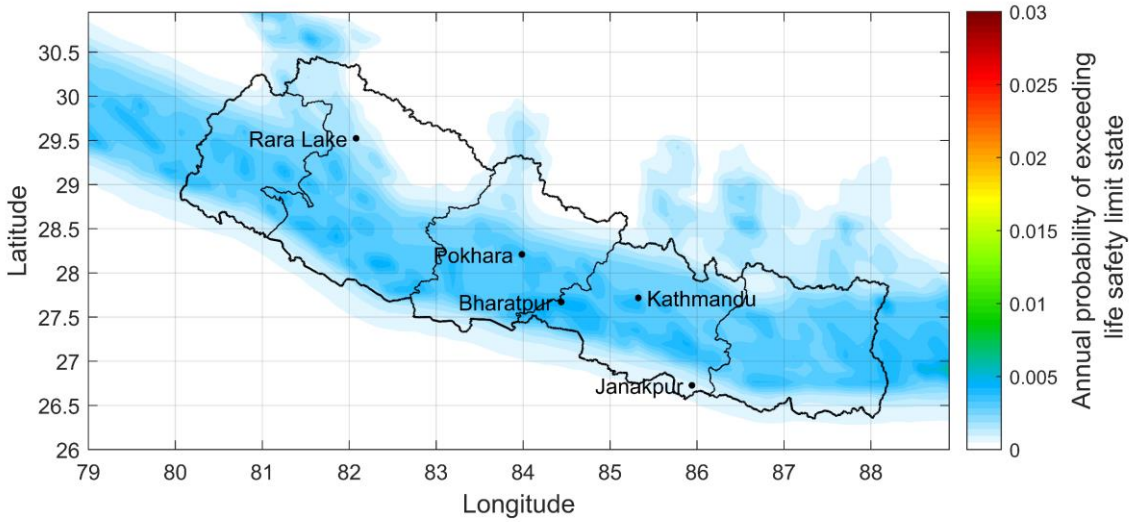

Figure 3. 25: Annual probability of exceeding LS for the bare model

Figure 3.24 shows that the annual probability of exceeding DL is in the range of 0.010 to 0.025 for most of Nepal. As this structure is a school, it would be considered to have an importance class III according to Eurocode 8. According to Eurocode standards, for buildings of importance class III for DL, the annual probability of exceedance should be lower than 0.030 (Pinto et al. 2014), as shown in Table 3.13. The annual probability of exceeding DL is lower than this for all locations across Nepal. Figure 3.24 also indicates that the risk level to the template school varies significantly based on its location. If the template school were located on the northern border, it would have an annual probability of exceeding DL of 0.003, which is almost ten times lower than for Bharatpur, where the annual probability of exceeding DL is

0.025. For this comparison, LS limit state is assumed to be equivalent to SLS as LS is described as being the "*post-earthquake damage state in which a structure has damaged components but retains a margin of safety against the onset of partial or total collapse*" (ASCE/SEI 41-17, 2017) and SLS is defined as "*loss of use of non-structural systems and a residual capacity to resist horizontal actions*" (Pinto et al., 2014). Figure 3.25 shows that the annual probability of the bare model exceeding LS ranges from 0 to 0.0050 across Nepal. This exceeds the threshold for LS, which is set to 0.0032 (Pinto et al., 2014).

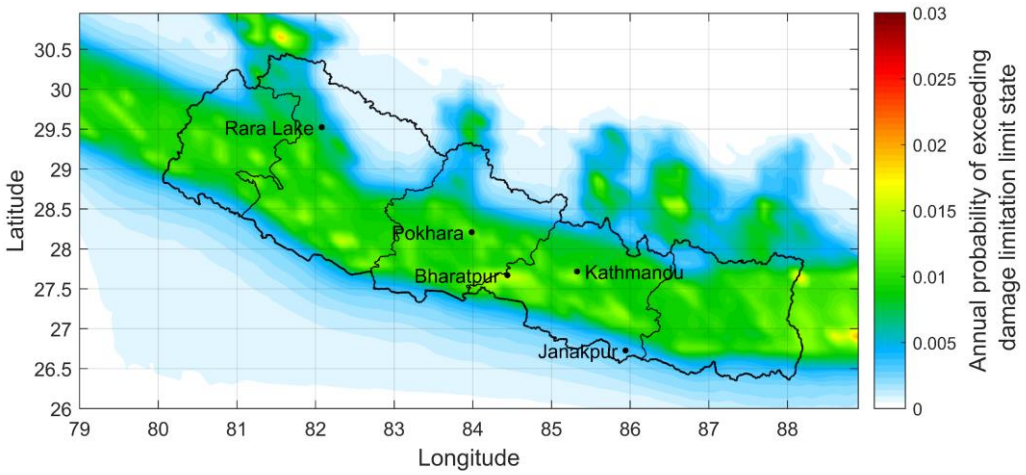

Figure 3. 26: Annual probability of exceeding DL for the bare model

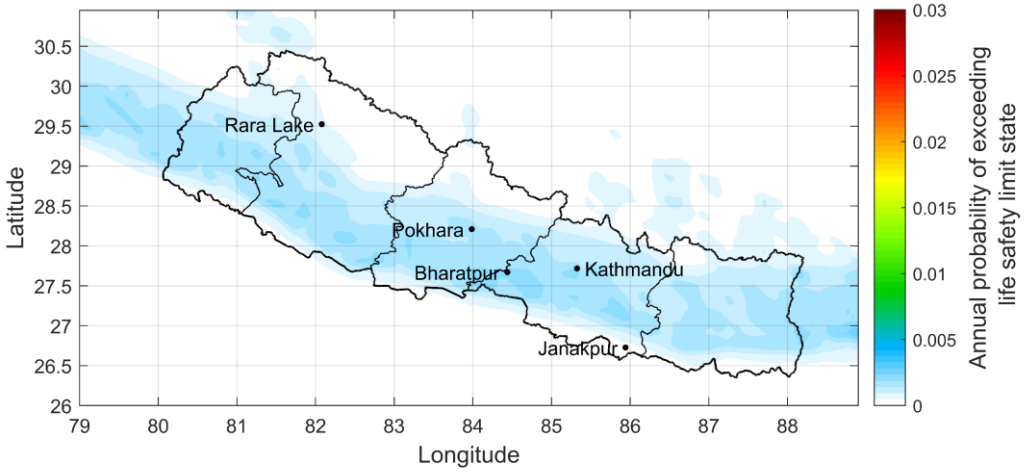

Figure 3. 27: Annual probability of exceeding LS for the bare model

Figure 3.26 shows that the annual probability of the infilled model exceeding DL ranges from 0 to 0.018. This is below the maximum allowable level of 0.03 (Pinto et al., 2014). It can be seen the annual probability of exceeding DL is significantly lower for the infilled model relative to the bare model. This is due to the structural contribution of the infills and the change

of the DL threshold recommended in structural engineering practice. Figure 3.27 shows that the annual probability of the infilled model exceeding LS ranges from 0 to 0.0025, which is below the threshold of 0.0032 (Pinto et al. 2014). This emphasises how the structural contribution of infills pushes the risk below the critical thresholds set up according to European standards and can make the difference between a school being compliant or non-compliant according to risk-based requirements of codes. This observation has implications for the realisation of masonry infills that, especially in high-hazard areas of the country, need to be constructed with reasonable care and a high level of quality control on mortar and bricks.

Table 3. 13: Maximum annual probability of exceedance of DL and LS for the two models and corresponding thresholds (Pinto et al. 2014).

Limit State	Bare	Infilled	Threshold
Damage Limitation	0.025	0.018	0.030
Life Safety	0.0050	0.0025	0.0032

3.7 Literature Benchmarking

The fragility curves from Section 3.6.1 can be compared to other fragility curves in Literature. Giordano et al. (2021) used an empirical approach to derive a series of fragility curves for Nepalese schools. These fragilities were carried out for different building materials and building types. The fragility curve most comparable to our structure was referred to as "*RC Frame*". However, it is stated that this includes structures with unreinforced masonry infills. Table 3.14 shows the fragility parameters from Giordano et al. (2021) for DS2, DS3 and DS4. Giordano et al. (2021) present their findings in terms of damage states according to the European Macroseismic Scale (Grünthal et al., 1998), where ds2 represents "*moderate damage*", ds3 represents "*substantial to heavy damage*", and ds4 represents "*very heavy damage*" It also shows the fragility parameters for the DL and LS limit states for this study's bare and infilled model. The fragility curves can be seen in Figure 3.28. In Table 3.14 and Figure 3.28, DS2 has been equated to DL as they represent the point where there is a minor amount of damage to the structure. Life safety has been equated to DS4 as both represent a significant level of damage but pre-collapse.

Table 3. 14: Comparison of the fragility parameters for the infilled structures in Giordano et al. (2021) and the bare and infilled Pahar Trust structure.

		DS2	DS3	DS4	DS5
Giordano et al. (2020)	η (g)	0.19	0.27	0.77	1.13
	β	1.08	1.04	0.88	0.84
	η (g)	0.178	N/A	0.465	N/A

Bare model (this study)	β	0.249	N/A	0.250	N/A
Infilled model (this study)	η (g)	0.245	N/A	0.644	N/A
	β	0.204	N/A	0.211	N/A

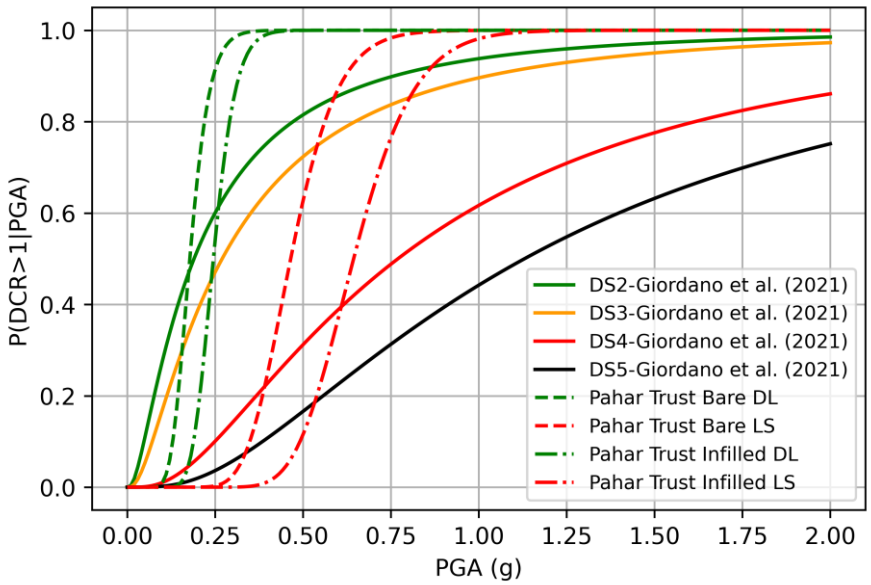

Figure 3. 28 Comparison of the Fragility curves from Giordano et al. (2021) and the bare and infilled model from this chapter.

It can be seen from Figure 3.28 that Giordano et al. (2021) has a significantly higher β value for all fragility curves. This is expected from empirical fragility curves due to them being derived from many different buildings. These buildings could vary in height, area, material properties, age and quality control. In contrast, the variability in our numerical model is due to the record-to-record variability. Although all the structures in Giordano et al. (2021) are exposed to the same earthquake, it should be noted that due to them being across Nepal, they will have varying ground motion based on distance from the epicentre and site conditions. For DS2/DL, the empirical fragility from Giordano et al. (2021) has a η value between the bare and the infilled model from this study. For DS4/LS, the η value from Giordano et al. (2021) exceeds those from this numerical study; however, with a difference of 16%, this is within the variability expected in fragility analysis. When comparing the η value from Giordano et al. (2021) to the infilled structure from this study, we can see that it is significantly lower in Giordano et al. (2021). This is likely due to a combination of factors, including Giordano et al. (2021) looking at existing buildings and the high level of quality control on the Pahar Trust structure.

3.8 Conclusions

This study developed a nonlinear finite element model of a template school in Nepal and carried out a non-linear time history analysis. The focus of this study was to assess how a template school design affected the seismic risk to schools in Nepal. Fragility analyses were carried out for the exceedance of limit states and the occurrence of pounding. This chapter did not assess other potential risks to the structures, including construction quality, landslides and liquefaction as cascading hazards for structures induced by earthquakes.

A numerical fragility curve for the probability of the structure incurring pounding was carried out. This fragility analysis was carried out on a bare model of the school where the structural contribution of the infills was not considered. The bare model is significantly less stiff and, therefore, more likely to exhibit pounding. The resultant fragility curve showed that the structure had a 50% probability of pounding at a PGA level of 2.77 g.

The fragility analysis for code-based limit states was carried out for an FE model without masonry infill and a model with masonry infill. The results showed that an earthquake with an $AvgSA_{mod}$ of 0.6 g would give a 50% probability of exceeding DL and that an earthquake with an $AvgSA_{mod}$ of 1.1 g would give a 50% probability of exceeding LS for the bare model. The infilled model had a 50% probability of exceeding DL for an earthquake with an $AvgSA_{mod}$ of 0.37 g and had a 50% chance of exceeding LS with an earthquake with an $AvgSA_{mod}$ of 1.07 g. The results of the cloud analysis also demonstrated that none of the Gorkha 2015 ground motion recordings caused the template school to exceed LS or DL.

The cloud analysis was then carried out with an intensity measure of PGA. This allowed the fragility curves to be combined with the pounding hazard curve and then integrated with the hazard curves. Hazard curves were interpolated from data provided by Stevens et al. (2018) and were then integrated with the fragility curves to find an annual probability of exceeding each limit state. The bare structure has a maximum annual probability of exceeding DL of 0.025 and a maximum annual probability of exceeding LS of 0.0050. The infilled structure had a maximum annual probability of exceeding DL of 0.018 and a maximum annual probability of exceeding LS of 0.0025. Except for the bare model for LS, all of these annual probabilities of exceedance values are lower than the threshold values set out according to European regulations (Pinto et al., 2014). This is a very encouraging result for a template school as it complies with risk thresholds levels for school buildings in Europe, setting a very high standard in terms of accepted societal risk.

This chapter shows that using a single design for a structure across an area of varying seismic hazard results in a highly varied seismic risk. It was demonstrated that the varying hazard resulted in the template school having a significantly higher level of risk around Pokhara and Kathmandu than along the northern border. The risk threshold for a school building was exceeded for the bare model. However, this was not the case with the infilled model. This showed that accounting for the structural contribution of infills can be very important to have an accurate picture of the implicit risk of a structure across a large area. On the other hand, this also emphasizes how quality controls on template schools have to include non-structural elements (i.e., mortar and bricks) to ensure that the additional seismic performance they can provide are effectively guaranteed. The properties of infills have been assumed from regional South-Asian studies to be realistic and avoid overestimations. One critical aspect is the cement to sand ratio that needs specific control during the construction to ensure that the infill's structural contribution can be relied upon in an earthquake. Further action to limit losses during the life of the school template could be to have implemented a gap between the non-structural infills and the reinforced concrete elements. This would decrease the damage from more minor earthquakes, increase the drift capacity for damage limitation and reduce potential repair costs.

.

Chapter 4: RC Masonry Infills in Nepal: Calibration of the Spectral Method FAST

Part of this chapter is based on the following reference:

Cross T, De Luca F, Woods GED, Giordano N, Pokhrel RM and De Risi R, (2021) FAST NEPAL: Regionally Calibrated Spectral Method for Reinforced Concrete With Masonry Infills. *Front. Built Environ*. 7:689921. doi: 10.3389/fbuil.2021.689921[1]

Objectives of this chapter

Following the numerical finite element (FE) approach to deriving fragility curves in Nepal in the previous chapter, this chapter will derive fragility curves using the FAST method for RC buildings with infills. The FAST method is a vulnerability assessment method for RC frames with masonry infills, applicable in data-scarce environments. It does not require detailed structural designs of the building. It also has the advantage of using various parameters that can be calibrated based on knowledge of local practices and materials. The objectives of this chapter are as follows:

- To modify the FAST method for the Nepalese context. This will involve updating the masonry's shear cracking stress (τ_{cr}) using Nepalese tests on local masonry. It will also include updating the inter-storey drift ratio (IDR) thresholds that define the limits of the EMS-98 scale (Grünthal, G., 1998).
- Applying the Nepal FAST methodology to the Pahar Trust school building, discussed in depth in the previous chapter. The results can then be compared with the last chapter's numerical fragilities as a point of validation for the Nepalese adapted version of the FAST method
- Finally, the Nepal FAST Method will be applied to a building database from Kathmandu to derive generalised fragility curves. Based on the FAST method results,

[1] The first authors contribution included: methodology, data curation, analysis , data visualisation and writing. Co-authors reviewed and supervised the work. Parts of the initial investigation and writing were carried out at part of Woods (2018) masters thesis.

the expected damage under the Gorkha 2015 earthquake will be compared to the observed damage data for the same building catalogue.

4.1 Introduction

The FAST method (De Luca et al., 2014; De Luca et al., 2015) is a rapid method for assessing the vulnerability of reinforced concrete (RC) infilled buildings on a large scale, up to heavy damage state (i.e., damage state 3) according to the EMS-98 scale (Grünthal et al., 1998). It was applied to Italian and Spanish earthquake damage data from the recent events occurring in L'Aquila 2009 (Italy), Lorca 2011 (Spain), Emilia 2012 (Italy), and Central Italy 2016 (De Luca et al., 2014, 2015, Manfredi et al., 2014; De Luca et al., 2017) and compared with damage data and improved against refined structural assessment approaches (e.g., Scala et al., 2020). In this study, the FAST method is adapted for the case of Nepalese RC buildings with infills by accounting for the Nepalese building codes (NBC-105 1994; NBC-105 2020), local construction practice, and materials for RC infilled buildings (e.g., Gautam and Chaulagain 2016; Gautam et al. 2015; Brando et al. 2017).

The first stage in the FAST method is to establish the approximate capacity curve (CC) for a building or a building class. The capacity curve represents the inelastic behaviour of a structure in terms of spectral displacement and spectral acceleration. The FAST method makes the conservative assumption that each building's damage mechanism will be a soft-storey plastic collapse of the ground floor, with the stiff, infilled walls failing first and the RC frame undergoing plastic failure later. The CC is calculated considering the contribution of the two materials in parallel. It is necessary to know the RC's design base shear and the cracking shear strength of the masonry infills (τ_{cr}).

The masonry infill is made from brittle bricks, which, at low PGAs, make the structures very stiff, but this stiffness will begin to degrade due to brittle failure once their cracking shear stress is reached. Once the maximum shear stress of the RC frame is obtained, the FAST method assumes the masonry infills have obtained their residual strength, as shown in Figure 4.1a. These stages correspond to Damage States (DS) One to Three of EMS-98 (Grünthal et al., 1998), with the point that the peak shear stress is reached corresponding to DS1, the degradation of infills corresponding to DS2 and the total collapse of the walls corresponding to DS3 (see De Luca et al. 2014 and De Luca et al. 2015 for further details). The capacity curve can be represented in the spectral acceleration ($S_a(T)$) versus spectral displacement ($S_d(T)$) plane. Incremental dynamic analysis (IDA) is an analysis method to estimate the performance

of a structure under seismic loading (Vamvatsikos & Cornell, 2002). Other methods have since been developed, such as the double impulse pushover (DIP) (Akehashi & Takewaki, 2019). Having determined the CC curve, it is possible to evaluate the approximate IDA Curve (IDA or IN2) as the CC and the IDA curve are related by a strength reduction factor–ductility–period (R-μ-T) relationship (see Figure 4.2). The R-μ-T (Dolšek & Fajfar 2004) relationship is a well-established method of finding the IDA from the SPO (also known as SPO2IDA). It is based on a series of equations to relate the constant reduction factor (R) and the mean ductility factor. These equations can be found in Dolšek & Fajfar (2004) and use the corner period between the constant acceleration and constant velocity in the elastic spectrum (T_c) and the corner period between the constant velocity and constant displacement part of the elastic spectrum (T_R).

The attainment of damage thresholds at the first storey can be computed as a function of the Inter-storey Drift Ratio (IDR) for the infills based on experimental results for the kind of infills. The next step is to convert the IDR into $S_d(T)$ by assuming an approximation of the structure's deformed shape, depending on the number of storeys present in the building. This is important because one of the most critical assumptions in the FAST method is that failure of walls occurs at the ground floor. The final stage in the FAST method converts the S_a of the structure, which corresponds to each damage state, into PGA. This allows for comparison with the PGA for the site established from a shake map of the specific location. This can be done using a smooth spectrum (e.g. a code spectrum) or a recorded spectrum.

4.1.1 Capacity curve

As previously mentioned, the capacity curve is formed of the contribution of the RC frame and the masonry infill working in parallel. Figure 4.1a demonstrates the stress-strain of the RC-infilled frame and the individual contribution of each of the materials. Figure 4.1b shows how this pushover curve is approximated for the FAST methodology.

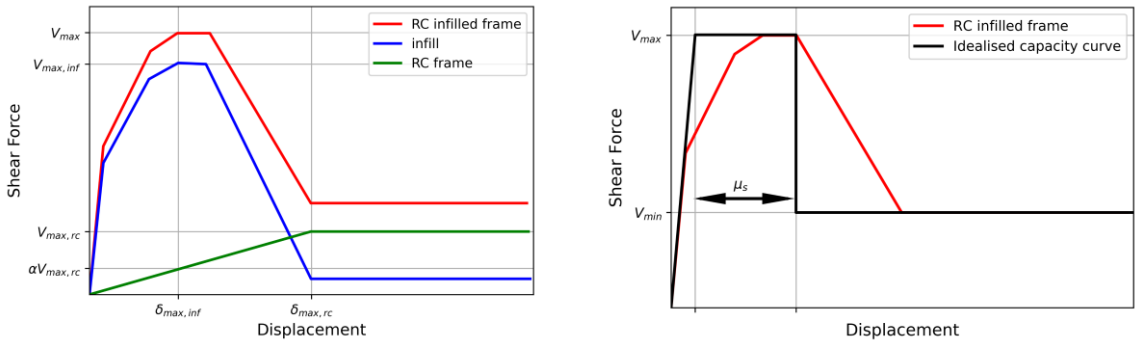

(a) *(b)*

Figure 4. 1: (a) Pushover curve for a masonry-infilled RC frame. (b) Capacity curve idealisation for the FAST methodology

It can be seen from Figure 4.1b that the idealised capacity curve follows an initial stiffness similar to that of the pushover. μ_s is the available ductility up to the degradation of the infills. The lateral resistance of the infills then decreases to their residual strength. It should be noted in Figure 4.1a that α is the RC frame's contribution to the lateral resistance at the peak lateral load relative to RC's maximum contribution. Figure 4.2a shows the linear idealisation from Figure 4.1b in spectral acceleration-displacement space. In this figure, $C_{s,max}$, $C_{s,min}$, μ_s and ω are indicated. These four parameters are required for deriving the CC, and the equation for each of them is shown in Equation 4.1 to Equation 4.4. Figure 4.2b shows the capacity curve and the IDA curve together and the various damage states.

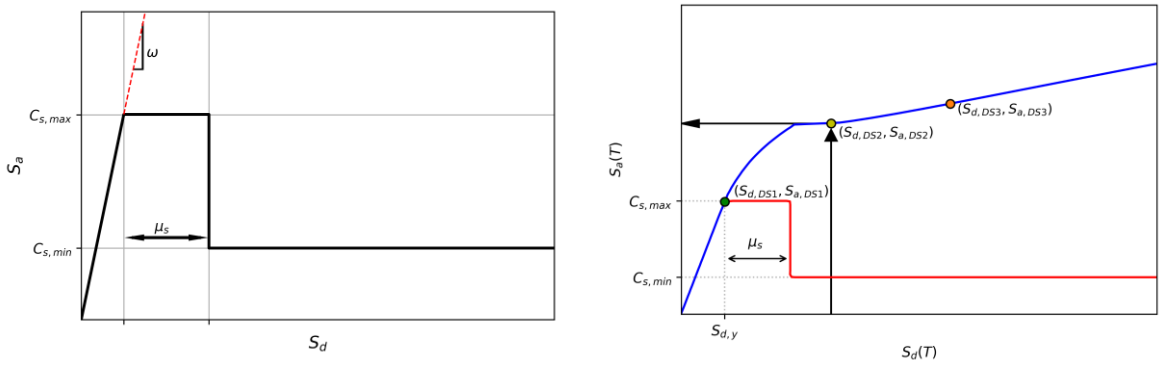

(a) (b)

Figure 4. 2: (a) Quadrilinear idealised capacity curve in spectral acceleration-displacement space 12 (b) Capacity curve (red), approximate IDA curve (blue) and damage thresholds for DS1 (green circle), DS2 (yellow circle) and DS3 (orange circle) represented in the $S_d(T)$ - $S_a(T)$ plane used in the FAST method.

$$C_{s,max} = \alpha \cdot C_{s,design} + \frac{1.3 \cdot \tau_{cr} . \rho_w}{N \cdot m \cdot \lambda} \qquad (4.1)$$

$$C_{s,min} = C_{s,design} + \frac{\beta \cdot 1.3 \cdot \tau_{cr} . \rho_w}{N \cdot m \cdot \lambda} \quad (4.2)$$

$$C_{s,design} = S_{a,d}(T) \cdot R_\alpha \cdot R_\omega \quad (4.3)$$

$$T = \kappa \cdot T_0 \quad (4.4)$$

$C_{s,max}$ (Equation 4.1) is the inelastic acceleration of the equivalent single degree of freedom (SDOF) system at which the maximum strength is obtained (De Luca et al., 2014). $C_{s,\ min}$ (Equation 4.2) is the inelastic acceleration of the equivalent SDOF system at the attainment of the RC structure's plastic collapse mechanism (all the infills of the storey involved in the mechanism have attained their residual strength). T is the equivalent period computed from the elastic period T_0 of the infilled building given in Equation 4.4, where κ is the amplification coefficient linking the initial period and the equivalent elastic period. The amplification coefficient is assumed to be 1.4 based on detailed analytical data (Verderame et al., 2012, Verderame et al., 2013; Manfredi et al., 2013). In Equations 4.1 and 4.2, N is the number of storeys, m is the average mass of each storey normalised by the building area (assumed equal to 0.8 t/m^2), λ is a coefficient for the evaluation of the first mode participation mass with respect to the total mass of the multiple degrees of freedom (MDOF) model according to Eurocode 8. ρ_w is the ratio between the infill area (A_w) evaluated along one of the building's principal directions and the building area A_b. The α coefficient accounts for the RC element's strength contribution at the attainment of the infill peak strength. The β coefficient accounts for the infill's residual strength contribution after attaining the bare RC structure's peak lateral resistance (see De Luca et al., 2014; De Luca et al., 2015). $C_{s,design}$ is the peak design spectrum value for the design spectrum that the structure was most likely designed to.

Equation 4.2 and Equation 4.3 assume that the maximum shear stress of the infills (τ_{max}) is $1.3\tau_{cr}$, as found in Fardis (1997). Recent research (Blasi et al. 2018) has found the relationship to be $1.44\tau_{cr}$ for hollow bricks and $1.55\tau_{cr}$ for solid bricks based on analytical and experimental results.

T_0 is the initial period of the structure based on the initial stiffness. This can be found using finite element analysis, as shown in Section 3.3.4. Where a finite element is unavailable or not

possible, an approximation of the initial period can be made using Equations 4.5 to 4.7 (Ricci et al., 2011). In these equations, N is the number of storeys, H is the structure's height, and A_{inf} is the ratio of infill area to building area in plan in percent.

$$T_0 = 0.049N \tag{4.5}$$

$$T_0 = 0.016H \tag{4.6}$$

$$T_0 = 0.023\frac{H}{\sqrt{A_{inf}}} \tag{4.7}$$

Equations 4.5 to 4.7 can be applied to the Pahar Trust template school detailed in Chapter 3. The number of storeys (N) equals 2, the height (H) is 6.55 m, and the A_{inf} is 5%. Equation 4.5 gives an initial period of 0.098s, Equation 4.6 gives an initial period of 0.105s, and Equation 4.7 gives an initial period of 0.067s. The finite element model gave a period of 0.092s. In this case, all of the approximations are relatively accurate, with Equation 4.5 overestimating the initial period by 6.5%, Equation 4.6 overestimating the period by 14.1% and Equation 4.7 underestimating by 27%.

4.2 FAST Nepal

4.2.1 Design Spectra

The first of the Nepalese codes covering RC buildings is "Nepal Building Code (NBC) 201:1994: the Mandatory Rules of Thumb for RC buildings" (NBC-201, 1994), which provides guidance for all stages, from the preliminary investigation to the design of the structures and the procurement of materials. This guide is aimed at owner-builders and is designed to offer easy-to-follow advice for safer construction. Examples of the prescriptions given in NBC 201 (1994) are: to ensure that there are at least two load-bearing walls in each direction for the building, establish standards for the quality of cement used, adequately anchor rebars and provide straightforward advice for assessing the soil capacity. In terms of materials, "*all cement used shall be Ordinary Portland cement conforming to NS:049-2041, with a cement-sand mix of 1:6 and 1:4 and small quantities of freshly hydrated lime to give plasticity. All bricks used shall be burnt red clay bricks with a size of 240 x 115 x 57 mm with a crushing strength not less than 3.5 N/mm^2. All walls should have a thickness of at least one half of a brick, but not*

more than one brick. All mild steel bars should have a strength of 250 N/mm^2" (NBC-201, 1994).

The second code for RC buildings is "NBC 105:1994, Seismic design of Buildings in Nepal" (NBC-105, 1994), which is a standard of good practice that acts to supplement IS 4326 (IS 4326, 1976). This code establishes that the "Seismic Coefficient Method" may be used for any building under 40 m in height which does not have an irregular configuration, abrupt changes in lateral resistance with height or unusual size or importance. It also establishes the general principles for ductile design to dissipate energy from the building. It states that the structural system must have identifiable load paths to the ground, be symmetrical and have uniform storey stiffness and connection of the foundations (NBC-105, 1994).

Furthermore, NBC 105 (1994) establishes the spectrum for design. The design horizontal seismic force coefficient ($C_d(T_i)$) shall be calculated using the formula shown in Equation 4.8, where $C(T_i)$ is the ordinate of the basic response spectrum for a translational period (T_i) for each of the soil types described in Table 4.1. In Equation 4.8, Z is the seismic zoning factor (1.0 for Kathmandu), I is the importance factor for the building (1.0 for residential buildings), and K is the structural performance factor representing the importance of the component to the building's structural integrity.

$$C_d(T_i) = C(T_i) \cdot Z \cdot I \cdot \mathrm{K} \tag{4.8}$$

Table 4. 1: Soil classification for NBC 105 (1994), T_{ci} is the corner period for each ground type

Type I	**Type II**	**Type III**
Rock or Stiff soil, sites with bedrock but less than 20m very stiff cohesive material (>100 kPa) or cohesionless material with standard penetration test values > 30	Site unsuitable for Type I or type III	Ground with a depth of soil greater than those recommended in NBC 105
T_{c1}=0.4	T_{c2}=0.5	T_{c3}=1.0

The spectral shape for NBC 105 (1994) shown in Figure 4.3a is defined based on the soil type. Three soil type categories are defined: Type I represents the stiffer (i.e. rock) soil, and Type II and III are progressively softer according to the description provided in Table 4.1. Each soil's class is characterised by a corner period (T_{ci}) which affects the spectral shape. Equation 4.9 provides the expression for the design spectra presented in Figure 4.3a.

$$C(T_i) = \begin{cases} 0.08, & T(s) < T_{ci} \\ \dfrac{0.08 \cdot T_{ci}}{T(s)}, & T(s) \geq T_{ci} \end{cases} \quad (4.9)$$

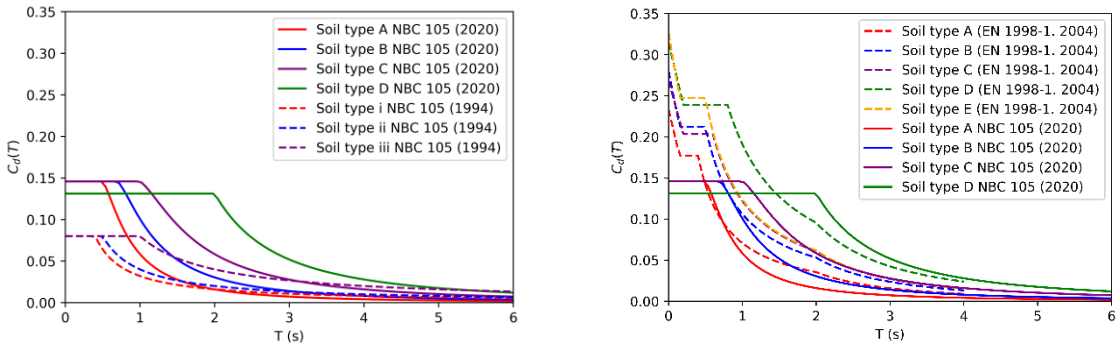

(a) *(b)*

Figure 4. 3: (a) A comparison of the ULS design spectra for an RC Moment resisting frame in Kathmandu for the old Nepalese design code (NBC 105, 1994) and the updated Nepalese design code (NBC 105, 2020). 07 (b) A comparison of the SLS design spectra, for an RC Moment resisting frame in Kathmandu, for the updated Nepalese design code (NBC 105, 2020) and Eurocode 8 with a behaviour factor equal to 4.95 (EN 1998-1, 2004) .

In 2010, the Nepal Department of Urban Development and Building Construction (UNDP, 2010) released a series of recommendations for improving the earthquake resilience of buildings by enhancing construction practices in addition to design and material advice. This advice includes size and depth of foundations (1500 mm, set on original soil), positioning and size of concrete reinforcing bars for beams and columns (minimum overlap distance, locations, examples of beam/column joints reinforcements, standard hooks for stirrups and a mesh design for concrete slabs). The recommendations also suggested other best design practice rules referring to international seismic design standards.

In 2020, the Nepal National Building Code for seismic design was updated. This revision includes updated conditions for using the "Seismic Coefficient Method" (now referred to as the "equivalent static method"). It also has updated soil type classification criteria, as shown in Tables 4.2 and 4.3. Many improvements are implemented in NBC 105 (2020) compared to NBC 105 (1994). These improvements include the provision of the elastic time history, non-linear time history analysis and non-linear static analysis. Elastic time history analysis and non-linear methods are recommended to verify the performance of existing or retrofitted structures or to verify that the specific response parameters are within the limits of acceptability assumed during design. NBC 105 (2020) also gives significantly more detailed provisions for the reinforcement design, including requirements for longitudinal reinforcement, transverse reinforcement, dimension limits and joint details. NBC 105 (2020)

updates the design spectrum (C_d) to be used to identify the horizontal base shear coefficient (design coefficient) ($C_d(T_1)$). Figure 4.3a compares the design spectrum for the old Nepalese design code (NBC 105, 1994) and the updated design code (NBC 105, 2020). Figure 4.3b shows how the design spectra for the updated Nepalese design code (NBC 105, 2020) compares to Eurocode 8 (EN 1998-1, 2004).

Table 4. 2: Soil classification criteria for NBC 105 (2020)

Soil Type	Description
Soil Type A - Stiff or Hard Soil Sites	Sites with bedrock, including weathered rock with an unconfined compressive strength greater than 500 kPa, overlain by less than 20 m of: **I.** Very stiff cohesive material with an unconfined compressive strength greater than 100 kPa, or **II.** Very dense cohesionless material with N > 30, where N is the standard penetration test (SPT) value.
Soil Type B - Medium Soil Sites	Sites where the depth of soil does not exceed those stipulated in Table 4.3.
Soil Type C - Soft Soil Sites	Sites where the depth of soil of a particular type exceeds those stipulated in Table 4.3.
Soil Type D - Very Soft Soil Sites	Soil site which comprises of: **I.** More than 10 m depth of cohesive soil with undrained shear strength less than 12.5 kPa **II.** More than 10 m depth of cohesionless soil with SPT N-values less than 4

Table 4. 3: Minimum depth criteria for the classification of Type B and Type C soils from NBC 105 (2020)

Cohesive Soils		
	Representative Undrained Shear Strength (kPa)	**Minimum Depth of Soil (m)**
Soft	12.5 - 25	20
Firm	25 - 50	25
Stiff	50 - 100	40
Very Stiff	100 - 200	60
Cohesionless Soils		
	Representative SPT values (N)	**Minimum Depth of Soil (m)**
Loose	4 - 10	40
Medium Dense	10 - 30	45
Dense	30 - 50	55
Very Dense	> 50	60
Gravels	> 30	100

As previously mentioned, $C_{s,design}$ is the peak design spectrum value for the design spectrum most likely used in the relevant area. In the case of Nepal, we can assume that structures are designed to NBC 105 (1994) if constructed before 2020 and NBC 105 (2020) if built after 2020.

4.2.2 Ductility Assessment

μ_s is defined as the available ductility up to the degradation of the infills relative to the displacement at $_{Vmax}$. μ_s is found to be 2.5 (Manfredi et al., 2012) for Mediterranean masonry buildings, typically formed of hollow clay bricks. This may not be representative of the available ductility in Nepalese RC with infill structures as they are formed of solid clay bricks. To find a more accurate ductility value for hollow clay bricks, we can apply a piecewise linear fit to the analytical static pushover (SPO) analysis in Chaulagain (2016a). In Chaulagain (2016a), several pushover analyses are carried out on various RC buildings with infills formed of solid clay bricks with cement mortar; these are summarised in Table 4.4. There were five building versions with varying reinforcement depending on what code the reinforcement was designed to. The first building was designed to current construction practices (CCP). CCP is specified as "*buildings are not properly designed, and their construction is not supervised by engineers*". The structures with the irregular top level are not included in the available ductility assessment. Linear interpolation of the initial stiffness is applied using the equal-area (equal-energy) method, where the area under the curve and the linear-interpolation are equal at the maximum base shear. This is the method used by Eurocode 8 and has a relatively limited error between the curve and piecewise-linear fit (see De Luca et al., 2013). The elastic segment continues to the maximum shear resistance, V_{max}. The horizontal section of the piecewise idealisation continues to the maximum point of the pushover curve, as shown in Figure 4.4. The static pushover curves are given for buildings NRCB1, NRCB3, NRCB4 and NRCB5. Due to the irregular top level in NRCB3 and NRCB4, we will not include these in assessing the available ductility. The obtained μ_s values for engineered and non-engineered buildings are 2.01 and 3.33, with an average (2.67) close to the original 2.5 value assumed in previous versions of the FAST method. Such values can be used for engineered and non-engineered building classes, as identified by their year of construction.

Table 4. 4: Summary of building characteristics from Chaulagain (2016b)

Name	X bays	Y bays	Storeys	Comments	Engineered/Non-engineered
NRCB1	2	2	3	Regular	Non-engineered construction
NRCB2	3	2	3	Regular	Non-engineered construction
NRCB3	3	3	3	Irregular at top level	Engineered RC-MRF
NRCB4	3	3	3	Irregular at top level	Engineered RC-MRF
NRCB5	3	2	3	Regular	Engineered construction

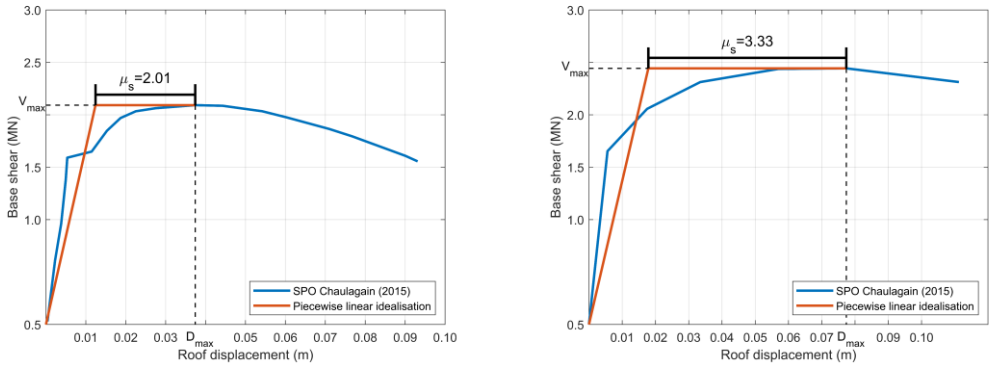

(a) *(b)*

Figure 4. 4: The piecewise approximation of the SPO curves from Chaulagain (2016b) to allow calculation of μ_s. (a) NRCB1 (b) NRCB5

4.2.3 Damage States

To carry out the FAST method, it is required to establish the interstorey drift level at which a specific damage state is exceeded. Cardone and Perrone (2015) use experimental data from the pushover of masonry-infilled RC frames to establish the IDR to exceed a given damage state. The interstorey drift ratio required to exceed DS1 is referred to as IDR1 etc. To compare inter-storey drift ratio (IDR) and EMS-98 (Grünthal et al., 1998) damage states, data must be collected and a probability distribution formed for each damage state. The data for IDR1, IDR2 and IDR3 was gathered from Cardone and Perrone (2015), with the number of tests equalling 14, 12 and 15, respectively. Cardone and Perrone (2015) present data for solid and hollow bricks, however, only the values for the solid bricks are used as this is what is typically implemented in Nepal. Additional datasets of infills have been recently made available in literature, such as Blasi et al. (2021), but they do not have data for all three damage states required here. The data from Cardone and Perrone (2015) was fitted with three different distributions (Figure 4.5), Normal, Log-Normal and Generalised Extreme Value (GEV). In Table 4.5, the fitted parameters for the distribution are presented. Since the GEV distribution is a three-parametric distribution and the Normal and Log-Normal are two-parametric, an information criterion accounting for this difference must be used to identify the most efficient distribution for the data considered. The Akaike Information Criteria has the advantage of considering the number of parameters in the distribution, compared to chi-squared or Kolmogorov Smirnov. The Akaike Information Criteria in its basic version (AIC) (Equation 4.10) is improved (AIC_C) to account for a limited data sample and to avoid overfitting (Equation 4.11). The improved version is used to rank the different fits investigated (Akaike, 1974). In Equations 4.10 and Equation 4.11, k is the number of parameters in the model, L is

the maximum likelihood from the fit, and *n* is the number of samples. AIC_C is suggested for cases where the sample size is fewer than 50 (Cavanaugh, 1997). The Akaike Information Criteria has the advantage of considering the number of parameters in the distribution, compared to chi-squared or Kolmogorov Smirnov.

$$AIC = 2k - 2\,ln(L) \tag{4.10}$$

$$AIC_C = AIC + \frac{2k^2 + 2k}{n - k - 1} \tag{4.11}$$

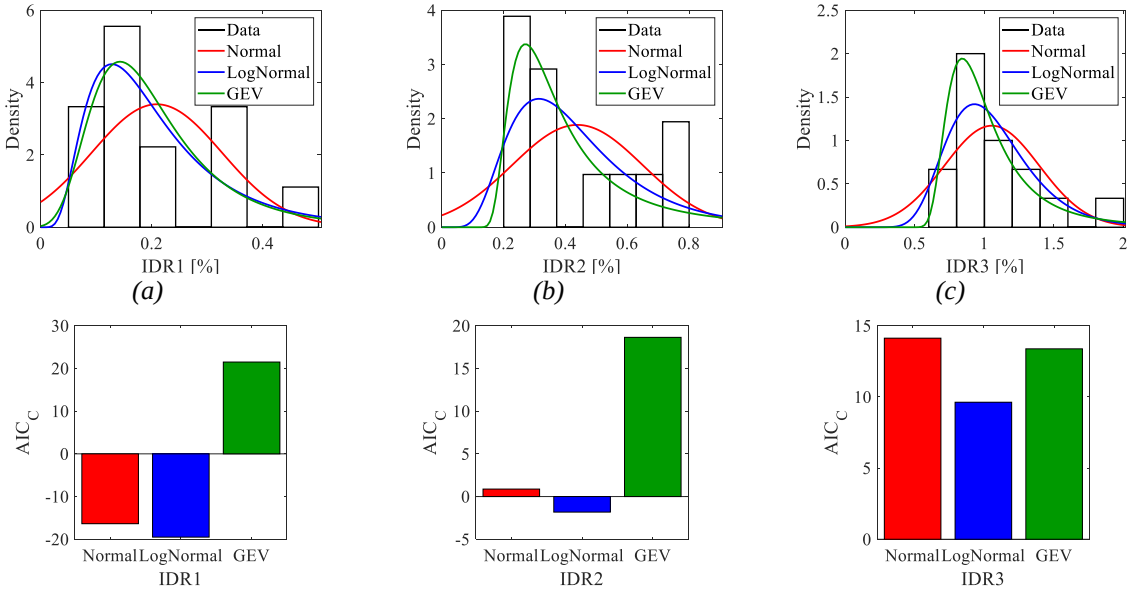

Figure 4. 5 Plot data gathered for IDR thresholds for solid clay bricks for the Damage States one to three (a), (b), (c), and AIC_C values for fits (d), (e), (f), respectively.

The AIC_C value is compared for each fit, with the lowest value denoting the most efficient for that data set. The AIC_C found that the Log-Normal Distribution best represents the Global Data for all the variables considered (IDR1, IDR2, IDR3). This distribution is commonly used for variable distributions used in earthquake engineering for fragility analysis (e.g., Porter et al., 2007; De Luca et al., 2015).

Table 4. 5: Parameters of fitted distribution for the IDR for EMS-98 (Grünthal et al., 1998) damage states one to three (IDR1, IDR2, IDR3)

Distribution	**Normal**		**LogNormal**		**GEV**		
Variables	**μ**	**σ**	**log μ**	**log σ**	**k**	**μ**	**σ**
IDR1	0.2090	0.1173	-1.7158	0.5832	0.1215	0.0809	0.1519
IDR2	0.4385	0.2115	-0.9299	0.4789	0.4554	0.1193	0.3114
IDR3	1.0533	0.3410	0.0100	0.2906	0.2563	0.1950	0.8834

In particular, the median results can be compared with those calibrated in De Luca et al. (2015) for hollow clay brick infills (i.e., IDR1 = 0.1%, IDR2 = 0.4%, and IDR3 = 0.8%). The median value obtained for IDR2 in Table 4.5 (i.e. IDR2 = exp(-0.9299) = 0.39%) is very similar to the value obtained in the calibration for hollow clay bricks (De Luca et al., 2015). For the case of IDR1 and IDR3, the difference is more significant (i.e. IDR1 = exp(-1.7158) = 0.18%, IDR3 = exp(0.010) = 1.0%) with the values for solid clay bricks being larger. The logarithmic standard deviations obtained for IDR1, IDR2 and IDR3 are lower with respect to the value suggested by Colangelo (2012) (i.e., 0.60, 0.67, 0.47) for hollow clay brick infills. Colangelo's values are used in previous applications of FAST method (see De Luca et al., 2015).

4.2.4 Cracking shear strength

Regionalised data for the shear cracking strength is required to improve the FAST methodology for the Nepalese context. An established catalogue using global tests is collated, and its distribution is then updated using Nepalese data. The global data was gathered from the MADA masonry database (Augenti et al. 2012) and had a total size of 48 tests (Meli 1973, Abrams 1992, Zarri 1992, Riddington and Jukes 1994, Zhuge et al., 1996, Andreaus and Moroder 1991, Yi et al., 2004, Valluzzi et al., 2002 and Caliò 2011). The same fitting procedure is applied as in Section 4.2.3. The fitted distributions can be seen in Figure 4.6. This data is subsequently referred to as τ_{global}. Data from 24 shear tests on solid brick infill made with cement mortar was gathered from the EPSRC SAFER project database and provided by one of the project partners (NSET, 2017). The fitted distributions for this data can be seen in Figure 4.7. This data is subsequently referred to as τ_{Nepal}. The AIC_c values are also shown for each of the fitted distributions, and it can be seen that the most efficient fit for both τ_{global} and τ_{Nepal} is Log-Normal.

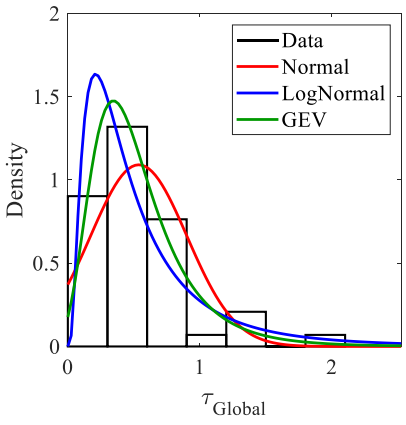

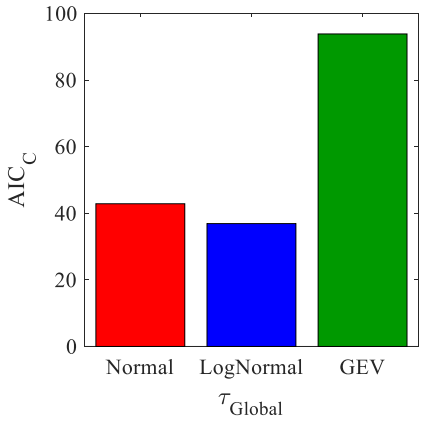

(a) *(b)*

Figure 4. 6: (a) Distribution of τ_{global} data from Mada database and (b) AIC_C value of the investigated fits.

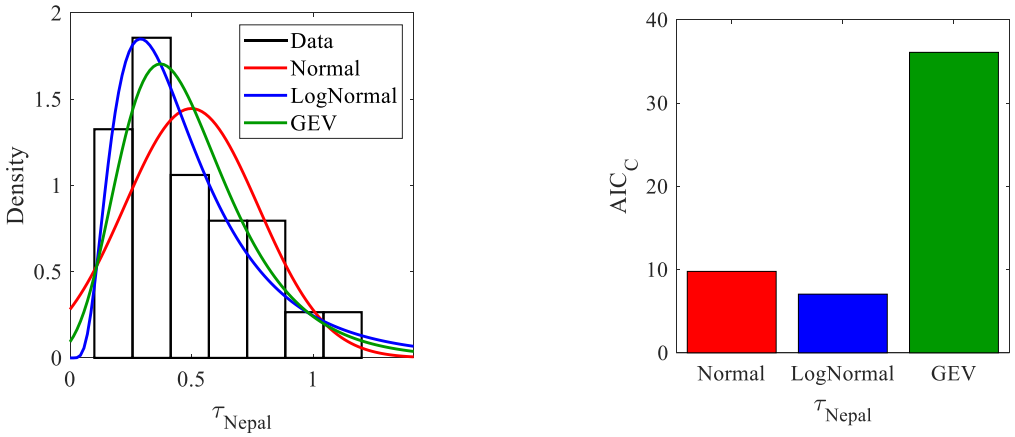

(a) *(b)*

Figure 4. 7: (a) Distribution of Nepalese Shear Stress (τ_{Nepal}) and (b) AICC comparison of the distributions.

Since the Nepalese and Global data are both Log-Normal, it is possible to use a closed-form solution for Bayesian updating of the global data (prior data) using the Nepalese tests as additional information (likelihood). The global data set (i.e., τ_{global}) is updated using Equations 4.12, 4.13 and 4.14 (Ang and Tang, 1984; Benjamin & Cornell, 1970), where $\mu log(G)$ and $\sigma log(G)$ are the mean and standard deviation of the logarithm of τ_{global} (i.e., the prior global data). $\mu log(N)$ and $\sigma log(N)$ are the mean and standard deviation of the logarithm of τ_{Nepal}, n_G is the number of data points for the global dataset, and n_N is the number of the new Nepalese data. The results of Equations 4.12 and 4.14 are the posterior log-normal distribution parameters for τcr (i.e., $\tau_{Updated}$ in Table 4.6).

$$\mu log\,(B) = \frac{\mu log\,(G)\,n_G + \mu log\,(N) n_N}{n_G + n_N} \tag{4.12}$$

$$s'' = \sqrt{\frac{((n_G - 1)\sigma log\,(G) + n_G \mu log\,(G)^2) + ((n_N - 1)\sigma log(N) + n_N \mu log\,(N)^2) - (n_G + n_N)\mu log\,(B)}{n_G + n_N - 1}} \tag{4.13}$$

$$\sigma \log(B) = s'' \cdot \sqrt{\frac{n_G + n_N - 1}{2}} \cdot \frac{\Gamma\left(\frac{n_G + n_N - 3}{2}\right)}{\Gamma\left(\frac{n_G + n_N - 2}{2}\right)} \tag{4.14}$$

Table 4. 6: Distribution parameters for shear cracking

Distribution	log μ	log σ
Tau Global (τ_{Global})	-0.8797	0.8283

Tau Nepal (τ_{Nepal})	-1.0292	0.7695
Tau Updated ($\tau_{Updated}$)	-0.9295	0.8959

The results of the Bayesian updating of the Log-Normal distribution for τ_{cr} are shown in Figure 4.8. The distribution for the Nepalese Bricks is very similar to that of the Global data set. This is probably because of the common use of cement mortar and can indicate a reasonably good practice for mixing the mortar. It is worth noting that these tests do not necessarily represent the standard practice. For example, reconnaissance reports have shown different standards in the quality of mortars of infill walls in the same buildings (e.g., Build Change Org, 2015). The Bayesian updating positively affects the standard deviation relative to the Global data set.

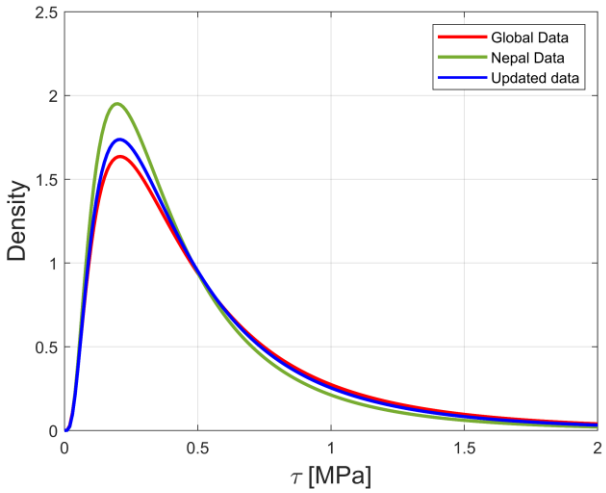

Figure 4. 8: Comparison of Nepalese Shear data to Global Shear data and Updated data

The capacity curve equations (Equations 4.1 and Equation 4.2) presented by De Luca et al. (2015) has been modified for solid clay bricks, whereby the $\tau_{max}=1.55\tau_{cr}$ instead of $\tau_{max}=1.3\tau_{cr}$, as is used for hollow clay bricks (Blasi et al., 2018).

4.2.5 Relative contribution of the RC Frame

The RC frame's relative contribution to the lateral resistance at the peak lateral load (α) is defined as the lateral resistance of the RC frame at the peak resistance of the building compared to the residual lateral resistance of the frame. This is indicated in Figure 4.1. A value of 0.5 is used in De Luca et al. (2014). The relative contribution of the RC frame at peak lateral load will be affected by many factors, including infill material, the thickness of infill, RC design of

the frame and the number and size of openings. As the FAST method is applied using a limited number of structural properties, 0.5 is used as an approximation. A more recent analytical assessment of RC buildings with masonry infills shows that the RC frame's relative contribution decreases with a higher τ_{cr} value. This relationship is given in Equation 4.15 (Scala et al., 2020). It is shown by Scala et al. (2020) that this equation has a greater efficiency for τ_{cr} values between 0.27 MPa and 0.47 MPa. However, it should be noted that at a high τ_{cr} value, the α value starts to increase again (i.e., the contribution of RC would increase as the infill's strength increases). As this cannot be the case, at τ_{cr} values greater than 0.47 MPa, the α is set to 0.41, the minimum polynomial point.

$$\alpha = \begin{cases} 2.70{\tau_{cr}}^2 - 2.57\tau_{cr} + 1.02 & \tau_{cr} \leq 0.47\ MPa \\ 0.41 & \tau_{cr} > 0.47\ MPa \end{cases} \quad (4.15)$$

4.3 Single Building Validation – Pahar Trust School

The Nepal FAST methodology developed in Section 4.2 is applied to a single RC building with masonry infills. The results are compared to numerical work previously carried out in Chapter 3 to assess the validity of the Nepal FAST methodology. Further details of the structural layout and materials can be found in Chapter 3, along with more information on the non-linear model of the school and the time history analysis. When the cloud analysis was carried out in Section 3.4.2, the damage limitation (DL) limit state is defined at the IDR where all infills have exceeded their peak shear resistance (Ricci et al., 2016), which is found to be an IDR of 0.19%. The life safety (LS) limit state is defined as 2.0 % (ASCE/SEI 41-17, 2017). The α value is calculated using the τ_{cr} of 0.05 MPa from Chapter 3 using Equation 4.15 to give an α value of 0.898. The fragilities can then be integrated with the hazard maps provided by Stevens et al. (2018) to find the seismic risk as with the numerical fragilities in Section 3.6.2.

4.3.1 Assessing fragility.

The FAST methodology is applied using the approach laid out in Section 4.1 with the updated parameters laid out in Section 4.2. The building is assumed to be compliant with NBC 105 (1994), and therefore the design spectrum shown in Figure 4.3a is used. The available ductility μ_s is assumed to take a value of 3.13 as the building can be considered engineered. The IDR for DS1, DS2 and DS3 are assumed to be distributed as laid out in Section 4.2.4. The mean τ_{cr} value is assumed to be 0.05 MPa as this is the value used in Chapter 3, which is from a regionalised material test on 1:6 cement sand mortar as used in the school building. Using this

τ_{cr} value allows a like-for-like comparison of the fragilities. The coefficient of variation of the τ_{cr} is assumed to be equal to the value set out in Section 4.2.4. It would be preferable to use a standard deviation value from the source of the 0.05 MPa (Shakya et al., 2016), however, no standard deviation is provided; therefore the coefficient of variation from Section 4.2.4 is used. The RC frame's contribution at the peak lateral load (α) is assumed to correspond to the τ_{cr} distribution with Equation 4.15. 100 samples were carried out in the Monte Carlo simulation to generate the fragility curves, and the mean fragility parameters were calculated for DS1, DS2 and DS3.

It should be noted that the mean IDR for DS1, DS2 and DS3 are 0.18%, 0.39% and 1.01%, respectively, and the DL and LS limit state IDR from Chapter 3 are 0.19% and 2.00%, respectively. These results can be seen in Table 4.7. It can be noted that the IDR for the DL limit state lies between the means for DS1 and DS2, and the IDR for the LS limit state exceeds DS3. Figure 4.9 shows the FAST methodology's fragilities and the numerical fragilities from Chapter 3. The fragility curves derived from the FAST-NEPAL method are expressed in EMS-98 DSs (Grünthal, 1998). In contrast, the fragilities in Chapter 3 are expressed in terms of Eurocode conventional limit states. Hence, the benchmarking needs to be supported by additional comparisons even if this does not harm its preliminary benchmarking value.

Table 4. 7: IDR for the damage states used in the FAST method (DS1, DS2, DS3) and the limit states used in Chapter 3 (DL, LS)

	DL	**LS**	**DS1**	**DS2**	**DS3**
IDR (%)	0.19	2.00	0.18	0.39	1.01

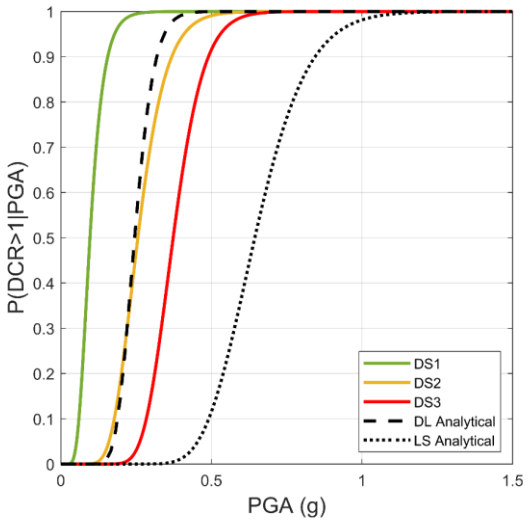

Figure 4. 9: Fragility curves for DS1, DS2 and DS3 using the Nepal FAST methodology and DL and LS limit state using a detailed analytical approach in Chapter 3.

The fragility curves derived with the Nepal FAST method are significantly more conservative than the numerical curves. This is to be expected due to the approximate nature of the approach. There is a robust matching between DS2 and DL limit state with a η value of 0.248 g and 0.245 g. DS2 is compared to DL as both represent a low level of damage that does not impede the use of the structure. Previous studies have drawn this equivalence (Kallioras et al., 2019). It should be noted that both DS2 and DL limit state represents the point at which the masonry infills degrade. It can be seen from Figure 4.9 that the Nepal FAST methodology gives a slightly larger β value, which is to be expected due to the higher level of variability in the FAST method caused by varying parameter values (τ_{cr}, IDR1, IDR2, IDR3). The η value of the LS limit state (0.644 g) from Chapter 3 substantially exceeds that of the DS3 from this study (0.366 g). This is due to the previously mentioned conservative nature of the FAST methodology. The parameters that form each of the fragility curves in Figure 4.9 are summarised in Table 4.8.

Table 4. 8: Fragility parameters for fragility curves from the numerical and FAST approach.

	DS1 (FAST)	**DS2 (FAST)**	**DS3 (FAST)**	**DL (Numerical)**	**LS (Numerical)**
η (g)	0.091	0.248	0.366	0.245	0.644
β	0.3211	0.2795	0.1900	0.205	0.211

4.3.2 Assessing Risk.

Using the same risk assessment method applied in Section 3.6.2, we can use the fragility curves from the FAST method applied to the Pahar Trust School and the hazard maps from Stevens et al. (2018) to assess the risk to the schools across Nepal. The hazard curve at each geographical point is interpolated from the two data points provided, as outlined in Section 3.2.1. The integration is carried out using Equation 3.14. Figure 4.10, Figure 4.11, and Figure 4.12 show the annual probability of exceeding DS1, DS2, and DS3, respectively.

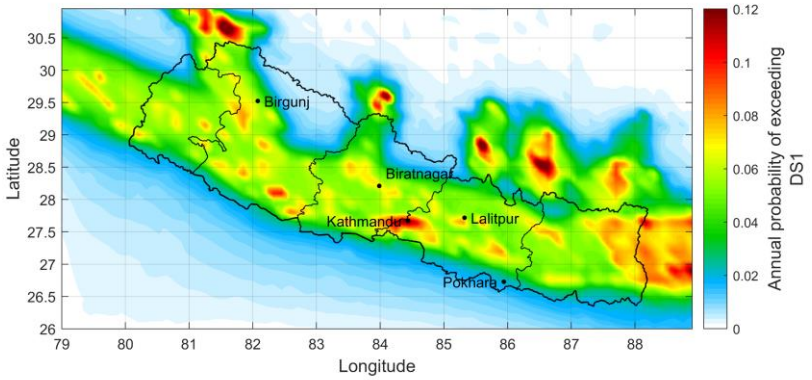

Figure 4. 10: Annual probability of Pahar Trust school template design exceeding DS1 based on the FAST method.

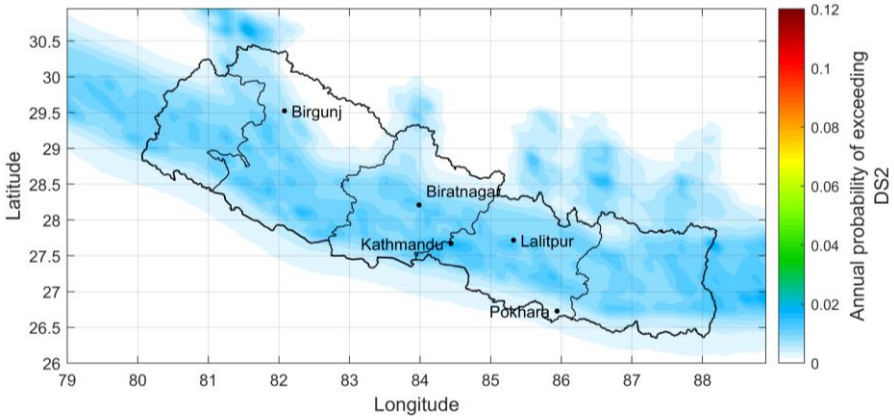

Figure 4. 11: Annual probability of Pahar Trust school template design exceeding DS2 based on the FAST method

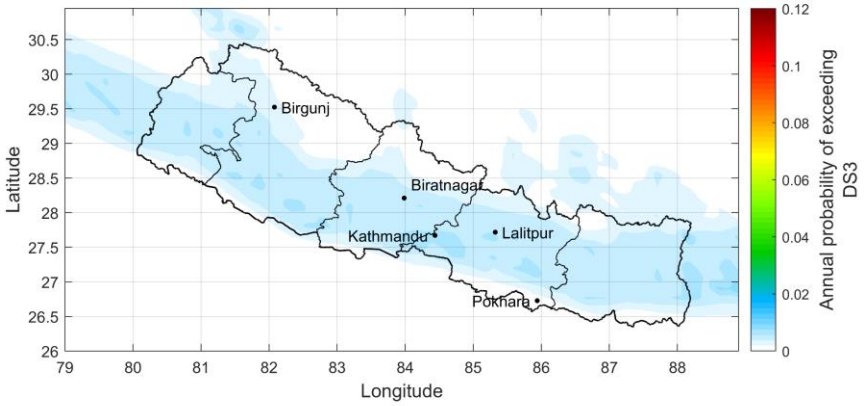

Figure 4. 12: Annual probability of Pahar Trust school template design exceeding DS3 based on the FAST method

It can be seen from Figure 4.10 that the annual probability of exceeding DS1 is 0.12 on parts of the southern edge of Nepal, with most of the country having an annual probability of exceeding DS1 of over 0.05. Although the FAST methodology has various conservative assumptions, this risk assessment for DS1 far exceeds typically acceptable values. Figure 4.11 and Figure 4.12 show a maximum annual probability of exceedance of 0.02 and 0.01 for DS2 and DS3. This is far greater than what might be considered acceptable.

Table 4. 9: Comparison of risk values (mean annual frequency of exceedance) at the five most populated cities in Nepal

	FAST Method			Numerical Risk (Chapter 3)	
	DS1	DS2	DS3	DL	LS
Kathmandu	0.0851	0.0143	0.0068	0.0140	0.0022
Pokhara	0.0730	0.0120	0.0056	0.0117	0.0018
Lalitpur	0.0477	0.0091	0.0044	0.0029	0.0003
Biratnagar	0.0187	0.0030	0.0011	0.0034	0.0004
Birgunj	0.0211	0.0035	0.0014	0.0091	0.0014

Table 4.9 shows the risk levels from this chapter and Chapter 3 at the 5 most populous cities in Nepal. As stated previously, DL sits between DS1 and DS2 in terms of IDR, and LS exceeds DS3. In Kathmandu, it can be seen that for DS2, the risk value is 0.0143 compared to the numerical risk value from Chapter 3, which gives a value of 0.0140 for DL. This shows a very small difference. The DS3 value in this study shows a mean annual frequency of 0.0068 compared to the LS of Chapter 3, which shows a MAF of 0.0022. This difference can be attributed to the conservative nature of the FAST method. Many factors result in the FAST method being inherently conservative, including the assumption of a soft-storey plastic collapse of the ground floor, with the stiff, infilled walls failing first and the RC frame undergoing plastic failure later. Other assumptions include the assumption that after a design code is released, all structures are designed and constructed to that code. Nepal has a problem with code compliance caused by over 80% of buildings being built by their owner (Dixit, 2004). This often results in low levels of quality assurance and code implementation. The FAST method has the potential to be improved by collecting more localised data on material properties and by quantifying code compliance.

4.4 Application of Nepal FAST to Ward-35 building database

4.4.1 Gorkha 2015 earthquake.

Details of the 2015 Gorkha earthquake and its effects on Nepal can be found in Section 2.2. On April 25th, 2015, a magnitude ($\mathbf{M}_W$) 7.8 earthquake struck Nepal at 06:11 UTM in the district of Lamjung in the Gandaki administrative zone, 77 km from the capital of Kathmandu (population 1.5 million). The earthquake was followed by three aftershocks of $\mathbf{M}_W$ greater than 6.0. They were at 06:15 am, and 06:45 am on April 25th, and 07:36 am on April 26th. Another significant event of $\mathbf{M}_W$ 7.3 occurred at 07:05 am on May 12th, 2015, followed by another aftershock of $\mathbf{M}_W$ 6.3 at 07:36 am (Lizundia et al. 2016). Figure 4.10 shows the peak ground acceleration (PGA) shake maps for the two main events (i.e., April 25th and May 12th) according to USGS (2018). These shake maps are obtained based on a single station recording located in the centre of Kathmandu (KATNP), more than 200 km from the event's epicentre. They do not provide a very detailed description of the shaking in the city's urban area.

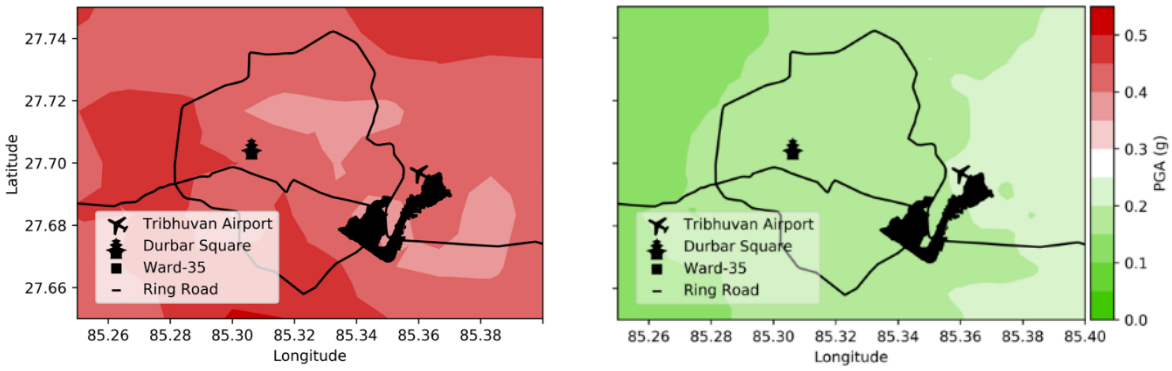

(a) *(b)*

Figure 4. 13: PGA shake map of the earthquake event occurring on (a) April 25th, 2015 (Mw 7.8) and (b) May 12th, 2015 (Mw 7.3) (USGS 2018) and the location of Ward 35 buildings.

Kathmandu's metropolitan area is split into 35 administrative wards. This study uses data collected from Ward-35 (further details in Section 4.4.2), shown in Figure 4.13. For the primary event (Figure 4.13a), the PGA that the buildings experienced varies across Ward 35, with the parts of the ward closer to the airport experiencing a lower PGA. However, for the second event (Figure 4.13b), the PGA that Ward-35 experienced is similar according to the USGS shake map.

4.4.2 Building Database for Ward-35

The damage database of Ward-35 of Kathmandu is a collection of 6869 RC frame buildings with masonry infills of fired clay brick (Marhatta et al., 2007). The database was assembled for cadastral and census purposes in Ward-35 of Kathmandu (Genesis Ltd, 2016). The damage was graded using the EMS-98 (Grünthal, 1998) grading system. See the aggregated damage data in Figure 4.14 and the disaggregated data considering the number of stories in Table 4.10.

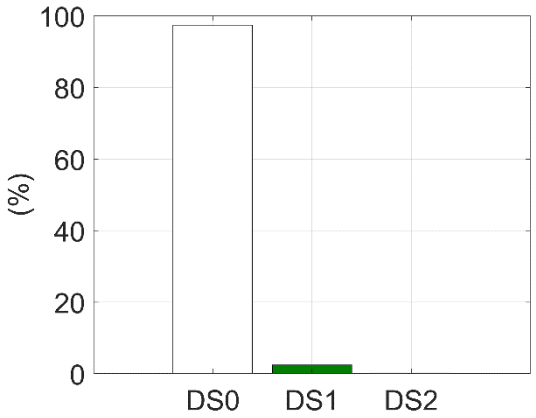

Figure 4. 14: Distribution of observed damage in Ward-35 Buildings

Table 4. 10: Damage state by building height

Class	Number of Buildings	DS0 [#]	DS0 [%]	DS1 [#]	DS1 [%]	DS2 [#]	DS2 [%]
RC total	6869	6693	97.43	172	2.434	11	0.147
1-Storey	456	441	96.71	14	3.070	1	0.219
2-Storey	1312	1267	96.57	42	3.201	3	0.229
3-Storey	2951	2874	97.39	73	2.474	4	0.136
4-Storey	2150	2111	98.19	37	1.721	2	0.093
>5-Storey	361	354	98.06	6	1.66	1	0.28

The data was collected by Genesis Ltd (2016) for the Nepalese government months after the 2015 earthquake and finalised in June 2016. Due to early reconstruction, any significantly damaged or collapsed buildings were not included in the database (the database was assembled for census purposes and not for post-earthquake damage evaluation). The damage evaluation is based on the limited photographic documentation available for each building in the database, which is not highly reliable but still a useful preliminary testbed for the Nepal FAST method.

Ward-35 of Kathmandu did not suffer significant damage, as shown by documentation collected in post-earthquake reconnaissance reports (e.g., Goda et al., 2015; Gautam and Chaulagain 2016; Build Change Org, 2016, Gautam et al., 2015; Lizundia et al., 2016; Shakya

and Kawan 2016). Most of the buildings are of recent construction, with 16% of buildings built since 2010 when the new NBC was released with advice on improved construction practices. Almost 40% of the buildings in the database were constructed between 1994 and 2010. This means they were built after the release of NBC 1994. Only 2.8% of the buildings surveyed were built before 1994. However, more than 40% of the buildings could not have their age determined (i.e., na), as shown in Figure 4.15a. Genesis collected information on the age of construction, the number of storeys (Figure 4.15b) and the presence of roof tanks (Figure 4.15c) that can affect the vulnerability of the structure significantly, as seen in many post-earthquake reports (e.g., Shakya and Kawan 2016). The ratio in-plan (LX/LY) for each building (i.e., the shape factor of the circumscribing rectangular shape around the building footprint) is provided in the database and is shown in Figure 4.15d. LX/LY is a fundamental variable used in the FAST method (De Luca et al., 2017).

The buildings range from one storey to eleven storeys, with 70% being three to four storeys. This matches well with the number of storeys for which the FAST method was previously calibrated (De Luca et al., 2015). Other sources for Nepal, such as Chaulagain et al. (2015), report a similar range of heights. This height range is because the owners build most buildings for their own family, not multiple resident apartment complexes seen in other countries.

According to the World Housing Encyclopedia (Marhatta et al., 2007), most buildings in Nepal are square or rectangular in plan. This matches the data in Figure 4.15d, with 82% having an in-plan ratio of 1-2. Databases such as De Luca et al. (2015) used to calibrate the FAST method in the Mediterranean area are predominantly square or rectangular. The Nepalese buildings often have large balconies, which may mean that these ratios seem smaller than they are. Only 130 (1.9%) of the buildings are classified as having "Soft Storeys", but this datum was not used since the Genesis database of Ward-35 did not allow a strict structural interpretation of this condition. I.e., distinguishing between soft-storey configuration only on the front side of the building or full pilotis configuration (e.g., Kappos et al. 2006; Verderame et al. 2011). Of much more significant concern is that 94% of the buildings had roof water tanks (Figure 14.5c). These tanks cause substantial increases in the building mass on the highest level. They are supported using non-designed supports that are typically not earthquake resistant and are unaccounted for in the building design stage. As the water tank volume is not quantified, it is impossible to account for this in the Nepal FAST methodology.

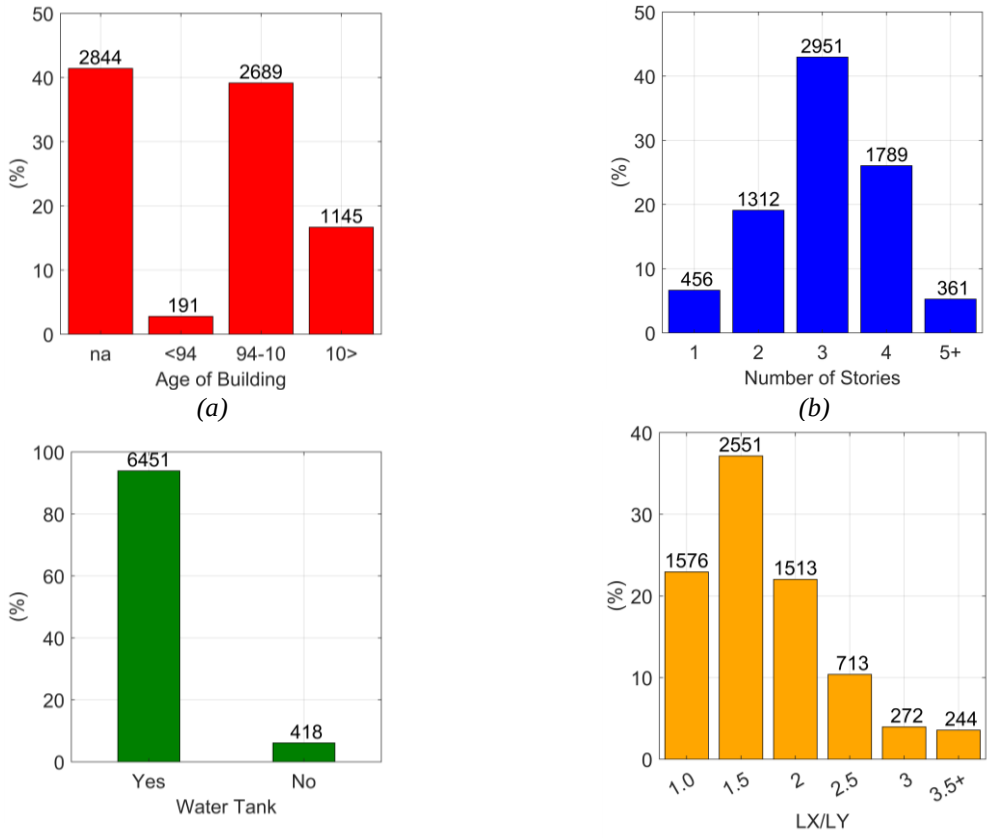

Figure 4. 15: Bar charts of (a) age of buildings in the database, (b) number of storeys, (c) the presence of roof tanks, (d) in-plan ratios for the buildings as collected from GIS (LX/LY)

4.4.3 Application of FAST Nepal to Ward-35 of Kathmandu

The Nepal FAST method is then applied to the building database for Ward-35 of Kathmandu. The FAST analysis was performed assuming a distribution of damage states laid out in Section 4.2.3, an updated τ_{cr} distribution in Section 4.2.4, and an updated relative contribution of RC (α) as laid out by Section 4.2.5. For the estimation of C_{design} (i.e., the inelastic design acceleration coefficient of the bare RC structure), an assumption was made based on the building's age of construction (see Figure 4.15a). As the mandatory rule of thumb introduced in 2010 (UNDP, 2010) did not affect the design spectrum of the NBC 105 (1994), the $S_{a,d}(T)$ is assumed equal to 0.08 g for all buildings. The value of R_α (the structural redundancy factor) and R_ω (the over-strength material factor) were taken respectively equal to 1.0 and 1.0 for buildings where the age was not available (na in Figure 4.15a) and pre-1994 buildings (no-code buildings). R_α and R_ω were taken respectively equal to 1.0 and 1.45 for 1994-2010 buildings. This assumption considers the steel overstrength guaranteed by industrial quality control (IS 456, 1978; De Luca et al., 2014; Galasso, 2014). After 2010, 1.1 and 1.45 were used for R_α and R_ω due to the release of the Nepal Department of Urban Development and Building Construction (UNDP, 2010) guidelines and a greater degree of code compliance. 1.1 is the R_α

used in previous FAST studies (De Luca et al. 2014) and based on Borzi and Elnashai (2000). The Monte Carlo simulation was run for 100 iterations for each building, with the variable parameters being τ_{cr}, α, DS1, DS2, and DS3. The Monte Carlo simulation results from each building were used to form a fragility curve for each building in the database.

4.4.4 Comparison with Damage Data

The FAST analysis was performed for each of the structures, with the mean value of the 100 iterations being taken to define the required PGA to exceed a specific damage state for each particular building. The damage state for each of the structures in response to the April 2015 Gorkha Earthquake can then be computed and is shown in Table 4.11 and Figure 4.16. These values can then be directly compared to the observed damage states shown in Table 4.10. It can be noted that the buildings that have exceeded DS3 have not been separated from those that exceeded DS2. This is because the Ward-35 database does not separate buildings that have exceeded DS2 and DS3. Therefore, to directly compare results, DS2 and DS3 have been considered together. As expected, the Nepal FAST methodology tends to overestimate the level of damage in the buildings. This is particularly evident in structures of four storeys or more. This is due to some of the conservative assumptions made in the Nepal FAST methodology. However, the method still accurately captures the dominance of DS0.

Table 4. 11: Damage state by building height for the Ward-35 buildings using the FAST method

Class	Number of Buildings	DS0 [#]	DS0 [%]	DS1 [#]	DS1 [%]	DS2 [#]	DS2 [%]
RC total	6869	3919	57.05	2585	37.63	364	5.30
1-Storey	456	455	99.78	1	0.22	0	0
2-Storey	1312	1281	97.63	26	1.98	5	0.38
3-Storey	2951	1736	58.86	1186	40.21	27	0.91
4-Storey	1789	445	24.87	1259	70.37	85	4.75
>5-Storey	361	1	0.27	113	31.30	247	68.4

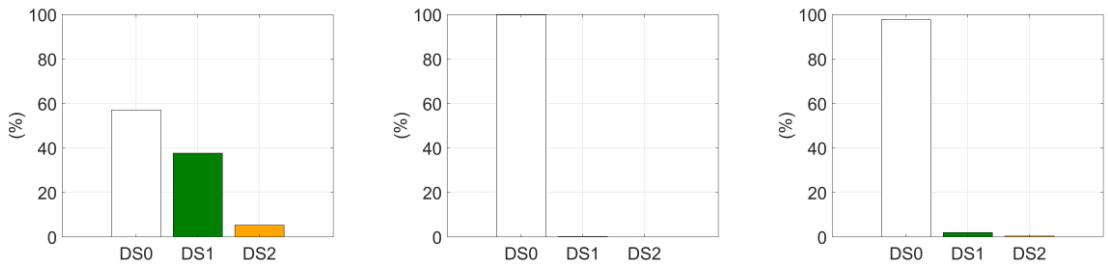

(a) *(b)* *(c)*

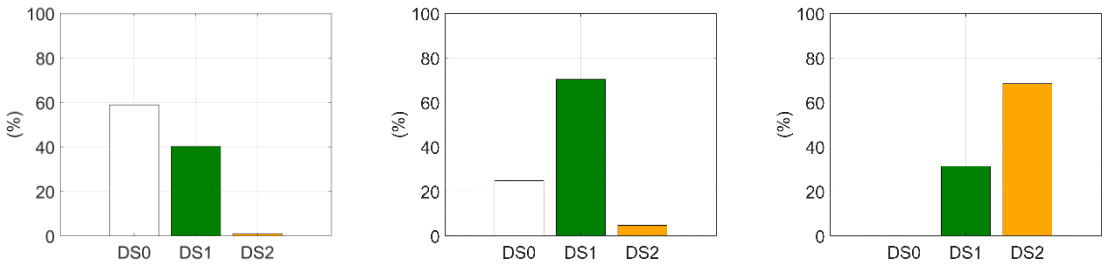

(d) *(e)* *(f)*

Figure 4. 16: Distribution of damage for (a) total data set, (b) 1-storey Buildings, (c) 2-storey Buildings, (d) 3-storey Buildings and (e) 4-storey Buildings, (f) 5+ storey Buildings obtained from the deterministic version of the FAST method.

Comparing Table 4.10 and Table 4.11 for the >5-storeys class (i.e., 5-storeys or higher), FAST predicts that the number of buildings in DS1 is 113 and in DS2 is 247. This is greater than the actual numbers of 6 for DS1 and 1 for DS2. For 4-storey structures, the FAST method predicted 655 buildings for DS1 and 38 for DS2. This was an overestimate as the database had 31 buildings exceeding DS1 and 1 exceeding DS2. The FAST method tends to underestimate damage for a lower number of storeys as compared to the values for the 1-storey and 2-storey classes. This underestimation is because FAST cannot account for the differences in compliance with codes and good practices for a single-storey building compared to a multiple storey building. The latter trend has some counterparts in Mediterranean practice. It explains the general phenomenon that analytical approaches underestimate one-storey buildings' vulnerability and overestimate multiple-storey buildings (e.g., De Luca et al., 2017).

4.4.5 Fragility Curves FAST-Nepal

Fragility curves were obtained through Monte Carlo simulation with $\tau_{updated}$, IDR1, IDR2, IDR3, and α varying for each iteration of each building of the dataset. The Monte Carlo simulation ran 100 iterations for each building, and then the fragilities were obtained for DS1, DS2, and DS3. For each damage state, the mean (μ) and the mean plus and minus one standard deviation (σ) were obtained, as shown in Figure 4.17. In Figure 4.17d, the mean fragilities for the 3 damage states are represented together. The fragilities are compared with the PGA values for the May 12th (0.16 g) and April 25th (0.28 and 0.32g) Gorkha earthquakes (see Figure 4.13). The value of 0.28g for the April 25th earthquake is represented in Figure 4.17d. The results obtained account implicitly for the predominant design approach observed in Ward-35, and they reflect the differences in design as assumed in Section 4.4.2.

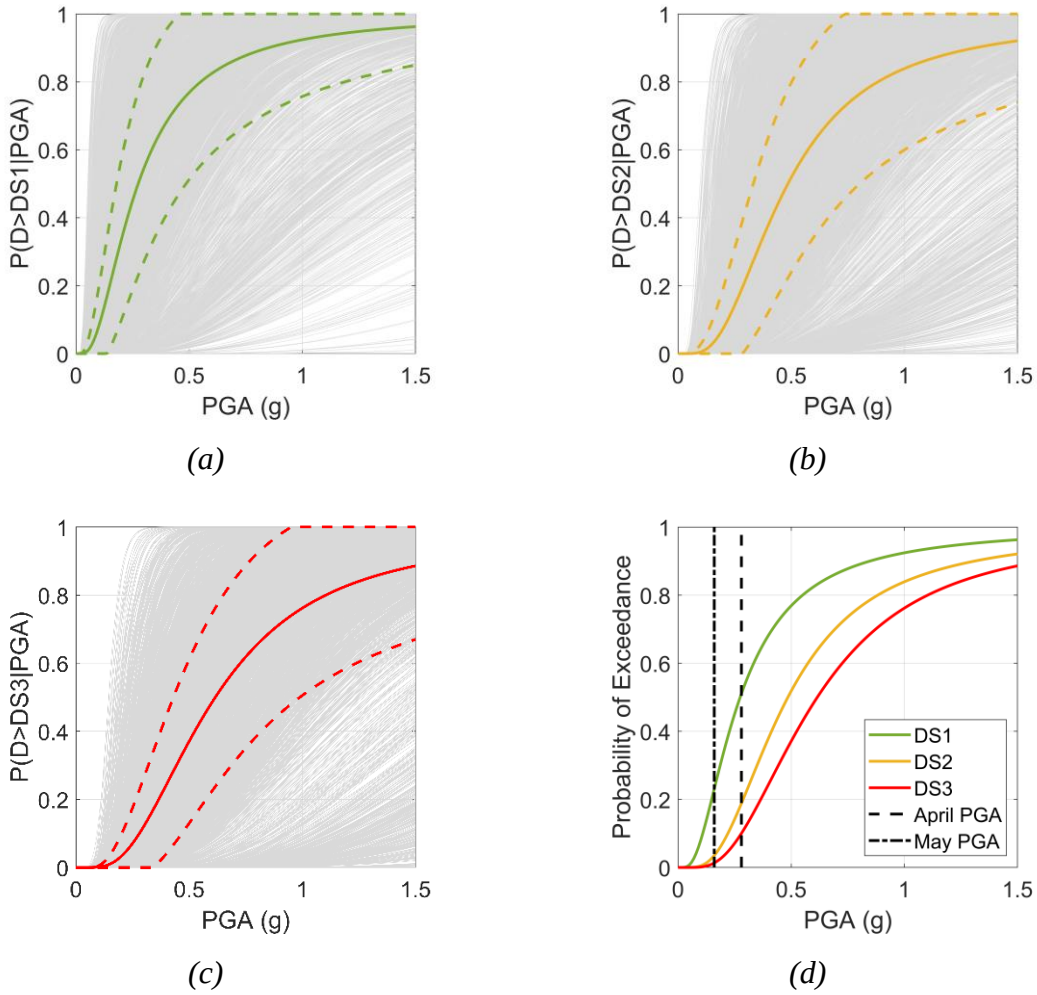

Figure 4. 17: Fragility curves for (a) DS1, (b) DS2, (c) DS3 associated with the buildings in the database presented in Section 4.4.2 and (d) the comparison of the mean of the class for all the three DSs compared with the maximum PGA as obtained from the shake maps in Figure 4.13

Recent PSHA studies carried out by Stevens et al. (2018) have shown Ward-35 to have a 475-year return period earthquake (10% probability in 50 years) of 0.64 g. This would lead to a 45% probability of exceeding DS3, a 60% probability of exceeding DS2, and an 80% probability of exceeding DS1. Due to the conservative nature of some of the assumptions of the FAST methodology, this can be considered a worst-case scenario. Still, it far exceeds the probability of exceedance thresholds set out in European regulations (Pinto et al., 2014). Such PSHA studies and the consequences suggested by these fragilities, if these events were to be realised, can bring into question the validity of having a design anchorage PGA value for Kathmandu of 0.35g (NBC 105, 2020).

4.5 Comparison of Ward-35

The fragility curves from the FAST methodology on Ward-35 can now be compared to other fragility curves. Figure 4.18 compares the fragility curves from the numerical assessment in Chapter 3 and the FAST results on Ward-35. It can be seen that the Ward-35 data has a significantly larger β value. This uncertainty in the FAST results can be attributed to the FAST method being applied to 100 varying iterations of 6869 buildings, and the results are then averaged. In contrast, the Pahar Trust analysis uses a detailed finite element model applied to various ground motions. It should also be noted that the two models do not use the same shear cracking (τ_{cr}) strength of masonry. The Pahar Trust model uses a significantly lower value. This results in the η value for the fragility curves of the Pahar Trust structure being lower than if the two studies had used the same τ_{cr} value.

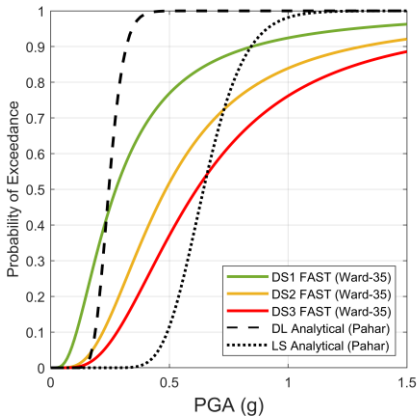

Figure 4. 18: Fragility curves for DS1, DS2 and DS3 using the Nepal FAST methodology on Ward-35 and DL and LS limit state using a detailed analytical approach in Chapter 3.

Giordano et al. (2021) presents fragility curves for Nepalese schools formed of RC frames with masonry infills. These fragility curves are derived from empirical data collected by the World Bank (2020) SIDA (Structural Integrity and Damage Assessment) project. This dataset contained the damage data of 17,595 schools after the Gorkha 2015 earthquake. Figure 4.19 compares the Giordano et al. (2021) fragility curves and the fragility curves from Section 4.4. It can be seen that both of the sets of fragility curves have a relatively high β value. This is likely because both fragility curves have been derived from a varying building catalogue. We can see that the fragility curves from Giordano et al. (2021) indicate a higher probability of exceeding DS2 and DS3 at all PGA values (i.e. more fragile). There are a number of reasons the Giordano et al. (2020) results may show higher levels of fragility. As the Giordano results are based on buildings all over Nepal, there may not be as code-conforming buildings as Ward-35. Furthermore, many of the buildings in Ward-35 are relatively new, with 56% of buildings

being built since 1994. This means they are more likely to have been designed to a more modern code.

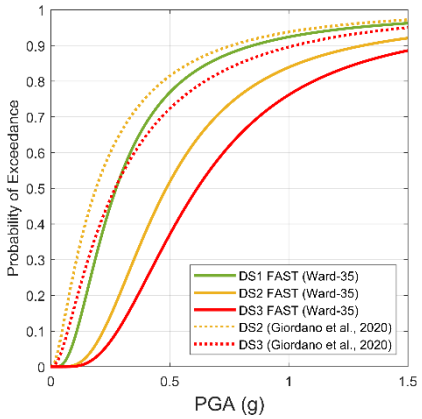

Figure 4. 19: Fragility curves for DS1, DS2 and DS3 using the Nepal FAST method on Ward-35 and DS2 and DS3 from Giordano et al. (2021)

Chaulagain et al. (2016a) carried out a non-linear analysis on a finite element model of a building. Further details of this study can be found in Section 4.2.2. In Figure 4.20a, the fragility curves of these non-engineered structures are compared to the pre-94 fragilities from the FAST analysis in Section 4.4.5. The assumption can be made that as NBC 105 (1994) was not released until 1994, the buildings built before this were not code compliant. Figure 4.20a shows that the FAST-Nepal method closely matches DS3 and extensive damage in Chaulagain et al. (2016a). It can be seen that the FAST method predicts the buildings to be significantly less likely to exceed moderate damage (i.e. DS2) compared to Chaulagain et al. (2016a). Chaulagain et al. (2016a) also provide the fragility curve for the collapse limit state. As expected, this limit state requires a significantly higher PGA to exceed DS3 from the FAST-Nepal method.

Figure 4.20b shows the comparison of the FAST-Nepal results from buildings constructed between 1994 and 2010 and Chaulagain et al. (2016a) NBC structure. The NBC building is specified as one designed according to NBC 105 (1994). It can be seen that relative to the Chaulagain et al. (2016a) results, FAST-Nepal underestimates the fragility for the moderate damage limit state (i.e. DS2) and overestimates the fragility for the extensive damage limit state (i.e. DS3).

Finally, the comparison is made for the post-2010 case, as shown in Figure 4.20c. Chaulagain et al. (2016a) specify the final category of building to be NBC+, which relates to the building being designed to NBC 105 (1994) and UNDP (2010). This is the same assumption specified in Section 4.4.3 for the post-2010 buildings. It can also be seen that FAST-Nepal

underestimates the fragility for the moderate damage limit state (i.e., DS2) and overestimates the fragility for the extensive damage limit state (i.e. DS3), as was the case with the 1994 to 2010 case.

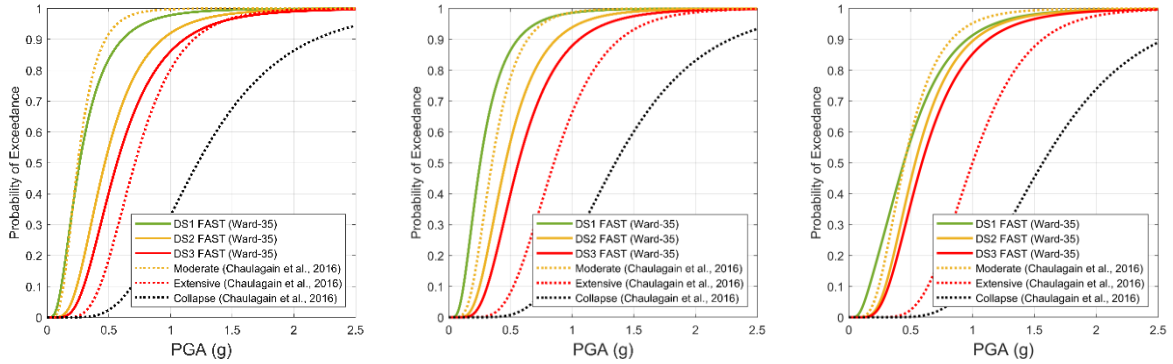

(a) (b) (c)

Figure 4. 20: Fragility curves for DS1, DS2 and DS3 using the Nepal FAST methodology on Ward-35 and moderate, extensive, and collapse from Chaulagain et al. (2016a) for (a) Pre-94 structures, (b) 94-10 structures, (c) Post-10 structures

4.6 Conclusions

The spectral-based FAST method is modified for the regional case of Nepal. A comparison is then carried out using numerical fragilities from Chapter 3. Damage data relating to reinforced concrete infilled buildings in Ward-35 of Kathmandu was used as a testbed to make a first validation of the method. Damage data from Ward-35 is not the best possible benchmark for the Nepal version of FAST. The data collection was not carried out immediately after the event as it was carried out for census purposes. Hence, further benchmark literature comparisons were carried out. However, the database still provides a preliminary insight into the methodology's accuracy for its application in Nepal.

The FAST method has previously been calibrated for European seismic events using direct damage comparison with field data in the cases of Lorca 2011 (De Luca et al., 2014), Emilia 2012 (Manfredi et al. 2014) and Central Italy 2016 (De Luca et al., 2017) earthquakes and in terms of fragility curves for the case of L'Aquila 2009 earthquake (De Luca et al., 2015). Compared to other spectral-based analytical approaches for vulnerability estimation, it has the main advantage of using several parameters calibrated from experimental data to account for the buildings' regional characteristics. The analysis can be performed quickly, avoiding any finite element modelling of the structure or building class.

In this study, the FAST methodology was modified for the Nepalese case using localised data of the shear cracking strength (τ_{cr}) and updating the prior log-normal distribution to get an updated distribution for τ_{cr}. The IDR for DS1, DS2 and DS3 were updated based on Cardone and Perrone's (2015) data. The available ductility (μ_s) was updated using analytical pushover analyses on Nepalese RC with masonry infill buildings from Chaulagain (2016b), with the assigned μ_s value varying based on the age of the building (and therefore likelihood of it being considered as engineered). Finally, the RC frame's relative contribution to the lateral resistance at the peak lateral load (α) was updated using recent work on the relationship between τ_{cr} and α (Scala et al., 2020).

The Nepalese version of the FAST method was applied to a 2-storey RC with infill building from Chapter 3. The modified parameters listed above were used except for $\tau_{cr,}$ where the value from Chapter 3 was used to allow a like-for-like comparison. The results showed a strong level of matching (0.248 g and 0.245 g) between the damage-limitation limit state and DS2, which both represent the point at which the masonry infills degrade. At the life-safety limit state, it was shown that the FAST methodology was considerably more conservative than the numerical fragilities. This can be expected due to the conservative assumptions made throughout the FAST method.

The Nepalese version of the FAST methodology was then applied to the building database for Ward-35 of Kathmandu. Although the FAST method accurately captured the dominance of DS0, it still overestimated the level of damage relative to the observed level from the database. This could be due to the FAST methodology's conservative nature but could also be due to the data being collected by Genesis Ltd (2016) for the Nepalese government months after the 2015 earthquake for census purposes. Some of the more heavily damaged buildings could have been repaired by that point. The FAST method overestimated the level of damage for one and two-storey structures. This is a common occurrence for analytical approaches (De Luca et al., 2017) and can be attributed to smaller buildings being less likely to be code conforming.

Finally, the fragility curves derived using the FAST method on the Ward-35 building database were compared to fragility curves from literature. The first comparison was against empirical fragility curves from Giordana et al. (2020). These fragility curves were derived from damage data on over 17,000 RC with infill schools from across Nepal. The results showed that the fragility curves from the FAST method found the buildings to be more robust relative to the empirical fragilities. There are several possible reasons for this, including the age and,

therefore, the construction quality of the buildings in Ward-35. The ward-35 fragilities were then compared to numerical fragilities from Chaulagain et al. (2016a). The fragilities were split up based on which code they were designed to. The ward-35 buildings were therefore split up dependent on which code they were likely designed to, based on the age of construction. The FAST method underestimated the fragility relative to the numerical fragility. This is likely due to conservative assumptions, such as when a building is designed to a code, it is designed to the lowest permissible capacity.

The FAST method is an established vulnerability evaluation method used for the rapid assessment of building stock to assess RC buildings' vulnerability with masonry infills. After modifying some of the parameters to make it more suitable for the Nepalese context, it was validified with analytical fragilities and collected damage data. These comparisons showed that the methodology was generally conservative relative to the collected and analytical data but was generally more accurate a capturing low-level damage. The findings of this study imply that the building stock in Ward-35 of Kathmandu would experience significant structural damage in the event of a large earthquake.

Chapter 5: Numerical-experimental validation of modelling strategy of irregular stone masonry

---

Part of this chapter is based on the following reference:

Cross T, De Luca F, De Risi R, Camata G, and Petraca M, (2022) Micro-modelling of stone masonry template buildings as a strategy for seismic risk assessment in developing countries. *Currently under Review*[1]

This chapter aims to validate the application of masonry micro-modelling for the case of irregular stone masonry with mud mortar. Irregular stone masonry with mud-mortar is the most frequently used construction technique, with 43% of Nepalese buildings being formed of mud-bonded masonry, as shown in Figure 2.1. This is achieved by first considering previous studies which have applied this method to regular brick masonry with cement mortar. A continuous micro-model of a set of regular brick masonry piers will be used to verify that the micro-model has a shear response similar to previous studies (Magenes et al., 2020). The material properties of the brick unit will then be updated for the case of stone using properties from CNR-DT 212/2013 (2014). The shear capacity of these piers will then be compared to those calculated using a code-based approach (CNR-DT 212/2013., 2014). A comparison of irregular masonry pier capacities will then be carried out using a micro-model, analytical code-based model and experimental results from Senaldi et al. (2018). This will be carried out on a squat and slender pier. A comparison of the effect of a regularisation process will be carried out for the case of irregular stone masonry to assess the effect of irregular geometry on the shear capacity. The objectives of this chapter are as follows:

- Review current uses of continuous micro-modelling to model the capacity of masonry piers and structures.
- Develop a continuous micro-model of a regular masonry pier and ensure the shear response matches previous studies (Magenes et al., 2020).

[1] The first authors contribution included: methodology, data curation, analysis , data visualisation and writing. Co-authors reviewed and supervised the work

- Update models from current literature for the case of stone blocks with cement mortar and validate these using a code-based analytical assessment method (CNR-DT 212/2013., 2014)
- Validate masonry micro-modelling for the case of stone irregular masonry with cement mortar. This is validated by comparing the masonry micro-model with analytical models (CNR-DT 212/2013., 2014) and using experimental work from Senaldi et al. (2018).
- Investigate the effect of using an equivalent regular masonry approximation to evaluate the importance of replicating the irregular geometry for an irregular masonry wall. This will be done by comparing the shear capacity of the two numerical models and the experimental results.

5.1 Background of masonry modelling

Due to the non-linear response of masonry and high levels of residual damage, modelling masonry can be a highly complex process. The use of performance-based design has significantly increased the demand for accurate masonry models for use in static pushover analysis and non-linear dynamic analysis. The heterogeneous nature of masonry results in extensive material properties being required for both the mortar and the unit to model the masonry accurately. Furthermore, information about the arrangement of these materials is necessary to model the masonry accurately.

Modelling techniques for masonry can be largely separated into three categories. These are detailed micro-modelling, simplified micro-modelling and macro-modelling (Angelillo et al., 2014). Micro-modelling considers the geometry and material properties of the units and the mortar and uses constitutive laws to assess the response of the masonry. This is the most computationally demanding modelling technique but gives the most accurate results when correctly applied. Micro-modelling can be further separated into detailed and simplified micro-models where detailed micro-models consider the mortar brick interface explicitly. This is shown in Figure 5.1. Macro-modelling considers masonry as a homogeneous material, where the material properties can be found from experimental tests on wallettes of that masonry typology.

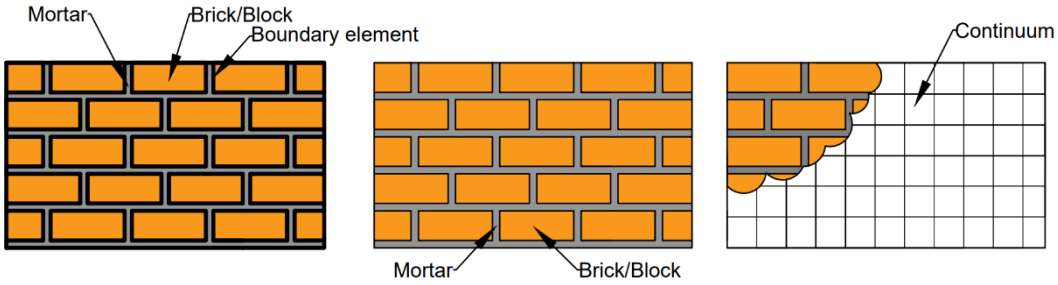

Figure 5. 1: Modelling techniques for masonry walls (a) detailed micro-modelling (b) simplified micro-model (c) macro-model (Cross et al., 2021) (Inspired by Figure from Lourenço, (1996))

Simplified micro-modelling, also called meso-modelling, was first developed by Page (1978), who proposed a finite element (FE) model where elastic brick elements were separated by linkage elements that simulated the mortar joints. These linkage elements were assumed to have a very high compressive strength with non-linear deformation characteristics, low tensile strength and shear strength dependent on the bond strength and the amount of compression. The material properties for this model could be obtained through a uniaxial test on the brick and a masonry panel. This model was further improved by Lotfi and Shing (1994) to simulate the initiation and propagation of interface fractures (cracks). This was achieved through a dilatant interface constitutive model. Snyman and Martin (1992) first proposed a dilatant interface model to model discontinuities leading to interface fractures. This model also accounts for histories of opening, closing and sliding of the fractures. Micro-modells can be split up into continuous micro-models and mesoscale masonry models. Mesoscale models typically represent the stone or brick as an elastic material, and the non-linearity is concentrated in boundary elements between the brick elements (Macorini et al., 2013). Continuous micro-models have now been developed such that both the mortar and the brick follow and tension/compression damage model. Further details on how this is implemented can be found in Section 2.6.3.2. This damage model requires input parameters shown in Table 5.1. These material properties can be found by carrying out material tests on the constituent parts of masonry. The material tests for mortar and brick/stone are typically less extensive and require less heavy machinery relative to material tests of masonry wallettes. Further details on the material tests can be found in Section 2.4.1.

Table 5. 1 Parameters required for tension/compression damage model for masonry constituents

Material Property	**Symbol**
Young's modulus	E

Tensile strength	f_t
Tensile fracture energy	G_t
Compressive elastic limit	f_{c0}
Compressive peak strength	f_{cp}
Compressive residual strength	f_{cr}
Compressive strain at peak strength	e_p
Compressive fracture energy	G_c

Since the development of this tension/compression damage model (Petracca et al., 2017), it has been applied numerous times in literature (Abdulla et al., 2017; Siano et al., 2018). It has typically been used for regular brick masonry, and therefore a series of comparisons must be carried out to validate it for irregular stone. These comparisons will be carried out using experimental results (Senaldi et al., 2018) and code-based analytical capacities (CNR-DT 212/2013., 2014).

5.2 Comparison of the Analytical and Numerical Capacity of a Regular Brick and Stone Masonry Pier

5.2.1 Regular Brick Masonry Pier

An initial comparison of a standard brick masonry pier with cement mortar is carried out. These specific piers have been modelled in literature with several different modelling approaches using various software (Magenes et al., 2020). The three piers all act as a cantilever with no constraints at the top. The horizontal and vertical load is applied to the top as a line load. Table 5.2 shows the geometry of these piers. The comparison is carried out for brick masonry with cement mortar, despite the fact it has been carried out previously, to verify that the finite element model responds similarly to previous studies.

Table 5. 2. The geometry of three piers used for initial validation of masonry micro-modelling with regular brick masonry

	Specimen 1 (Square)	Specimen 2 (Slender)	Specimen 6 (Squat)
Height (m)	2.5	2.5	2.5
Length (m)	2.5	1.25	5
Depth (m)	0.5	0.5	0.5

The masonry micro-model is implemented using STKO. STKO (Scientific Toolkit for Opensees) is a GUI for opensees which generates input files for opensees allowing the creation of complex geometries, making it particularly suitable for masonry structures. STKO also implements paralisation technologies to allow large opensees models to be implemented over multiple processors, dramatically decreasing runtime. STKO also improves the model's efficiency using a bespoke recorder, allowing improved methods to inspect results before simulations are completed. An initial comparison is carried out on a two-dimensional (2D) vs three-dimensional (3D) model to confirm that a 3D model is not required for this initial validation. The response of the 3D model is identical to the 2D model, so a 2D model is used for this section to save on computational demand. The masonry pier is fixed in both rotation and displacement at the bottom. The top level has an equal degree of freedom for all degrees to replicate typical experimental setups. As there is no fixed restraint at the top level, the shear height is taken as the height of the pier for the analytical approach. Both the brick and mortar are implemented to the finite element (FE) model using the quad element and DamageTC3D (Petracca et al., 2017), further details on this material can be found in Section 2.4.3.2. The material properties used are given in Table 5.3, taken from (Magenes et al., 2020). An implicit/explicit (also referred to as implex) integration scheme is used for the non-linear constitutive model (Oliver et al., 2008). The implicit/explicit integration method has been shown to significantly reduce the run time for the continuous micro-modelling of masonry (Petracca et al., 2021). Unlike the discrete element method (DEM), continuous micro-modelling does not provide a provision for element detachment, such as frictional effects once detachment has occurred. Interface elements are not used in continuous micro-modelling but have been implemented in the discrete element method, which account for frictional sliding (Lemos, 2007).

Table 5. 3 Material properties used for the first stage of micro-modelling validation. Taken from (Magenes et al., 2020)

	Brick	Mortar
Young's Modulus (GPa)	5	0.35
Poisson's Ratio	0.15	0.15
Tensile strength (MPa)	1.00	0.085
Tensile fracture energy (N/mm)	0.08	0.015

Compressive elastic limit (MPa)	0.8	0.8
Peak compressive strength (MPa)	2.67	2.67
Residual compressive strength (MPa)	0.1	0.1
Strain at peak strength	0.01	0.03
Compressive fracture energy (N/mm)	0.6	10

The initial check is carried out to ensure that the single brick masonry pier has a capacity similar to the shear capacity calculated from a code-based approach. The flexural capacity of the pier is calculated using the analytical code-based method given in CNR-DT 212/2013. (2014) and shown in Equation 5.1. V_{pf} is the flexural shear capacity, calculated from the ultimate moment capacity (M_{pf}) and the shear height (h'). As this pier has no constraints at the top, the shear height is taken to be equal to the height of the pier. M_{pf} can be calculated in Equation 5.2, where l and t are the pier's length and thickness, respectively, σ_0 is the average normal compressive stress given by Equation 5.3 where N is the vertical load, and f_m is the average compressive strength of the masonry. This analytical approach is carried out with normal vertical stress values ranging from 0% to 100% of the compressive strength for each pier detailed in Table 5.2. In Equation 5.2 the 0.85 is a stress block approximation first derived for an RC beam in flexure (Whitney, 1937) and is applied to masonry piers in structural codes such as CNR-DT 212/2013. (2014) and section 7.8.2.2.1 in NTC-2018 (MIT, 2018).

$$V_{pf} = \frac{M_{pf}}{h'} \tag{5.1}$$

$$M_{pf} = 0.5 l^2 t \sigma_o \left(1 - \frac{\sigma_o}{0.85 f_m}\right) \tag{5.2}$$

$$\sigma_o = \frac{N}{lt} \tag{5.3}$$

The ultimate shear capacity is calculated using Equation 5.4 from CNR-DT 212/2013. (2014) for the case of "*irregular masonry or when, even in the presence of regular texture, the blocks*

are weaker than the mortar". In Equation 5.4, f_t is the tensile strength of the mortar and τ_0 is the shear strength under no compressive load. b is given by Equation 5.5.

$$V_t = lt\frac{1.5\tau_0}{b}\sqrt{1+\frac{\sigma_0}{1.5\tau_0}} = lt\frac{f_t}{b}\sqrt{1+\frac{\sigma_0}{f_t}} \tag{5.4}$$

$$b = \frac{h}{l} \tag{5.5}$$

For the case of the regular brick masonry piers detailed in Table 5.2, the shear height is equal to the height of the pier. The compressive strength of the masonry is taken from CNR-DT 212/2013. (2014).

These formulations are used to find the shear capacity relative to the vertical load and are shown in Figures 5.2b, 5.2d, and 5.2f for the square, slender and squat piers, respectively. These figures show the analytical flexural capacity with and without the stress block approximation implemented by the codes. A pushover is then carried out on the three numerical models with a range of vertical loads. These pushover curves can be seen in Figures 5.2a, 5.2c, and 5.2e. The peak shear capacities from the numerical models are plotted in Figures 5.2b, 5.2d, and 5.2f. It can be seen from the pushover curves that the greater the vertical load, the lower the displacement at failure. It also shows that the greater the vertical load, the lower the initial stiffness. The square pier shown in Figure 5.2b has a robust matching between the numerical and analytical capacities. The numerical results sit between the V_{Flex} with the stress block approximation and the V_{flex} without the stress block approximation. The numerical model of the slender pier (specimen 2) (Figure 5.2d) also has a substantial degree of matching with the analytical model. The squat pier (specimen #6) (Figure 5.2f) successfully shows that due to the shear failure mechanism being activated, the capacity is significantly below the analytical V_{flex}, however, it does not entirely reduce to the level of the analytical shear capacity (V_{shear}).

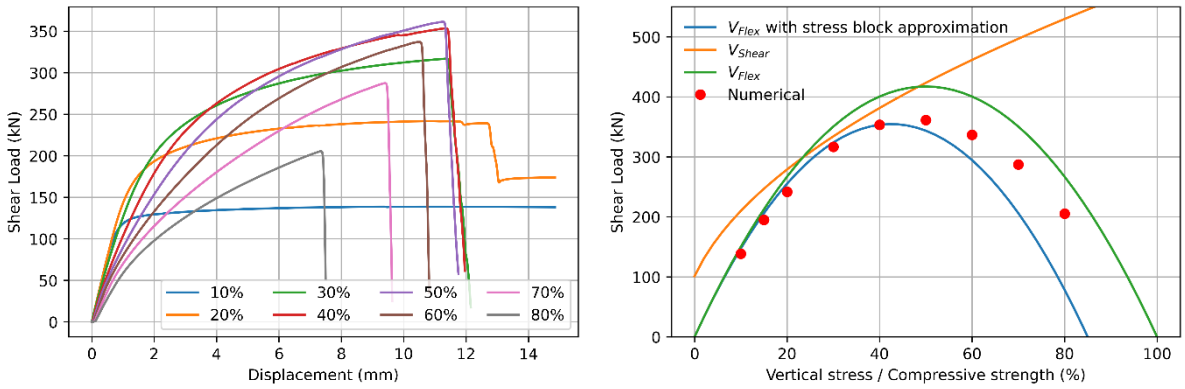

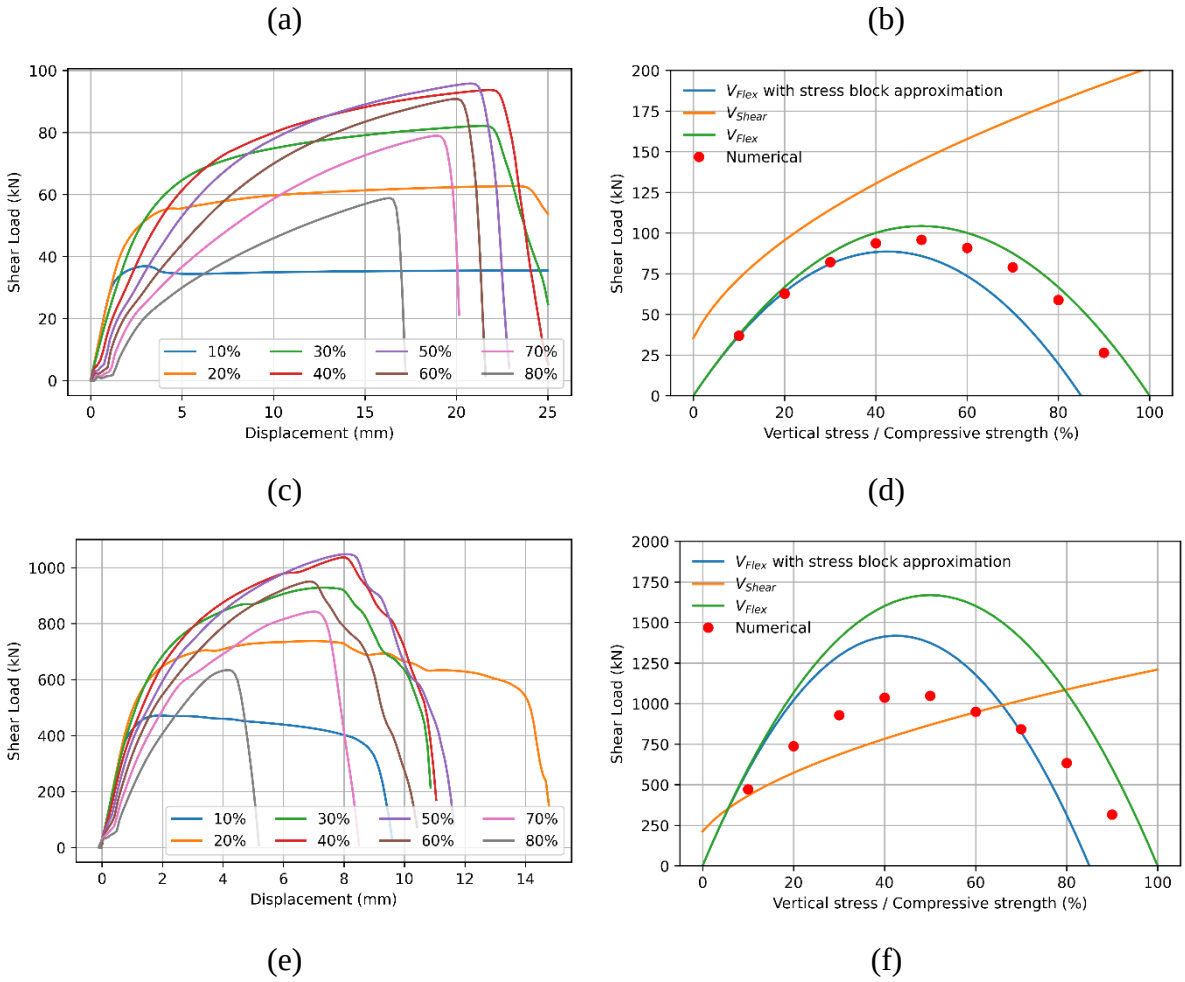

Figure 5. 2: (a) SPO of square pier with varying vertical compression ratios. (b) Numerical and analytical capacities for square pier. (c) SPO of slender pier with varying vertical compression ratios. (d) Numerical and analytical capacities for slender pier. (e) SPO of squat pier with varying vertical compression ratios. (f) Numerical and analytical capacities for squat pier.

The material damage can indicate the cracking pattern and hence can be used to identify the failure mechanism. Further information on the material damage parameter can be found in Section 2.4.3.2. Figure 5.3a shows that damage profiles for the square wall with a vertical stress equal to 10% of the compressive strength. It can be seen the failure mechanism is flexural for the specimen, with the vertical load equal to 10% of the compressive strength. This is indicated by tensile cracking at the bottom left corner of the pier and compressive crushing at the right corner of the pier, and the rest of the pier acting as a rigid body. Figure 5.3b shows the damage pattern for the same panel with the vertical stress equal to 60% of the compressive strength. It can be seen the pier undergoes significantly more diagonal shear cracks. This failure mechanism is typically a property of the geometry, loading and boundary conditions, with more squat piers more likely to exhibit diagonal shear cracking failure. A fixed condition at the top level will reduce the pier's shear height and make a diagonal shear failure mechanism more likely. In a situation where both shear and flexural failure occur simultaneously, this is called

hybrid failure. Figure 5.3c shows specimen #2 (slender) with a vertical stress equal to 10% of the compressive strength. It can be seen that this is a nearly purely flexural failure with minimal diagonal shear cracking. Figure 5.3d shows specimen 2 with a vertical stress equal to 38% of the compressive strength. It shows the failure mechanism is still flexural, but a small about of shear cracking has started in the compressive corner of the pier. Figure 5.3e shows a hybrid failure mechanism with roughly equal amounts of diagonal shear cracking and flexural shear cracking, however, in Figure 5.3f, when the vertical stress is increased to 38% of the compressive strength, diagonal shear cracks dominate the failure mechanism.

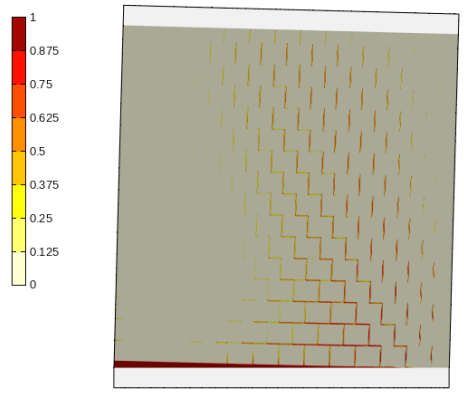

(a)

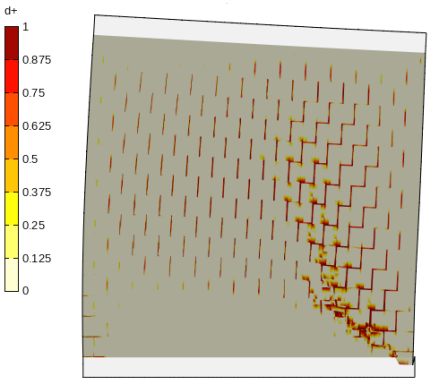

(b)

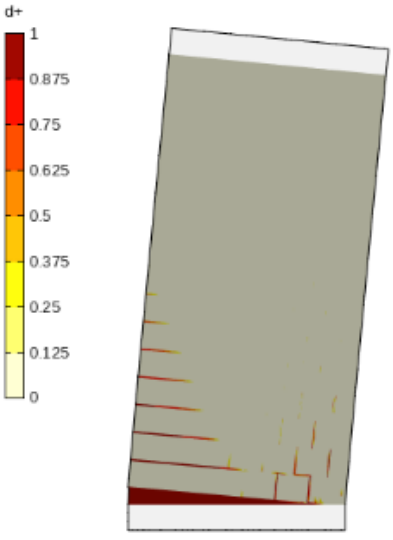

(c)

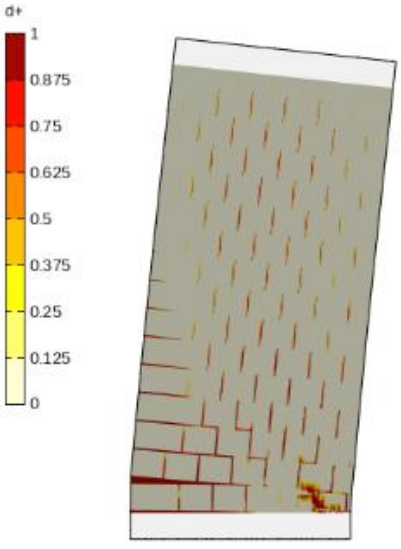

(d)

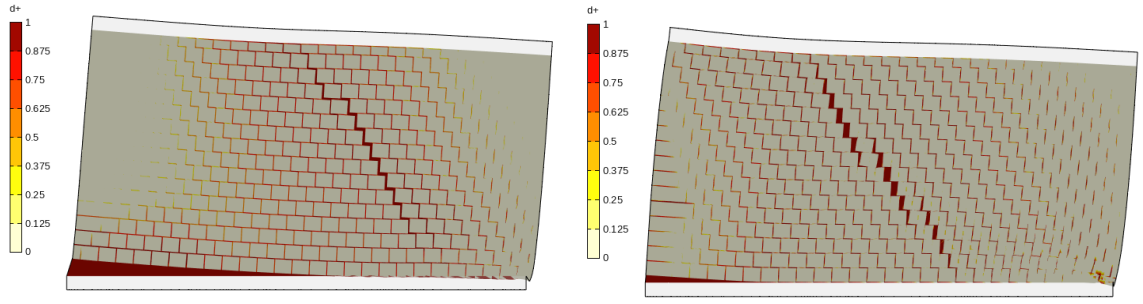

(e) *(f)*

Figure 5. 3: Damage patterns for (a) Specimen #1 with a vertical stress of 10% of the compressive strength, (b) Specimen #1 with a vertical stress of 60% of the compressive strength, (c) Specimen #2 with a vertical load of 10% of the compressive strength, (d) Specimen #2 with a vertical load of 38% of the compressive strength, (e) Specimen #6 with a vertical load of 10% of the compressive strength. (f) Specimen #6 with a vertical stress equal to 38% of the compressive strength

This validation of the brick masonry pier ensures the FE model responds similarly to previous studies (Magenes et al., 2020). This validation of the implementation is carried out using the results from Magenes et al. (2020), who also used STKO and got results the same as the model presented in this study. It also ensures that the numerical model correctly captures the piers shear capacity and identifies the failure mechanism accurately.

5.2.2 Regular Stone Masonry Pier

The material properties of the brick are modified using stone parameters from CNR-DT 212/2013. (2014). The same verification is carried out. This allows the verification that a regular stone wall with cement mortar has a similar capacity when assessed using the continuous micro-model and a code-based analytical approach. The stone properties were taken for the "*squared stone masonry*" from CNR-DT 212/2013. (2014). This gave a compressive strength of masonry of 700 N/mm^2 and shear strength of 0.105 N/mm^2. Therefore, the f_t will be 0.1575 N/mm^2 using Equation 5.6 from CNR-DT 212/2013. (2014). The same SPO analysis was completed using the material properties shown in Table 5.4 for the piers detailed in Table 5.2.

$$f_t = 1.5\tau_0 \tag{5.6}$$

Table 5. 4 Material properties used for validation of micro-modelling of regular stone masonry with cement mortar

	Stone	Mortar
Young's Modulus (GPa)	15	0.35
Poisson's Ratio	0.15	0.15

Tensile strength (MPa)	3.00	0.1575
Tensile fracture energy (N/mm)	0.08	0.015
Compressive elastic limit (MPa)	0.8	0.8
Peak compressive strength (MPa)	7.00	7.00
Residual compressive strength (MPa)	0.1	0.1
Strain at peak strength	0.01	0.03
Compressive fracture energy (N/mm)	1.8	10

Figures 5.4a, 5.4c and 5.4e show the pushover response for the three piers detailed in Table 5.2. Figures 5.4b, 5.4d and 5.4f show how the peak shear capacities compare to those calculated using CNR-DT 212/2013. (2014). As with the regular brick masonry, there is a close matching in the shear capacity of the pier with a varied vertical load. When the failure mechanism is dominated by a flexural failure, according to the analytical calculation, the numerical capacity typically lies between the V_{flex} line and the V_{flex} *with stress block approximation* line, as shown in Figure 5.4. Although the reduction in capacity caused by the V_{shear} line is captured, the numerical model does not fully capture the shear failure, and the failure mechanism shows a hybrid failure mechanism.

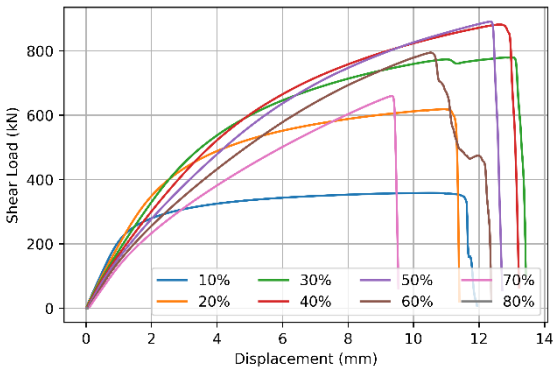

(a)

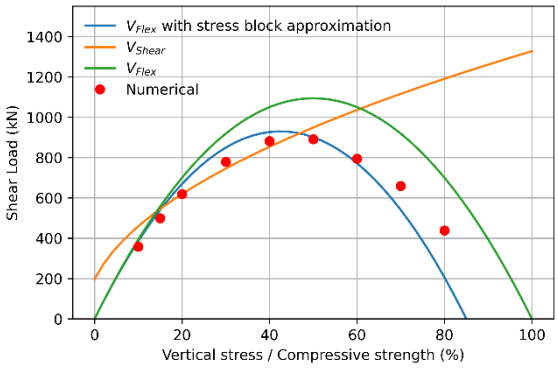

(b)

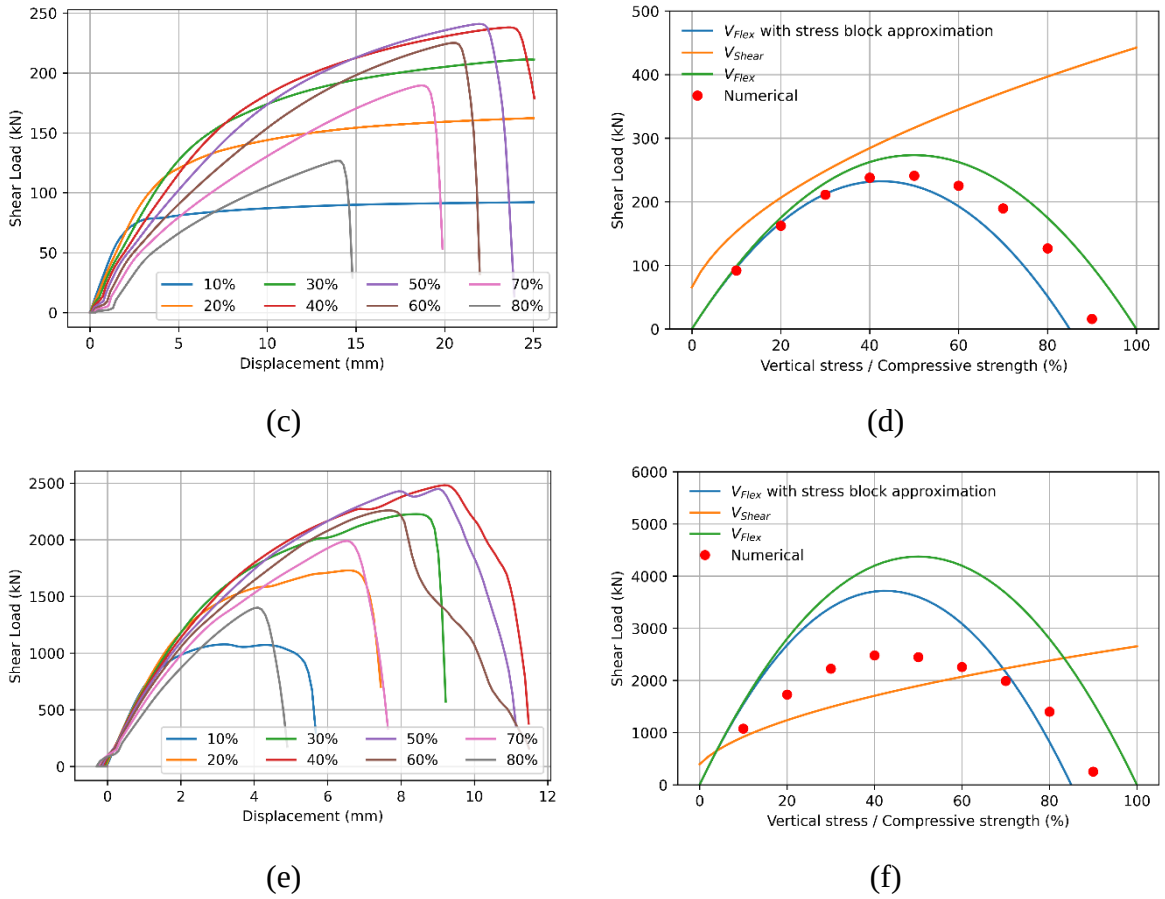

Figure 5. 4: (a) SPO of stone square pier with varying vertical compression ratios. (b) Numerical and analytical capacities for stone square pier. (c) SPO of slender stone pier with varying vertical compression ratios. (d) Numerical and analytical capacities for slender stone pier. (e) SPO of squat stone pier with varying vertical compression ratios. (f) Numerical and analytical capacities for squat stone pier.

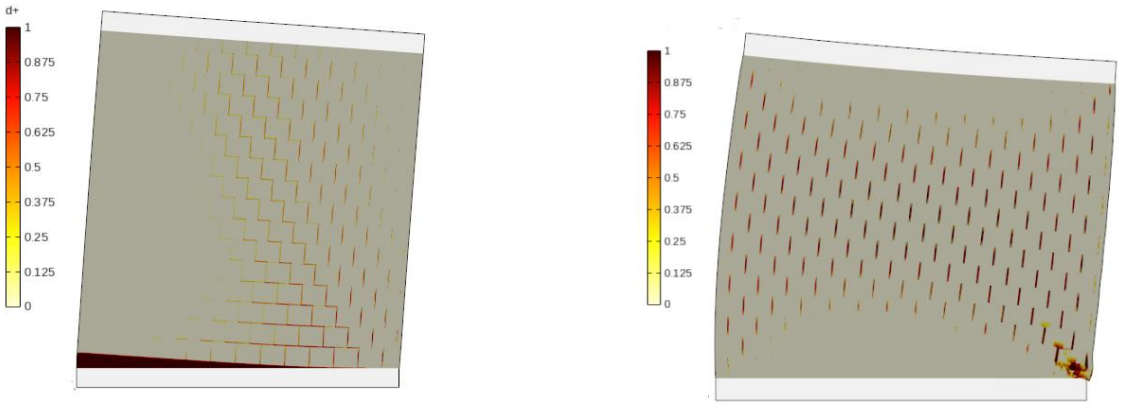

(a) *(b)*

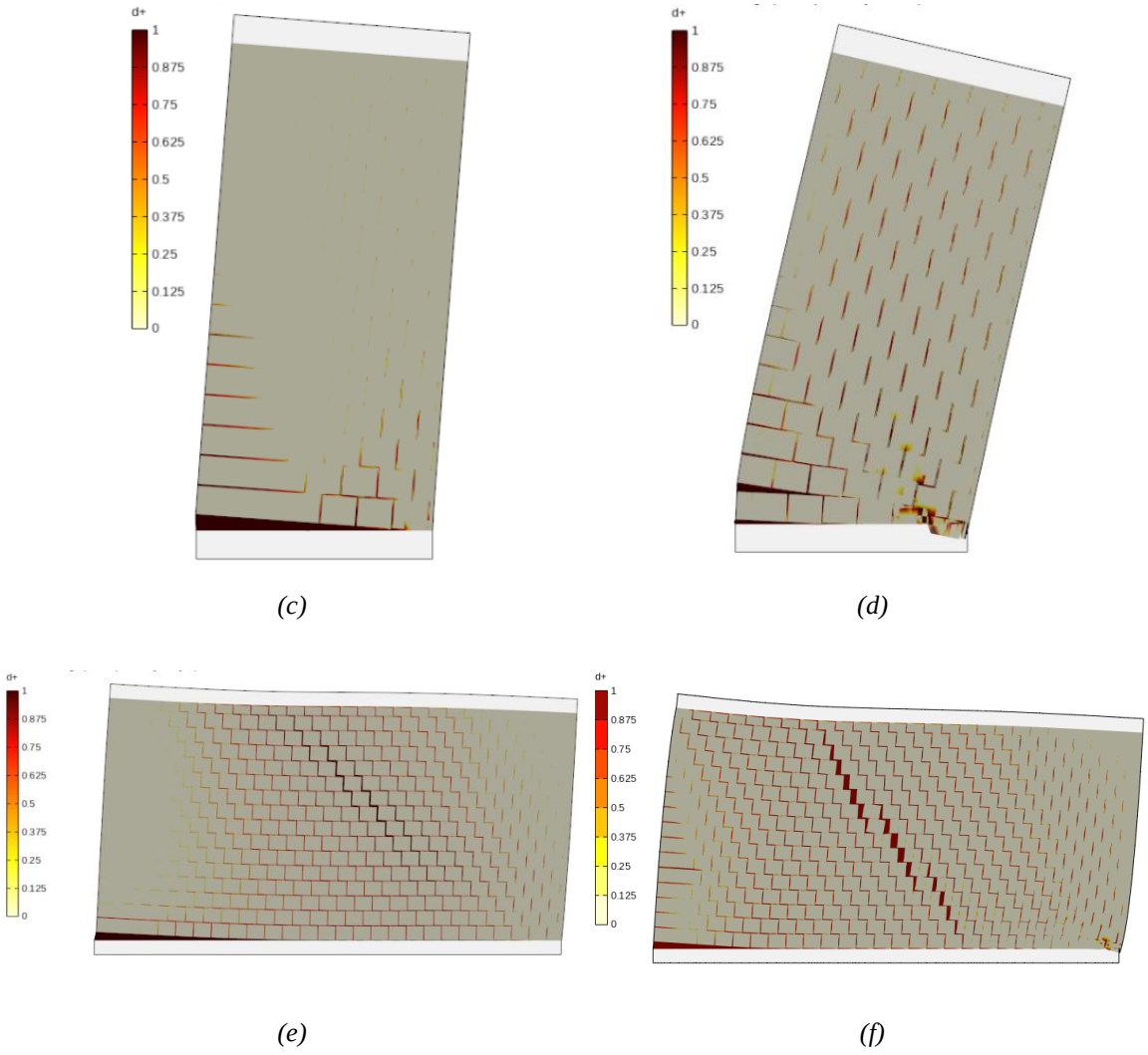

Figure 5. 5: Damage patterns for (a) Specimen 1 with a vertical compression ratio (VCR) of 10%, (b) Specimen 1 with a VCR of 60%, (c) Specimen 2 with a VCR of 10%, (d) Specimen 2 with a VCR of 40% of the compressive strength, (e) Specimen 6 with a VCR of 10%, (f) Specimen 6 with a VCR of 40%

The cracking pattern can be observed using the material damage as with the brick piers. It can be seen in Figure 5.5a that, as with the brick masonry wall, at low levels of vertical compression, the failure mechanism is almost purely flexural. Figure 5.5b shows that when the vertical compression is increased to 40% of the compressive strength, the failure mechanism is a shear flexural hybrid, as indicated by the diagonal shear cracks and the tensile cracking in the bottom left corner. Figure 5.5c shows that the slender pier exhibits a predominantly flexural failure under low vertical load and a hybrid failure when the vertical compression ratio increases to 40%, as shown in Figure 5.5d. Finally, it can be seen in Figures 5.5e and 5.5f that the squat wall shows diagonal shear cracks at both 10% and 40%, as expected based on the analytical approach.

This section has reproduced the numerical SPO results for a regular masonry wall from Magenes et al. (2020). This showed the continuous micro-model has a shear response that corresponded to previous studies. The material properties were modified to correspond to values given by CNR-DT 212/2013. (2014). The analytical capacity was found using the equations provided by CNR-DT 212/2013. (2014). This showed the continuous micro-modelling of a regular stone masonry wall accurately captured the peak shear resistance of the piers. The damage patterns were then used to show that the micro-model correctly identified the failure mechanism of the piers.

5.3 Comparison of the Numerical, Analytical and Experimental Capacity of an Irregular Stone Masonry Pier

5.3.1 Experimental Campaign

Experimental tests on masonry piers are used to validate this modelling technique. A similar approach was carried out by Malomo et al. (2019), where the pushover response and failure mechanism were compared to experimental results for a squat and slender pier. The experimental campaign used for this study was carried out by Senaldi et al. (2018) at the University of Pavia, to investigate the seismic risk to natural stone buildings in Basel, Switzerland. A series of four pseudo-static cyclic pushover tests were carried out on irregular stone masonry piers. Two of the piers were squat, and two were slender. Key details of the piers are given in Table 5.5. Two hydraulic actuators were used to induce a vertical load. Details of the vertical load for each of the piers are shown in Table 5.5. Once the required vertical load had been achieved, a fixed rotation was maintained using hybrid control of the vertical actuators, whereby they would maintain a constant combined axial load, and the two actuators would have a displacement that was equal to each other (hence fixed rotation). With a fixed vertical load, a cyclic pseudo-static horizontal load is applied with the pattern shown in Figure 5.6. These cyclic displacements are applied until completion or until the specimen fails. The peak displacement in each of the four piers is shown in Table 5.5. The four piers were formed of irregular stone masonry with cement mortar. A 10 mm layer of hydraulic lime plaster followed by 5 mm of non-hydraulic lime plaster was applied to one side of the wall to allow the cracking pattern to be clearly observed.

Table 5. 5: Geometry, loading and peak displacement of experimental tests carried out by Senaldi et al. (2018)

		CT01	**CT02**	**CS01**	**CS02**
		Squat	Squat	Slender	Slender
Dimensions (mm)	Length	1150	1150	600	600
	Height	1450	1450	1800	1800
	Depth	300	300	300	300
Vertical loading		σ/f_c=0.3 f_c=1.3 N/mm^2 σ=0.39 N/mm^2 UDL = 117 N/mm	σ/f_c=0.2 f_c=1.3 N/mm^2 σ=0.26 N/mm^2 UDL = 78 N/mm	σ/f_c=0.3 f_c=1.3 N/mm^2 σ=0.39 N/mm^2 UDL = 117 N/mm	σ/f_c=0.45 f_c=1.3 N/mm^2 σ=0.585 N/mm^2 UDL = 175.5 N/mm
Peak displacement		θ_{max}=1.75% 25.4 mm	θ_{max}=3% 43.5 mm	θ_{max}=5% 90 mm	θ_{max}=3% 54 mm

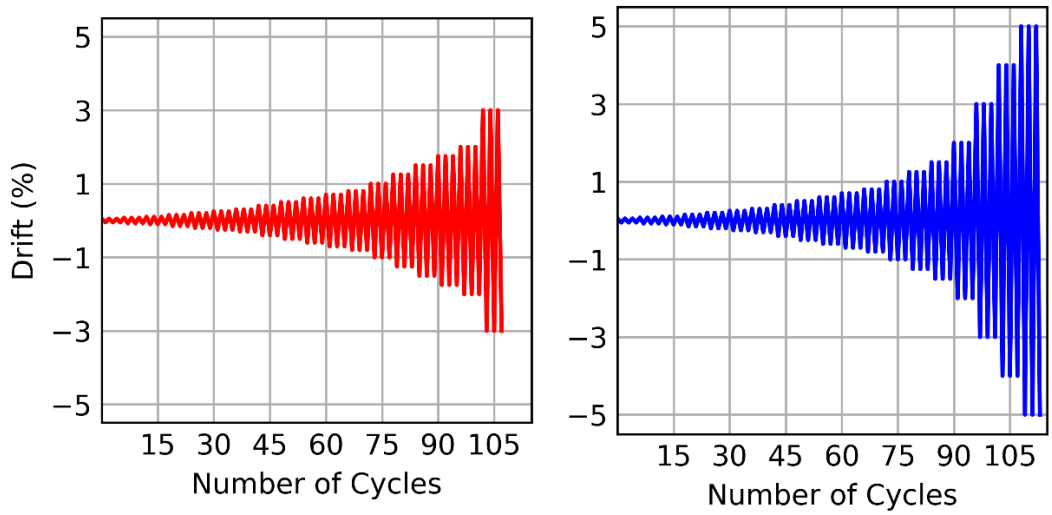

(a) *(b)*

Figure 5. 6 Lateral displacement applied to the (a) Squat piers (CT01 and CT02) (b) Slender piers (CS01 and CS02),(adapted from Senaldi et al. (2018))

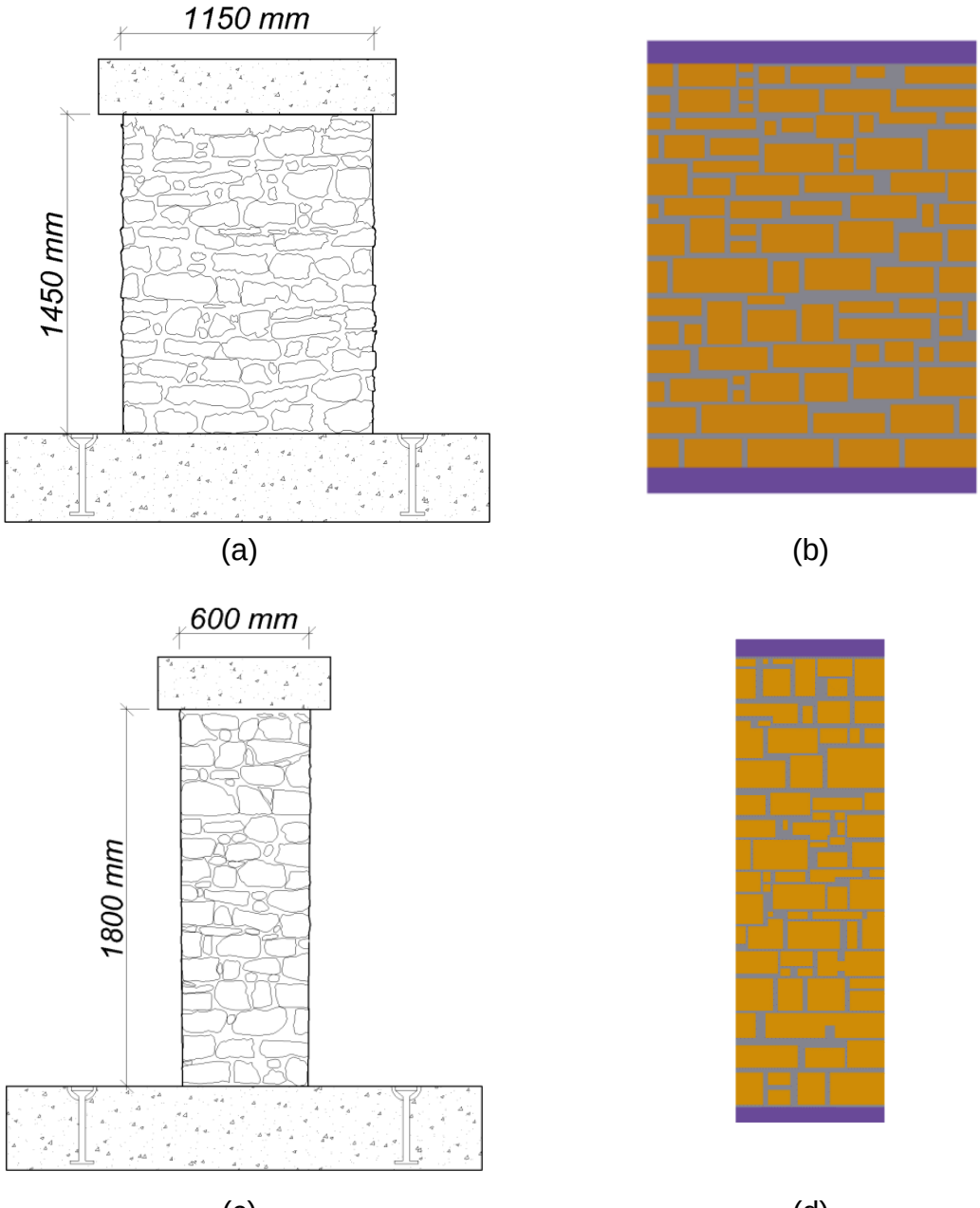

Figure 5. 7 (a) Experimental setup of irregular stone masonry squat pier (Senaldi et al., 2018) (b) Continuous micro-model of squat pier (c) Experimental setup of irregular stone masonry slender pier (Senaldi et al., 2018) (b) Continuous micro-model of slender pier

The key material properties required for the analytical calculation of the shear capacity of a masonry pier are the compressive strength of mortar (f_m) and the tensile strength of mortar (f_t). These values are obtained from a series of 44 tests on mortar prisms (Guerrini et al., 2017) taken as part of the same experimental campaign as the pushover of the piers.

Each mortar sample was split into three prisms, each measuring 160 mm x 40 mm x 40 mm. A three-point flexural bending test was carried out on each of the samples. The supports were positioned 120mm apart, and the load was applied at the mid-point. The tensile strength of the mortar was then found using Equation 5.7, where $F_{max,i}$ is the peak vertical load of the i^{th}

sample, and W_i is the elastic section modulus of the ith sample. The average of the three prisms from each mortar sample are taken. The results of the 44 mortar samples are shown in Figure 5.8a. The mean value is 0.6, with a coefficient of variation of 23%. It should be noted that this tensile strength is significantly higher than what is typically found in mortar. CNR-DT 212/2013. (2014) gives tensile mortar values ranging from 0.039 MPa to 0.525 MPa. It should be noted that these values are mean values however CNR-DT 212/2013. (2014) does provide a standard deviation. For the assessment of capacity, the mean value is used however, a characteristic value is typically used for design purposes.

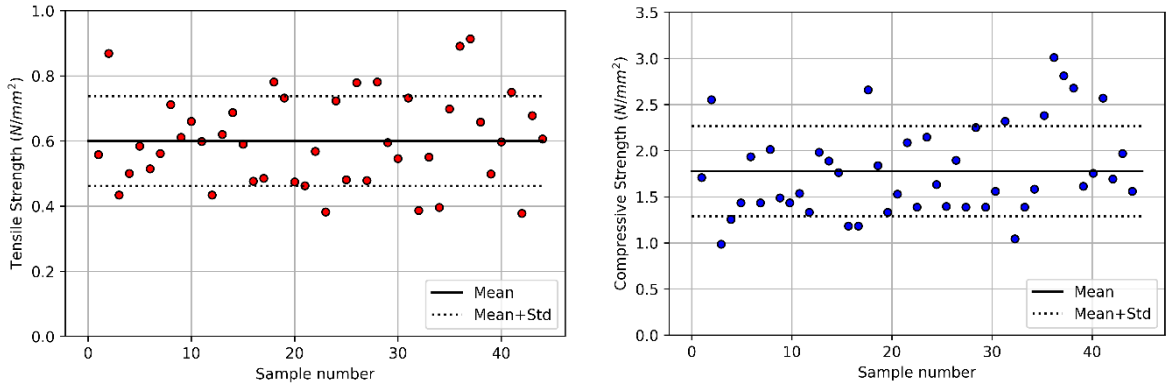

(a) *(b)*

Figure 5. 8 Results of (a) tension and (b) compression tests of mortar prisms (recreated using data from Guerrini et al., 2017)

$$f_{mt} = \frac{1}{3}\sum_{i=1}^{3}\frac{F_{max,i}\ell}{4W_i} \tag{5.7}$$

The compression tests are carried out on the remaining mortar stubs from the flexural tests. 264 mortar prisms are tested, each with a 40 mm x 40 mm cross-sectional area. Each of the 44 mortar specimens has 6 sub-samples, and they are tested under compression with the peak vertical resistance being recorded. The average of the six sub-samples is used as the compressive strength of that sample. The results of the compression tests are shown in Figure 5.8b, where the average is 1.75 N/mm^2, and the coefficient of variation is 28%. This compressive strength lies inside the expected values from literature which range from 1.4 MPa to 7 MPa (CNR-DT 212/2013., 2014).

The two irregular masonry piers from Senaldi et al. (2018) are developed into detailed masonry micro-models as outlined for the regular masonry in Section 5.2. Note that all stones must be converted to an appropriate equivalent quadrilateral, and the dimensions must be rounded to the nearest 10 mm to allow a constant mesh of 10 mm x 10 mm. A fixed rotation condition is

applied to the top level of the pier to replicate the condition applied to the experimental work. The pushover is carried out with a vertical stress ranging from 0.13 MPa to 0.65 MPa. Although a cyclic analysis is carried out in the experimental work, a SPO is carried out on the numerical model to find the peak strength for comparison with the analytical approach. Once the vertical loading has been applied, a constant vertical load is maintained.

The analytical code-based approach in Section 5.2 is applied to these piers where the f_m value is 1.75 MPa, f_t is 0.6 MPa, and t is 300 mm. The analytical capacities are shown in Figure 5.9a and Figure 5.9b for the squat and slender pier. It should be noted that the V_{shear} is not shown on the figure as the values are significantly higher than the flexural values and, therefore not relevant for this comparison. The analytical capacity is shown with and without the stress block approximation. Further details on this can be found in Section 5.2.

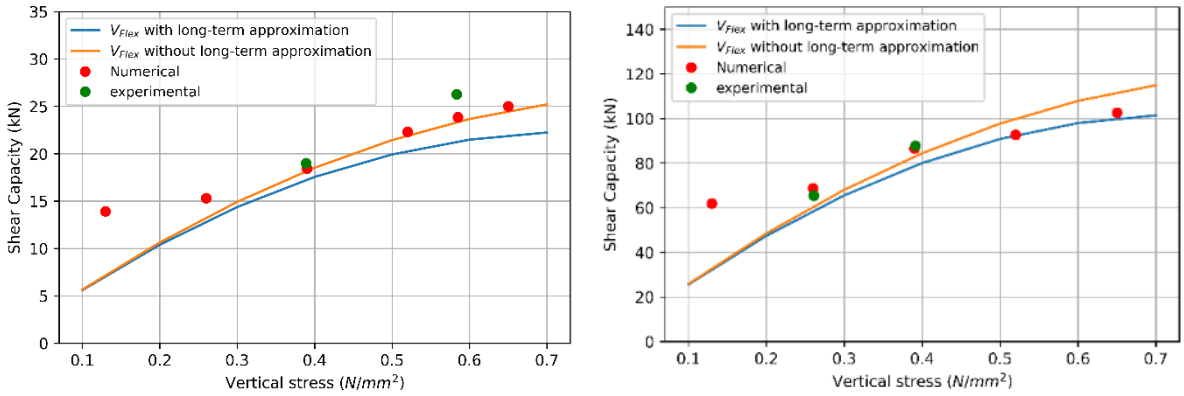

(a) *(b)*

Figure 5. 9: The shear capacities of the experimental, numerical and analytical model for the (a) slender (CS01 and CS02) and (b) squat piers (CT01 and CT02)

It can be seen in Figure 5.9 that there is a strong level of matching between the numerical, analytical and experimental shear capacities. The numerical model over estimates the shear capacity relative to the analytic at low vertical loads. The analytical assumes no tensile strength in the mortar, whereas the numerical model assumes a tensile strength of 0.6 MPa. It can be seen that for the slender pier, the numerical model strongly agrees with the analytical model however the experimental lies slightly higher. The experimental has a shear capacity that is 3.1% higher than the numerical at a vertical load of 0.39 MPa (CS01). The experimental shear capacity is 11.6% higher than the numerical at a vertical load of 0.58 MPa (CS02). The comparisons are shown in Table 5.6. For the slender piers (CT), there is a very close matching between the experimental and numerical. For the slender pier with a vertical load of 0.26 MPa (CT02) the experimental is 2.7% higher than the numerical. For the slender pier with a vertical

load of 0.39 MPa (CT01) the experimental is 5.7% lower than the numerical. It should be noted that the close matching the micro-modelling and the analytical approach brings into question the necessity of micro-modelling. The analytical expression does not have the provision for a flexible roof structure and the interaction between masonry walls and RC bands. These details are explained further in Sections 6.2.3 and 6.2.4.

Table 5. 6 Analytical, numerical and experimental shear capacities of masonry piers detailed in Senaldi et al. (2018)

	Analytical shear capacity (CNR-DT 212/2013., 2014) (kN)	Numerical shear capacity (kN)	Experimental (Senaldi et al., 2018) shear capacity (kN)
CT01 (Squat)	82.9	86.5	89
CT02 (Squat)	60.8	68.7	65
CS01 (Slender)	18.2	18.4	19
CS02 (Slender)	23.3	23.8	27

In the experimental campaign conducted by Senaldi et al. (2018), a 10 mm layer of hydraulic lime plaster was overlaid with 5 mm of non-hydraulic lime plaster. This allowed the observation of the cracking pattern, as shown in Figures 5.9a and 5.9c. Figure 5 shows the numerical and experimental cracking pattern for CT01 and CS01 specimens in Senaldi et al.'s campaign. CT01 is chosen for comparison as this is the only experimental specimen to display diagonal shear cracking. It can be seen from Figure 5.10 that the numerical model accurately captures the diagonal shear cracks. The experimental specimen shows diagonal cracks in both directions due to the cyclic load applied. Figures 5.10c and 5.10d show the experimental and numerical cracking for CS01. The numerical model of CS01 accurately captures the flexural failure mechanism of the slender column. Based on the correct identification of the shear capacity and failure mechanism for these four irregular stone masonry piers, the continuous element micro-modelling has been validified against Senaldi et al.'s experimental results for the case of irregular stone masonry. CS02 and CT02 both indicated hybrid failure mechanisms where slight diagonal shear cracks are evident, but the failure mechanism is dominated by a flexural failure mechanism.

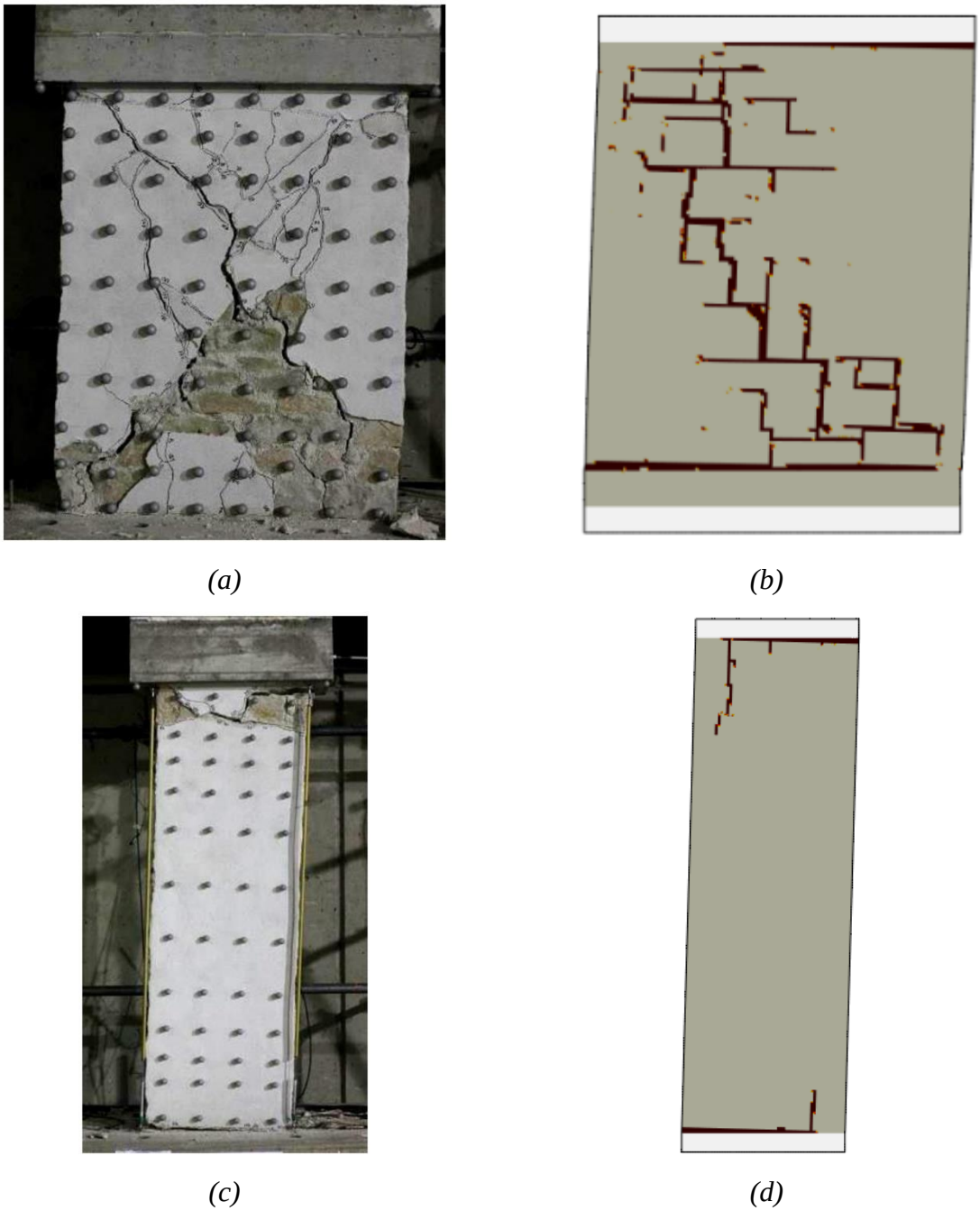

(a) *(b)*

(c) *(d)*

Figure 5. 10: Cracking pattern for (a) CT01 (experimental) (b) CT01 (numerical) (c) CS01 (experimental) (d) CS01 (numerical) (experimental figures have been obtained from Senaldi et al. (2018))

This section has used analytical and experimental results to validate the continuous micro-modelling for the case of irregular stone masonry. Experimental work carried out by Senaldi et al. (2018) was used as a benchmark case. A numerical model was created using the approximate dimensions of the experimental piers. An SPO analysis was carried out on the slender and squat pier for a range of vertical loads. The analytical shear capacity was calculated using CNR-DT 212/2013. (2014). The numerical and analytical models used material

properties from Guerrini et al. (2017), who carried out material testing as part of the same experimental campaign as Senaldi et al. (2018). The results showed good matching between the analytical and numerical results however, the numerical shear capacity values at low compressive strength were higher in the numerical approach as the analytical approach does not consider the tensile strength of mortar. The experimental peak shear values closely matched the numerical results, with the shear capacity for CS02 being 11% higher than the numerical value. This is likely due to the natural variability in masonry, and this level of discrepancy is considered acceptable in a material with such a great variation.

The cyclic pushover is carried out for the irregular continuous micro-model to allow a visual comparison with the experimental cyclic response. As the raw data is not provided by Senaldi et al. (2018) it is not possible to overlay the data. Figure 5.11a shows the experimental cyclic pushover of CS01 with the envelope indicated in red and Figure 5.11b shows the numerical cyclic pushover with the envelope shown in red. It can be seen that there is a close matching between the two envelopes however the experimental setup indicated a significantly higher level of plasticity with respect to the numerical model. It should be noted that the cyclic pushover is not taken to 5% for the numerical model due to convergence issued however it can be seen that the drift exceeds 1% drift which is typically beyond code-based drift capacity for masonry piers (CNR-DT 212/2013., 2014).

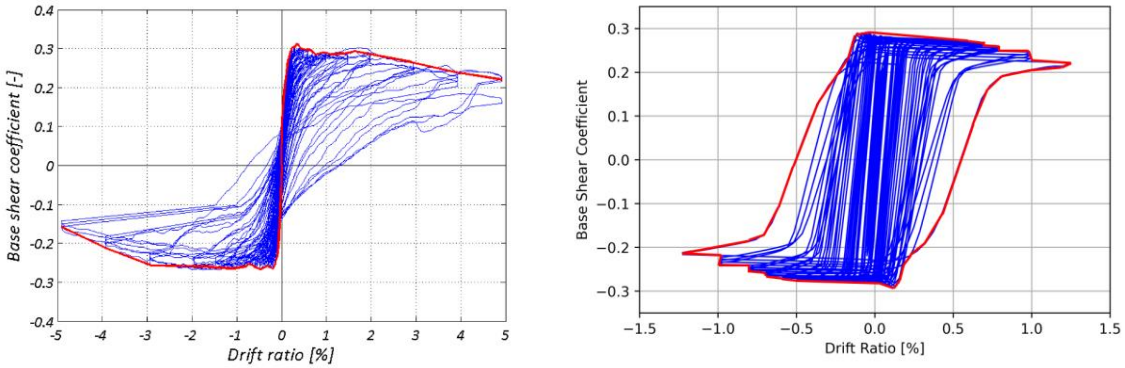

(a) (b)

Figure 5. 11 Comparison of the cyclic response of the slender pier (a) experimental results from Senaldi et al. (2018) (b) result from irregular continuous micro-model

5.4 Equivalent Regular Masonry Wall

The final part of the masonry modelling technique validation ensures that there is no significant difference in response between a regular and irregular masonry pier. Measuring every stone in

a building is not feasible, so an approximation must be made. A regularisation process is applied to the irregular masonry to create an equivalent regular masonry which has:

1. Similar mortar to stone ratio
2. Similar average size stone
3. Similar average mortar thickness

The regularisation method was applied by taking measurements from a diagram of the irregular masonry pier. These dimensions were then used to find the average mortar thickness, average stone size and stone-to-mortar ratio. There is the potential to automate the laborious task using image processing technology, as demonstrated by Ibrahim et al. (2020).

A micro-model of the two piers from Senaldi et al. (2018) is approximated using the three criteria above to evaluate the effect of using an equivalent regular wall. A summary of the three regularisation criteria is given in Table 5.7. It can be seen that the difference between regular and irregular are kept below 10% for all three of the requirements. Figure 5.12 shows the difference in the geometry between the regular and irregular masonry walls.

Table 5. 7 Summary of geometric characteristics of the irregular and equivalent regular masonry walls.

	Irregular wall	Regular wall	Difference
Mortar thickness	19.1 mm	17 mm	5%
Stone size	12003 mm^2	11833 mm^2	3%
Stone to mortar ratio	3.00	2.83	7%

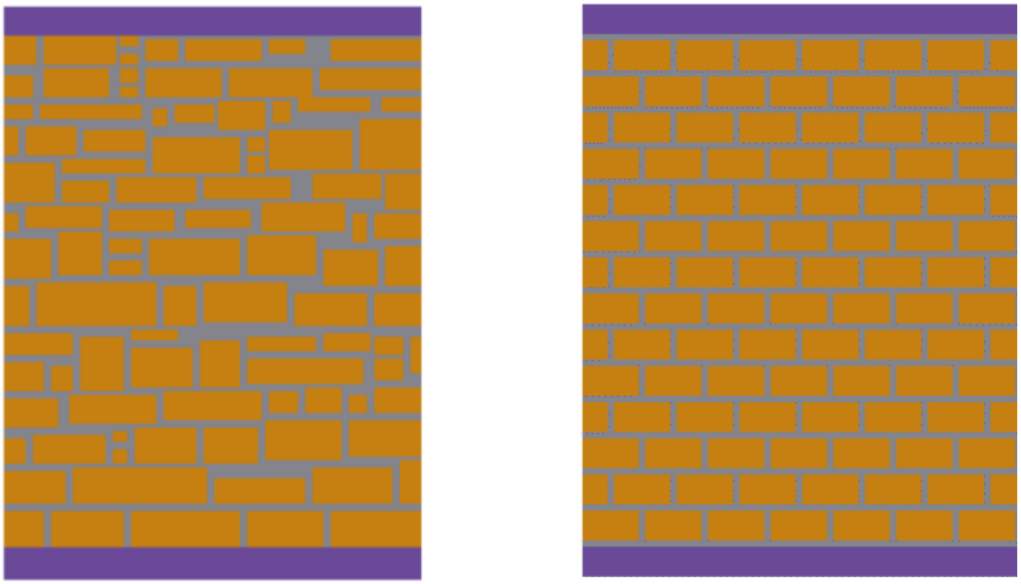

(a) (b)

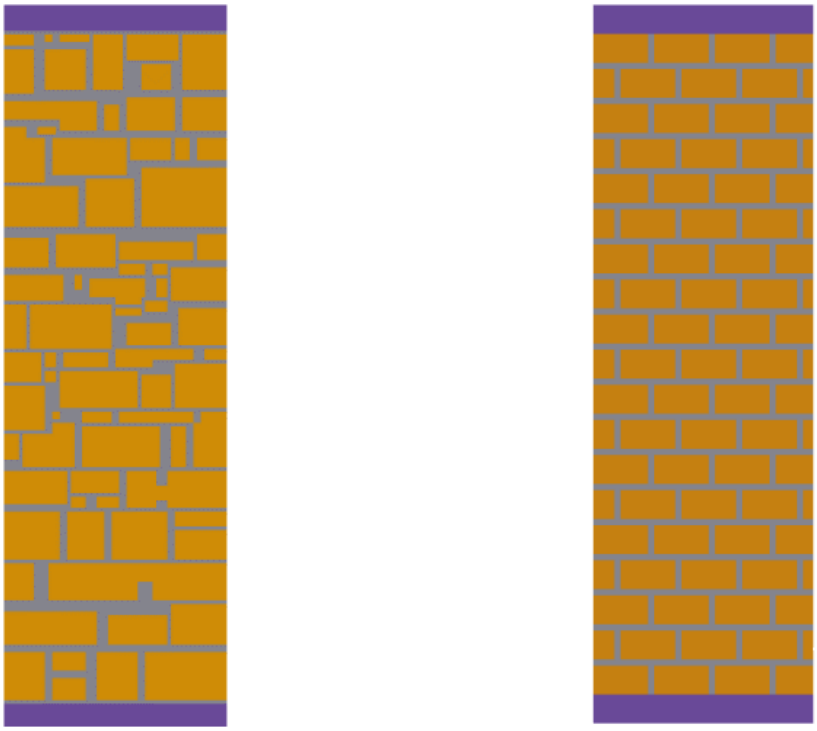

(c) (d)

Figure 5. 12 Differences in the masonry layout for the regular and irregular piers. (a) Squat Irregular (b) Squat Regular (c) Slender Irregular (d) Slender Regular

The material properties are kept constant between the regular and irregular piers. Figure 5.12 shows the pushover curves, and it can be seen that there is little difference. Figure 5.12 also shows the experimental curves from Senaldi et al. (2018). It can be seen that they typically have a closely matching peak shear strength. The initial stiffness is very similar for CT01 (squat pier with a high vertical loading). The peak shear resistance for the irregular pier is 3.9% higher than the regular pier. It can be seen in the irregular pier that there is a significant redistribution of stresses which does not occur in the regular pier. The irregular geometry can lead to a scenario where there is a more direct or less direct (dependant on the geometry) path for crack propagation. This can have an effect on stress redistribution. The tension/compression damage model applied to this model replicates the crack propagation using the tension and compression damage scalar indicated in Equation 2.33. This has been shown to capture the crack propagation for masonry accurately. The pushover for CT02 (squat pier with a low vertical loading) can be seen in Figure 5.12b. The equivalent regular model matches the initial stiffness. However, the equivalent regular model has a peak response that is 10.7% higher than the irregular model. For both slender piers (CS01 and CS02), the regular model has a slightly

higher elastic stiffness and a slightly higher peak shear capacity. The peak shear capacity for the regular model is 9.2% and 9.8% higher for CS01 and CS02, respectively.

The experimental curves show a relatively close matching level considering the inherent variability of masonry structures. It can be seen that in CT02, the peak response is relatively closely matched between the experimental and the numerical curves. The numerical model of CT01 does not accurately capture the loss of strength in the experimental model. The experimental model experienced a gradual loss of strength in contrast to the numerical model, which experienced a sudden loss in strength followed by a gradually increasing shear strength. CT02 and CS01 show exceptionally good matching throughout the pushover curve. CS02 generally shows good matching however the numerical results have lower initial stiffness.

Overall it can be seen that the regularisation process does not have a significant effect on the pushover response of an irregular masonry pier. The elastic stiffness remained unchanged for the squat pier and slightly reduced for the slender pier. In the squat pier, the peak shear resistance is slightly lower than in the regular model. This may be expected as the squat pier is more likely to exhibit diagonal shea cracks. The regular model provides a more direct crack path for the diagonal shear cracks in comparison to the irregular model. The slender piers failure mechanism is a flexural failure where the layer of mortar at the top and bottom fails (as shown in Figure 5.10). This failure mechanism is less affected by the irregularity of the stones as long as there is a layer of mortar at the bottom layer.

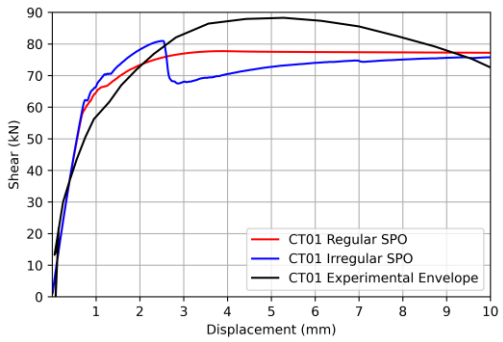

(a)

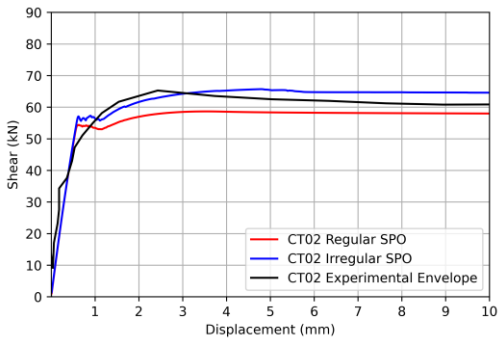

(b)

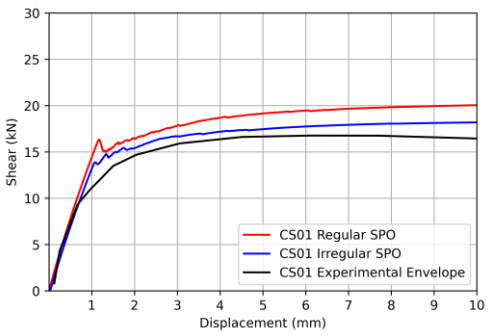

(c)

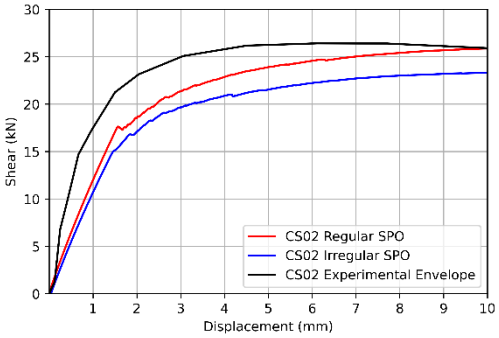

(d)

Figure 5. 13: Pushover of the regular and irregular masonry piers for (a) CT01 (b) CT02 (c) CS01 (d) CS02

5.5 Conclusions

This chapter aimed to validate the use of continuous micro-modelling for the case of irregular stone masonry with mud mortar using a combination of code-based analytical and experimental results. The initial stage of this verification was to ensure the continuous micro-modelling of brick masonry provided the same shear capacity as previous studies (Magenes et al., 2020). The material properties of the block were then updated using properties of stone masonry from CNR-DT 212/2013. (2014) to form a regular stone pier with cement mortar. The shear capacity of the numerical model was compared to the code-based analytical capacities calculated using CNR-DT 212/2013. (2014). The results showed that the numerical model accurately modelled the shear capacity when the failure mechanism was flexural. When the failure mechanism was shear, the numerical model overestimated the pier's lateral capacity, however it was significantly reduced relative to the flexural failure capacity. Using the material damage, we could observe the cracking pattern, which meant we could identify the failure mechanism. The numerical model correctly identified each piers' failure mechanism at a range of vertical compression ratios.

The next validation stage was to create a continuous micro-model of an irregular stone masonry pier and verify the capacity relative to code-based analytical and experimental capacity. Experimental work carried out by Senaldi et al. (2018) was used as a point of comparison. The geometry from Senaldi et al. (2018) was roughly turned into a series of quadrilaterals for the micro-model. The material properties used for the analytical and numerical model were taken from a series of material tests carried out by Guerrini et al. (2017) as part of the same experimental campaign as Senaldi et al. (2018). The code-based analytical approach from CNR-DT 212/2013. (2014) was used to find the pier's shear capacity. The results showed a

strong level of matching between the analytical, numerical and experimental. The material damage was then used to identify the cracking pattern. These were compared to the observed cracking patterns in the experimental campaign, and it could be seen there was a strong level of matching between the two.

Finally, a comparison was carried out on the necessity of accurately modelling the irregular geometry. A set of criteria were laid out for an equivalent regular wall. A continuous micro-model of an equivalent regular wall was developed, and the pushover response was compared to the irregular. The results of this showed a similar peak response and similar elastic modulus.

These verification steps have shown that using continuous micro-modelling for the case of irregular stone masonry accurately captures the pushover response, and it is not necessary to model all the irregularities in the wall, and instead, an equivalent regular geometry can be used.

Chapter 6: Seismic Risk Assessment for Masonry Health Centre

Part of this chapter is based on the following reference:

Cross T, De Luca F, De Risi R, Camata G, and Petraca M, (2022) Micro-modelling of stone masonry template buildings as a strategy for seismic risk assessment in developing countries. *Currently under Review* [1]

Objectives of this chapter

This chapter carries out a seismic risk assessment for a template health centre formed of unreinforced masonry with mud mortar. Continuous micro-modelling will be used to model the health centre, and a static pushover (SPO) analysis will be used to obtain the pushover curve. This pushover curve will then be used to derive an equivalent single degree of freedom (SDOF) system. Non-linear time history analysis will then be used for both the multiple degree of freedom (MDOF) and SDOF models. Using the results of these analyses, fragility curves will be obtained. These fragility curves will then be integrated with seismic hazard curves from Stevens et al. (2018) to find the mean annual frequency of exceeding a given limit state. Finally, the mean annual frequency values will be compared to values from literature and codes as a reference point.

The main objective of this chapter is to use the latest modelling methods to quantify the seismic risk to a template health centre. Pahar Trust provides the health centre design, and as it is a template structure, it could be recreated across Nepal. This research should quantify the seismic risk of using this design and inform Pahar Trust of the more appropriate locations to locate the health centre. By making a more informed decision on the use of this health centre, Pahar Trust will be making an active contribution to ensuring that Nepal's infrastructure is more resilient to future earthquakes. The main objectives of this chapter are as follows:

[1] The first authors contribution included: methodology, data curation, analysis , data visualisation and writing. Co-authors reviewed and supervised the work

- Develop a detailed continuous micro-model of Pahar trust masonry health centre, using the modelling approach detailed in Chapter 5, accounting for the masonry, RC bands, and timber roof.
- Use the SPO analysis to derive an equivalent SDOF model of the building.
- Carry out NLTHA using 74 different ground motions. Incremental dynamic analysis is carried out on the SDOF model, and a cloud analysis is carried out on the MDOF model.
- Compare the fragility curves from the cloud analysis on the MDOF system and the IDA on the SDOF to draw conclusions on the necessity of using the MDOF given the increased computational demand.
- Benchmark the fragility curves against six different sets of fragility curves from literature.
- Integrate the fragility curve with hazard curves from Stevens et al. (2018) to find the seismic risk to the structure at all points across Nepal. These risk values are then compared to benchmark values from codes and literature.

6.1 Introduction

Unreinforced stone masonry with mud mortar is one of Nepal's most common building materials due to its relative abundance of materials and ease of construction. This typically consists of locally-sourced boulders, rubble stone or semi-dressed stone and the mortar is commonly formed of mud. This building typology does not usually perform well seismically, as demonstrated by the fact most damaged and collapsed buildings after the 2015 Gorkha earthquake were formed of stone masonry with mud mortar (Bothara et al. 2016). In Nepal, more recently, in rural contexts, a nominal amount of reinforcement is added to stone masonry in horizontal reinforced concrete (RC) bands, as shown in Figure 6.1 (Schildkamp et al., 2021). Further details on these reinforced concrete bands can be found in Section 2.2.

Figure 6. 1: Irregular Nepalese stone mud masonry health centre with horizontal RC bands (Pahar Trust, 2020)

In Nepalese stone masonry, the stone is typically locally sourced, and the mortar is generally formed of locally sourced mud which adds additional uncertainty to the material properties. Regionally sourced experimental data is not very common. When available for Nepalese masonry (e.g., Adhikari & D'Ayala, 2019), they are typically for masonry assemblage instead of the individual masonry constituents (stone and mortar) and they refer to bricks rather than stone (e.g. Parajuli et al., 2020).

Masonry is a notoriously complex material to model accurately due to its high concentration of irregularities and imperfections and highly non-linear deformation response. An irregular formation of masonry adds further geometric uncertainties to masonry modelling. A high variation in masonry workmanship further adds to the uncertainty (Giamundo et al., 2014).

Pahar Trust is a non-governmental organisation (NGO) founded in the UK whose stated objective is to improve education, health, and sanitation for remote communities in Nepal. One of their methods of achieving this is constructing schools and health centres. Many NGOs use a template structure approach whereby a single design is replicated multiple times to reduce the project design costs. Furthermore, certain structures, such as schools, must conform to specific government guidelines (Nepal Department of Education, 2016). This approval process can be costly and time-consuming; hence a template design is used to avoid repeating the process for each project. Pahar Trust has provided a template design for a single-storey stone mud masonry building. This structure has nominal reinforcement in horizontal RC bands and a single reinforcing bar in each corner, further details on the nominal reinforcing requirements are set out in Section 2.2. This is shown in Figure 6.1.

Previous studies have derived equivalent single degree of freedom (SDOF) models from detailed multiple degree of freedom (MDOF) numerical models. These SDOF models are used for cloud or incremental dynamic analysis (IDA) to derive fragility curves. The SDOF methodology significantly reduces the computational demand of the analysis; however, it relies on the assumption that the MDOF response is dominated by a global mode of deformation (Graziotti et al., 2016). The SDOF approach will not explicitly consider local failures that could occur due to dynamic loads in an NLTHA of an MDOF model. This paper will compare the

fragility results of an SDOF model and an MDOF model to quantify the effect of the SDOF idealisation.

The continuous micro-modelling technique used in Cannizzaro et al. (2021), Petracca et al. (2017) and validated in Chapter 5 is used in this study to perform a series of non-linear time-history analyses (NLTHA) on one of the Pahar Trust masonry template structures. The modelling technique was verified for irregular stone masonry in Chapter 5. A numerical model will then be developed for Pahar Trust's template health centre in stone masonry. 74 NLTHA will then be carried out to perform a cloud analysis and derive fragility curves. The fragility curve of a structure is the relationship between a ground motion intensity measure (PGA or $S_a(T_1)$) and the probability of exceeding a given limit state (damage limit state or limit state for the prevention of collapse). Further details on fragility curves and different methods of deriving them can be found in Section 2.5.2. The fragility curves from this detailed micro-modelling approach will then be compared to those derived using an established SDOF idealisation approach. These fragilities will then be benchmarked against other fragility curves for Nepalese stone masonry structures from literature. Finally, the MDOF and SDOF fragility curves are integrated with the seismic hazard map of Nepal to quantify the seismic risk to the structure across an area of varying seismic hazard.

6.2 Modelling Pahar Trust Health Centre

Pahar Trust is a UK based charity that aims to improve education, health and sanitation in disadvantaged communities in Nepal. As part of this work, they carry out the construction of schools and health centres. Pahar Trust has provided the design of a single-story irregular masonry health centre. The design they provided is a template design that may be replicated across Nepal with only minor modifications based on site conditions and locally available materials. The building is made of locally available stone and mud mortar and is 2.74 m tall (not including the roof). The roof is made from a series of timber trusses. The structure uses a series of three reinforced concrete (RC) bands at the sill, lintel and roof level. This is common practice in many rural buildings in Nepal (Schildkamp et al., 2019). The layout is shown in Figure 6.2a, where it can be seen that there is a six-inch seismic gap. The pounding assessment in Section 3.3 show that a two-storey RC building with masonry infills was not susceptible to pounding across a six-inch seismic gap. The pounding would occur if the interstorey drift ratio (IDR) exceeded 5.5% (6 inches drift over 2.74 m height) or both structures experienced 2.8% IDR and were out of phase. The masonry would undergo complete collapse before 2.8% IDR; therefore, pounding is not considered in this study. As it is assumed there is no structural

interaction between the two structures on each side of the seismic gap, this study will only consider the structure to the left of the seismic gap, as indicated in green in Figure 6.2a. Figure 6.2b shows one of Pahar Trust's completed health centres in Gumlek, 33 miles south-east of Pokhara.

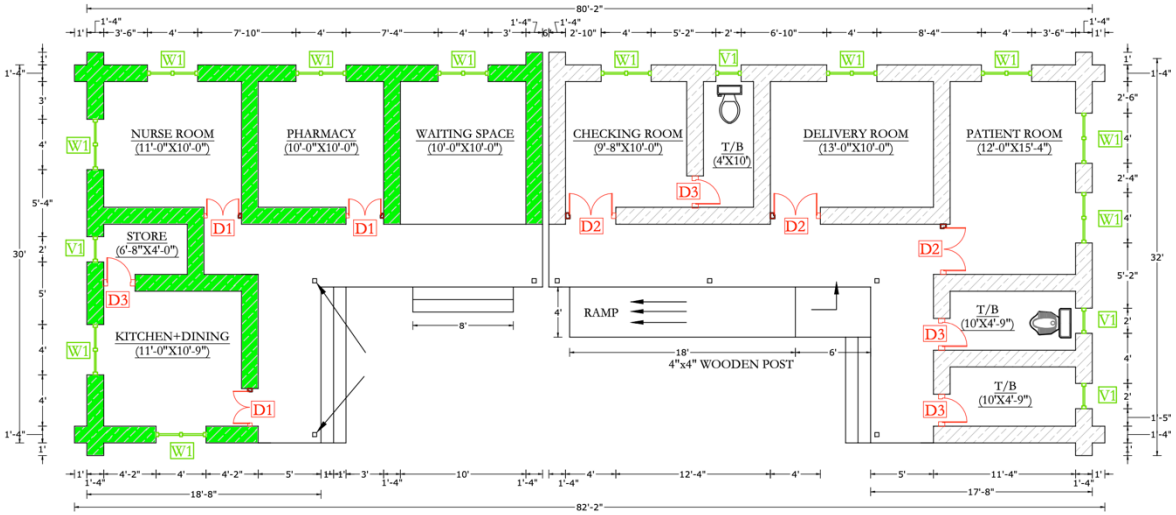

(a)

(b)

Figure 6. 2: (a) Room plan of Pahar Trust template health centre. The building highlighted in green is used for this study (b) Photograph of Gumlek Health Centre (Pahar Trust, 2020)

6.2.1 Mud Mortar Properties

As the validation in Chapter 5 was carried out using irregular stone masonry with cement mortar, appropriate mud mortar properties must be selected using literature. A wide range of compressive and tensile strength values of mud mortar are available in literature. A selection are shown in Table 6.1. Many studies only present a tensile or compressive strength. In these

cases, an assumption is made that the compressive strength is a factor of 35 greater than the tensile strength, as shown in Equation 6.2, an asterisk indicates these in Table 6.1. Where the reference has provided the shear strength Equation 6.1 from CNR-DT 212/2013. (2014) is used to find the tensile strength. This value is a typical relationship between compressive and tensile from values in CNR-DT 212/2013. (2014). It should be noted that the compressive strength ranges from 0.036 MPa to 1.8 MPa, and the tensile strength ranges from 0.001 MPa to 0.048 MPa. This high variability level will likely be due to a combination of varying testing procedures, sample preparation, mortar component (i.e. different types of mud), and testing rigour.

$$f_t = 1.5\tau_0 \tag{6.1}$$

$$f_m = 35 f_t \tag{6.2}$$

*Table 6. 1: Tensile and compressive strength values for mud mortar from literature. *indicated Equation 6.1 has been used to calculate that value.*

Tensile strength (MPa)	Compressive strength (MPa)	Reference
0.027*	0.96	Build change (2019)
0.0029*	0.1	Sonda et al. (2019)
0.02	2.4	Adhikari & D'Ayala (2019)
0.001	0.036*	Kuinkel et al. (2019)
0.0053	0.83*	Parajuli & Kiyono (2015)
0.04*	1.4	Mishra, (2018)
0.014*	0.5	NBC-110:1994. (1994) (Note: Lime mortar)
0.048	1.8	World Bank (2019)

In Table 6.1, the Nepalese building code (NBC-110:1994., 1994) gives a compressive value of 0.5. This compressive strength value is indicated as a "*Minimum Compressive Strength at 28 days*", whereas a mean value is required for the numerical model. For the numerical model of the Pahar trust health centre, the values from Build change (2019) are used due to a high level of reporting on how the samples were created and tested furthermore, the values sit in the middle of the range with respect to the values shown in Table 6.1.

These material property values are based on a series of five vertical compression tests by Build change (2019) on mud mortar cubes. The mud was taken from Dhulikhel near Kathmandu University, the sample was taken from 1.00 m below the ground. The samples were dried and

passed through a 2 mm sieve. The mud was then mixed with water with a water-mud ratio of 0.31, this was on the advice of a local mason. The mortar was then formed into a series of 70.6 mm cubes. These were then tested in a vertical compression rig. During the test, the area of the sample reduced by 6%, this final area was used to calculate the compressive strength. Table 6.2 shows the results of the 5 tests, giving a mean compressive strength of 0.96 MPa and using Equation 6.2, a tensile strength of 0.027.

Table 6. 2: Results of vertical compression tests on mud-mortar from Build change (2019)

Sample Name	Sample Weight (g)	Vertical Load (kg)	Compressive Strength (MPa)	Distribution parameters (MPa)
S1	505	450	0.97	Mean=0.96 C.o.V=0.29
S2	500	330	0.71	
S3	460	500	1.08	
S4	460	620	1.34	
S5	470	310	0.67	

The elastic modulus of mud mortar is also required and could significantly impact the limit state displacement, although will not greatly affect the masonry strength capacity. Table 6.3 summarises the elastic modulus for mud mortar from three previous studies.

Table 6. 3 Elastic modulus values for mud mortar from literature

Elastic modulus (MPa)	Reference	Comments
33	(Parajuli, 2012)	11 samples
207	(Pun, 2015)	16 samples CoV=5.1%
1170	(Mishra, 2018)	3 Samples

6.2.2 Implementing the Masonry Walls

The masonry walls were implemented into the FE model using the damage model (Petracca et al., 2016) outlined in Section 2.6.3.2. A section of the masonry wall can be seen in Figure 6.3a. The material properties used in the FE model of the Pahar trust health centre are given in Table 6.4. The tensile and compressive strength from Section 6.2.1 was used. Other material properties were found using upper and lower limits based on findings from literature (Drougkas

et al., 2016; Gil et al., 2016; Sambu Potty, 2013; Thirumalini et al., 2011; Rhee et al., 2019; Costigan et al., 2015; Molina et al., 2017; Oliveira et al., 2006; Petracca et al., 2017) and then an optimisation process was used such that the response shape matched that of the experimental campaign in Section 5.3.1. The final material properties are shown in Table 6.4. It should be noted that the non-linear properties of stone have little effect on the structure's response as it is highly unlikely the stone will exceed the elastic limit. Both the mortar and the stone continuum use ASDShellQ4 shell element, which uses the AGQ6-I formulation for the membrane properties (Chen et al., 2004) and the MITC4 formulation (Dvorkin et al., 1984) for the shear-deformable bending part. The out-of-plane performance of the shell element has been validated experimentally for the case of masonry, where it was observed to have a close level of matching with out-of-plane SPO experimental walls for a masonry pier (Petracca et al., 2017). The masonry walls are assumed to be fixed in displacement and rotation at the ground level. Due to the Pahar trust health centre not having a rigid diaphragm a distributed mass is used across the face of the wall. The load of the masonry is taken as 22.00 kN/m^3 as recommended by the Indian Standard (IS875-2010., 2010). A wall thickness of 350 mm is used to find a distributed mass of 784 kg/m^2. Further details on the loading of the structure can be seen in Table 6.6.

Table 6. 4: Material properties used for stone and mortar in masonry micro-model

Material Property	Symbol	Stone	Mortar
Youngs Modulus	E	15.5 GPa	55 MPa
Tensile strength	f_t	10.97 MPa	0.0267 MPa
Tensile Fracture energy	G_t	0.366 N/mm	0.2 N/mm
Compressive elastic limit	f_{c0}	35.5 MPa	0.3 MPa
Compressive peak strength	f_{cp}	98.7 MPa	0.96 MPa
Compressive residual Strength	f_{cr}	27.3 MPa	0.1 MPa
Compressive strain at peak strength	e_p	0.015	0.03
Compressive fracture energy	G_c	120 N/mm	10 N/mm

6.2.3 Reinforced Concrete Bands

A series of three RC bands are integrated into the wall at the sill, lintel and roof level (i.e. the top of the wall). The RC band at sill level is 76 mm deep and has two 10 mm longitudinal reinforcing bars and an 8 mm u-hook shear link at 152 mm intervals. This is shown in Figure 6.3b. The lintel and roof level RC bands are 152 mm deep, have four 10 mm longitudinal reinforcing bars, and 8 mm shear links at 152 mm intervals. The concrete used is assumed to be M20 (IS456-2000, 2000), as has been used in previous projects by Pahar Trust (refer to Section 3.2.2). The Indian standard (IS456-2000, 2000) states that M20 has a characteristic compressive strength of 20 MPa, a mean strength of 30 MPa and Young's modulus of 22.3

GPa. The reinforcing steel is assumed to be FE500 (IS 1786, 2008) with a yield strength of 500 MPa and Young's modulus of 210 MPa.

The RC bands are implemented into the FE model using a fibre section on a force-based beam-column element (Taucer et al., 1991) using the Gauss-Lobatto integration method (Scott et al., 2006). Further details on the modelling of reinforced concrete can be found in Section 2.3.4. The mean value for concrete strength was used, and the corresponding tensile strength of 3.8 MPa was found using Equation 6.6 from IS456-2000 (2000). An equal degree-of-freedom condition was applied along the length of the beam-column element with the shell element above and below.

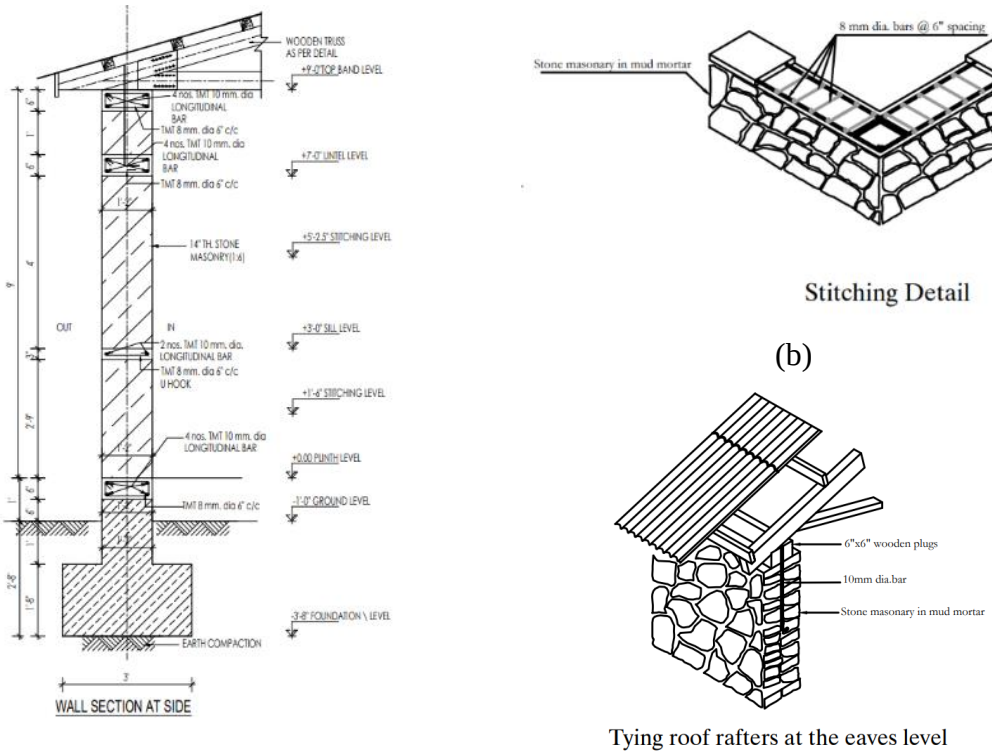

Figure 6. 3: (a) Section of the masonry wall with RC bands and roof connection (b) Detail of RC band at sill level (c) Detail of connection of timber roof and wall.

6.2.4 Timber Roof

The timber roof structure is implemented into the FE model using an elastic beam-column section. The timber is assumed to be Sal (Shorea Robusta) (NBC-112:1994., 1994) which has an elastic modulus (E) of 12.5 MPa. This model does not use a rigid diaphragm assumption that is often used for FE models. The timber member connections are conservatively assumed to be pinned. Previous studies have shown a lack of a rigid diaphragm can cause a significant

increase in the periods of the initial vibration modes (Langroudi et al., 2011). Furthermore, a rigid diaphragm ensures a global failure of the structure, which may not be the case for a single storey unreinforced masonry structure. The timber roof is shown in Figure 6.4, taken from STKO (Petracca, 2017b), the GUI used for pre-processing the finite element model.

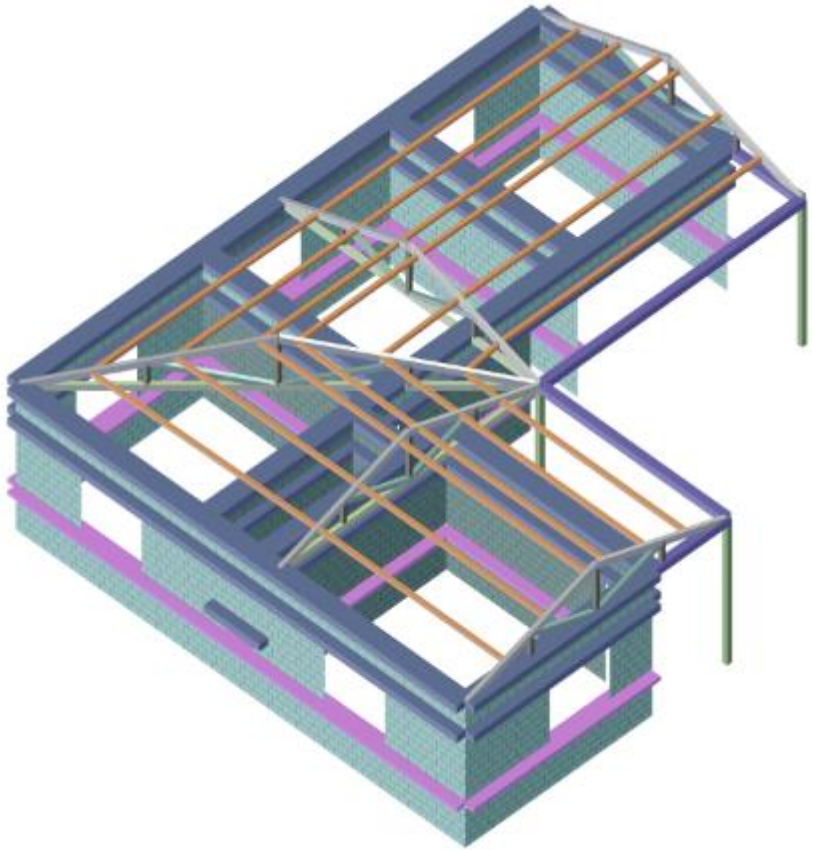

Figure 6. 4: Finite element model of Pahar Trust Health Centre taken from STKO (Petracca, 2017b)

6.2.5 Damping

Rayleigh damping is used with a damping ratio of 1.5%. Literature studies, shown in Table 6.5, have shown, using experimental data, that masonry requires a significantly lower level of damping relative to reinforced concrete, which will commonly use 2% (Dolšek & Fajfar, 2001). Vanin et al. (2020) and Lemos (2019) complete studies on stone masonry and use Rayleigh damping with a damping factor from 1%-2%.

Table 6. 5: Literature summary of damping ratios for masonry structures

Suggested damping ratio	Masonry typology	Modelling typology	Reference
1%	Stone, lime mortar	Equivalent frame method	(Vanin et al., 2020)
2%	Stone, mortar	Discrete element method	(Lemos, 2019)

2%	Clay Brick and lime mortar	Macro-modelling	(Graziotti et al. 2003)

6.2.6 Loading

Accurate structure loading is essential for both the gravity loading and for calculating the dynamic loading on the structure. Where possible, the Nepalese building codes are used for loading. If the Nepalese building codes are not available, the Indian standard is used. A summary of the model loading is shown in Table 6.6. If a range of weights is given in the codes, the upper end of the range is taken conservatively. The vast majority (79.5%) of the structure's mass is due to the masonry walls. These masonry walls are 350 mm deep and are covered in plaster. The plaster is assumed to be non-structural and 25 mm deep. It should be noted that the lintel and top-level RC bands are 0.6% reinforcement, therefore a density of 24.2 kN/m^3 is used for the density IS875-2010. (2010). The timber used is assumed to be Sal (Shorea Robusta). Sal is a hardwood commonly used for construction in Nepal. It has an elastic modulus of (E) of 12.5 MPa and a density of 865 kg/m^3 (NBC-112:1994., 1994). The structure has a total mass of 117.4 tonnes and a total weight of 1152 kN. The values in Table 6.6 are applied to the finite element model as a series of area and line loads. The gravity analysis is carried out, and the sum of the vertical reactions at the end of the gravity analysis is equal to the structure's weight. This check is carried out to validate that the loads are applied correctly.

Table 6. 6: Material properties and total weights for the Pahar trust health centre design.

Material	Units	Value	Area/Length	Total	Reference
Stone mud masonry	kN/m^3	22.00	Area of wall = 119.057 m^2 Depth of wall = 0.35 m Volume of wall = 41.67 m^3	916 kN	IS875-2010. (2010)
Plaster	kN/m^3	17.25	Area of wall = 119.057 m^2 Depth of wall = 0.025 m Volume of wall = 2.98 m^3	51.3 kN	IS875-2010. (2010)
RC Bands (Lintel and Top Band)	kN/m^3	24.2	Length = 110.57 m Width = 0.350 m Height = 0.152 m	142.5 kN	IS875-2010. (2010)
RC Bands (Sill Band)	kN/m^3	24.2	Length = 48.84 m Width = 0.350 m Height = 0.076 m	31.4 kN	IS875-2010. (2010)

Vertical strut (Timber)	kN/m^3	8.48	Length = 9.60 m Width = 0.076 m Height = 0.076 m	0.47 kN	NBC-112:1994. (1994).
Wooden Post	kN/m^3	8.48	Length = 8.748 m Width = 0.101 m Height = 0.101 m	0.76 kN	NBC-112:1994. (1994).
Inclined Strut	kN/m^3	8.48	Length = 15.19 m Width = 0.101 m Height = 0.076 m	0.99 kN	NBC-112:1994. (1994).
Rafter	kN/m^3	8.48	Length = 30.4 m Width = 0.127 m Height = 0.101 m	3.28 kN	NBC-112:1994. (1994).
Main Tie	kN/m^3	8.48	Length = 18.16 m Width = 0.076 m Height = 0.127 m	1.49 kN	NBC-112:1994. (1994).
Purlin	kN/m^3	8.48	Length = 86.64 m Width = 0.076 m Height = 0.076 m	4.24 kN	NBC-112:1994. (1994).

6.3 Demand Capacity Ratio

A fragility curve is a cumulative distribution function that describes the probability of a structure exceeding a given capacity limit given a ground motion of a given intensity. Further details on fragility curves and how to derive them can be found in Section 2.5.2. The demand and capacity is given in terms of some given engineering demand parameters (EDP). There are many different EDPs used for fragility analysis, and they come under two broad categories, direct or processed. Direct EDPs can be calculated directly from the analysis results, such as displacement, interstorey drift, or chord rotation. Processed EDPs characterise the performance in terms of damage or structural performance. Examples of processed EDPs are damage index or damage spectra.

6.3.1 Engineering Demand Parameters (EDP)

The performance of an unreinforced masonry structure is evaluated, assuming that the local and global failure mechanisms are independent (CNR-DT 212/2013., 2014). The performance is assessed by first identifying the geometry of the piers and spandrels. The performance

indicators are then assessed using a multi-level damage approach. The three damage criteria are: exceedance of threshold levels of drift in piers and spandrels, inter-storey drift in individual walls and response on a global level relative to the capacity curve (i.e. a fraction of the max resistance on the pushover curve). In this study, the criteria laid out by CNR-DT 212/2013 (2014) will be used to identify the damage limit state (SLD) and the limit state for the prevention of collapse (SLC).

The Pahar trust health centre is to be assessed to damage limit state (SLD) and the limit state for the prevention of collapse (SLC) from the Italian Code for existing structures (CNR-DT 212/2013, 2014). It should be noted that these are not the same as damage limitation (DL) and near collapse (NC) from Eurocode 8 Part 3 (EN 1998-3., 2005). The return period for the seismic action used in each limit state is detailed in Table 6.7.

Table 6. 7: Return periods for seismic actions for limit states in the Italian code for existing structures (CNR-DT 212/2013, 2014) and Eurocode 8 Part 3 (EN 1998-3., 2005)

Italian Code Limit state (CNR-DT 212/2013, 2014)	Return period (years)	Eurocode 8 part 3 Limit state (EN 1998-3., 2005)	Return Period (years)
Damage Limit State (SLD)	50	Damage Limitation (DL)	225
Severe damage limit state (SLS)	475	Significant Damage (SD)	475
Limit State for the Prevention of Collapse (SLC)	975	Near Collapse (NC)	2,475

Assessing EDP first requires the micro-model to be divided into piers and spandrels. This has been subject to many approaches, as the equivalent frame method (EFM) relies on an accurate system of dividing the wall into piers and spandrels. Four different methods can be used to divide a façade into piers and spandrels. The first method is AVG, where the line defining the boundary of the pier travels from the corner of the opening to the corner of the façade or corner of the next opening. This can be seen in Figure 6.5a. The MIN criterion uses the minimum height of the masonry wall between two openings. This can be seen in Figure 6.5b. The LIM criterion is broadly the same as the AVG criterion. However, the inclination of the borderline of the pier is limited to 30^{o}, as shown in Figure 6.5c. The final criterion is the LIN criterion which assumes a rigid lintel, and therefore, the boundary to the edge of the wall follows the same criterion as MIN. However, the same criterion as LIM is used between the openings, as shown in Figure 6.5d. Morandini et al. (2019) compared the effectiveness of the AVG criterion,

MIN criterion, and LIM criterion. They found that the AVG and LIM criteria produced a lower value for the maximum base shear. The MIN criterion resulted in a higher initial elastic stiffness and energy dissipation. Morandini et al. (2019) did not find that any criteria were more effective than another. The results were too sensitive to other parameters such as loading and masonry texture.

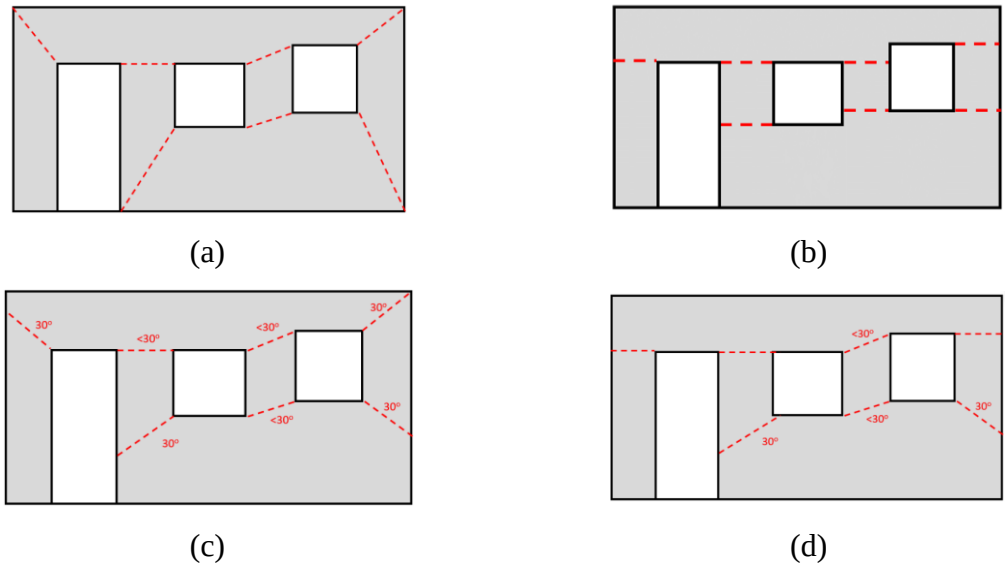

Figure 6. 5 Different pier spandrel discretisation methods. (a) AVG (b) MIN (c) LIM (d) LIN (recreated based on a figure from Morandini et al., 2019)

Malomo et al. (2019) carried out a study comparing the results of each of the four discretisation criteria with a discrete element method (DEM). The DEM is first validified against experimental work on two masonry piers, as with this study. One of which is slender and one of which is squat. After the experimental validation, eight irregular facades were created using the DEM and the EFM. For each layout, an EFM model was created with each criterion. The results showed that the MIN criterion was the most effective discretisation method to predict peak shear resistance. For this reason, we will use the MIN criterion as the discretisation method while assessing the EDP.

6.3.2 Damage Limit state (SLD)

Damage limit state (SLD) is defined as the level of damage in which the cost of damage is disproportionately high relative to the cost of the structure (EN 1998-1, 2004). In the Italian code for existing structures (CNR-DT 212/2013, 2014) damage limit state is referred to as "*stato limite di danno*" therefore the initialism of SLD is used to maintain consistency between this thesis and the Italian code. The damage limit state variable (Y_{SLD}) is defined by Equation 6.3, where $Y_{SLD,S}$ is the limit state variable at the structural element level (piers and spandrel), $Y_{SLD,M}$ is the maximum interstorey drift in any wall or diaphragm. $Y_{SLD,G}$ is the maximum ratio

of a control point's displacement to that control point's displacement at peak resistance on the pushover curve.

$$Y_{SLD} = maxY(Y_{SLD,S}; Y_{SLD,M}; Y_{SLD,G}) \tag{6.3}$$

$Y_{SLD,S}$ in Equation 6.3 is found using Equation 6.4, where $\Sigma_{SLD,F}$ is the percentage of spandrels in the building that have exceeded a threshold damage level. $\Sigma_{SLD,F}$ is given in Equation 6.5, where N_F is the number of spandrels, H is the Heaviside function, D_j is the drift of the given spandrel, and C_j is the capacity of the given spandrel. If the demand of the spandrel (D_j) exceeds the capacity (C_j) the Heaviside function is equal to one, other it is equal to zero. The drift capacity of the spandrel (C_j) is given as 0.8%-1.2% in Table 3.3 in CNR-DT 212/2013 (2014). For this study, 0.8% is used due to the notoriously brittle response of mud mortar. τ_{SLD} is defined as a maximum accumulated permissible damage for the damage limit state (SLD). CNR-DT 212/2013 (2014) suggests a τ_{SLD} value of 3%.

$$Y_{SLD,S} = \frac{1}{\tau_{SLD}} \max\left(\Sigma_{SLD,F}, \Sigma_{SLD,M}\right) \tag{6.4}$$

$$\Sigma_{SLD,F} = \frac{1}{N_f} \sum_{f} H\left(\frac{D_j}{C_j} - 1\right) \tag{6.5}$$

$$\Sigma_{SLD,M} = \frac{\sum_m A_j H\left(\frac{D_j}{C_j} - 1\right)}{\sum_m A_j} \tag{6.6}$$

The cumulative damage to piers, $\Sigma_{SLD,M}$, is the percentage, weighted by the area of piers, that exceeds the capacity C_j, as shown in Equation 6.6. A_j is the area on plan of the relevant pier, H is the Heaviside function, D_j is the demand of the relative pier, and C_j is the capacity of the given pier at SLD. The drift capacity of the pier is 0.4%-0.8% if the failure is caused by bending and 0.25%-0.4% if the damage is caused by shear for SLD, as shown in Table 3.2 in CNR-DT 212/2013 (2014). The damage pattern from the SPO showed the dominant failure mechanism to be shear. Hence 0.25% is used for the shear capacity of the piers.

$Y_{SLD,G}$ is the maximum ratio of the displacement of a control point relative to the displacement of the point at peak resistance in the static pushover analysis. Due to this structure not having a rigid diaphragm, this check will be carried out at all nodes at the structure's roofline (top of the masonry wall). The displacement at peak shear resistance is evaluated for each point in the x and y-direction.

6.3.3 Limit state for the prevention of collapse (SLC)

The limit state for the prevention of collapse variable Y_{SLC} is calculated using Equation 6.7, where $Y_{SLC,S}$, $Y_{SLC,M}$ and $Y_{SLC,G}$ are the same limit state variables as for the damage limit state.

$$Y_{SLC} = maxY(Y_{SLC,S}; Y_{SLC,M}, Y_{SLC,G}) \quad (6.7)$$

$Y_{SLC,S}$ is given by Equation 6.8, where τ_{SLC} is the maximum allowable damage for the Limit state for the prevention of collapse (SLC). A recommended value of 3% has been used previously (CNR-DT 212/2013., 2014). In Equation 6.8 $\Sigma_{SLC,M}$ is the percentage weighted by the area of piers that exceed SLC capacity, as per Table 3.2 in CNR-DT 212/2013 (2014).

$$Y_{SLC,S} = \frac{1}{\tau_{SLC}} \Sigma_{SLC,M} \quad (6.8)$$

$Y_{SLC,M}$ is the limit state variable associated with the macro-elements and is defined using the same equation as the damage limit state (SLD) except $\theta_{SLC,M}$ is the drift threshold for SLC. This is given as 0.6% in Section 3.4.4 of CNR-DT 212/2013 (2014). $Y_{SLC,G}$ is the limit state variable for the global displacement. This corresponds to the displacement of a control node when the overall shear resistance has been reduced by 60%.

6.4 Single Degree of Freedom

An established single degree of freedom (SDOF) approach is used to assess the fragility of the Pahar Trust Health Centre. This approach uses the response from a static pushover (SPO) to define the response of the SDOF model. The SPO curve is idealised using a multi-linear approximation. Due to the low computational demand of the SDOF model, an incremental dynamic analysis (IDA) can be used to derive fragility curves. Although the SDOF model significantly reduces the computational runtime of the analysis, it has several drawbacks with respect to the MDOF model. The SDOF cannot explicitly model the local failure mechanisms. Furthermore, the SDOF cannot model the interaction between the bi-direction displacement in the MDOF model. The SDOF model also cannot model the torsional effects, whereas this is accounted for implicitly in the MDOF model. This study seeks to quantify the effects of these assumptions on the final fragility curves of the two modelling approaches.

6.4.1 Static Pushover Analysis

A static pushover (SPO) analysis was independently carried out in the x and y-direction (longitudinal and transversal directions as indicated in Figure 6.6b). As there is no rigid diaphragm, the lateral load is applied in a pattern proportional to the masses. Due to the flexible roof structure, the choice of control node for the pushover will affect the final pushover curve. The point at the roof level of greatest displacement was used as a control node to avoid

structural instability. The material damage is made out of the tensile damage index (d^+) and the compressive damage index (d^-). These damage indexes range from 0 (completely intact material) to 1 (completely damaged material). Further details on how they affect the stress tensor can be found in Section 2.4.3.2. The material damage can be used to identify the cracking pattern in masonry. The material damage at the peak base shear can be seen in Figure 6.6 and 6.7 for the pushover in the x and y-direction, respectively. The diagonal cracks imply a shear failure in the in-plane walls. The engineering demand parameters (EDPs) are calculated throughout the SPO to identify the point of the pushover curve where the capacity is first exceeded. That point of the pushover curve is then used on the SDOF model as the displacement capacity. The SPO is carried out independently in the x and y direction. This ensures that the capacity thresholds are based on a uni-directional loading allowing it to be compatible with the SDOF model.

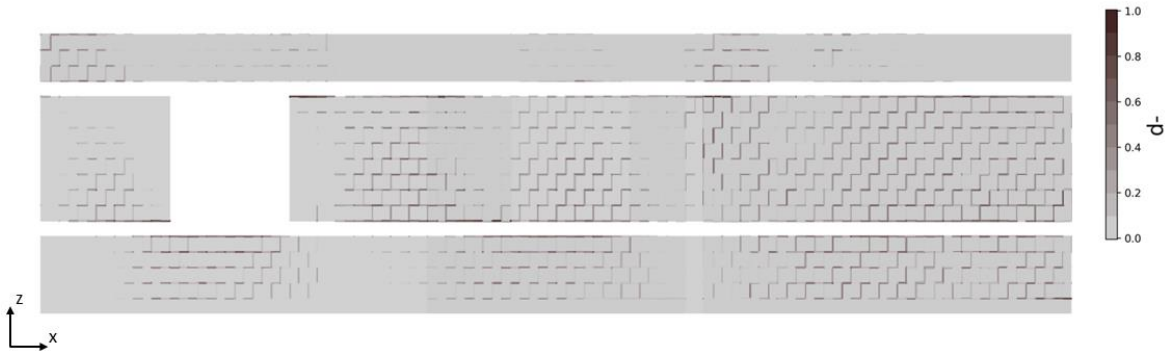

(a)

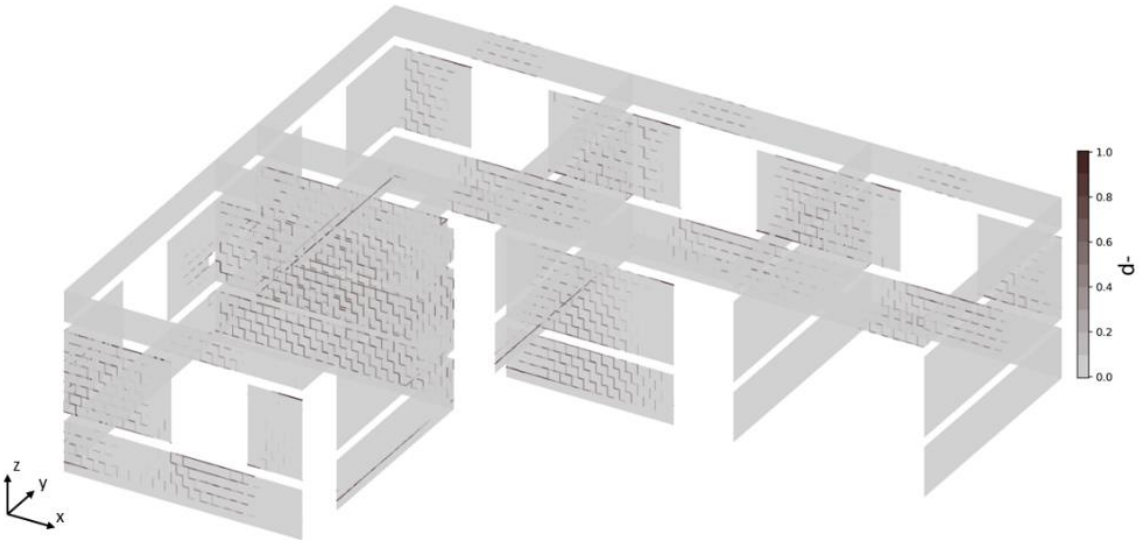

(b)

Figure 6. 6: Material tensile damage (d-) where 0 indicates the material is undamaged, and 1 indicates complete failure of the material (cracking pattern) for the static pushover in the x direction (a) View in the X-Z plane. (b) 3D view

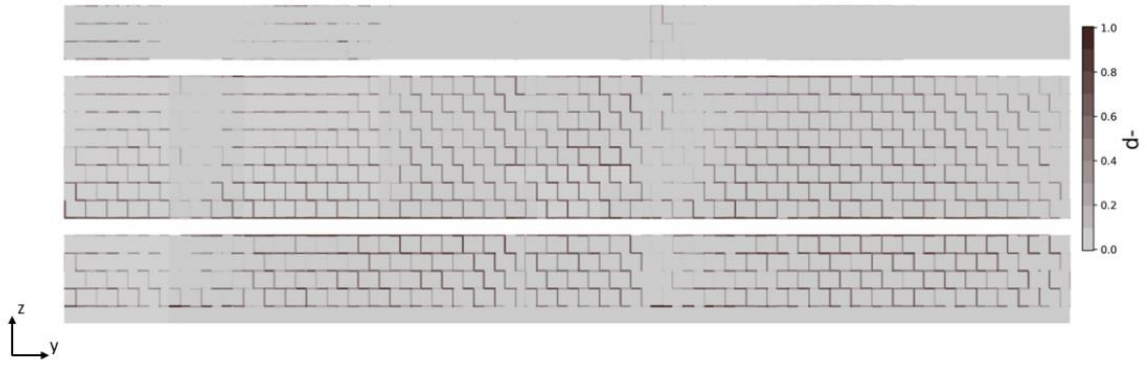

(a)

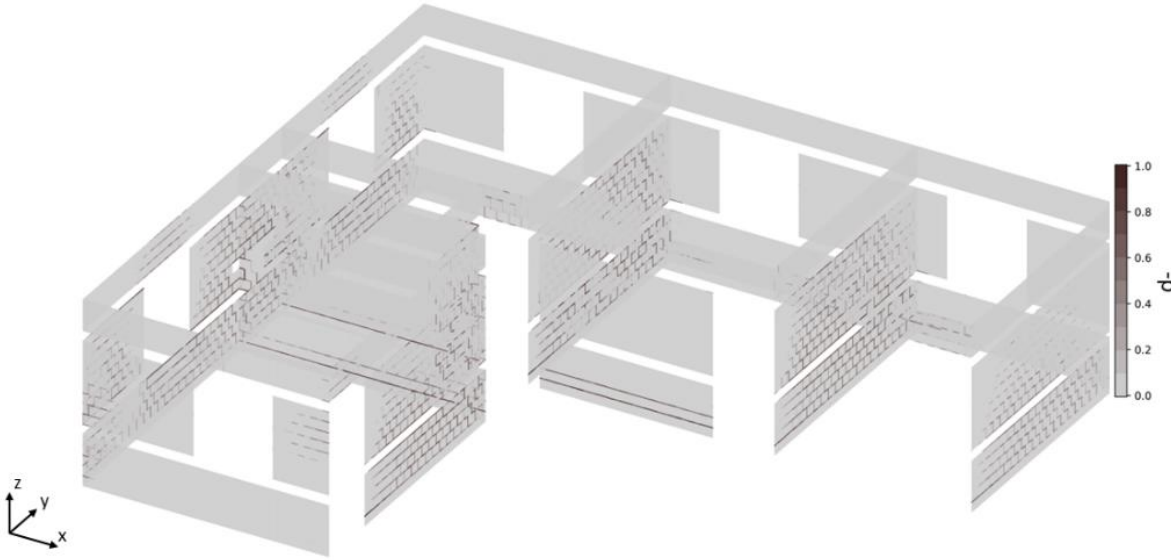

(b)

Figure 6. 7: Material tensile damage (d-) where 0 indicates the material is undamaged, and 1 indicates complete failure of the material (cracking pattern) for the static pushover in the y direction (a) View in the X-Z plane. (b) 3D view

6.4.2 Single-degree of Freedom (SDOF) Idealisation

A quadrilinear and bilinear idealisation of the pushover curve are investigated. The quadrilinear idealisation is based on De Luca et al. (2013). The initial linear section is based on the secant stiffness of the pushover curve at 5% to 10% of the yield or peak base shear. The stiffness of the strain hardening section of the curve is such that the segment finishes at the peak strength, and the area difference is minimised between the two curves. The strain softening part of the

idealisation minimises the area difference in the strain softening section. Finally, a residual section is implemented if it improves the area difference criteria. A pinching hysteretic model is employed with degrading strength and stiffness. The SDOF is modelled using OpenSees using the pinching4 material. Full properties of the SDOF response and hysteretic model can be found in Table 6.8. The quadrilinear idealisation in the x-direction and y-direction can be seen in Figure 6.8. The bilinear idealisation is based on an equal-area criterion and an intercept of the bilinear idealisation at 70% of the peak shear resistance, as shown in Figure 6.9.

Table 6. 8 Properties of the Pinching4 uniaxial material (OpenSees, 2012) employed for SDOF approximation

Property	Symbol	X-Pushover	Y-Pushover
Values defining force points on the positive response envelope	**[ePf1, ePf2, ePf3, ePf4]**	[788, 1059, 1007, 1007] kN	[961, 1292, 890, 890] kN
Values defining force points on the negative response envelope	**[eNf1, eNf2, eNf3, eNf4]**	[788, 1059, 1007, 1007] kN	[961, 1292, 890, 890] kN
Values defining deformation points on the positive response envelope	**[ePd1, ePd2, ePd3, ePd4]**	[0.817, 2.281, 4.558, 10.040] mm	[0.773, 2.477, 6.394, 10.262] mm
Values defining deformation points on the negative response envelope	**[eNd1, eNd2, eNd3, eNd4]**	[0.817, 2.281, 4.558, 10.040] mm	[0.773, 2.477, 6.394, 10.262] mm
Ratio of the deformation at reloading to the maximum historic deformation in the positive and negative direction	**rDispP/rDispN**	0.5	0.5
Ratio of the force at reloading to force to the maximum historic deformation in the positive and negative direction	**fForceP/fForceN**	0.25	0.25
Ratio of strength developed upon unloading from negative load to the maximum strength developed under monotonic loading	**uForceP/ uForceN**	0.05	0.05

As can be seen in Figures 6.8 and 6.9, although the bilinear is adequate for the case of the pushover in the x-direction where there is a low level of strength degradation, in the y-direction it can be seen there is a high level of strength degradation that is not captured by the bilinear approximation. For this reason, the quadrilinear approximation is used for the IDA. This quadrilinear idealisation is implemented in the SDOF model using the pinching4 model in OpenSees. A 1.5% damping ratio is used, as set out in Section 6.2.5, to be consistent with the MDOF model.

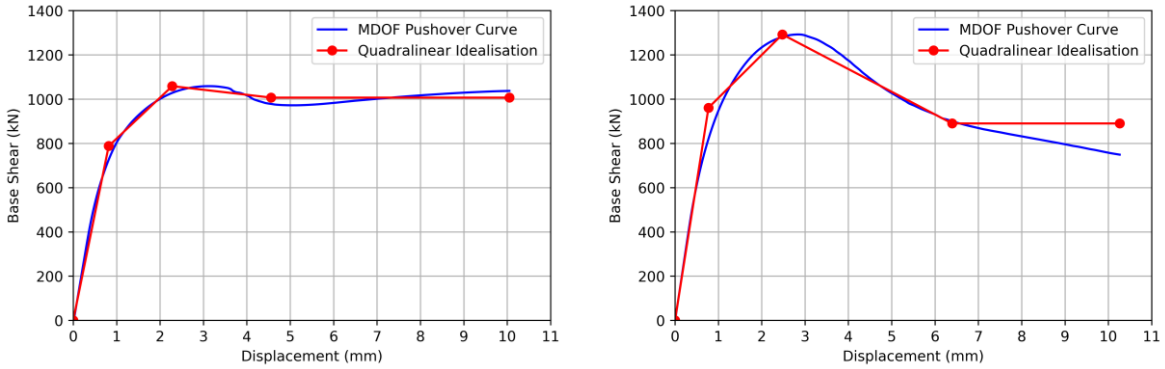

(a) (b)

Figure 6. 8. Quadralinear approximations of MDOF pushover curve for SDOF model. Idealisation is based on De Luca et al. (2013) (a) x-direction (b) y-direction

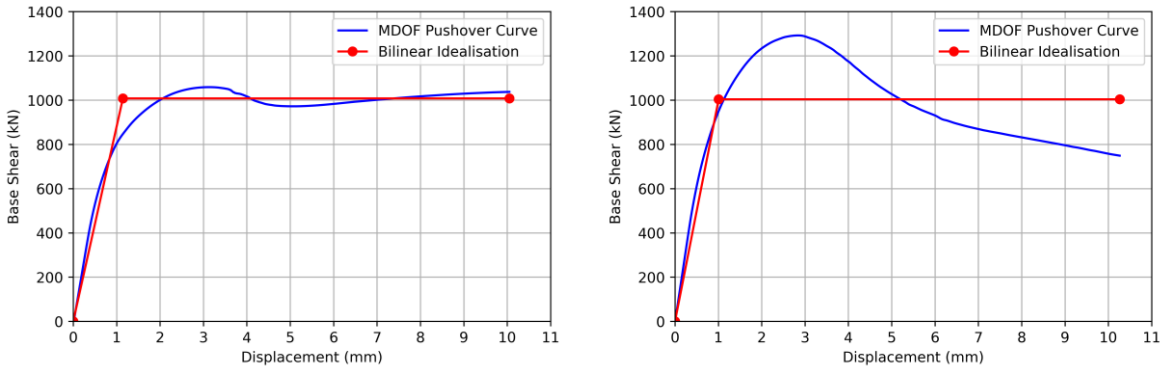

(a) (b)

Figure 6. 9 Bilinear approximations of MDOF pushover curve for SDOF model. Idealisation is based on equal area and an intercept at 0.7V_{max} (a) x-direction (b) y-direction

6.4.3 Ground Motion Selection

The NLTHA was carried out using three ground motion suites. The first ground motion suite (GM1) is the far-field ground motions from FEMA P695 (2009). This consists of 22 pairs of horizontal ground motions and is available on the PEER NGA West 2 (2014) ground motion database. They are referred to as far-field as the rupture distance is greater than 10 km. The Fourier transform can be seen in Figure 6.10a, and details of the ground motions can be found in Table 3.9. The spectral acceleration of GM1 can be seen in Figure 6.11a. These ground motions were also used in Chapter 3 to assess the RC infilled Pahar trust school.

The second ground motion suite (GM2) is a code compatible ground motion suite. It should be noted that code-compliant ground motion selection criteria are typically site-specific and use an anchorage PGA value. This is not appropriate for a template design because the same design is applied over an area of varying seismic hazard. This ground motion selection will be based on the application of EN 1998-3 (2005) to a health centre in Kathmandu. Eurocode 8 type 1 spectral shape for soil class C is used (the most common soil type in Kathmandu valley). Chaulagain et al. (2015) suggest a value of 0.38 g for a 475 year return period earthquake. This value is used for the anchorage PGA. However, it should be noted that subsequent probabilistic seismic hazard analysis (PSHA) studies have given significantly higher values (e.g. 0.60 g from Stevens et al. (2018)). Further details on PSHA studies can be found in Section 2.5.1. EN 1998-3 (2005) states that the arithmetic mean of the 5% dampened elastic response spectrum should at no point be lower than 90% of the design spectrum. The code compatible ground motion suite is formed of 10 pairs of horizontal recordings from the PEER NGA West 2 (2014) ground motion database. The ground motions are listed in Table 3.3, and the Fourier transform is shown in Figure 6.10b. This ground motion selection was used in Chapter 3 for the assessment of pounding. The spectral acceleration of GM2 can be seen in Figure 6.11b. It can be seen that the PGA is significantly higher for GM2, with a mean value of 0.786 g compared to 0.421 g for GM1.

The third ground motion suite is formed of five pairs of horizontal recordings from the Gorkha 2015 earthquake. Four of the ground motion pair are provided by the Faculty of Engineering, Hokkaido University, Japan (Rupakhety et al., 2017). The final Gorkha ground motion is provided by USGS (2016). The Gorkha earthquake was the largest recorded Nepalese earthquake, with a moment magnitude of 7.8 Mw. A summary of the recordings can be found in Table 3.10, the Fourier transform is shown in Figure 6.10c, and the spectral acceleration is shown in Figure 6.11c. Although it can be seen that the PGA is significantly lower for GM3, the spectral acceleration at high periods is significantly increased due to the amplification caused by soft soils in Kathmandu Valley.

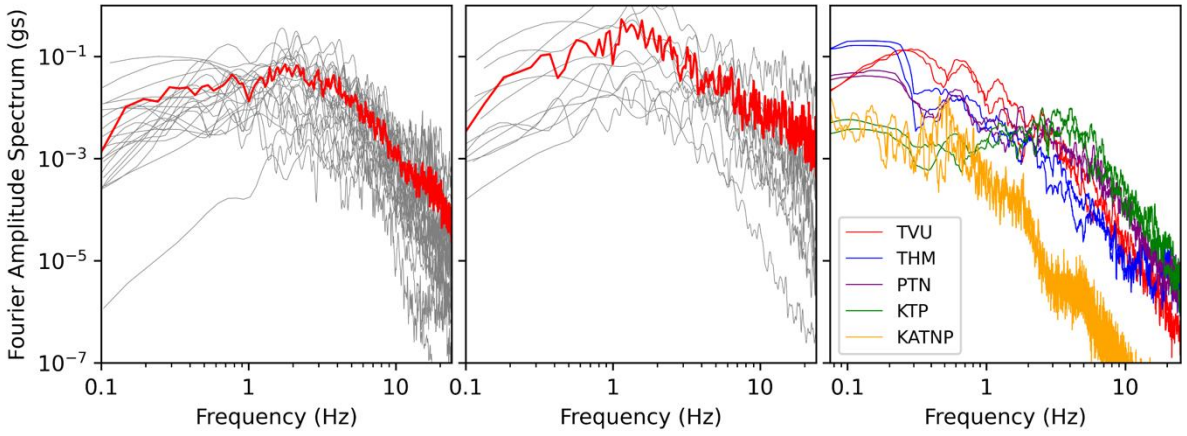

(a) (b) (c)

Figure 6. 10 . Fourier Transform of (a) GM1 (FEMA P695 Far Field) (b) GM2 (Code compatible) (c) GM3 (Gorkha 2015 recordings)

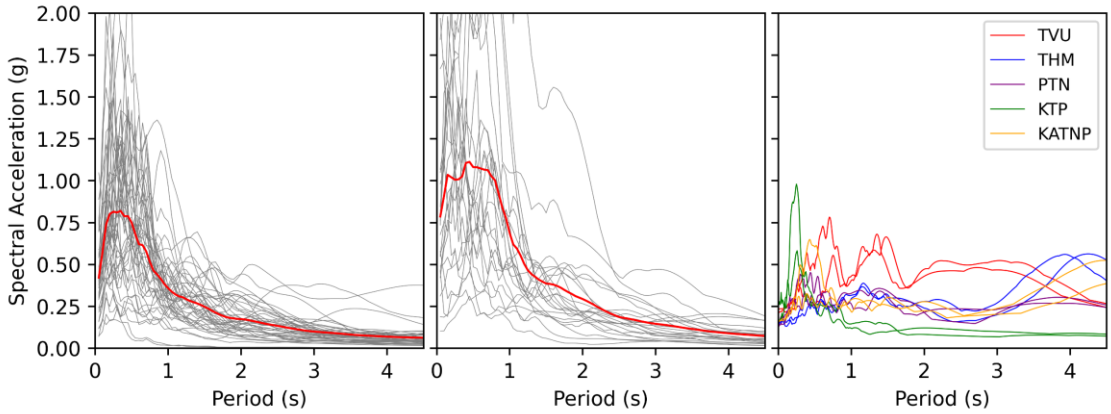

(a) (b) (c)

Figure 6. 11: Fourier Transform of (a) GM1 (FEMA P695 Far Field) (b) GM2 (Code compatible) (c) GM3 (Gorkha 2015 recordings)

6.4.4 IDA Results

The incremental dynamic analysis (IDA) is carried out for each ground motion in Section 6.4.3 from 0.0 g to 1.5 g with 100 increments. The results of the IDA can be seen in Figures 6.12a and 6.12b. The robust fragility tool (Jalayer et al., 2015) was used to derive the fragility curves from the IDA curves. These results can be seen in Figures 6.12c and 6.12d, and the cumulative distribution function (CDF) parameters are shown in Table 6.9.

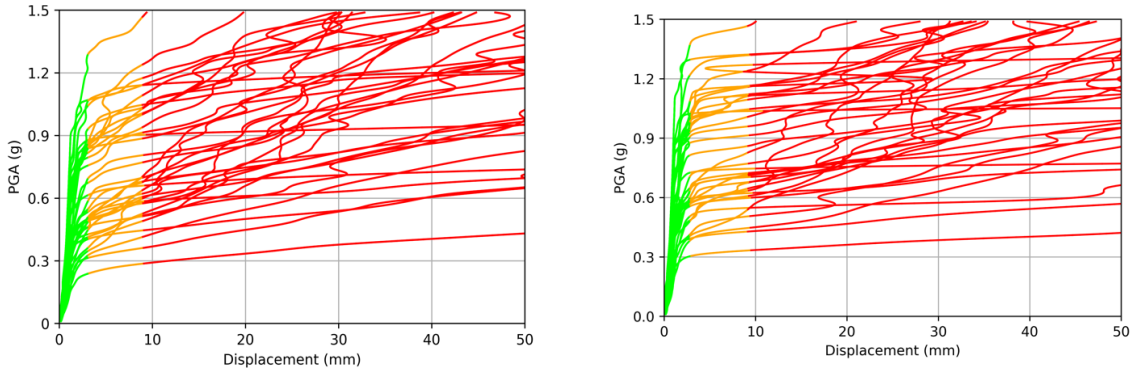

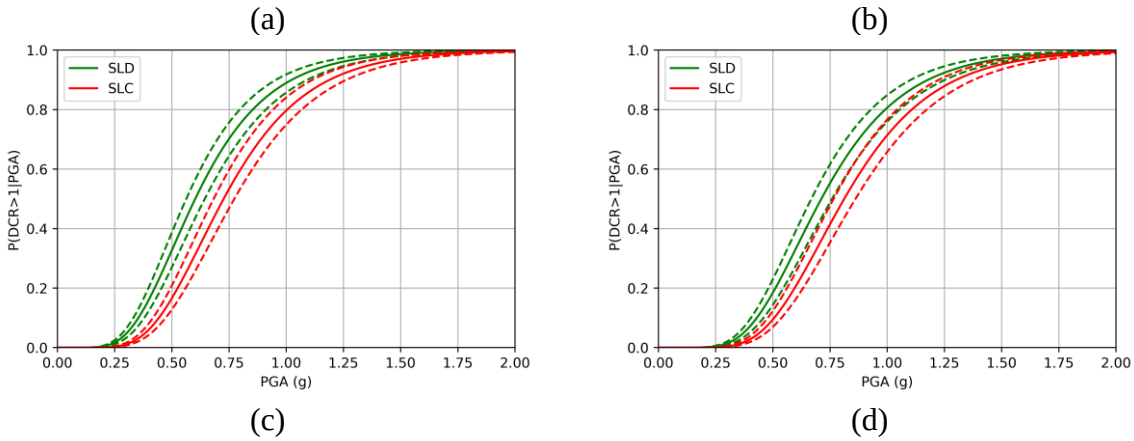

Figure 6. 12: Results of IDA on SDOF quadrilinear idealisation of the masonry structure. (a) IDA in x-direction, (b) IDA in y-direction (c) fragility curve in x-direction (d) fragility curve in y-direction

Table 6. 9: Fragility parameters for IDA results of equivalent SDOF model where η is the median and β is the logarithmic standard deviation of the lognormal fragility curves

Direction	Limit State	η (g)	β
x	Damage Limit State (SLD)	0.603	0.414
	limit state for the prevention of collapse (SLC)	0.727	0.385
y	Damage Limit State (SLD)	0.712	0.393
	limit state for the prevention of collapse (SLC)	0.812	0.368

From Table 6.9, significantly higher η values are observed in the y-direction with respect to the x-direction. This is due to a difference in the failure mechanism caused by the irregularity in the structure, leading to a significantly lower peak shear resistance in the x-direction. The fragility curves in the x-direction will be used as this is the critical case.

6.5 Multiple Degree of Freedom Analysis

A non-linear time history analysis (NLTHA) is carried out on the full multiple degree of freedom (MDOF) model for each ground motion pair, set out in Section 6.4.3. The motions are swapped for each horizontal direction for each ground motion pair, as implemented in the European (EN 1998-1., 2004) and US (FEMA P-1050., 2015), leading to 74 analyses. The engineering demand parameters outlined in Section 6.3 are applied for each analysis to find a peak demand capacity ratio (DCR). Due to the brittle nature of stone masonry with mud mortar, the larger earthquakes led to dynamic instability.

6.5.1 Cloud Analysis

Cloud analysis makes use of the results of NLTHA in terms of intensity measure (IM) of the earthquake (i.e. PGA, S_a) and the peak demand capacity ratio (DCR) of the FE model to find a fragility curve. A simple cloud analysis is obtained by carrying out linear regression of the IM and DCR in log space to obtain a and b. This gives the median DCR given IM ($\eta_{DCR|Sa}$) as shown in Equation 6.9. The logarithmic standard deviation of the DCR given an IM value ($\beta_{DCR|Sa}$) is given by Equation 6.10, where DCR_i and $s_{a,i}$ are the DCR and IM from each analysis in the NLTHA. Finally, the fragility function is obtained using a cumulative lognormal distribution function shown in Equation 6.11.

$$\ln\ \eta_{DCR|S_a}(S_a) = \ln\ a + b \cdot \ln\ (S_a) \tag{6.9}$$

$$\beta_{DCR|S_a} = \sqrt{\sum_{i=1}^{N} \left(\ln\ DCR_i - \ln\left(a \cdot {S_{a,i}}^{b}\right)\right)^2 / (N-2)} \tag{6.10}$$

$$P(DCR > 1 \mid S_a) = \Phi\left(\frac{\ln \eta_{DCR|S_a}}{\beta_{DCR|S_a}}\right) = \Phi\left(\frac{\ln\ a \cdot S_a^b}{\beta_{DCR|S_a}}\right) \tag{6.11}$$

The brittle nature of stone mud masonry caused some of the analyses to collapse, also referred to as dynamic instability. Jalayer et al. (2017) developed a modified version of the cloud analysis which can be used to find fragility curves when some of the analyses undergo dynamic instability. The formulation of the fragility curve is given in Equation 6.12. In Equation 6.12, the term $P(DCR_{LS}>1|S_a,NoC)$ is the probability of the limit state being exceeded, given that the analysis did not collapse. This is found by carrying out a conventional cloud analysis on the results that did not collapse (NoC), as shown in Equation 6.13. The probability of collapse at a given intensity measure ($P(C|Sa)$) is required. This is obtained using logistic regression, as shown in Equation 6.14. The term $P(DCR_{LS}>1|S_a,C)$ is the probability of a limit state being exceeded, given that the building collapsed. This can be assumed to be equal to one.

Figure 6.13a shows the linear regression in log space of the analysis results that did not collapse. Figure 6.13b shows the fragility curves from the analysis results that did not collapse. Figure 6.13c shows the collapsed (C) and non-collapsed analysis (NoC) logistic regression in Equation 6.14. Finally, Figure 6.13d illustrates the final fragility analysis as calculated using Equation 6.12.

$$P(DCR_{LS} > 1 \mid S_a) = P(DCR_{LS} > 1 \mid S_a, NoC) \cdot \left(1 - P(C \mid S_a)\right) + P(DCR_{LS} > 1 \mid S_a, C) \cdot P(C \mid S_a) \tag{6.12}$$

$$P(DCR_{LS} > 1 \mid S_a, NoC) = \Phi\left(\frac{\ln \eta_{DCR_{LS}|S_a,NoC}}{\beta_{DCR_{LS}|S_a,NoC}}\right) = \Phi\left(\frac{\ln\ a \cdot S_a^b}{\beta_{DCR_{LS}|S_a,NoC}}\right) \tag{6.13}$$

$$P(C \mid S_a) = \frac{1}{1 + e^{-(\alpha_0 + \alpha_1 \cdot \ln\ S_a)}} \tag{6.14}$$

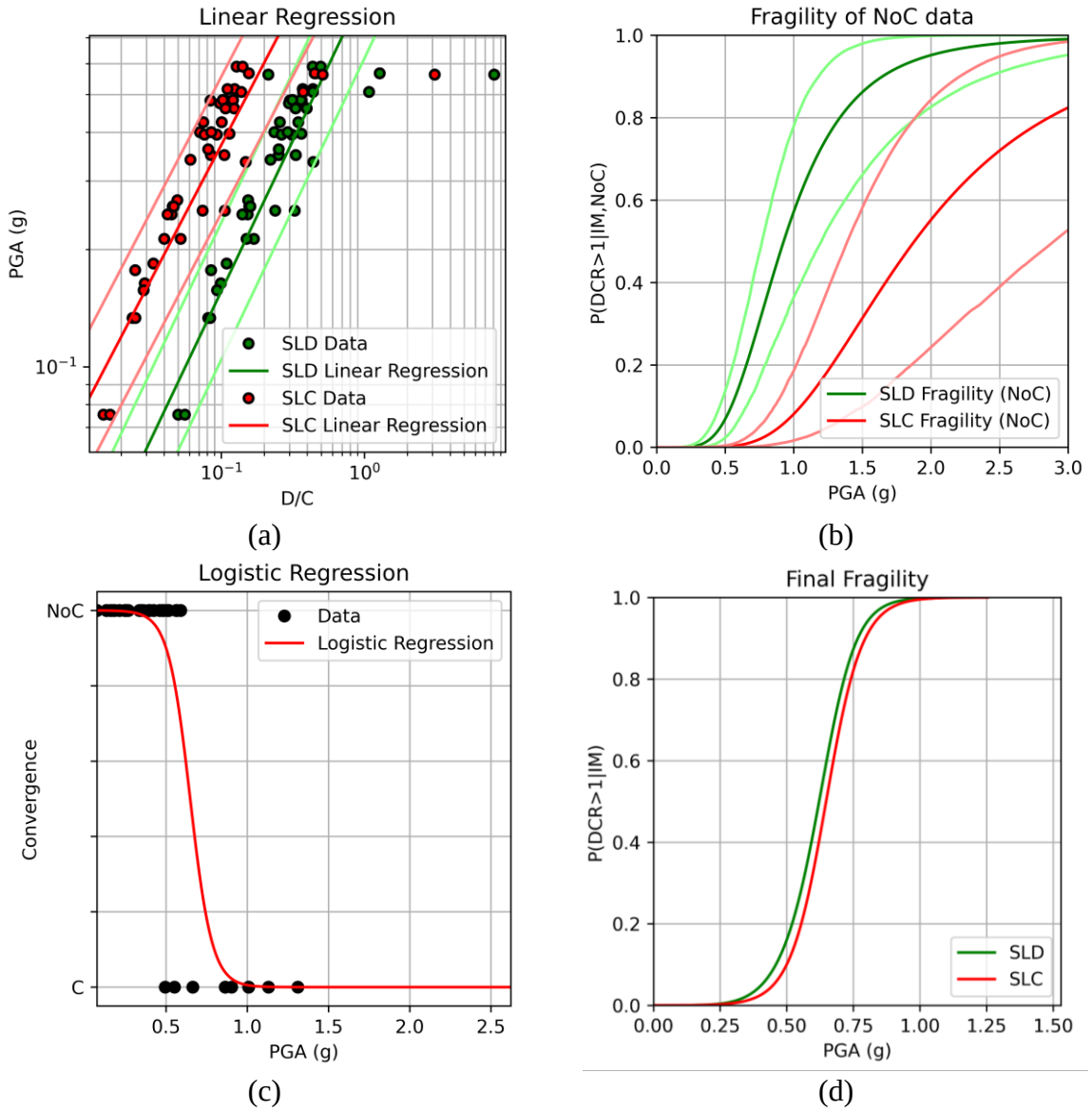

Figure 6. 13 (a) Linear regression of NLTHA results, (b) Classic cloud analysis carried out on NoC results, (c) Logistic regression of dynamic instability against PGA, (d) Final fragility curve of all NLTHA results

Table 6.10 shows the fragility parameters of the MDOF fragility curves. The Jalayer et al. (2017) formulation does not return a lognormal fragility function. Therefore, a lognormal cumulative distribution function is fitted using a η of the median value and the β is derived using Equation 6.15, where 84th and 16th are the 84th and 16th percentile values, respectively.

$$\beta = \frac{\log(84^{th}) - \log(16^{th})}{2} \tag{6.15}$$

Table 6. 10: Fragility parameters for IDA results of equivalent SDOF model.

Limit State	η (g)	β
Damage Limit State (SLD)	0.622	0.191
Limit State for the Prevention of Collapse (SLC)	0.647	0.173

Comparing the values in Table 6.9 and Table 6.10 for SLD, the η is 3% higher for the MDOF model. For the limit state for the prevention of collapse (SLC), the SDOF model has a η value that is 12% higher than the MDOF model. These differences are likely due to the detailed micro model accounting for a variety of different failure mechanisms and dynamic responses. These differences are relatively small, and the SDOF model's computational time was several orders of magnitude lower than the MDOF model. On the other hand, the overestimation of collapse capacity by 12% in the SDOF model emphasises the importance of local failure mechanisms in the stone masonry with mud mortar structure, making the micro-modelling approach worth pursuing for template structures (i.e., one structural model for the risk assessment of a large region).

6.6 Computational Run Time

The main advantage of the SDOF model compared to the MDOF model is the significantly reduced computational demand. A sample analysis was carried out using an 11th Gen Intel Core i7-11850H and carrying out the NLTHA for the unscaled KTP recording from the Gorkha earthquake. The SDOF model has a run time of 0.418s compared to the MDOF model which has a run time of 89,865s (24 hrs 57 min 45 sec). The SDOF model was composed of one element between two nodes. One node is fixed and the other is free in one direction. In contrast the MDOF is formed of 39,786 connected by a series of 111,276 elements. All nodes except the ground nodes are unrestrained. This drastic difference in run time confirms that carrying out an IDA on the MDOF model is not feasible.

6.7 Literature Comparison

The fragility curves derived in Sections 6.4.4 and 6.5.1, respectively, can be compared to values from literature. It should be noted there are several factors that can affect the fragility curve,

such as the assessment method (analytical vs numerical vs empirical), the material/material properties of the structure and the height of the building. Other factors such as layout, mass and assessment method (i.e. cloud vs IDA) will cause minor variations in fragility values. Table 6.11 shows the parameters for a series of Nepalese masonry fragility curves from literature and the fragility parameters from this study. It can be seen that there is a high level of variability in the η (median) values for each of the damage states. For example, for DS2, Guragain (2015) gives a η value of 0.08 g, and Martins & Silva (2020) provide a η value of 0.53 g. It can be seen that this study shows the buildings to have a low level of fragility (i.e. high η values) relative to many studies in literature. There are three main reasons for this: material properties, building height, code conformity and fragility assessment method.

The studies shown in Table 6.12 use the European macroseismic scale (EMS-98) (Grünthal, 1998), therefore, it is necessary to draw an equivalence between EMS-98 damage states and CNR-DT 212/2013. (2014) limit states. The CNR limit states are defined in *Section 2.1.1* of CNR-DT 212/2013. (2014). SLD is assumed to be parallel to DS2, with both of them being defined as a low level of damage, and the building remains usable. SLC is assumed parallel to DS4, with both of them being defined as heavy damage to structural components. These parallels are shown in Table 6.11.

Table 6. 11: Comparison of EMS-98 (Grünthal, G., 1998) damage states and CNR-DT 212/2013. (2014) limit states

Description	EMS-98 (Grünthal, G., 1998)	CNR-DT 212/2013. (2014)
Light damage	DS1	
Moderate/extensive damage	DS2	Damage limit state (SLD)
Near collapse	DS3	Severe damage limit state (SLS)
Collapse	DS4	Limit state for the prevention of collapse (SLC)

The first point of comparison is with the World Bank (2019), which conducted a fragility assessment on a single storey Nepalese building made from dressed stone with mud mortar. A comparison of the fragility curves for the SDOF approximation, the MDOF and the fragility curves from the World Bank (2019) are shown in Figure 6.14. The World Bank (2019) uses

the limit states provided by ASCE 41–06. (2007), where damage limit state (SLD) can be equated to immediate occupancy (IO), and the limit state for the prevention of collapse (SLC) can be equated to collapse prevention (CP). It can be seen from the pushover curves in Figure 6.14b that this study results in a building that is not only significantly stiffer but also reaches collapse at a significantly lower drift value. The structure in this study reaches collapse at a roof drift level of 0.30%. This limit state point was assessed using the multiscale approach in CNR-DT 212/2013. (2014), which assesses global performance, element level performance and strength degradation. Further details of this approach can be found in Section 6.3. The Pahar trust health centre exceeded SLD and SLC in the SPO due to excessive drift in a pier. At the point of exceeding SLC, the peak global drift was 0.3% in this study, and The World Bank (2019) has a roof drift of 1.86%. In comparison, Morandi et al. (2018) assessed the ultimate drift ratio for various masonry typologies using experimental data. They found an average ultimate drift of 0.30% and a standard deviation of 0.12% for shear failure. The difference in initial stiffness can be accounted for in material properties with The World Bank (2019) using an elastic modulus of 240 MPa. In this study, we have used an elastic modulus value of 15,500 MPa and 55 MPa for the stone and mortar respectively, for the reasons outlined in Section 6.2. As shown in Figure 6.14a, the Pahar trust health centre has a significantly higher η value relative to The World Bank (2019) at SLD due to the higher capacity and higher stiffness values. The fragility curves for SLC are closely aligned between this study and The World Bank (2019), with a η of 0.727 g and 0.72 g, respectively.

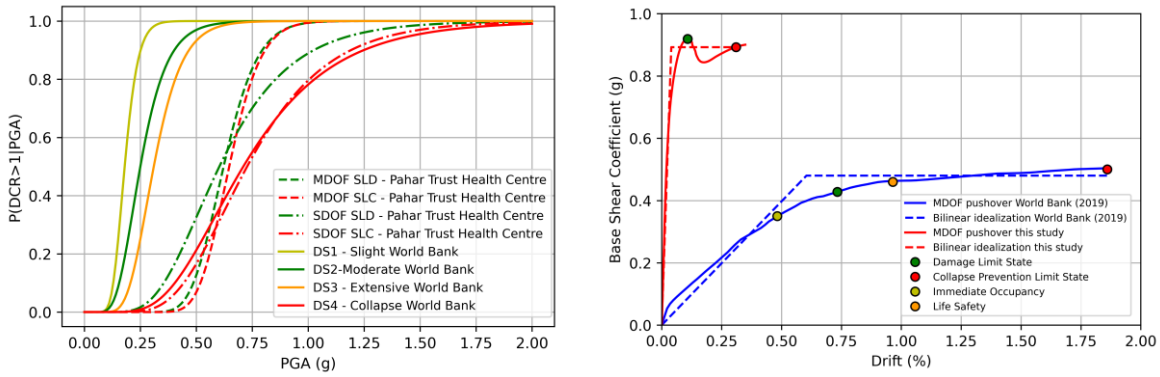

(a) (b)

Figure 6. 14 Comparison of the (a) Fragility and (b) pushover curves of single-storey stone mud masonry structures from The World Bank (2019) and this study.

Guragain (2015) also derived numerical fragilities for Nepalese masonry structures. Guragain (2015) created an applied element method (AEM) for a single-storey stone mud masonry structure. A tensile strength of mortar of 0.078 MPa was used, and a Young's modulus of mortar

of 0.04 MPa. These values were based on a diagonal shear compression test by Sakurai (2011). The resultant fragilities from this study are shown in Figure 6.15. It can be seen that compared to the fragilities from this study, the η values is significantly lower. There are several potential reasons for this. Guragain (2015) carries out the analysis for 6 different structures and then combines the results, some of these structures are two-storey. None of the structures in Guragain (2015) have a reinforcing band, this would result in the structure being more likely to collapse due to a local failure.

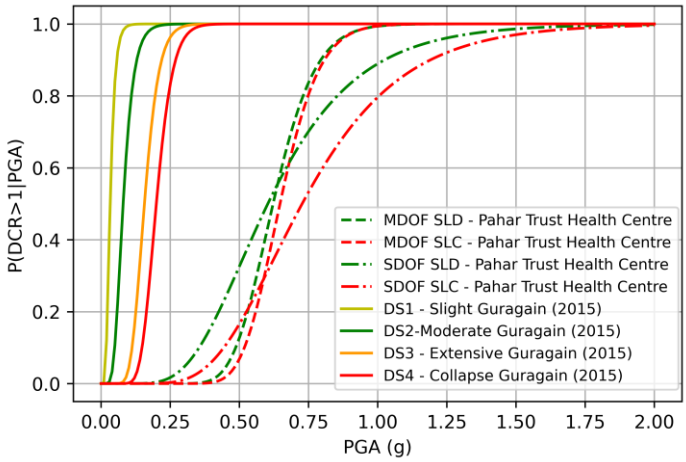

Figure 6. 15 Fragility curve for a single storey stone mud masonry Nepalese building from Guragain (2015) and this study.

Several studies have derived analytical fragilities for masonry structures. Giordano et al. (2021) derived the fragility curves for stone-mud, brick-mud and brick cement Nepalese masonry buildings. The analysis is carried out for single and multiple story buildings. A Monte Carlo simulation is carried out with varying several parameters. An analytical capacity curve is formulated, and the demand is found using the capacity spectrum method (CSM). It can be seen from Figure 6.16 that the fragility curves for single storey stone-mud masonry buildings from Giordano et al. (2021) have significantly lower η values. This study also uses the elastic modulus from The World Bank (2019) of 240 MPa. Analytical fragilities are typically lower than detailed numerical models as the analytical approximation of capacity has a conservative nature. An example of this is applying a "Section thickness reduction factor" for the thickness of the wall. This reduction factor has a linear distribution between 0.3 and 0.7; hence an average reduction factor of 0.5 is used.

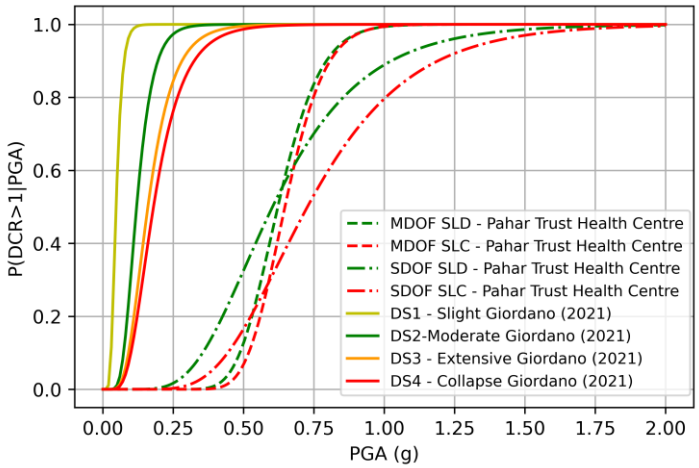

Figure 6. 16: Fragility curve for a single storey stone mud masonry Nepalese building from Giordano et al. (2021) and this study.

Several empirical fragility studies have been carried out, using historical damage data from Nepal to derive fragility curves for a specific building typology. Empirical fragility curves typically have significantly higher β values relative to analytical and numerical fragilities due to variability in building height, area material properties etc. Details for the derivation of empirical fragility curves can be found in Section 2.5.2.1. Analytical fragilities can be derived, accounting for these uncertainties using the FAST method (De Luca et al., 2014; De Luca et al., 2015). Giordano et al. (2020) derived a series of empirical fragilities for different building typologies using damage data from 17,595 school buildings after the Gorkha 2015 earthquake. Giordano et al. (2020) derived fragility curves for "Unreinforced masonry bearing wall, low-rise" structures. These empirical fragility curves are compared to the fragilities from this study in Figure 6.17a. It can be seen that these fragility curves have significantly lower η values relative to this study. It should be noted that Giordano et al. (2020) consider the buildings to be "pre-code", which is not the case with Pahar Trust health centre. As a result, the buildings from Giordano et al. (2020) are significantly more fragile.

Gautam et al. (2018) derive empirical fragility curves for unreinforced stone masonry with mud or cement mortar. These fragilities are derived from damage data from Nepalese earthquakes in 1934, 1980, 1988, 2011, and 2015. Using damage data from multiple earthquakes adds record-to-record variation to the fragility curves. As building techniques have developed since 1934, these earlier records may not represent the quality of structure in Nepal today. Figure 6.17b compares the fragility curves from this study and Gautam et al. (2018). It can be seen that the η values for Gautam et al. (2018) are significantly lower than from our study, likely due to the Pahar trust health centre being a modern single-storey structure designed to modern

codes. The empirical fragility curves from Gautam et al. (2018) are from buildings that may be over 100 years old and therefore have been designed to a lower level and also degraded over time.

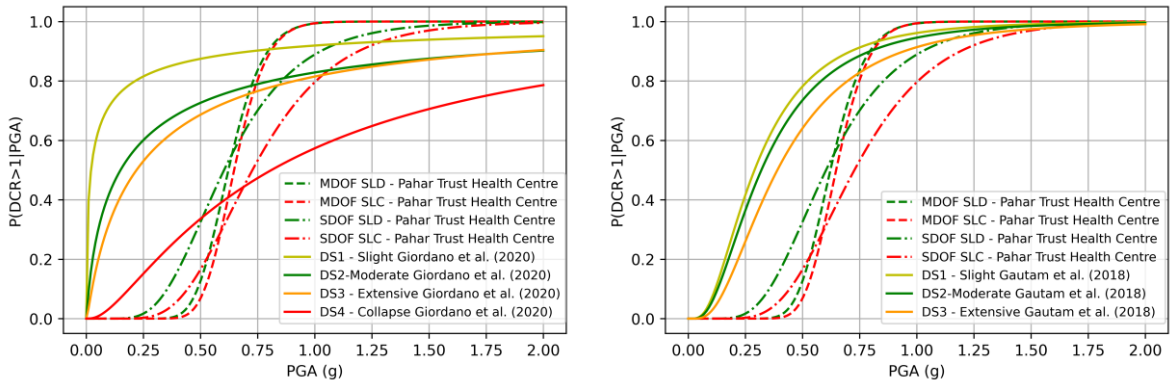

(a) (b)

Figure 6. 17 Comparison of the fragilities from this study and the empirical fragilities from (a) Giordano et al. (2020) (b) Gautam et al. (2018)

Martins et al. (2020) use a method of assessing the fragility most similar to the one in this study, where non-linear time history analysis (NLTHA) is carried out on a single degree of freedom (SDOF) oscillator. A separate pushover curve was specified for each building type. In Martins et al. (2020), for the single storey unreinforced masonry building, a height of 2.8m is assumed, a yield drift of 0.14% and an ultimate drift of 0.6%. In comparison, our model has a height of 2.74 m, a yield drift of 0.172% and an ultimate drift of 0.497. Building height and drift ratios are similar between this study and Martins et al. (2020). The pushover and limit drifts can be seen in Figure 6.18a. The yielding period is calculated using Equation 6.16, where *H* is the structure's height. For a structure that is 2.8 m tall, this would give a period of 0.15s, which is significantly higher than the Pahar Trust health centre period. Equation 6.17a is used to find the spectral displacement (S_d), where $\delta roof$ is the roof displacement, and Γ is the first mode participation factor. Equation 6.17b is then used to find the spectral acceleration (S_a). For unreinforced masonry, Martins et al. (2020) assume $\delta roof$ equal to 0.14% drift for yield and a Γ value of 1.4. The resultant pushover and limits can be seen in Figure 6.18a, in *Sa-Sd* space, and the fragility curves can be compared to the Pahar Trust health centre in Figure 6.18b. It should be noted that Martins & Silva (2020) present their fragility findings with an intensity measure of spectral acceleration at 0.3 seconds ($S_a(0.3)$). To allow a like for like comparison with this study and other literature values, this is converted to PGA using a scaling relationship based on the ground motion prediction equation (GMPE) proposed by Boore et al. (2014). The

spectral acceleration value is multiplied by a scaling factor given by Equation 6.18, where $\widehat{PGA}_{GMPE}$ is the average PGA value obtained in the GMPE and $\widehat{Sa_{(0.3)}}_{GMPE}$ is the average spectral acceleration value at 0.3 seconds. The GMPE used in Equation 6.18 assumes normal faulting, a Vs30 value of 300 m/s, a magnitude range of **M**w 5 to **M**w 8 and a distance range of 1 km to 30 km (Novelli et al., 2021). For the case of 0.3 seconds, a scaling factor of 1.9965 is used.

$$T_y = 0.062H^{0.9} \tag{6.16}$$

$$S_d = \frac{\delta_{\text{roof}}}{\Gamma} \tag{6.17a}$$

$$S_a = S_d\left(\frac{2\pi}{T}\right)^2 \tag{6.17b}$$

$$PGA(g) = Sa_{(0.3)}\frac{\widehat{PGA}_{GMPE}}{\widehat{Sa_{(0.3)}}_{GMPE}} \tag{6.18}$$

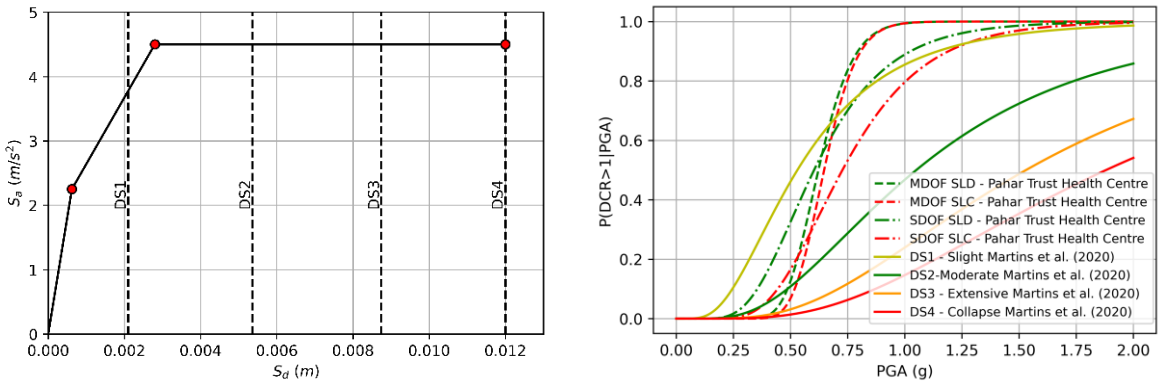

(a) (b)

Figure 6. 18 (a) pushover curve of single-storey unreinforced masonry structure from Martins et al. (2020). (b) comparison of fragility curves from Martins et al. (2020) and this study.

It can be seen from Figure 6.18b that there is a significantly higher level of dispersion (β) in the Martins et al. (2020) fragility relative to the ones from this study. This is primarily due to the Martins et al. (2020) fragility curves being for a range of one-storey unreinforced masonry structures. In contrast, the fragility curves from this study are for a specific structural design. The η value at SLD limit state is 0.603 g for the SDOF model in our study compared to 0.53 g for DS2 from Martins et al. (2020). This small difference is likely due to the difference in initial stiffness and therefore initial period. While there is no direct relationship between the initial period and SLC or SLD in Eurocode 8 Part 1 4.3.1(7) (EN 1998-1., 2004), once cracking has occurred, the elastic flexural and shear stiffness can be taken as one half of the initial stiffness. The masonry micro-model used in this study has a damage model laid out in Section 2.6.3.2,

which inherently reduces the structure's stiffness once cracking has occurred. The η value for SLC limit state for the SDOF model in this study is 0.727 g compared to 0.94 g in Martins et al. (2020). This significant difference could be due to the difference in the period.

Overall, relative to fragility curves from literature, the curves from this study have a higher η value, particularly for the SLD limit state. The η value for SLD is higher in this study than in any of the benchmark studies, and for the SLC limit state, the SDOF model is higher than three of the five benchmark studies. The higher η value is likely due to the Pahar trust health centre having a modern code-compliant seismic design. Furthermore, as it is a new structure, it has not undergone any degradation. It can also be seen that this study has a lower β than many of the literature studies. This is likely due to the fragility curve being for a specific design as opposed to a type of building, therefore, all the variation is caused by record-to-record variability. In contrast, many literature studies vary in building characteristics such as height, mass, etc.

Table 6. 12 Summary of the η values (median) for the fragility curves for stone masonry buildings in Nepal

Reference	**Approach**	**Material**	**DS1 (g)**	**DS2/ SLD (g)**	**DS3 (g)**	**DS4/SLC (g)**
Giordano et al,. (2021)	Analytical	Rubble stone mud masonry	0.047	0.12	0.16	0.18
Gautam et al,. (2018)	Empirical	Stone masonry (mortar is mud or cement)	0.29	0.32	0.39	N/A
Giordano et al,. (2020)	Empirical	Unreinforced masonry	0.021	0.15	0.22	0.81
Guragain,. (2015)	Numerical	Brick with mud	0.033	0.080	0.157	0.200
Martins & Silva (2020)	Analytical/ Numerical	Unreinforced masonry	0.27	0.53	0.75	0.94
World Bank (2019)	Numerical	Dressed stone in mud masonry	0.15	0.23	0.32	0.72
SDOF (This Study)	Numerical	Dressed stone in mud masonry	N/A	0.603	N/A	0.727
MDOF (This Study)	Numerical	Dressed stone in mud masonry	N/A	0.622	N/A	0.647

6.8 Seismic Risk Assessment

The seismic hazard map used for this risk assessment is provided by Stevens et al. (2018). The hazard map provides two points on the hazard curve, and the rest of the curve is obtained using a second-order approximation detailed in Section 3.4. Using the hazard curve at each geographic point and the fragility curves derived in Sections 6.4.4 and 6.5.1, the annual probability of exceeding the damage limit state and the limit state for the prevention of collapse can be found across Nepal. Equation 6.19 shows the integration of the fragility and hazard curves where P_{LS} is the annual probability of exceeding a given limit state, $P_{ls/s}$ is the fragility curve, and $H(s)$ is the hazard curve. This integral can be solved numerically using Equation 6.20, where $H(S_i)$ is the hazard at a given PGA and $P_{ls/scgi}$ fragility at the midpoint of i and i+1. This numerical integration is carried out using the fragility curves for the damage limit state and the limit state for the prevention of collapse, for the SDOF and MDOF model and the hazard curves at each geographic point. The results can be seen in Figures 6.19 and 6.20.

$$P_{LS} = \int_0^{\infty} P_{ls/s} \left(\frac{dH(s)}{ds} \right) ds \tag{6.19}$$

$$P_{LS} = \sum_{i=1}^{n} [H(s_i) - H(s_{i+1})] \, P_{ls/Scgi} \tag{6.20}$$

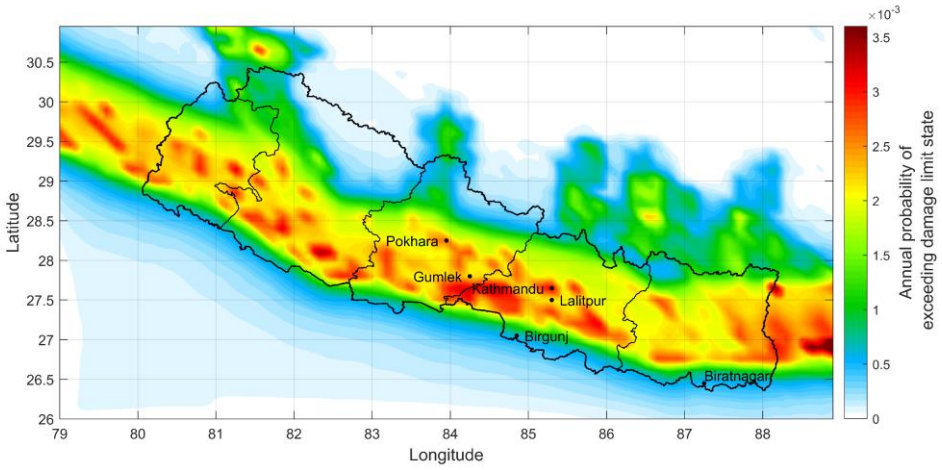

(a)

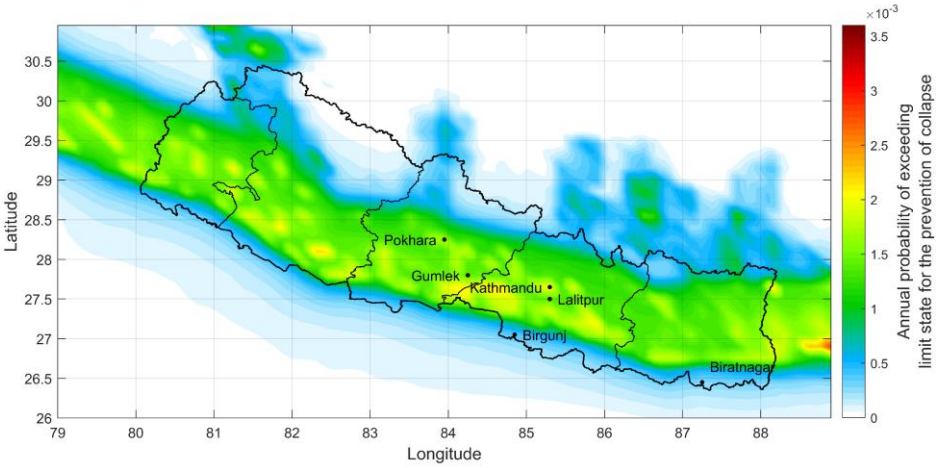

(b)

Figure 6. 19: Annual probability of the SDOF idealisation of the building exceeding (a) Damage limit state (b) Limit state for the prevention of collapse

Pinto et al. (2014) presented a series of target risk values for structures of different importance classes and different limit states. For the Pahar Trust health centre, we can assume an importance class iii as the consequences can be considered in line with schools and assembly halls but not as severe as a hospital. Pinto et al. (2014) risk values are for the assessment of existing Italian structures, and therefore as Italy is a developed country, there is a low level of acceptable socio-economic risk.

Figure 6.19 shows the mean annual frequency of exceeding SLD and SLC across Nepal. The five most populated cities in Nepal Kathmandu, Pokhara, Lalitpur, Biratnagar and Birgunj (Government of Nepal, 2012), are also indicated on the risk maps in Figure 6.19. These cities and the corresponding mean annual frequency for exceeding each limit state are shown in Table 6.13. The average risk values across Nepal and the threshold values from Pinto et al. (2014) are also shown in Table 6.13. Table 6.13 indicates that the SDOF model does not exceed the threshold risk value for SLD in any of the largest cities. Table 6.13 shows that the SDOF exceeds SLC threshold risk values in Kathmandu and Pokhara.

The results for the MDOF model are shown in Figure 6.20 and Table 6.13. It can be seen that, as with the SDOF system, the thresholds are never exceeded for the SLD limit state. For the SLC limit state, the MDOF exceeds the threshold risk values in Kathmandu only. It can be seen that for both Birgunj and Biratnagar, the risk values are significantly below the threshold value, this emphasises the effect that the varying seismic hazard has on the risk values across Nepal.

There are several reasons why the threshold risk values could have been exceeded for the SLC limit state in some regions of Nepal. The threshold risk values presented by Pinto et al. (2014) are for existing Italian structures. This may not be appropriate for Nepalese structures as the risk values in Pinto et al. (2014) are based on socio-economic consequences, which may not be consistent between Nepal and Italy.

It should also be noted that this study was carried out with a seismic hazard Map from Stevens et al. (2018), which has significantly higher PGA values relative to the value presented in the Nepalese Building Code, even in its most recent version released in 2020 (NBC-105:1994, 1994; NBC-105:2020, 2020). Using Kathmandu as a point of comparison, for the 475 year return period earthquake, Stevens et al. (2018) give a PGA of 0.61 g, in contrast for the 500 year return period NBC-105:1994 (1994) provides a PGA value of 0.36 g, and NBC-105:2020 (2020) gives a 475 year return period PGA value of 0.35 g. It can be seen from Table 2.3 that there have been many PSHA studies on Nepal with varying PGA values for a 475-year earthquake in Kathmandu. The value of 0.36 g is significantly lower than all studies shown in Table 2.3. This is likely because if a PGA value as high as 0.61 g was implemented into the Nepalese building codes, the criteria for the design of structures could be considered unobtainable and, therefore would bush down code compliance. Therefore, by using the PSHA study by Stevens et al. (2018), the seismic risk values are significantly higher than they would have been if other PSHA studies were used.

As noted in Section 6.2, this design is a template design, and it has been implemented in Gumlek, a village 33 miles southeast of Pokhara. The seismic risk values for the building in Gumlek can be seen in Table 6.13. The Gumlek health centre does not exceed the threshold risk values from Pinto et al. (2014). This implies that the seismic risk to the Gumlek health centre is lower than what is accepted in Italy for class iii structures, however it also implies that this building could not be replicated at all points across Nepal with an equal level of safety.

Table 6. 13 Mean annual frequency for cities

	SDOF SLD	SDOF SLC	MDOF SLD	MDOF SLC
Kathmandu	0.0032	**0.0021**	0.0022	**0.0019**
Pokhara	0.0026	**0.0017**	0.0018	0.0015
Lalitpur	0.0021	0.0014	0.0015	0.0013
Biratnagar	0.0005	0.0003	0.0003	0.0002
Birgunj	0.0006	0.0003	0.0004	0.0003
Average across Nepal	0.0016	0.0010	0.0011	0.0009
Gumlek	0.0021	0.0013	0.0015	0.0012

Target Italian risk value for Class iii (Pinto et al., 2014)	0.03	0.0015	0.03	0.0015

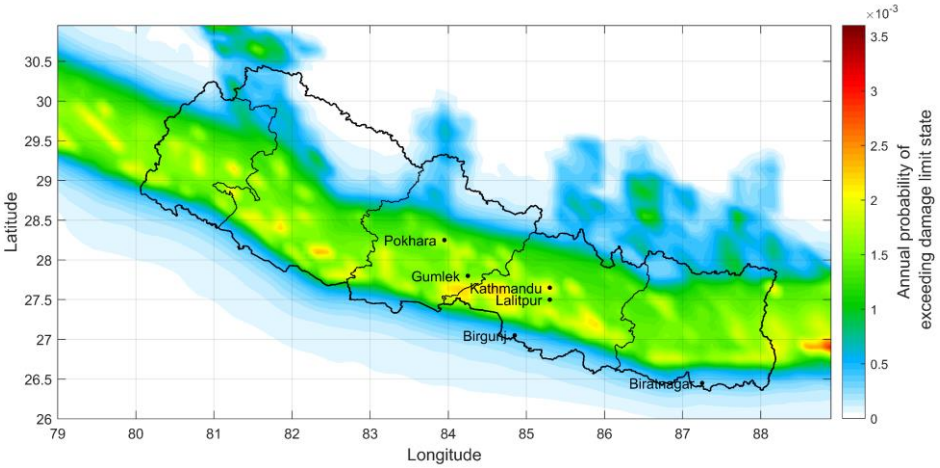

(a)

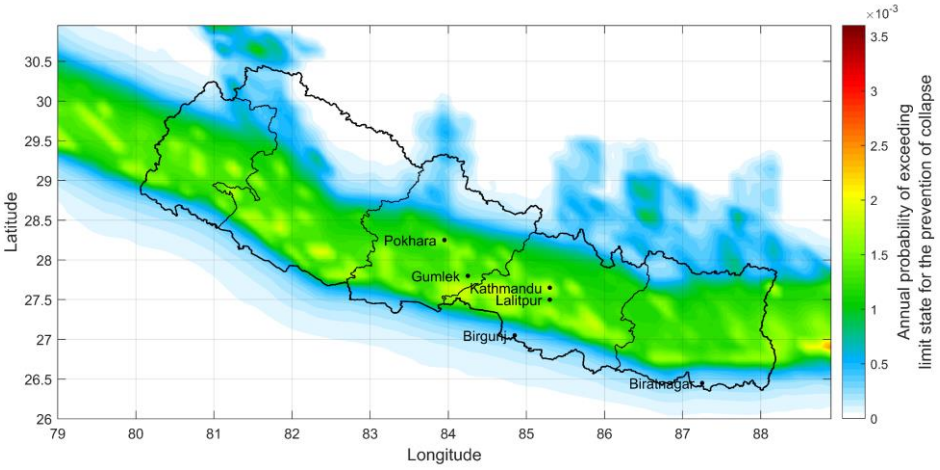

(b)

Figure 6. 20. Annual probability of the MDOF idealisation of the building exceeding (a) Damage limit state (b) Limit state for the prevention of collapse

6.9 Conclusions

This chapter used continuous micro-modelling to carry out a seismic risk assessment for an unreinforced template health centre across Nepal. The masonry modelling technique was validified for the case of irregular masonry in Chapter 5. This masonry modelling technique was then applied to a template health centre design provided by Pahar Trust (2020). A static

pushover (SPO) was carried out to find the lateral response. The SPO curve was then used to form an SDOF model. An IDA was carried out on the SDOF, and the results were used to find fragility curves. These fragility curves were compared with literature values. A series of 74 NLTHA was then carried out on the full MDOF model, and a modified version of the cloud analysis was used to derive the fragility curves accounting for non-convergence cases. These fragility curves were also compared to literature values. Finally, a complete seismic risk assessment was carried out across Nepal for both the MDOF and SDOF models.

A continuous masonry micro-model was created for the Pahar Trust template health centre, and a non-linear static analysis was performed. A bilinear and a quadrilinear idealisation as to evaluate the most suitable approach. The quadralinear was used to create an equivalent SDOF model of the building. An IDA was carried out on the equivalent SDOF to find fragility curves for the damage limit state and the limit state for the prevention of collapse. The η value for SLD was 0.603 g and for SLC was 0.727 g. These values were compared to a series of values from literature where the SLD value was relatively high compared to literature values. The SLC value was found to be greater than three of the literature values and smaller than two of the literature values.

A non-linear time history analysis was carried out on the full MDOF model. The ground motions used were formed of FEMA P695 (FEMA P695, 2009), a compatible spectrum set, and Gorkha 2015 recordings. A modified version of the cloud analysis (Jalayer et al., 2017) that allowed for collapsed cases was used from the non-linear time history analysis results to derive the fragility curves. These fragility curves were benchmarked against literature values. As with the SDOF model, the η was relatively high for the damage limit state and was mid-ranking for the limit state for the prevention of collapse.

This study has demonstrated that a high-fidelity micro-model can capture local failure mechanisms, making it a suitable option for masonry template structures and assessing regional risk. This kind of modelling can account for mortar and stone properties independently. This is an advantage in developing countries where the possibility of carrying out experimental campaigns on masonry wallettes is relatively limited, and simple tests on stone and mortar can be more easily conducted.

The fragility curves obtained for the damage limit state and the limit state for the prevention of collapse through the 3D non-linear micro-model of the structure are relatively close to each other. This shows the inherent brittle nature of the stone with mud mortar structural typology

even in the presence of horizontal reinforced concrete bands, which typically improves the local ductility of the piers.

From a risk evaluation point of view, the Pahar Trust design of the health centre shows acceptable risk values in line with thresholds from developed countries, even in areas with very high seismicity in Nepal. This indicates that the template design approach for single storey structures with simple seismic detailing (e.g., horizontal reinforced concrete bands) can be a convenient option for non-Governmental organisations even when operating in countries with highly variable seismicity.

Chapter 7: Conclusions and Further Work

7.1 Conclusions

This thesis has used state of the art modelling techniques to assess the seismic risk to Nepalese buildings. Nepal has a large seismic hazard due to its proximity to the Indian and Eurasian plate boundary. Due to economic restraints, Nepalese infrastructure has a high level of seismic vulnerability. In recent years substantial efforts have been made to reduce the seismic risk. Nepal first released seismic design codes in 1994 (NBC 105, 1994) and has subsequently made them a legal requirement in all cities across the country. This thesis sought to quantify the seismic risk to a template reinforced concrete structure and an unreinforced masonry structure. It also aimed to develop an established risk assessment method (the FAST method) for the Nepalese context and use it to evaluate the risk to RC structures in an area of Kathmandu.

This thesis derived fragility curves for various structures and structural typologies. These fragility curves were integrated directly with the seismic hazard to assess the seismic risk. Although seismic hazard is not the focus of this research, it has a significant effect on the final risk values. In Nepal, PSHA studies have resulted in varying results for the seismic hazard. NBC 105 (1994) presented a seismic hazard map with Kathmandu having a 500-year return PGA of 0.36 g. Although this value is considered low, other pre-Gorkha PSHA studies gave Kathmandu a 475-year return earthquake ranging from 0.38 g to 0.525 g (Parajuli et al., 2010; Thapa and Guoxin, 2013; Chaulagain et al., 2015). After the Gorkha 2015 earthquake, PSHA studies have used the data from Gorkha and have found a 475-year return earthquake with a PGA of 0.55 g to 0.75 g (Pokhrel et al., 2019; Stevens et al., 2018; Rahman and Bai., 2018; Subedi and Parajuli, 2016). These PSHA values are significantly higher with respect to NBC 105 (2020) hazard map, which gives a 475-year return earthquake in Kathmandu of 0.35 g. It is assumed that this low PGA value is to make the design level set in the Nepalese design codes obtainable and therefore increase code compliance.

After reviewing the relevant literature for this thesis in Chapter 2, a seismic risk assessment was carried out for a template masonry infilled RC school design provided by Pahar Trust. Pahar Trust is a Bristol-based charity that uses template design to construct schools and health centres across Nepal efficiently. A template design is where a single design is used in multiple locations with only minor variations based on site conditions and locally available materials. The design of a Pahar Trust school was used to develop a finite element model. The seismic risk was assessed with and without considering the structural contributions of the masonry

infills. Non-linear time history analysis (NLTHA) was used to carry out a cloud analysis to derive the fragility curves at different limit states. These fragility curves were compared to empirical fragility curves from literature. The fragility curves from this study had similar median values to those derived based on damage data from Gorkha 2015. The fragility curves were then integrated with the seismic hazard to find the seismic risk. These risk values were then compared against benchmark values from literature. This study showed that a template structure could be used across Nepal if adequately designed. This study also showed the necessity of considering the structural contribution of the masonry infills, with the bare model resulting in risk values that exceeded threshold values set out in literature.

The implications of Chapter 3 are that when adequately designed, a template design of a masonry infilled RC frame structure can be used across an area of varying seismic hazard. This study should give Pahar Trust the confidence to maintain this strategy for the design of schools. As the seismic risk values in parts of Nepal were significantly lower than the benchmark values, this could imply that the building is over-designed in certain scenarios. Due to the fact that the bare model exceeded the benchmark risk threshold value, this highlights the importance of explicitly considering the structural contribution of the infills.

In Chapter 4 the FAST method was updated for the Nepalese context. The FAST method is a spectral based, rapid assessment method for the seismic vulnerability of masonry infilled RC frame structures. This method had previously been calibrated for Mediterranean masonry infills. Chapter 4 aimed to update the FAST method using local material properties and interstorey drift ratios. The Nepal Fast method was then applied to the structure used in Chapter 3, and the fragility curves were compared. The fragility curves showed a relatively close degree of matching. The Nepal FAST method was then applied to a catalogue of 6869 RC infilled buildings from Ward-35 of Kathmandu. The damage data obtained from the Nepal FAST method with the Gorkha ground motion was compared to the observed damage after the Gorkha earthquake. These results showed that the Nepal FAST method was conservative and resulted in damage values that were significantly higher than what was observed.

The Nepal FAST method developed in Chapter 4 has the potential to be implemented by local authorities within Kathmandu and other urban environments in Nepal to allow a more informed decision on where seismic investment should be used. Although the Nepal FAST was shown to overestimate the damage, it can still be used to assess the comparative risk of specific areas relative to other regions. By using a small number of characteristics of the buildings to

determine the risk, the local government can carry out a low-cost seismic risk assessment of target areas before allocating funds for seismic investment. The FAST method can also be used to investigate the effect on the risk of making minor alterations to the design codes, such as the aspect ratio in plan etc.

In Chapter 5, a validation of continuous micro-modelling for the case of irregular stone masonry was carried out. Continuous micro-modelling is a detailed finite element method of modelling masonry. It has previously been shown to accurately capture the shear capacity of a regular brick masonry pier. A numerical model of a regular stone pier was used to ensure that the shear capacity matched code based analytical values from CNR-DT 212/2013. (2014). The second stage of the validation involved creating a numerical model of two irregular masonry piers from an experimental campaign carried out by Senaldi et al. (2018). The shear capacity of the numerical model was compared to the experimental work at a variety of vertical compression ratios. The comparison was also carried out for the code-based approach. All these results showed a strong level of matching. The final step of the masonry modelling validation was comparing an irregular masonry pier and an equivalent regular pier. A set of three criteria were set out to create an equivalent regular pier. This is an essential part of creating a continuous micro model of an irregular masonry structure as it is impossible to obtain every stone's dimension in the structure. The pushover response of the irregular and regular piers had a strong level of matching.

Chapter 5 successfully validated the use of continuous micro-modelling for irregular stone masonry. This validation verifies that this modelling technique is diverse in its application and can successfully capture the capacity and failure mechanism of a laterally loaded masonry pier at a range of vertical compression ratios. This validation gives the confidence in Chapter 6 to use continuous micro-modelling to assess the seismic risk to an unreinforced stone masonry building.

In Chapter 6, a detailed masonry micro-model was formed based on the design of a URM health centre in Nepal provided by Pahar Trust. A static pushover (SPO) was carried out, and the resultant pushover curve was used to form an equivalent SDOF system. This SDOF system was used as a point of comparison to assess the necessity of carrying out the full NLTHA of a detailed MDOF model. An IDA was carried out on the SDOF model, and the results were used to obtain a fragility function. A cloud analysis was then carried out on the detailed MDOF to obtain fragility curves. The MDOF and SDOF fragility curves were then compared to values from literature. It was found that the fragility analysis from this chapter gave results that were

typically slightly higher than other values in the literature, indicating the Pahar Trust health centre was more resistant to earthquakes relative to other equivalent structures. Finally, a seismic risk assessment was carried out with hazard data from Stevens et al. (2018) to find the varying risk across Nepal.

The results from Chapter 6 showed that due to the seismic design, in the form of nominally reinforced seismic bands, the fragility curves for Pahar Trust health centre were significantly higher (indicating a more seismically resilient structure) than the values in literature. This can give Pahar Trust confidence in its design. The risk values indicated that the structure exceeded the European level for acceptable risk in some small areas across Nepal. This highlights the importance of considering the seismic hazard when using a template design approach.

The key findings in this thesis are as follows:

- Considering the structural contribution of masonry infills is critical in obtaining accurate risk values for RC structures with masonry buildings. It can be the difference between being within benchmark acceptable risk values or not.
- A seismic risk assessment on a template RC structure with masonry infills showed that a properly designed code-compliant design could be implemented at any location across Nepal, and the seismic risk value was below acceptable European levels.
- The Nepal FAST method can be used to make a rapid vulnerability assessment of RC structures with masonry infills. Compared to observed data from Gorkha, the Nepal FAST method was shown to capture the dominance of DS1 accurately, however it did overestimate the likelihood of DS2 and DS3.
- Continuous masonry micro-modelling can be used in the case of irregular stone masonry, and it has been validated using experimental and analytical results.
- An equivalent regular pier can be used to assess the pushover capacity of an irregular masonry pier.
- Although not capturing local failure mechanisms, an SDOF approximation of a URM building gives a broadly similar risk values to the MDOF model.
- A template design of a URM health centre with mud mortar can be implemented across Nepal however, when a seismic risk assessment is carried out with the latest PSHA studies (Stevens et al., 2018), the risk values can exceed European threshold levels in some locations.

I believe this work should give Pahar Trust and other NGOs the confidence to continue to apply the template school model across areas with a varying level of seismic hazard. This work highlights the necessity for NGOs to ensure a high level of quality assurance is implemented on-site and that local codes are adhered to. This work should also allow people to use masonry micro-modelling for the case of irregular mud stone masonry where it is applicable and necessary.

7.2 Limitations and Further Work

Although this work covered many aspects of the seismic risk assessment of template RC and URM structures in Nepal, there are still many aspects which could be the subject of further research.

Chapters 3, 4 and 6 presented fragility curves for buildings or building types. Further work could be carried out relating these fragility curves to expected repair costs. Consequence functions are used to relate the fragility curves to the damage ratio. Previous studies (Giordano et al., 2021) have used generic consequence functions (HAZUS-FEMA, 2015) to estimate the cost of various earthquake scenarios. A bespoke set of consequence functions for the context of Nepal would require local information about the repair costs of different damage states. These functions would allow the fragility functions from Chapters 3 and 6 to be used to predict the expected loss for Pahar Trust after an earthquake.

The Nepal FAST method has the potential for further work to evaluate the reasons for its conservative nature. This further work could involve investigating the level of code compliance across Nepal. Some studies (Dixit, 2004) claim there is a low level of code compliance, although these have not been quantified and, therefore, cannot be built into the Nepal FAST method. The τ_{cr} value could be found experimentally on Nepalese masonry as opposed to using a collection of tests on hollow clay bricks.

Further validation could be carried out using an equivalent regular wall in place of an irregular wall. As previously discussed, it is not feasible to accurately measure every stone in an irregular masonry structure therefore set of three criteria were used to create an equivalent regular wall. In Chapter 5, this was validated using a set of experimental results. Further work could be carried out on the concept of an equivalent regular wall, including experimental work on irregular vs equivalent regular.

Further work could be carried out on the suitability of different modelling conditions. For example, linear geometric non-linearities were used in this study to save a computational run

time. An initial test of the pushover results was compared, and it could be seen that the SPO curve was very closely matched for linear and corotational geometric non-linearities. A complete comparison of the effect of the geometric nonlinearities could be carried out for the case of NLTHA. Work could also be carried out on the feasibility and advantages of using 3D finite elements in the model and how this could affect the mortar layer cracking.

One of the main limitations of this work was the lack of reliable data on the constituents of Nepalese masonry. This was highlighted in Section 6.2.1, where literature values of the compressive strength of mud mortar ranged from 1.8 MPa to 0.036 MPa. This level of variation brings into question which values can be considered reliable. A full experimental campaign could not only provide a reliable mean value of material properties but could also provide a distribution to allow an investigation into how a varying mortar strength affects the global strength of the structure.

References

ABAQUS. (2013) Online Documentation, *SIMULIA Inc*

Abdulla, K. F., Cunningham, L. S., & Gillie, M. (2017). Simulating masonry wall behaviour using a simplified micro-model approach. *Engineering Structures, 151*, 349-365.

Abrams, D.P. (1992). June. Safe limits for lateral capacity of cracked URM walls. *Proc. of 6th Canadian Masonry Symposium (Vol. 1, pp. 235-246).*

Adam, C., Heuer, R., & Lenhardt, W. (2013) Trade-offs in ground motion selection techniques for collapse assessment of structures.

Adhikari, R. K., & D'Ayala, D. (2019). 2015 Nepal Earthquake: Seismic Performance and Post-Earthquake Reconstruction of Stone Masonry Buildings.

Akaike, H. (1974). A new look at the statistical model identification IEEE Trans Auto Control 19 (6): 716–723.

Akehashi, H., & Takewaki, I. (2019). Optimal viscous damper placement for elastic-plastic MDOF structures under critical double impulse. *Frontiers in Built Environment*, 5, 20.

Al-Chaar, G. (2002). Evaluating Strength and Stiffness of Unreinforced Masonry Infill Structures. *Construction Engineering Research Laboratory.*

Andreaus, U., and Moroder, M. (1991). Stato dell'arte sui legami costitutivi dei solidi murari.

Ang, A. H. S., & Tang, W. H. (1984). Probability concepts in engineering planning and design, vol. 2: Decision, risk, and reliability. *JOHN WILEY & SONS, INC., 605 THIRD AVE., NEW YORK, NY 10158, USA, 1984, 608.*

Angelillo, M., Lourenço, P. B., & Milani, G. (2014). Masonry behaviour and modelling. In *Mechanics of masonry structures* (pp. 1-26). Springer, Vienna.

ASCE (2005) Seismic Design Criteria for Structures, Systems and Components in Nuclear Facilities. American Society of Civil Engineers, ASCE Standard 43-05.

ASCE 41–06. (2007) Seismic rehabilitation of existing building. *American Society of Civil Engineers, ASCE,* Reston

ASCE 7 10. (2010). Minimum Design Loads for Buildings and Other Structures. American Society of Civil Engineers. Reston, VA.

ASCE/SEI 41-17. (2017). Seismic Evaluation and Retrofit of Existing Buildings. *American Society of Civil Engineers. Reston, VA.*

Asimaki, D., Mohammadi, K., Mason, H., Adams, R., Rajaure, S. and Khadka, D., (2017). Observations and Simulations of Basin Effects in the Kathmandu Valley during the 2015 Gorkha, Nepal, Earthquake Sequence. *Earthquake Spectra*, 33(1_suppl), pp.35-53.

Asteris, P. G., Antoniou, S. T., Sophianopoulos, D. S., & Chrysostomou, C. Z. (2011). Mathematical macromodeling of infilled frames: state of the art. *Journal of Structural Engineering*, *137*(12), 1508-1517.

ASTM: ASTM E 519-02 (2002) standard test method for diagonal tension (Shear) in masonry assemblages. ASTM International, West Conshohocken, PA;

Augenti, N., Parisi, F. and Acconcia, E. (2012). MADA: online experimental database for mechanical modelling of existing masonry assemblages. Fifteenth World Conference on Earthquake Engineering

Baker, J. W. (2007, December). Measuring bias in structural response caused by ground motion scaling. In *8th Pacific Conference on Earthquake Engineering, Singapore* (Vol. 8).

Baker, J. W. (2013). An introduction to probabilistic seismic hazard analysis. *White paper version*, *2*(1), 79.

Barbosa, A. R., Fahnestock, L. A., Fick, D. R., Gautam, D., Soti, R., Wood, R., ... & Rodrigues, H. (2017). Performance of medium-to-high rise reinforced concrete frame buildings with masonry infill in the 2015 Gorkha, Nepal, earthquake. *Earthquake Spectra*, *33*(1_suppl), 197-218.

Bayat, M., Daneshjoo, F. and Nistico, N. (2015). A novel proficient and sufficient intensity measure for probabilistic analysis of skewed highway bridges. Structural Engineering and Mechanics, 55(6), pp.1177-1202.

Bayraktar, A., Şahin, A., Özcan, D. M., & Yildirim, F. (2010). Numerical damage assessment of Haghia Sophia bell tower by nonlinear FE modeling. *Applied Mathematical Modelling*, 34(1), 92-121.

BCDP. (1994). Building Code Development Project: Seismic Hazard Mapping and Risk Assessment for Nepal; UNDP/UNCHS (Habitat) Subproject: NEP/88/054/21.03. Min. Housing Phy. Planning, Kathmandu.

Benjamin, J. R., & Cornell, C. A. (1970). Probability, statistics, and decision for civil engineers. McGraw Hill.

Blasi, G., De Luca, F. and Aiello, M. (2018). Brittle failure in RC masonry infilled frames: The role of infill overstrength. *Engineering Structures, 177, pp.506-518.*

Blasi, G., De Luca, F., Perrone, D., Greco, A., & Antonietta Aiello, M. (2021). MID 1.1: Database for Characterization of the Lateral Behavior of Infilled Frames. Journal of Structural Engineering, 147(10), 04721007.

Bommer, J. and Acevedo, A. (2004). The Use of Real Earthquake Accelerograms as Input to Dynamic Analysis. *Journal of Earthquake Engineering*, 8(sup001), pp.43-91.

Borzi, B., & Elnashai, A. S. (2000). Refined force reduction factors for seismic design. *Engineering Structures, 22(10), 1244-1260.*

Bothara, J. K., Dhakal, R. P., Dizhur, D., & Ingham, J. M. (2016). The challenges of housing reconstruction after the April 2015 Gorkha, Nepal earthquake. *Technical Journal of Nepal Engineers' Association, Special Issue on Gorkha Earthquake 2015, XLIII-EC30, 1*, 121-134.

Brando, G., Rapone, D., Spacone, E., O'Banion, M., Olsen, M., Barbosa, A., Faggella, M., Gigliotti, R., Liberatore, D., Russo, S., Sorrentino, L., Bose, S. and Stravidis, A., (2017). Damage Reconnaissance of Unreinforced Masonry Bearing Wall Buildings after the 2015 Gorkha, Nepal, Earthquake. *Earthquake Spectra*, 33(1_suppl), pp.243-273. [DOI: 10.1193/010817EQS009M]

Brignola, A., Frumento, S., Lagomarsino, S., & Podestà, S. (2008). Identification of shear parameters of masonry panels through the in-situ diagonal compression test. *International Journal of Architectural Heritage*, *3*(1), 52-73.

Build Change Org. (2015). Nepal Earthquake Reconnaissance Report. http://www.buildchange.org/locations/nepal/ (version October 2015 last accessed September 2020).

Build Change. (2019). *Seismic Safety and Resilience of Schools in Nepal: Small Scale Material Testing*. Kathmandu.

Building Seismic Safety Council. (1988) NEHRP recommended provisions for the development of seismic regulations for new buildings. BSSC

Caliò, I. (2011). La prova di scorrimento con martinetto piatto. Proceedings of the XIV ANIDIS *(Italian Nacional Association of Earthquake Engineering), p.157.*

Caliò, I., Marletta, M., & Pantò, B. (2012). A new discrete element model for the evaluation of the seismic behaviour of unreinforced masonry buildings. *Engineering Structures*, *40*, 327-338.

Cannizzaro, F., Castellazzi, G., Grillanda, N., Pantò, B., & Petracca, M. (2021). Modelling the nonlinear static response of a 2-storey URM benchmark case study: comparison among different modelling strategies using two-and three-dimensional elements. *Bulletin of Earthquake Engineering*, 1-30.

Cardone, D., & Perrone, G. (2015). Developing fragility curves and loss functions for masonry infill walls. *Earthquakes and Structures, 9(1), 257-279.*

Cavanaugh, J. E. (1997). Unifying the derivations of the Akaike and corrected Akaike information criteria, *Statistics & Probability Letters, 31: 201–208, doi:10.1016/s0167-7152(96)0012*

CEN. (2002). EN 1052–1: Methods of test for masonry—part 1: determination of compressive strength. European Committee for Standardisation, Brussels, Belgium

CEN. (2007). EN 1052–3: Methods of test for masonry—part 3: determination of initial shear strength. European Committee for Standardisation, Brussels, Belgium

Cervera, M., Oliver, J., & Faria, R. (1995). Seismic evaluation of concrete dams via continuum damage models. Earthquake engineering & structural dynamics, 24(9), 1225-1245.

Chan, W., 1955. The ultimate strength and deformation of plastic hinges in reinforced concrete frameworks. *Magazine of Concrete Research*, 7(21), pp.121-132.

Chaulagain, H., Gautam, D., & Rodrigues, H. (2018). Revisiting major historical earthquakes in Nepal: Overview of 1833, 1934, 1980, 1988, 2011, and 2015 seismic events. *Impacts and insights of the Gorkha earthquake*, 1-17.

Chaulagain, H., Rodrigues, H., Silva, V., Spacone, E. and Varum, H. (2016a). Earthquake loss estimation for the Kathmandu Valley. *Bulletin of Earthquake Engineering, 14(1), pp.59-88.*

Chaulagain, H., Rodrigues, H., Silva, V., Spacone, E., & Varum, H. (2015). Seismic risk assessment and hazard mapping in Nepal. *Natural Hazards, 78(1), 583-602*.

Chaulagain, H., Rodrigues, H., Spacone, E. and Varum, H., (2015b). Seismic response of current RC buildings in Kathmandu Valley. Structural Engineering and Mechanics, 53(4), pp.791-818.

Chaulagain, H., Rodrigues, H., Spacone, E., & Varum, H. (2012). Reflections on the seismic vulnerability associated to common RC buildings in Nepal. *15th WCEE*, 24-28.

Chaulagain, H., Rodrigues, H., Spacone, E., & Varum, H. (2016b). Seismic safety assessment of existing masonry infill structures in Nepal. *Earthquake Engineering and Engineering Vibration, 15(2), 251-268.*

Chen, X. M., Cen, S., Long, Y. Q., & Yao, Z. H. (2004). Membrane elements insensitive to distortion using the quadrilateral area coordinate method. *Computers & Structures*, 82(1), 35-54.

Chen, Y., Qian, F., Scarpa, F., Zuo, L., & Zhuang, X. (2019). Harnessing multi-layered soil to design seismic metamaterials with ultralow frequency band gaps. *Materials & Design*, *175*, 107813.

Choi, E., DesRoches, R. and Nielson, B. (2004). Seismic fragility of typical bridges in moderate seismic zones. *Engineering Structures*, 26(2), pp.187-199.

Chopra, A. K. (2007). *Dynamics of structures*. Pearson Education India.

Chrysostomou, C. (1991). Effects of degrading infill walls on the nonlinear seismic response of two-dimensional steel frames. *PhD Thesis*.

Chrysostomou, C. Z., Gergely, P., & Abel, J. F. (1992, July). Nonlinear seismic response of infilled steel frames. In *Proceedings of the 10th world conference on earthquake engineering, Madrid, Spain* (pp. 4435-4437).

CNR-DT 212/2013. (2014). Guide for the Probabilistic Assessment of the Seismic Safety of Existing Buildings Guide for the Probabilistic Assessment of the Seismic Safety of Existing Buildings.

Colangelo F. (2012). A simple model to include fuzziness in the seismic fragility curve and relevant effect compared with randomness. *Earthquake Engineering and Structural Dynamics 41, 969–986.*

Cornell, C. A. (1968). Engineering seismic risk analysis. Bulletin of the seismological society of America, 58(5), 1583-1606.

Cornell, C. A., Banon, H., & Shakal, A. F. (1979). Seismic motion and response prediction alternatives. *Earthquake Engineering & Structural Dynamics*, *7*(4), 295-315.

Costigan, A., Pavía, S., & Kinnane, O. (2015). An experimental evaluation of prediction models for the mechanical behavior of unreinforced, lime-mortar masonry under compression. Journal of Building Engineering, 4, 283-294.

Crisafulli, F. (1997). Seismic behaviour of reinforced concrete structures with masonry infills. *PhD Thesis.*

Cross, T., De Luca, F., & De Risi, R. (2020, September). An experimental comparison of micro-modelling and meso-modelling for an unreinforced masonry wall. In *17th World Conference on Earthquake Engineering*.

Cross, T., De Luca, F., De Risi, R., Rana, TR., Mitchell, T & Sweetman, A. (2019). Pounding in Nepalese School Buildings. SECED 2019 Proceedings

Cross, T., De Luca, F., De Risi, R., Ranamagar, T. R., Mitchell, T., & Sweetman, A. (2020). Mapping the seismic safety of RC" template schools" in Nepal. *International Journal of Disaster Risk Reduction*, *51*, 101844.

Cundall PA (1971) A computer model for simulating progressive, large-scale movements in blocky rock systems. In: Symp. ISRM, Nancy, pp 129–136

D'Ayala, D., Galasso, C., Nassirpour, A., Kumar Adhikari, R., Yamin, L., Fernandez, R., Lo, D., Garciano, L. and Oreta, A., (2020). Resilient communities through safer schools. International Journal of Disaster Risk Reduction, 45.

da Porto, F., Guidi, G., Garbin, E., & Modena, C. (2010). In-plane behavior of clay masonry walls: experimental testing and finite-element modelling. *Journal of structural engineering*, *136*(11), 1379-1392.

D'Altri, A. M., de Miranda, S., Milani, G., & Castellazzi, G. (2020). A numerical procedure for the force-displacement description of out-of-plane collapse mechanisms in masonry structures. *Computers & Structures*, *233*, *106234.*

De Luca, F. and Verderame, G. (2013). A practice-oriented approach for the assessment of brittle failures in existing reinforced concrete elements. Engineering Structures, 48, pp.373-388.

De Luca, F., Giordano, N., Gryc, H., Hulme, L., McCarthy, C., Sanderson, V., & Sextos, A. (2019). Nepalese school building stock and implications on seismic vulnerability assessment. In *2nd international conference on earthquake engineering and post disaster reconstruction planning. Bhaktapur, Nepal* (pp. 319-328).

De Luca, F., Vamvatsikos, D., & Iervolino, I. (2013). Near-optimal piecewise linear fits of static pushover capacity curves for equivalent SDOF analysis. *Earthquake engineering & structural dynamics*, *42*(4), 523-543.

De Luca, F., Verderame, G. M., & Manfredi, G. (2015). Analytical versus observational fragilities: the case of Pettino (L'Aquila) damage data database. *Bulletin of Earthquake Engineering*, *13*(4), 1161-1181.

De Luca, F., Verderame, G. M., Gómez-Martínez, F., & Pérez-García, A. (2014). The structural role played by masonry infills on RC building performances after the 2011 Lorca, Spain, earthquake. *Bulletin of Earthquake Engineering*, *12*(5), 1999-2026.

De Luca, F., Woods, G. E., Galasso, C., & D'Ayala, D. (2018). RC infilled building performance against the evidence of the 2016 EEFIT Central Italy post-earthquake reconnaissance mission: empirical fragilities and comparison with the FAST method. *Bulletin of Earthquake Engineering*, *16*(7), 2943-2969.

De Luca, F., Woods, G.E., Galasso, C. and D'Ayala, D., (2017). RC infilled building performance against the evidence of the 2016 EEFIT Central Italy post-earthquake reconnaissance mission: empirical fragilities and comparison with the FAST method. *Bulletin of Earthquake Engineering, pp.1-27.*

Deierlein, G. G., Reinhorn, A. M., & Willford, M. R. (2010). Nonlinear structural analysis for seismic design. *NEHRP seismic design technical brief*, *4*, 1-36.

Disaster Emergency committee. (2016). NEPAL EARTHQUAKE APPEAL [online] Available at: [https://www.dec.org.uk/appeal/nepal-earthquake-appeal] [Accessed 31 August 2022].

Dixit, A. M. (2004). Promoting safer building construction in Nepal. In 13th World Conference on Earthquake Engineering.

Dizhur, D., Dhakal, R. P., Bothara, J., & Ingham, J. (2016). " Building Typologies and Failure Modes Observed in the 2015 Gorkha (Nepal) Earthquake" *Vol. 49, No. 2 Response*.

Dolšek, M. And Fajfar, P., (2001). Soft Storey Effects in Uniformly Infilled Reinforced Concrete Frames. *Journal of Earthquake Engineering*, 5(1), Pp.1-12.

Dolšek, M., & Fajfar, P. (2004). Inelastic spectra for infilled reinforced concrete frames. Earthquake engineering & structural dynamics, 33(15), 1395-1416.

Drougkas, A., Roca, P., & Molins, C. (2016). Compressive strength and elasticity of pure lime mortar masonry. Materials and structures, 49(3), 983-999.

Dvorkin, E. N., & Bathe, K. J. (1984). A continuum mechanics based four-node shell element for general non-linear analysis. Engineering computations.

Eads, L., Miranda, E. and Lignos, D. (2015). Average spectral acceleration as an intensity measure for collapse risk assessment. *Earthquake Engineering & Structural Dynamics*, 44(12), pp.2057-2073.

Ebrahimian, H., Jalayer, F., Lucchini, A., Mollaioli, F. and De Dominicis, R. (2014). Case studies on relative sufficiency of alternative intensity measures of ground shaking. Second European conference on earthquake engineering and seismology.

Elliott, J., Jolivet, R., González, P., Avouac, J., Hollingsworth, J., Searle, M. and Stevens, V., (2016). Erratum: Corrigendum: Himalayan megathrust geometry and relation to topography revealed by the Gorkha earthquake. Nature Geoscience, 9(9), pp.728-728.

EN 1015-11. (2019). European Standard. Methods of test for mortar for masonry - Part 11: Determination of flexural and compressive strength of hardened mortar. *Brussels: BSi.*

EN 1990-1. (2000). Eurocode 0: - Basis of structural design [Ebook] (1st ed.). Brussels: BSi.

EN 1996-1-1. (2005). Eurocode 6: Design of masonry structures - Part 1-1: General rules for reinforced and unreinforced masonry structures [Ebook] (1st ed.). *Brussels: BSi*.

EN 1998-1. (2004). Eurocode 8: Design of structures for earthquake resistance - Part 1: General rules, seismic actions and rules for buildings [Ebook] (1st ed.). Brussels: BSi.

EN 1998-3. (2005). Eurocode 8: Design of structures for earthquake resistance -Part 3: Assessment and retrofitting of buildings [Ebook] (1st ed.). *Brussels: BSi.*

Fardis. MN. (1996). Experimental and numerical investigations on the seismic response of RC infilled frames and recommendations for code provisions. *Report ECOEST-PREC8 No 6. Prenormative research in support of Eurocode 8*

Favvata, M. (2017). Minimum required separation gap for adjacent RC frames with potential inter-story seismic pounding. *Engineering Structures*, 152, pp.643-659.

FEMA P-1050. (2015) NEHRP recommended seismic provisions for new buildings and other structures, Washington, DC, FEMA P-695

FEMA P-58-1 (2018). Seismic Performance Assessment of Buildings. Washington, D.C.

FEMA P695. (2009) Quantification of building seismic performance factors. Technical Report prepared by the Applied Technology Council for the Federal Emergency Management Agency, Washington, DC, FEMA P-695

FEMA, Hazus–MH 2.1 (2015) Technical Manual, 2015. https://www.fema.gov/hazus-mh-user-technical-manuals.

Filippou F.C., Popov, E.P., and Bertero, V.V. (1983). "Effects of Bond Deterioration on Hysteretic Behavior of Reinforced Concrete Joints". Report EERC 83-19, Earthquake Engineering Research Center, University of California, Berkeley.

Flenga, M. G., & Favvata, M. J. (2021). Fragility curves and probabilistic seismic demand models on the seismic assessment of RC frames subjected to structural pounding. Applied Sciences, 11(17), 8253.

Galasso, C. (2014). *Probabilistic Analysis of Flexural Overstrength for New Designed RC Beams*. in *Second European Conference on Earthquake Engineering*.

Gautam, D., & Chaulagain, H. (2016). Structural performance and associated lessons to be learned from world earthquakes in Nepal after April 25th 2015 (MW 7.8) Gorkha earthquake. *Engineering Failure Analysis*, *68*, 222-243.

Gautam, D., Bhetwal, K. K., Rodrigues, H., Neupane, P., & Sanada, Y. (2015, October). Observed damage patterns on buildings during 2015 Gorkha (Nepal) earthquake. In Proceedings of 14th international symposium on new technologies for urban safety of mega cities in Asia (pp. 29-31).

Gautam, D., Fabbrocino, G., & de Magistris, F. S. (2018). Derive empirical fragility functions for Nepali residential buildings. Engineering Structures, 171, 617-628.

GB50010-2010 (2010) National Standard of the People's Republuic of China GB 50010-2010 Code for Design of Concrete Structures

GENESIS Ltd, Shree Da Ram Prajapati (2016). Consultancy Services for Urban Base Map and Integrated Municipal GIS of Kathmandu Metropolitan City, Ward No -35. *Available upon request to the University of Bristol data repository.*

Gentile, R., Galasso, C., Idris, Y., Rusydy, I. and Meilianda, E., (2019a). From rapid visual survey to multi-hazard risk prioritisation and numerical fragility of school buildings. *Natural Hazards and Earth System Sciences*, 19(7), pp.1365-1386.

Gentile, R., Pampanin, S., Raffaele, D. and Uva, G., (2019b). Non-linear analysis of RC masonry-infilled frames using the SLaMA method: part 2—parametric analysis and validation of the procedure. Bulletin of Earthquake Engineering, 17(6), pp.3305-3326.

Ghimire, S., & Parajuli, H. R. (2016). Probabilistic seismic hazard analysis of Nepal considering uniform density model. In Proceedings of IOE Graduate Conference (pp. 115-122).

Giamundo, V., Sarhosis, V., Lignola, G. P., Sheng, Y., & Manfredi, G. (2014). Evaluation of different computational modelling strategies for the analysis of low strength masonry structures. *Engineering Structures*, 73, 160-169.

Gil, L., Bernat-Masó, E., & Cañavate, F. J. (2016). Changes in properties of cement and lime mortars when incorporating fibers from end-of-life tires. Fibers, 4(1), 7.

Gilder, C., Pokhrel, R., Vardanega, P., De Luca, F., De Risi, R., Werner, M., Asimaki, D., Maskey, P. and Sextos, A., (2020). The SAFER geodatabase for the Kathmandu Valley: Geotechnical and geological variability. *Earthquake Spectra*, p.875529301989995.

Giordano, A., Mele, E., & De Luca, A. (2020). Modelling of historical masonry structures: comparison of different approaches through a case study. Engineering Structures, 24(8), 1057-1069.

Giordano, N., De Luca, F. and Sextos, A., (2020). Out-of-plane closed-form solution for the seismic assessment of unreinforced masonry schools in Nepal. Engineering Structures, 203, p.109548.

Giordano, N., De Luca, F., & Sextos, A. (2021). Analytical fragility curves for masonry school building portfolios in Nepal. *Bulletin of Earthquake Engineering*, 19(2), 1121-1150.

Giordano, N., De Luca, F., Sextos, A., Cortes, F. R., Ferreira, C. F., & Wu, J. (2021). Empirical seismic fragility models for Nepalese school buildings. *Natural Hazards, 105(1), 339-362.*

Giordano, N., Norris, A., Manandhar, V., Shrestha, L., Paudel, D. R., Quinn, N., ... & Sextos, A. (2021). Financial assessment of incremental seismic retrofitting of Nepali stone-masonry buildings. International Journal of Disaster Risk Reduction, 60, 102297.

Goda, K., Kiyota, T., Pokhrel, R.M., Chiaro, G., Katagiri, T., Sharma, K. and Wilkinson, S. (2015). The 2015 Gorkha Nepal earthquake: insights from earthquake damage survey. *Frontiers in Built Environment, 1, p.8.*

Government of Nepal. (2012). National population and housing census 2011.

Government of Nepal. (2019). "Nepal Disaster Risk Reduction Portal." Retrieved July [available at: http://drrportal.gov.np/]

Graziotti, F., Magenes, G., & Penna, A. (2003) A Direct Method To Compute The Inelastic Displacement Demand Of Masonry Structures.

Graziotti, F., Penna, A., & Magenes, G. (2016). A nonlinear SDOF model for the simplified evaluation of the displacement demand of low-rise URM buildings. Bulletin of Earthquake Engineering, 14(6), 1589-1612.

Grimaz, S., Slejko, D., Cucchi, F., Barazza, F., Biolchi, S., Del Pin, E., ... & Moretti, A. (2016). The ASSESS project: assessment for seismic risk reduction of school buildings in the Friuli Venezia Giulia region (NE Italy). Bollettino di Geofisica Teorica ed Applicata, 57(2).

Grünthal, G. (1998). European macroseismic scale 1998. European Seismological Commission (ESC).

Guerrini, G., Senaldi, I., Scherini, S., Morganti, S., & Magenes, G. (2017). Material characterization for the shaking-table test of the scaled prototype of a stone masonry building aggregate. *Material characterization for the shaking-table test of the scaled prototype of a stone masonry building aggregate*, 105-115.

Guragain, R. (2015). Development of earthquake risk assessment system for Nepal. *University of Tokyo.*

Gutenberg, B., & Richter, C. F. (1944). Frequency of earthquakes in California. Bulletin of the Seismological society of America, 34(4), 185-188.

Holmes, M. (1961). Steel frames with brickwork and concrete infilling. *proceedings of the Institution of civil Engineers*, *19*(4), 473-478.

Ibrahim, Y., Nagy, B., & Benedek, C. (2020). Deep learning-based masonry wall image analysis. Remote Sensing, 12(23), 3918.

Iervolino, I., & Dolce, M. (2018). Foreword to the special issue for the RINTC (the implicit seismic risk of code-conforming structures) project. *Journal of Earthquake Engineering*, *22*(sup2), 1-4.

Iervolino, I., Spillatura, A., & Bazzurro, P. (2018). Seismic reliability of code-conforming Italian buildings. *Journal of Earthquake Engineering*, 22(sup2), 5-27.

IS 1077. (2005) Indian Standard: Common Burnt Clay Building Bricks Specification (Fifth Revision)

IS 1786. (2008). Indian Standard: High strength deformed steel bars and wires for concrete reinforcement- specification. (4th ed.).

IS 1893 (Part 1). (2002). Indian Standard: Criteria for Earthquake resistant design of structures. (4th ed.).

IS 4326. (1976). Earthquake resistant design and construction of buildings—Code of practice, *Bureau of Indian Standards, New Delhi.*

IS456-1978. (1978). Indian Standard Plain and Reinforced Concrete Code of Practice. Bureau of Indian Standards, New Delhi.

IS456-2000. (2000). Indian Standard Plain and Reinforced Concrete Code of Practice. Bureau of Indian Standards, New Delhi.

IS875-2010. (2010). Code of Practice for Design Loads (Other Than Earthquake) for Buildings and Structures. Part 1 Dead Loads—unit Weights of Building Materials and Stored Materials. Bureau of Indian Standards, New Delhi.

Israelsson, J. I. (1996). Short descriptions of UDEC and 3DEC. In *Developments in geotechnical engineering* (Vol. 79, pp. 523-528). Elsevier.

Jalayer, F., & Cornell, C. A. (2009). Alternative non-linear demand estimation methods for probability-based seismic assessments. *Earthquake Engineering & Structural Dynamics*, *38*(8), 951-972.

Jalayer, F., & Ebrahimian, H. (2017). Seismic risk assessment considering cumulative damage due to aftershocks. Earthquake Engineering & Structural Dynamics, 46(3), 369-389.

Jalayer, F., De Risi, R. and Manfredi, G. (2014). Bayesian Cloud Analysis: efficient structural fragility assessment using linear regression. *Bulletin of Earthquake Engineering*, 13(4), pp.1183-1203.

Jalayer, F., De Risi, R. and Manfredi, G. (2015). Bayesian Cloud Analysis: efficient structural fragility assessment using linear regression. Bulletin of Earthquake Engineering, 13(4), pp.1183-1203.

Jalayer, F., Ebrahimian, H., Miano, A., Manfredi, G. and Sezen, H. (2017). Analytical fragility assessment using unscaled ground motion records. *Earthquake Engineering & Structural Dynamics*, 46(15), pp.2639-2663.

Jones, S., Oven, K. and Wisner, B., (2016). A comparison of the governance landscape of earthquake risk reduction in Nepal and the Indian State of Bihar. *International Journal of Disaster Risk Reduction*, 15, pp.29-42.

Kallioras, S., Graziotti, F., & Penna, A. (2019). Numerical assessment of the dynamic response of a URM terraced house exposed to induced seismicity. Bulletin of Earthquake Engineering, 17(3), 1521-1552.

Kappos, A. J., Panagopoulos, G., Panagiotopoulos, C., and Penelis, G. (2006). A Hybrid Method for the Vulnerability Assessment of R/C and URM Buildings. *Bull. Earthquake Eng.* 4 (4), 391–413. doi:10.1007/s10518-006-9023-0

Karayannis, C. and Favvata, M. (2004). Earthquake-induced interaction between adjacent reinforced concrete structures with non-equal heights. *Earthquake Engineering & Structural Dynamics*, 34(1), pp.1-20.

Karmacharya, U., Silva, V., Brzev, S., & Martins, L. (2018). Improving the nepalese building code based on lessons learned from the 2015 M7. 8 Gorkha earthquake. In Impacts and Insights of the Gorkha Earthquake (pp. 135-172). Elsevier.

Kent, D. and Park, R., 1971. Flexural Members with Confined Concrete. *Journal of the Structural Division*, 97(7), pp.1969-1990.

Kiani, J., & Pezeshk, S. (2017). Sensitivity analysis of the seismic demands of RC moment resisting frames to different aspects of ground motions. *Earthquake engineering & structural dynamics*, *46*(15), 2739-2755.

Kim, J., & Han, S. (2013). Sensitivity analysis for seismic response of reinforced concrete staggered wall structures. *Magazine of concrete research*, *65*(22), 1348-1359.

Kohrangi, M., Bazzurro, P., Vamvatsikos, D. and Spillatura, A., (2017a). Conditional spectrum-based ground motion record selection using average spectral acceleration. *Earthquake Engineering & Structural Dynamics*, 46(10), pp.1667-1685.

Kohrangi, M., Kotha, S. and Bazzurro, P., (2017b). Ground-motion models for average spectral acceleration in a period range: direct and indirect methods. Bulletin of Earthquake Engineering, 16(1), pp.45-65.

Kramer, S. L. (2014). *Geotechnical earthquake engineering*. Harlow, Essex: Pearson Education Limited.

Kuinkel, M. S., Sukubhatu, S., & Shrestha, R. (2019, April). Physical Performance of Traditional Brick Mud Masonry. In *Khwopa Engineering College & Khwopa College of Engineering, 2019. Proceedings of the International Conference on Earthquake Engineering and Post Disaster Reconstruction Planning* (pp. 25-27).

Lagomarsino, S., Penna, A., Galasco, A., & Cattari, S. (2013). TREMURI program: an equivalent frame model for the nonlinear seismic analysis of masonry buildings. *Engineering structures*, *56*, 1787-1799.

Langroudi, J. R., Ranjbar, M. M., Hashemi, S. J., & Moghadam, A. S. (2011). Evaluation of roof diaphragm effect on seismic behavior of masonry buildings. In Memorias, 8th International Conference on Structural Dynamics EURODYN2011 (pp. 453-458).

Lemos, J. V. (2007). Discrete element modeling of masonry structures. *International Journal of Architectural Heritage*, *1*(2), 190-213.

Lemos, J. V. (2019). Discrete element modeling of the seismic behavior of masonry construction. *Buildings*, *9*(2), 43.

Liang, G., & Zhou, N. (2016). Background and reflections on Gorkha earthquake of April 25, 2015. *Natural Hazards*, *81*(2), 1385-1392.

Liauw T.C., and Kwan K., (1984). Non-linear behavior of non-Integral infilled frames, *Computers and Structures*, Vol.18, No.3, pp.551-560, 1984

Lin, J. and Weng, C. (2001). Probability analysis of seismic pounding of adjacent buildings. *Earthquake Engineering & Structural Dynamics*, 30(10), pp.1539-1557.

Lizundia, B., Shrestha, S.N., Bevington, J., Davidson, R., Jaiswal, K., Jimee, G.K., Kaushik, H., Kumar, H., Kupec, J., Mitrani-Reiser, J. and Poland, C. (2016). M7. 8 Gorkha, Nepal earthquake on April 25th, 2015 and its aftershocks. *EERI Earthquake Reconnaissance Team Report.*

Lombardi, L., (2019). Linear Time-History Analysis As EC8-Compliant Design Method For Simplified Performance-Based Earthquake Engineering Assessment. *Ph.D. University of Bristol*.

Lotfi, H. R., & Shing, P. B. (1994). Interface model applied to fracture of masonry structures. *Journal of structural engineering*, *120*(1), 63-80.

Lourenco, P. B., & Rots, J. G. (1997). A solution for the macro-modelling of masonry structures. In *Proceedings of the 11th International Brick/Block Masonry Conference* (pp. 1239-1249). Tongji University Shanghai, China.

Lourenço, P. J. B. B. (1997). Computational strategies for masonry structures.

Lourenço, P.B. (1996). Computational Strategies for Masonry Structures. PhD thesis, Delft University of Technology, The Netherlands.

Lu, D., Yu, X., Jia, M., & Wang, G. (2014). Seismic risk assessment for a reinforced concrete frame designed according to Chinese codes. Structure and Infrastructure Engineering, 10(10), 1295-1310.

Lubliner, J., Oliver, J., Oller, S., & Oñate, E. (1989). A plastic-damage model for concrete. *International Journal of solids and structures*, *25*(3), 299-326.

Mackerle, J. (2002). Finite element linear and nonlinear, static and dynamic analysis of structural elements, an addendum: A bibliography (1999–2002). Engineering Computations.

Macorini, L., & Izzuddin, B. (2011). A non-linear interface element for 3D mesoscale analysis of brick-masonry structures. International Journal for numerical methods in Engineering, 85(12), 1584-1608.

Macorini, L., & Izzuddin, B. A. (2013). Nonlinear analysis of masonry structures using mesoscale partitioned modelling. *Advances in engineering Software*, *60*, 58-69.

Magenes, G., & Calvi, G. M. (1997). In-plane seismic response of brick masonry walls. Earthquake engineering & structural dynamics, 26(11), 1091-1112.

Magenes, G., & Fontana, A. D. (1998, October). Simplified non-linear seismic analysis of masonry buildings. In *Proc. Br. Masonry Soc. No. 8* (pp. 190-195).

Magenes, G., Camata, G., Cattari, S., Caliò, I., Calderoni, B., de Miranda, S., & Saetta, S. (2020). *Progetto DPC-ReLUIS 2019-2021 – WP10 TASK 10.3 – Uso dei software di calcolo nella verifica sismica degli edifici in muratura v1.0* (pp. 204-246). Retrieved from *https://www.reluis.it/it/wp10-task-10-3-uso-dei-software-di-calcolo-nella-verifica-sismica-degli-edifici-in-muratura-v1-0.html*

Mainstone, R. J. (1974). On the stiffness and strength of in-filled frames. *Proc. Supplement, Trans. of Inst. Of Civil Eng. State Univ. of New York.*

Malomo, D., Morandini, C., Penna, A., & DeJong, M. J. (2019, September). Assessing the reliability of the equivalent-frame idealisation of URM façades with irregular opening layouts by comparison with the discrete micro-models. In *SEDEC 2019 Conference, Greenwich, London* (pp. 1-9).

Mander, J. B., Priestley, M. J., & Park, R. (1988). Theoretical stress-strain model for confined concrete. *Journal of structural engineering*, *114*(8), 1804-1826.

Manfredi G, Verderame GM, Prota A, Ricci P, De Luca F, (2013) 2012 Emilia earthquake. Italy, Reinforced concrete buildings response. Bull Earthq Eng

Manfredi, G., Prota, A., Verderame, G. M., De Luca, F., & Ricci, P. (2014). 2012 Emilia earthquake, Italy: reinforced concrete buildings response. Bulletin of Earthquake Engineering, 12(5), 2275-2298.

Manfredi, G., Ricci, P., and M Verderame, G. (2012). Influence of Infill Panels and Their Distribution on Seismic Behavior of Existing Reinforced concrete Buildings. Open Construction Building Techn. J. 6 (1). doi:10.2174/1874836801206010236

Marhatta, Y. B., Bothara, J. K., Magar, M. B., and Chapagain, G. (2007). *Report*. Housing Report Pillar Walaghar (URM Infilled RC Frame Buildings) *(No. 145).*

Martins, L., & Silva, V. (2020). Development of a fragility and vulnerability model for global seismic risk analyses. *Bulletin of Earthquake Engineering*, 1-27.

Meguro K, Hakuno M (1990) Fracture analysis of concrete structures by the modified distinct element method. Concr Libr JSCE 16:125–137

Meli, R. (1973). June. Behavior of masonry walls under lateral loads. *Fifth world conference on earthquake engineering.*

Menegotto, M. & Pinto, P.E. (1973). Method of analysis for cyclically loaded RC plane frames including changes in geometry and nonelastic behaviour of elements under combined normal force and bending. *Proc. IABSE Symposium*, Lisbon, Portugal.

Ministry of Education, Science & Technology. (2021) Central Level Project Implementation Unit (Education) Available: http://www.moepiu.gov.np/index.php Last accessed 12th Jan 2022.

Mishra, A. K. (2019). Development of building bye-laws in Nepal. *J Adv Res Const Urban Arch*, *4*(3&4), 17-29.

Mishra, C. (2018, October). Mechanical Properties of Components of Nepalese Historical Masonry Buildings. In Proceedings of International Exchange and Innovation Conference on Engineering and Sciences, Interdisciplinary Graduate School of Engineering Sciences, Kyushu University (IEICES, 4, 118-123).

MIT (2018) NTC 2018: D.M. del Ministero delle Infrastrutture e dei trasporti del 17/01/2018. Aggiornamento delle Norme Tecniche per le Costruzioni (in Italian)

Molina, O., Vilarrasa, V., & Zeidouni, M. (2017). Geologic carbon storage for shale gas recovery. Energy Procedia, 114, 5748-5760.

Morandi, P., Albanesi, L., Graziotti, F., Piani, T. L., Penna, A., & Magenes, G. (2018). Development of a dataset on the in-plane experimental response of URM piers with bricks and blocks. Construction and Building Materials, 190, 593-611.

Morandini, C., Caserini, M., Malomo, D., Penna, A., & DeJong, M. J. (2019). Equivalent-frame models idealisation of laterally-loaded URM façades with irregular opening distributions. Equivalent-frame models idealisation of laterally-loaded URM façades with irregular opening distributions, 58-67.

Mouyiannou, A., Rota, M., Penna, A., & Magenes, G. (2014). Identification of suitable limit states from nonlinear dynamic analyses of masonry structures. *Journal of Earthquake Engineering*, *18*(2), 231-263.

Nakamura, N. (2016). Extended Rayleigh damping model. *Frontiers in Built Environment*, *2*, 14.

NBC-105:1994. (1994). Nepal National Building Code. Seismic design of buildings in Nepal *Ministry of Housing and Physical Planning, Department of Building*

NBC-105:2020. (2020). Nepal National Building Code. Seismic design of buildings in Nepal *Ministry of Housing and Physical Planning, Department of Building*

NBC-110:1994. (1994). Nepal National Building Code. Plain and Reinforced Concrete *Ministry of Housing and Physical Planning, Department of Building*

NBC-112:1994. (1994). Nepal National Building Code. Timber *Ministry of Housing and Physical Planning, Department of Building*

NBC-201:1994. (1994). Nepal National Building Code. Mandatory rules of thumb for reinforced concrete buildings with masonry infills. *Ministry of Housing and Physical Planning, Department of Building*

NBC-202:1994. (1994). Nepal National Building Code. Mandatory rules of thumb load bearing masonary. *Ministry of Housing and Physical Planning, Department of Building*

NBC-203:2015. (2015) Nepal National Building Code Guidelines for Earthquake Resistant Building Construction: Low Strength Masonry

Nepal Department of Education, (2016). Guidelines For Developing Type Designs For School Buildings In Nepal. Kathmandu: Government of Nepal.

Nepal National Planning Commission. (2015). Nepal earthquake 2015: post disaster needs assessment, volume A: key findings. Kathmandu: Government of Nepal National Planning Commission.

Newmark, N. M., & Hall, W. J. (1982). Earthquake spectra and design. *Engineering monographs on earthquake criteria*.

Noh, N. M., Liberatore, L., Mollaioli, F. and Tesfamariam, S. (2017). Modelling of masonry infilled RC frames subjected to cyclic loads: State of the art review and modelling with OpenSees. *Engineering Structures, 150, pp.599-621.*

NSET (2001) The Kathmandu Valley Earthquake risk management action plan, a Product of the Kathmandu Valley Earthquake Risk Management Project

NSET Nepal National Society for Earthquake Technology. (2017). Data on cement mortar test from Nepal. *EPSRC SAFER project 2017-2020.*

O'Reilly, G. J., Perrone, D., Fox, M., Monteiro, R., Filiatrault, A., Lanese, I., & Pavese, A. (2019). System identification and seismic assessment modeling implications for Italian school buildings. *Journal of Performance of Constructed Facilities*, 33(1), 04018089.

Oliveira, D. V., Lourenço, P. B., & Roca, P. (2006). Cyclic behaviour of stone and brick masonry under uniaxial compressive loading. Materials and structures, 39(2), 247-257.

Oliver, J., Huespe, A. E., & Cante, J. C. (2008). An implicit/explicit integration scheme to increase computability of non-linear material and contact/friction problems. *Computer Methods in Applied Mechanics and Engineering*, *197*(21-24), 1865-1889

Opensees. (2012). *Pinching4 Material - OpenSeesWiki*. [online] Available at: [https://opensees.berkeley.edu/wiki/index.php/Pinching4_Material] [Accessed 4 August 2022].

Page, A. W. (1978). Finite element model for masonry. *Journal of the Structural Division*, *104*(8), 1267-1285.

Pahar Trust. (2019). Personal communication with Ted Cross, 18 August.

Pahar Trust. (2020). Pahar Trust Nepal. [online] Available at: https://www.pahar-trust.org/ [Accessed 24 Feb. 2020].

Panagiotakos, T. and Fardis, M. (1996). Seismic response of infilled RC frames structures. *11th world conference on earthquake engineering*

Pant, D. (2015). Nepal National Building Code (NBC): An Overview. Retrieved 15 January 2022, from http://learningfromearthquakes.org/2015-04-25-nepal/11-resources/78-nepal-national-building-code-nbc-an-overview#:~:text=Nepal%20national%20building%20code%20(NBC)%20was%20first%20drafted%20in%201994,document%20in%20all%20130%20municipalities.

Parajuli, H. R. (2012, September). Determination of mechanical properties of the Kathmandu World Heritage brick masonry buildings. In *The 15th World Conference on Earthquake Engineering, Lisbon, Portugal*.

Parajuli, H. R., Kiyono, J., Taniguchi, H., Toki, K., & Maskey, P. N. (2010). Probabilistic seismic hazard assessment for Nepal. *WIT Transactions on Information and Communication Technologies*, *43*, 405-416.

Parajuli, R. R., & Kiyono, J. (2015). Ground motion characteristics of the 2015 Gorkha earthquake, survey of damage to stone masonry structures and structural field tests. *Frontiers in Built Environment*, *1*, 23.

Parajuli, R. R., Furukawa, A., & Gautam, D. (2020, December). Experimental characterisation of monumental brick masonry in Nepal. In *Structures* (Vol. 28, pp. 1314-1321). Elsevier.

Park, R., Priestley, M. J. N., and Gill, W. D. (1982), "Ductility of square-confined concrete columns". *Journal of the Structural Division, 108, 929-950.*

Paulay, T., & Priestley, M. N. (1992). Seismic design of reinforced concrete and masonry buildings.

PEER NGA West 2. (2014). NGA-West2 -- Shallow Crustal Earthquakes in Active Tectonic Regimes. Pacific Earthquake Engineering Research Center. [Available at https://ngawest2.berkeley.edu/]

Perrone, D., Brunesi, E., Filiatrault, A. and Nascimbene, R., (2020b). Probabilistic estimation of floor response spectra in masonry infilled reinforced concrete building portfolio. *Engineering Structures, 202, p.109842.*

Perrone, D., O'Reilly, G. J., Monteiro, R., & Filiatrault, A. (2020a). Assessing seismic risk in typical Italian school buildings: From in-situ survey to loss estimation. *International journal of disaster risk reduction*, 44, 101448.

Petracca, M., Candeloro, F., and Camata, G. (2017b). STKO User Manual. Pescara: ASDEA Software Technology.

Petracca, M., Marano, C., Camata, G., & Pelà, L. (2021). Advanced tools for fast micro-modelling of masonry structures. In SAHC 2020: 12th International Conference on Structural Analysis of Historical Constructions (pp. 1-10). International Centre for Numerical Methods in Engineering (CIMNE).

Petracca, M., Pelà, L., Rossi, R., Oller, S., Camata, G., & Spacone, E. (2016). Regularisation of first order computational homogenisation for multiscale analysis of masonry structures. *Computational mechanics, 57(2), 257-276.*

Petracca, M., Pelà, L., Rossi, R., Oller, S., Camata, G., & Spacone, E. (2017). Multiscale computational first order homogenization of thick shells for the analysis of out-of-plane loaded masonry walls. Computer Methods in Applied Mechanics and Engineering, 315, 273-301.

Petracca, M., Pelà, L., Rossi, R., Zaghi, S., Camata, G., & Spacone, E. (2017a). Micro-scale continuous and discrete numerical models for nonlinear analysis of masonry shear walls. *Construction and Building Materials, 149, 296-314.*

Pinto, EP., Paolo F. (2014). Existing Buildings: The New Italian Provisions for Probabilistic Seismic Assessment. Geotechnical, Geological and Earthquake Engineering. *34. 97-130. 10.1007/978-3-319-07118-3_3.*

Pokharel, T., & Goldsworthy, H. M. (2017). Lessons learned from the Nepal earthquake 2015. *Australian journal of structural engineering*, *18*(1), 11-23.

Pokhrel, R.M., De Risi, R., Werner, M.J., De Luca, F., Vardanega, P.J., Maskey, P.N. and Sextos, A., (2019). Simulation-based PSHA for the Kathmandu Basin in Nepal.

Polyakov, S. (1960). On the interaction between masonry filler walls and enclosing frame when loading in the plane of the wall. *Transl Earthq Eng,* 2, pp.36-42.

Popovics, S. (1973). A numerical approach to the complete stress-strain curve of concrete. Cement and concrete research, 3(5), 583-599.

Porter, K., Kennedy, R. and Bachman, R. (2007). Creating fragility functions for performance-based earthquake engineering. *Earthquake Spectra, 23(2), pp.471-489.*

Pun, R. (2015). Improvement in seismic performance of stone masonry using galvanized steel wire (Doctoral dissertation).

Purwana, Y. M., DHI, R. H., & Setiawan, B. (2019). Seismic hazard analysis for Sutami Dam using probabilistic method. In *MATEC Web of Conferences* (Vol. 276, p. 05012). EDP Sciences.

Rahman, M. M., & Bai, L. (2018). Probabilistic seismic hazard assessment of Nepal using multiple seismic source models. *Earth and Planetary Physics*, *2*(4), 327-341.

Rajaure, S., Asimaki, D., Thompson, E., Hough, S. E., Ampuero, P., Martin, S. S., ... & Dhital, M. (2016). Strong motion observations of the Kathmandu valley response during the M7. 8 Gorkha earthquake sequence. *Tectonophysics*, *714*(715), 10-1016.

Ram, T. and Wang, G., (2013). Probabilistic seismic hazard analysis in Nepal. Earthquake Engineering and Engineering Vibration, 12(4), pp.577-586.

Rashmi, S., Jagadish, K. S., & Nethravathi, S. (2014). Stabilised mud mortar. *Int J Res Eng Technol*, *3*(Special Issue), 233-239.

Rhee, I., Lee, J. S., & Roh, Y. S. (2019). Fracture parameters of cement mortar with different structural dimensions under the direct tension test. Materials, 12(11), 1850.

Ricci, P., De Risi, M. T., Verderame, G. M., & Manfredi, G. (2016). Procedures for calibration of linear models for damage limitation in design of masonry-infilled RC frames. *Earthquake Engineering & Structural Dynamics, 45(8), 1315-1335.*

Ricci, P., Verderame, G. M., & Manfredi, G. (2011). Analytical investigation of elastic period of infilled RC MRF buildings. *Engineering structures*, *33*(2), 308-319.

Riddington, J.R., and Jukes, P. (1994). A comparison between panel, joint and code shear strength. *Proc. 10th IBMaC, Calgary, Canada, pp.1481-1490*.

Rilem, T. C. (1994). LUM B6 Diagonal tensile strength tests of small wall specimens, 1991. RILEM Recommendations for the testing and use of constructions materials, 488-489.

Roy, H. and Sozen, M., 1964. Ductility of Concrete. *Proceedings of the International Symposium on the Flexural Mechanics of Reinforced Concrete, ASCE*, pp.213–235.

Rupakhety, R., Olafsson, S., & Halldorsson, B. (2017). The 2015 Mw 7.8 Gorkha Earthquake in Nepal and its aftershocks: analysis of strong ground motion. *Bulletin of Earthquake Engineering*, 15(7)

Sakai, H., Imayama, T., Yoshida, K., & Asahi, K. (2017). Tectonics of the Himalayas. *Journal of the Geological Society of Japan*, *123*, 403-421.

Sakurai, K. (2011). "Experimental Study on Retrofitting of Masonry Houses Using PP-band Method for Shapeless Stone Masonry and 2-story Adobe Masonry Houses", MSc Dissertation, IIS, The University of Tokyo, Japan

Sambu Potty, N. (2013). Properties of Brick Masonry for FE modeling.

Save the Children. (2016). Save the Children's Earthquake Response in Nepal: A Special One-Year Progress Report April 2016. [online] Available at: [https://www.issuelab.org/resources/24364/24364.pdf] [Accessed 31 August 2022].

Scala, S., Ricci, P., Del Guido, C., Gómez-Martínez, F. and Verderame, G. (2020). Simplified Analytical Methodologies for Seismic Fragility Assessment of RC Buildings with Infills. *17th World Conference on Earthquake Engineering*. Sendai.

Schildkamp, M., & Araki, Y. (2019). Cost analysis of mountain schools in Nepal: comparison of earthquake resistant features in rubble stone masonry vs. Concrete block masonry. *Frontiers in Built Environment*, *5*, 55.

Schildkamp, M., & Araki, Y. (2019). School buildings in rubble stone masonry with cement mortar in seismic areas: literature review of seismic codes, technical norms and practical manuals. *Frontiers in Built Environment*, *5*, 13.

Schildkamp, M., Silvestri, S., & Araki, Y. (2020). Rubble Stone Masonry Buildings With Cement Mortar: Design Specifications in Seismic and Masonry Codes Worldwide. *Frontiers in Built Environment*, 176.

Schildkamp, M., Silvestri, S., & Araki, Y. (2021). Rubble Stone Masonry Buildings with Cement Mortar: Base Shear Seismic Demand Comparison for Selected Countries Worldwide. Frontiers in Built Environment, 7, 18.

Scott B D , Park, R & Priestley, M. J N (1982). Stress-strain behaivior of concrete confined by overlapping hoops at low and high strain rates. *ACI Journal, 79(1), 13-27*.

Scott, M. and Fenves, G. (2006). Plastic Hinge Integration Methods for Force-Based Beam–Column Elements. Journal of Structural Engineering, 132(2), pp.244-252.

Senaldi, I., Guerrini, G., Scherini, S., Morganti, S., Magenes, G., Beyer, K., & Penna, A. (2018, July). Natural stone masonry characterisation for the shaking-table test of a scaled building specimen. In Proceedings of the 10th International Masonry Conference, Milan, Italy (pp. 9-11).

Shahzada, K., Khan, A., Elnashai, A., Ashraf, M., Javed, M., Naseer, A. and Alam, B. (2012). Experimental Seismic Performance Evaluation of Unreinforced Brick Masonry Buildings. *Earthquake Spectra*, 28(3), pp.1269-1290.

Shakya, M., & Kawan, C. K. (2016). Reconnaissance based damage survey of buildings in Kathmandu valley: An aftermath of 7.8 Mw, 25 April 2015 Gorkha (Nepal) earthquake. *Engineering Failure Analysis, 59, 161-184.*

Sheikh, S. A. (1982, July). A comparative study of confinement models. In *Journal Proceedings* (Vol. 79, No. 4, pp. 296-306).

Shome, N., Cornell, C., Bazzurro, P. and Carballo, J. (1998). Earthquakes, Records, and Nonlinear Responses. Earthquake Spectra, 14(3), pp.469-500.

Shrestha, R. K., Parajuli, H. R., & Poudel, B. (2021). Building typologies and code compliance issues of reconstructed houses after 2015 Mw 7.8 Gorkha, Nepal earthquake: Experience from Dhading District earthquake. *Progress in Disaster Science*, *10*, 100155.

Siano, R., Roca, P., Camata, G., Pelà, L., Sepe, V., Spacone, E., & Petracca, M. (2018). Numerical investigation of non-linear equivalent-frame models for regular masonry walls. Engineering Structures, 173, 512-529.

Skrekas, P., Sextos, A. and Giaralis, A. (2014). Influence of bi-directional seismic pounding on the inelastic demand distribution of three adjacent multi-storey R/C buildings. *Earthquakes and Structures*, 6(1), pp.71-87.

Smith, B., & Carter, C. (1969). A method of analysis for infilled frames. *Proceedings of the institution of civil engineers*, *44*(1), 31-48.

Snyman, M. F., & Martin, J. B. (1992). A consistent formulation of a dilatant interface element. *International journal for numerical and analytical methods in geomechanics*, *16*(7), 493-527.

Soliman, M. and Yu, C., 1967. The flexural stress-strain relationship of concrete confined by rectangular transverse reinforcement. Magazine of Concrete Research, 19(61), pp.223-238.

Sonda, D., Miyamoto, K., Kast, S., & Khanal, A. (2019). The restoration and seismic strengthening of the earthquake-damaged UNESCO heritage palace in Kathmandu. *International Journal of Architectural Heritage*, *13*(1), 153-171.

Stavridis, A. and Shing, P., (2010). Finite-Element Modeling of Nonlinear Behavior of Masonry-Infilled RC Frames. *Journal of Structural Engineering*, 136(3), pp.285-296.

Stevens, V. L., & Avouac, J. P. (2016). Millenary Mw> 9.0 earthquakes required by geodetic strain in the Himalaya. *Geophysical Research Letters*, 43(3), 1118-1123.

Stevens, V., Shrestha, S. and Maharjan, D. (2018). Probabilistic Seismic Hazard Assessment of Nepal. *Bulletin of the Seismological Society of America, 108(6), pp.3488-3510*

Subedi, B., & Parajuli, H. R. (2016). Probabilistic seismic hazard analysis of Nepal. In *Proceedings of IOE Graduate Conference* (pp. 265-270).

Taucer, Fabio F, E Spacone, FC Filippou. (1991) A Fiber Beam-Column Element for Seismic Response Analysis of Reinforced Concrete Structures. Report No. UCB/EERC-91/17. Earthquake Engineering Research Center, College of Engineering, University of California, Berkeley.

Taylor, HPJ. (1972). Shear strength of large beams. ASCE Journal of Structural Division, Vol 98

Terzic, V. (2011). Force-based element vs. Displacement-based element. *University of Berkeley, OpenSees, NEES, & NEEScomm*.

Thapa, D.R. and Guoxin, W (2013). Probablistic seismic hazard analysis in Nepal. Earthquake Engineering and Engineering Vibration, 12: 577-586.

Thirumalini, P., Ravi, R., Sekar, S. K., & Nambirajan, M. (2011). Study on the performance enhancement of lime mortar used in ancient temples and monuments in India. Indian Journal of Science and Technology, 4(11), 1484-1487.

Tothong, P. and Luco, N., (2007). Probabilistic seismic demand analysis using advanced ground motion intensity measures. *Earthquake Engineering & Structural Dynamics*, 36(13), pp.1837-1860.

Tubaldi, E., Barbato, M., & Ghazizadeh, S. (2012). A probabilistic performance-based risk assessment approach for seismic pounding with efficient application to linear systems. *Structural Safety*, *36*, 14-22.

UBC-97. (1997) Uniform building code. International Conference of Building Officials. Whittier, California

UNDP. (United Nations Development Program) (2010). Recommendations for Construction of Earthquake Safer Buildings - Earthquake Risk Reduction and Recovery Preparedness Programme for Nepal Department of Urban Development and Building Construction, Kathmandu, Nepal (2010)

Unicef. (2018). UNICEF Nepal Paves Way To Build Back Better After Devastating Earthquakes. [online] Available at: https://www.unicef.org/nepal/stories/unicef-nepal-paves-way-build-back-better-after-devastating-earthquakes *[Accessed 11 March 2020]*.

United Nations. (2015). Office for the Coordination of Humanitarian Affairs. Nepal: Earthquake 2015 Situation Report No.17. Available: https://reliefweb.int/sites/reliefweb.int/files/resources/-OCHANepalEarthquakeSituationReportNo.17%20%2821May2015%29.pdf. Last accessed 3rd Jan 2022.

USGS. (2016). M 7.8 - 36km E of Khudi, Nepal Retrieved from https://earthquake.usgs.gov/earthquakes/eventpage/us20002926/executive

USGS. (2018). U.S. Geological Survey, [online]. *See https://www.usgs.gov/ (accessed 10/03/2020).*

Valluzzi, M.R., Tinazzi, D. and Modena, C., (2002). Shear behavior of masonry panels strengthened by FRP laminates. *Construction and Building materials, 16(7), pp.409-416.*

Vamvatsikos, D., & Cornell, C. A. (2002). Incremental dynamic analysis. Earthquake engineering & structural dynamics, 31(3), 491-514.

Vamvatsikos, D., (2014). Accurate Application and Second-Order Improvement of SAC/FEMA Probabilistic Formats for Seismic Performance Assessment. *Journal of Structural Engineering*, 140(2), p.04013058.

Vanin, F., Penna, A., & Beyer, K. (2020). Equivalent-frame modeling of two shaking table tests of masonry buildings accounting for their out-of-plane response. Frontiers in Built Environment, 6, 42.

Varum, H., Furtado, A., Rodrigues, H., Dias-Oliveira, J., Vila-Pouca, N., & Arêde, A. (2017). Seismic performance of the infill masonry walls and ambient vibration tests after the Ghorka 2015, Nepal earthquake. *Bulletin of Earthquake Engineering*, *15*(3), 1185-1212.

Varum, H., Vila-Pouca, N., Furtado, A., Oliveira, J., Arêde, A., & Rodrigues, H. (2016). The infilled RC structures performance in the 25th April, 2015 Gorkha Nepal earthquake: Observations and dynamic characterization tests. In *Brick and Block Masonry* (pp. 2517-2524). CRC Press.

Verderame GM, De Luca F, De Risi MT, Del Gaudio C, Ricci P, (2012) A three level vulnerability approach for the damage assessment of infilled RC buildings: the Emilia 2012 case, *V1.0. Available at http://www.reluis.it/*

Verderame GM, Ricci P, De Luca F, Del Gaudio C, De Risi MT (2013) Damage scenarios for RC buildings during the 2012 Emilia (Italy) earthquake. *Soil Dyn Earthq Eng*

Verderame, G. M., De Luca, F., Ricci, P., and Manfredi, G. (2011). Preliminary Analysis of a Soft-Storey Mechanism after the 2009 L'Aquila Earthquake. *Earthquake Engng. Struct. Dyn.* 40 (8), 925–944. doi:10.1002/eqe.1069

Westoby, L., Wilkinson, S., & Dunn, S. (2021). The road to recovery: Understanding the challenges affecting school reconstruction in rural Nepal following the 2015 Gorkha earthquake. *International Journal of Disaster Risk Reduction*, 56, 102120.

Whitney, C. S. (1937, March). Design of reinforced concrete members under flexure or combined flexure and direct compression. In Journal Proceedings (Vol. 33, No. 3, pp. 483-498).

Woods, G.E.D. (2018) RC Masonry Infills In Nepal: Calibration of the Spectral Method FAST. Undergraduate Research Report Number. 1718RP002m. Department of Civil Engineering, University of Bristol

World Bank (2019) Global library of school infrastructure. [Available at :https://gpss.worldbank.org/sites/gpss/files/2019-06/IB4_LBM_UCM-URM3_LR_LD.pdf]

World Bank. (2013). Haiti Rebuilds Its Schools. [online] Available at: https://www.worldbank.org/en/results/2013/09/03/schools-safety-haiti-reconstruction *[Accessed 11 March 2020]*.

Wu, J. Y., Li, J., & Faria, R. (2006). An energy release rate-based plastic-damage model for concrete. International journal of Solids and Structures, 43(3-4), 583-612.

Wu, T., Wei, H., Zhang, Y., & Liu, X. (2018). Axial compressive behavior of lightweight aggregate concrete columns confined with transverse steel reinforcement. *Advances in Mechanical Engineering*, *10*(3), 1687814018766632.

Yi, W.H., Oh, S.H. and Lee, J.H., (2004). August. Shear capacity assessment of unreinforced masonry wall. *In 13th World Conference on Earthquake Engineering (pp. 1-12).*

Zarri, F. (1992). Consolidamento delle murature di edifici antichi mediante iniezioni di malta. *Costruire in Laterizio, 25, pp.63-69*

Zhuge, Y., Corderoy, J. and Thambiratnam, D. (1996). Behavior of unreinforced brick masonry under lateral (cyclic) loading. TMS Journal, 14(2), pp.55-62.